Redox and Spectroscopic Properties of Protonated Species of Iron Porphyrin Nitroxlys and Their Analogues

Md. Hafizur Rahman
Marquette University

Recommended Citation

Rahman, Md. Hafizur, "Redox and Spectroscopic Properties of Protonated Species of Iron Porphyrin Nitroxlys and Their Analogues" (2017). *Dissertations (2009 -)*. 729.
http://epublications.marquette.edu/dissertations_mu/729

REDOX AND SPECTROSCOPIC PROPERTIES OF PROTONATED SPECIES OF IRON PORPHYRIN NITROXYLS AND THEIR ANALOGUES

By

Md. Hafizur Rahman, M.Sc.

A Dissertation submitted to the Faculty of the Graduate School,
Marquette University,
in Partial Fulfilment of the Requirements for
the Degree of Doctor of Philosophy

Milwaukee, Wisconsin

August 2017

ABSTRACT

REDOX AND SPECTROSCOPIC PROPERTIES OF PROTONATED SPECIES OF IRON PORPHYRIN NITROXYLS AND THEIR ANALOGUES

Md. Hafizur Rahman, M.Sc.

Marquette University, 2017

Nitrite reduction to ammonia or nitrous oxide involves a series of electron transfer and protonation steps which are carried out by assimilatory or dissimilatory nitrite reductases. In the assimilatory process, nitrite incorporated into the biomass while in the dissimilatory process, it is excreted from the cell and the reaction is a source of energy. The complexes that will be studied in this work are models for assimilatory (siroheme) and dissimilatory (heme d_1) nitrite reductases. Iron porphyrin nitrosyls were reduced in the presence of weak acids such as phenol and substituted phenols. Voltammetric techniques such as cyclic and rotating ring disk electrode (RRDE) voltammetry were employed to elucidate the reduction/protonation reaction mechanism and kinetics. Cyclic voltammograms showed two closely spaced waves for the reduction of Fe(OEP)(NO) (OEP= octaethylporphyrin) in the presence of substituted phenols. The first wave corresponded to a single electron reduction and the second wave was a multielectron process which was kinetically controlled. To determine the kinetics of the first protonation, RRDE voltammetry on the first wave was studied. UV-visible spectroelectrochemistry was carried out to identify the protonated species that were formed. The results indicated that the two-protonated species were present, which were identified as Fe(OEP)(HNO) and Fe(OEP)(NH_2OH). The formation of these two species was suppressed by adding the conjugate base of the substituted phenol to the solution. FTIR spectroelectrochemistry was also employed to confirm those protonated species. Fe(OEP)(HNO) and Fe(OEP)(NH_2OH) were generated chemically and verified by UV-visible, FTIR and NMR spectroscopy. Other models showed similar behavior with slight differences. A series of iron corrole nitrosyl complexes were also studied. Even though the one electron reduction species were stable in both the voltammetric and spectroelectrochemical timescale, the protonation of reduced species was not observed in the experimental time scale.

ACKNOWLEDGMENTS

Md. Hafizur Rahman, M.Sc.

I am grateful to my research advisor Dr. Michael D. Ryan for his guidance, valuable suggestions and encouragement throughout graduate study. I am thankful to him for his continuous support, patience and tremendous opportunity of working in his resourceful laboratory. The way of his teaching inspired me to learn more and incited me to think deeply about the fundamentals of my research work.

I also want to express my sincere appreciation to my committee members, Dr. Chieu D. Tran, Dr. Adam Fiedler and Dr. Jier Huang for their valuable suggestions and supports. I am thankful to all professors for their help in my course lectures and teaching assistantship. I want to thank Dr. Sheng Cai and Dr. Surgey Lindeman for their instrumental support. I am very grateful to all chemistry graduate students in Marquette University for the discussion and help for research. A great appreciation for Paul Dion, Mark Bartelt and Lori Callaghan for their assistance in my graduate study.

Finally, I wish to thank my parents, sisters, brothers and relatives in Bangladesh for their inspiration throughout doctoral program. I also appreciate support from Bangladeshi community in Milwaukee.

TABLE OF CONTENTS

CHAPTER 1

INTRODUCTION

CHAPTER 2

EXPERIMENTAL MATERIALS AND METHODS

CHAPTER 3

VOLTAMMETRY OF IRON PORPHYRIN NITROSYLS

CHAPTER 4

UV-VISIBLE SPECTROELECTROCHEMISTRY

CHAPTER 5

NUCLEAR MAGNETIC RESONANCE (NMR)

CHAPTER 6

FTIR SPECTROELECTROCHEMISTRY

CHAPTER 7

STUDY ON IRON CORROLE NITROSYLS

CHAPETR 8

LIST OF TABLES

LIST OF FIGURES

Chapter 1

Chapter 2

Chapter 3

Chapter 4

Chapter 5

Chapter 6

Chapter 7

CHAPTER 1 INTRODUCTION

1.1 Nitrogen in Nature

Nitrogen is distributed throughout the Earth with 6% in the atmosphere, 94% in the lithosphere, 0.006% in the hydrosphere and biosphere.[1] Organic nitrogen molecules like hormones, amino acids and nucleic acids are essential for the animals and plant kingdoms. Inorganic nitrogen, e.g. nitrate, nitrite and nitric oxide play an important role in the growth and reproduction of plants and auxotrophic bacteria. In addition, nitrite and nitric oxide serve as signaling molecule.[2,3] The distribution of nitrogen or nitrogen species is controlled by the nitrogen cycle which is an interconnected network of chemical transformations that recycle nitrogen among lithosphere, atmosphere, hydrosphere and biosphere.

For incorporation into the biomass, nitrogen must be reduced to ammonia from elemental nitrogen or from nitrate.[4] The assimilatory and dissimilatory reduction processes are shown in Figure1-1.

The supply of nitrogen in an assimilatable form can be obtained in two ways. Some plants enter symbiotic relationship with bacteria which can accumulate nitrogen from atmosphere while others rely on nitrate within the soil. In the agricultural field, nitrate fertilizers are used to enhance crop yield. Nitrate which is highly soluble can be leached from soil and accumulate in surface and ground water. Nitrate containing water has adverse effects on human health. On the other hand,

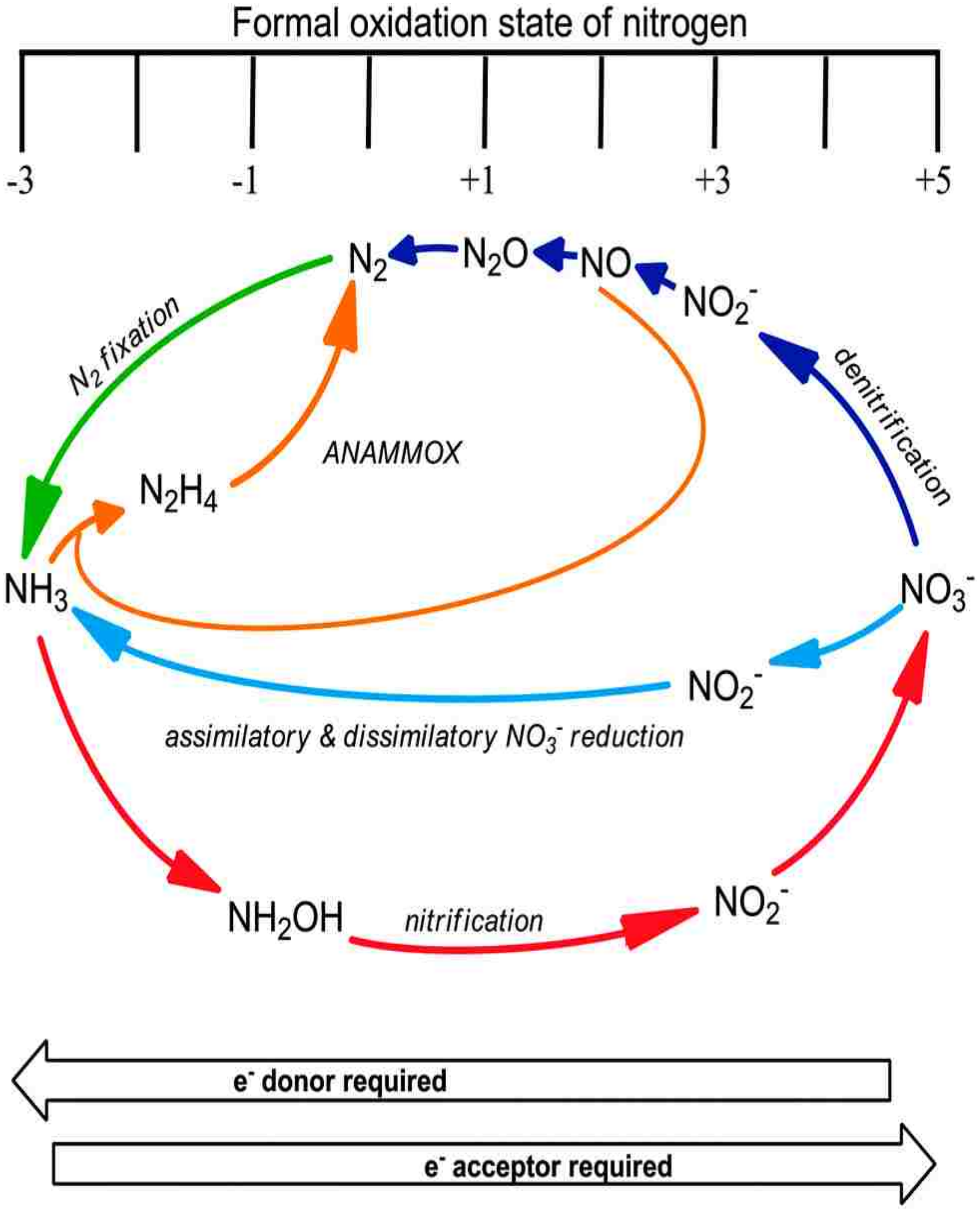

Figure 1-1. A Schematic representation of the bacterial nitrogen cycle.[3]

nitrate can be reduced by the bacterial dissimilatory process and can produce greenhouse gases like nitrous oxide. Thus, the nitrate assimilation pathway has ecological, agricultural and medical importance. The study of nitrate assimilation mechanism might improve the fertilizer efficiency by decreasing the cost of fertilizer while ecologically negative aspects of nitrate fertilization would be overcome.[5]

1.2 Assimilatory Nitrite Reduction

The reduction of nitrate to ammonia in the assimilatory process occurs in two enzymatic steps. [6] In the first step, the nitrate is converted to nitrite by a two-electron reduction by a molybdoenzyme nitrate reductase. In the second step, nitrite is reduced to ammonia by six electrons which is catalyzed by a heme containing enzyme. Assimilatory nitrite reductase is a soluble, multi-center redox enzyme commonly found in spinach,[7,8] *Neurospora* and vegetable marrow.[9] In higher plants, the electrons required for the reduction come from reduced ferredoxin which is supplied by the photosynthetic reaction.[10]

In fungi and bacteria, the enzyme uses reduced nicotinamide adenine dinucleotide phosphate as the electron donor.[11] The prosthetic group in assimilatory nitrite reductase has been identified as an isobacteriochlorin (siroheme)[12-20] which is connected to a (4F-4S) cluster[21-23] that accepts electrons from an electron donor and subsequently transfers them to the siroheme iron center which is the binding site of substrate, nitrite.

The structure of the siroheme macrocycle and a schematic diagram of the active center of sulfite reductase hemoprotein is shown in Figure 1-2.

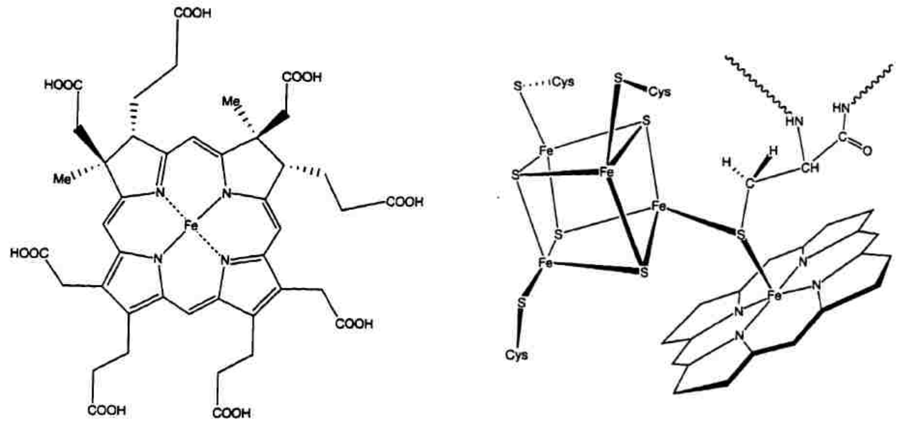

Figure 1-2. Structure of siroheme and active center of sulfite reductase hemoprotein.[26]

The isolation of assimilatory nitrite reductase is very difficult and most studies have been carried out with *E.coli* sulfite reductase, which is a complex of flavin and hemoprotein subunits (MW=670 kDa).[24] The catalytic subunit, hemoprotein, is similar to that which is present in plant nitrite reductases.[23-24] It has also been shown that the plant nitrite reductase and *E.coli* sulfite reductase have considerable amino acid homology. [25] The enzyme is large and complex, but the prosthetic groups are relatively small. The simplicity of prosthetic group allows scientist to synthesize model compounds such as porphyrins and hydroporphyrins and to study the reactions that are catalyzed by the enzyme. Although the enzymatic reduction process has not been fully elucidated yet, studies thus far have shown that the substrate nitrite binds to the siroheme iron center which is reduced to an iron nitrosyl, nitroxyl (HNO), hydroxylamine and then ammonia.[26]

$NO_2^- \rightarrow NO \rightarrow HNO \rightarrow NH_2OH \rightarrow NH_4^+$

Among these intermediates, only the enzyme bound nitrosyl has been found to be present during turnover.[27] Nitroxyl and hydroxylamine has been proposed as possible intermediates,[28,29] but experimental evidence is lacking.

1.3 Dissimilatory Nitrite Reduction

In this process, nitrite is reduced to dinitrogen, nitric oxide or nitrous oxide and the enzyme which catalyzes the initial reduction is called dissimilatory nitrite reductase.

The prosthetic group of one of these enzymes contains four hemes, two heme *c* (an iron porphyrin) and two heme *d*. It has been isolated from *Pseudomonas aeruginosa* bacteria and identified as a porphinedione (Figure 1-3).[30]

The process catalyzed by dissimilatory nitrite reductase is the reduction of nitrite to nitric oxide.[31]

$$NO_2^- \rightarrow NO \rightarrow N_2O \rightarrow N_2$$

Further reduction to N_2O and N_2 are catalyzed by separate enzymes.[32-35] It is notable that both assimilatory and dissimilatory nitrite reduction proceeds via an enzyme bound nitrosyl complex which is an important and stable intermediate in the reduction mechanism.

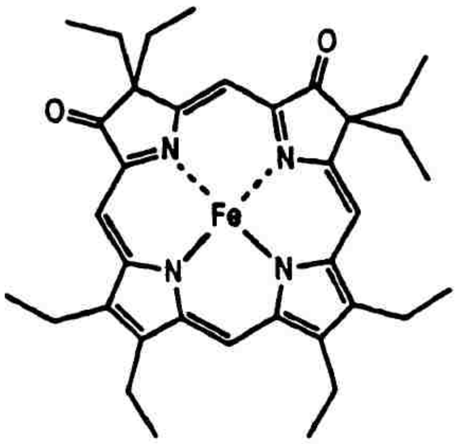

Figure 1-3. Structure of Heme d_1 Porphinedione.

1.4 Why Model Complexes

Even though the nitrite reductases are large and complex in structure, their small prosthetic group allows us to model those mechanistic processes in biology using synthetic porphyrins. It is very difficult to study the individual effects by studying only the proteins.

With model complexes, one can control the steric, electronic and environmental factors and document the influences on the redox mechanism, thus providing the interpretive framework for further study on the intact system. The models selected for analysis are sometimes readily available from nature or easily synthesized (TPPs and OEPs) in the laboratory. In recent years, capped and picket fence porphyrins have been studied to understand the molecular environmental effects of the several natural metalloproteins. The reactivity of synthetic models and their behavior as an electron acceptor or donor provide important insights to understand the possible electron transfer mechanism and other processes in vivo by large molecules.

1.5 Nitric Oxide as a Ligand

Nitric oxide is a gaseous, inorganic, uncharged diatomic molecule. The molecular orbital diagram shows a unpair electron in the antibonding orbital which might be responsible for the unique physiological functions of nitric oxide molecule (Figure1-4). Because of the electronegativity difference between oxygen and nitrogen, the bonding orbitals predominantly belong to oxygen and antibonding orbitals belong to nitrogen atom. The unpaired electron in the π* orbital is polarized toward to the nitrogen is the reason why the reaction of nitric oxide with transition metals occurs exclusively through the nitrogen atom.

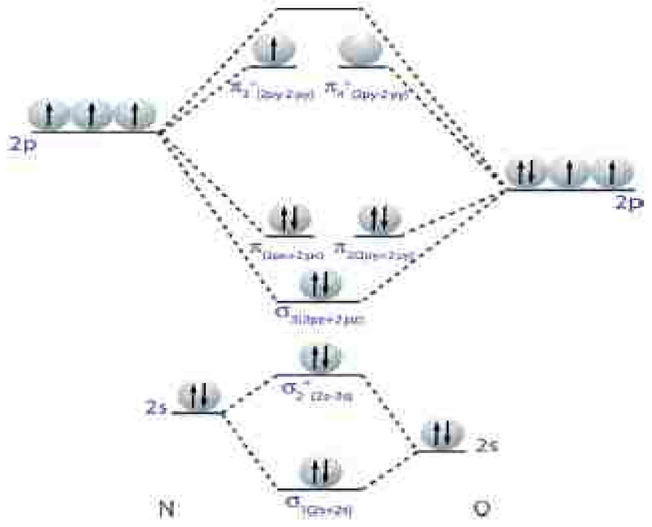

Figure 1-4. Qualitative energy level and molecular orbital diagram for NO.[36]

The molecular orbital diagram shows the radical nature of NO and a bond order of 2.5, which is consistent with its intermediary bond length (1.15 Å) between those of N_2 (1.06 Å) and O_2 (1.18 Å).[36] Because of these unique electronic properties, nitric oxide has drawn special attention from the scientific community. In the past, it was thought that the radical was a toxic reactive species. When the connection between endothelial derived relaxing factor and nitric oxide was made, it was surprise.[37-39,40] When the nitric oxide binds to an iron atom, a strong σ bond is formed by the donation of π* orbital electron to d_{z^2} of iron atom. In addition, significant π back bonding is observed between empty π* orbital of NO and t_{2g} orbitals of iron.[41]

Lymar and coworkers extensively studied the reduced nitric oxide species in aqueous medium.[42-44] The one electron reduced nitric oxide is isoelectronic with oxygen molecule (triplet ground state). This nitroxyl anion is easily protonated. The formation of the protonated species changes the ground state spin from triplet to singlet. This is a rare example of conjugate acid/base couples with different multiplicity. This acid/base equilibrium is spin forbidden and inherently slow. [45]

$$^{1}HNO \rightarrow {}^{3}NO^{-} + H^{+} \qquad (A)$$

$$^{1}HNO + OH^{-} \rightarrow {}^{3}NO^{-} + H_2O \qquad (B)$$

The slowness of the protonation/deprotonation depends on the energy of activation. Figure 1-5 depicts the energy necessity for activation. The intersystem barrier is responsible for the slowness of the reaction. The estimated energy 28 kJ/mol which is close to experimental E_a = 30 kJ/mol.

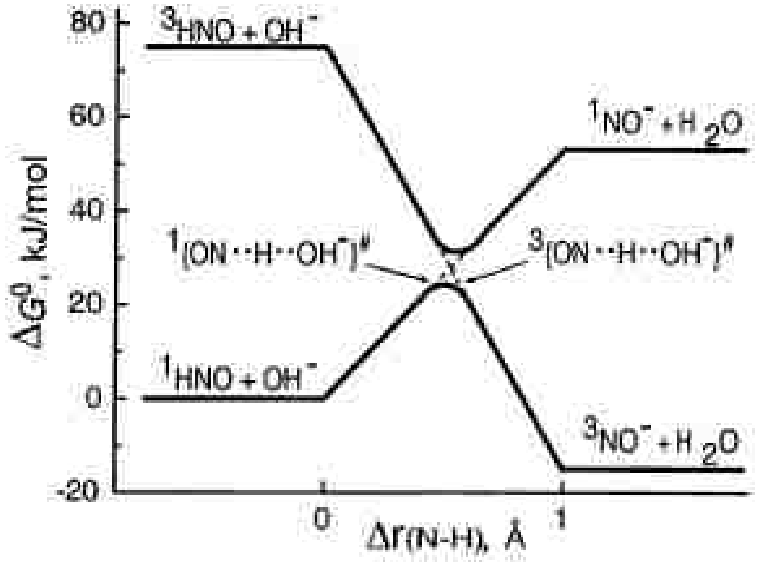

Figure 1-5. Free energy change drawn to scale for various reactions of the^{1}HNO + OH$^-$ couple in water. Solid lines approximate adiabatic energy profiles along the N-H distance change during proton transfer, ¢*r*(N-H), that is shown as a reaction coordinate.[43]

In aerobic conditions, the nitroxyl anion forms peroxynitrite.

$HNO/NO^- + O_2 \rightarrow ONOOH/ONOO^-$ (C)

The dimerization of HNO produces N_2O with rate constant $k = 8\times10^6\ M^{-1}s^{-1}$.[42] The redox potential for nitric oxide in triplet ground state is about -0.76 vs NHE. The production of singlet nitroxyl anion is energetically less favorable and the redox potential is -1.7 V vs NHE. The redox potential for the protonation on the nitroxyl anion is (NO, H^+/HNO = -0.14 V) and (HNO. $2H^+/NH_2OH$) = 0.7 V; the corresponding values at pH = 7 are -0.55 V and 0.3 V vs NHE.[42] The potentials for HNO are feasible in biological system which makes it a biological oxidant and reductant.

1.6 Iron Porphyrin Nitrosyls

Both assimilatory and dissimilatory nitrite reduction proceeds via an enzyme-bound nitrosyl complex, and further reduction of the nitrosyl generates different products such as ammonia in assimilatory nitrite reduction and nitrous oxide and dinitrogen in dissimilatory nitrite reduction. As nitrosyl is a key intermediate for the two types of nitrite reduction then the difference between the two reductions can be understood if the reduction mechanism of the nitrosyl can be elucidated. At present, the conversion of nitrosyl to ammonia or nitrous oxide is still not clear.

Besides the nitrite reductase, the Fe(II)(heme)(NO) complex also occurred in soluble guanylate cyclase (cGC) where the nitrosyl complex is a signal to promote its activation. [46, 47] It also binds to cytochrome c oxidase (CcOx). A physiological (normal condition) and pathophygiological (abnormal condition) interaction of NO with heme has been observed in human and animals (Figure 1-6).

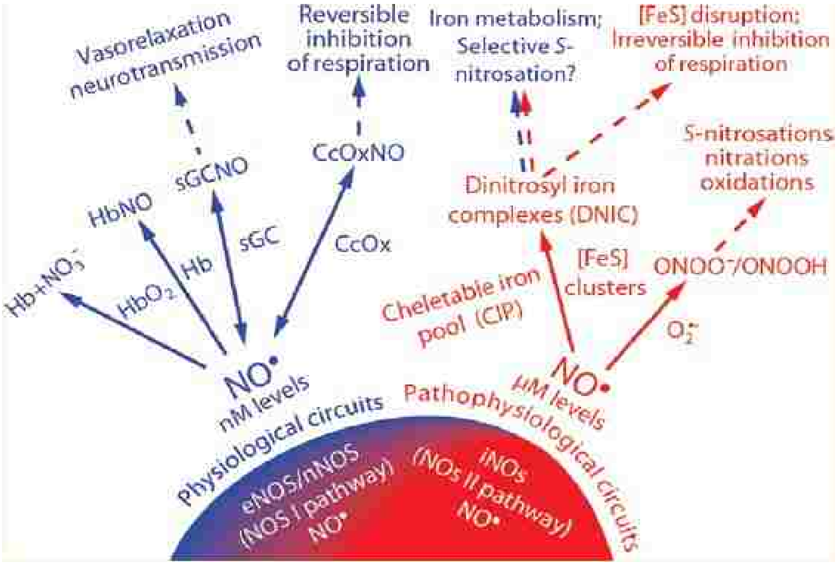

Figure 1-6. Nitric oxide interaction with different complexes.[36]

The electrochemistry,[48-55] molecular structure,[56-59] infrared spectroscopy,[60,61] electron paramagnetic resonance spectroscopy, [60-62,65,66] and resonance Raman spectroscopy[62-64] of iron nitrosyl porphyrin complexes have been reported. The X-ray crystallographic studies [56] showed that the Fe-N-O moiety is bent in Fe(II)(TPP)(NO) with angle 149.2° and is linear in Fe(III)(TPP)(NO)(ClO_4).[59] The deviation of iron atom from the mean plane of porphyrin core is 0.21 Å in Fe(TPP)(NO) and 0.29 A in Fe(OEP)(NO)(ClO_4). In 2000, Scheidt group showed that the Fe-N(NO) vector is several degrees off from the heme normal.[67] The equatorial Fe-Np bonds are correlated to the tilt of nitrosyl (Figure 1-7). The Fe-Np bonds become shorter when Fe-N-O tilted between those two pyrroles, other two Fe-Np bonds opposite to the tilt become lengthen and vice versa. Hoffmann et al. suggested that the tilting resulted from an increased interaction of the π* orbital of NO with the metal d_{z^2} orbital and that can be achieved by a sideways movement of nitrosyl with respect to the normal of heme (Figure 1-8).

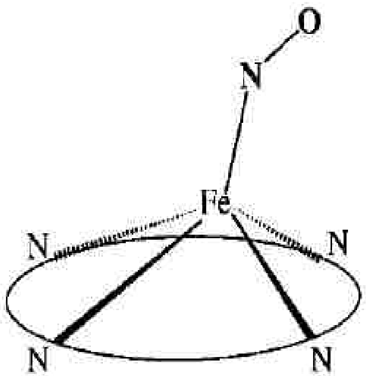

Figure 1-7. Diagram illustrating the nature of correlated tilt/asymmetry found in five-coordinated Fe(P)(NO) derivatives. The two equatorial Fe-Np bonds to the right (in the direction of the tilt) are shortened, while the Fe-Np bonds to the left are lengthened. The magnitudes of the distortion have been exaggerated for clarity.[67]

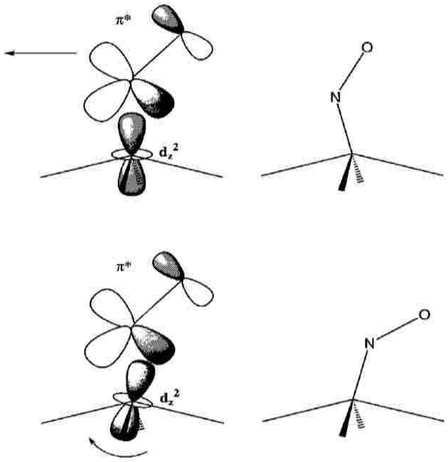

Figure 1-8. Diagram illustrating possible distortions leading to greater overlap of the half-occupied π*NO orbital with the iron d_{z2} orbital that leads to two different tilt directions.[67]

The spin state of iron plays a vital role in the behavior of macrocycles. The d^5 Fe (III) and d^6 Fe(II) ions in porphyrins can exhibit three different states as low-spin, intermediate – spin and high-spin (Figure 1-9). The spin state and stereochemistry of the iron center is controlled by the nature and number of axial ligands. Generally, coordination of strong field ligands to iron center gives low spin iron complex while a weak field ligand leads to high spin complex. The five-coordinated iron is out of porphyrin plane while the six-coordinated iron is in or nearly in the plane of the macrocycle. In the ferrous porphyrin complex, the iron is a little out of the plane because of its larger size compared to Fe(III) even though it is six coordinated. The intermediate spin was observed in 4-coordinate Fe(II) porphyrins such as Fe(TPP) in benzene or methylene chloride. [67]

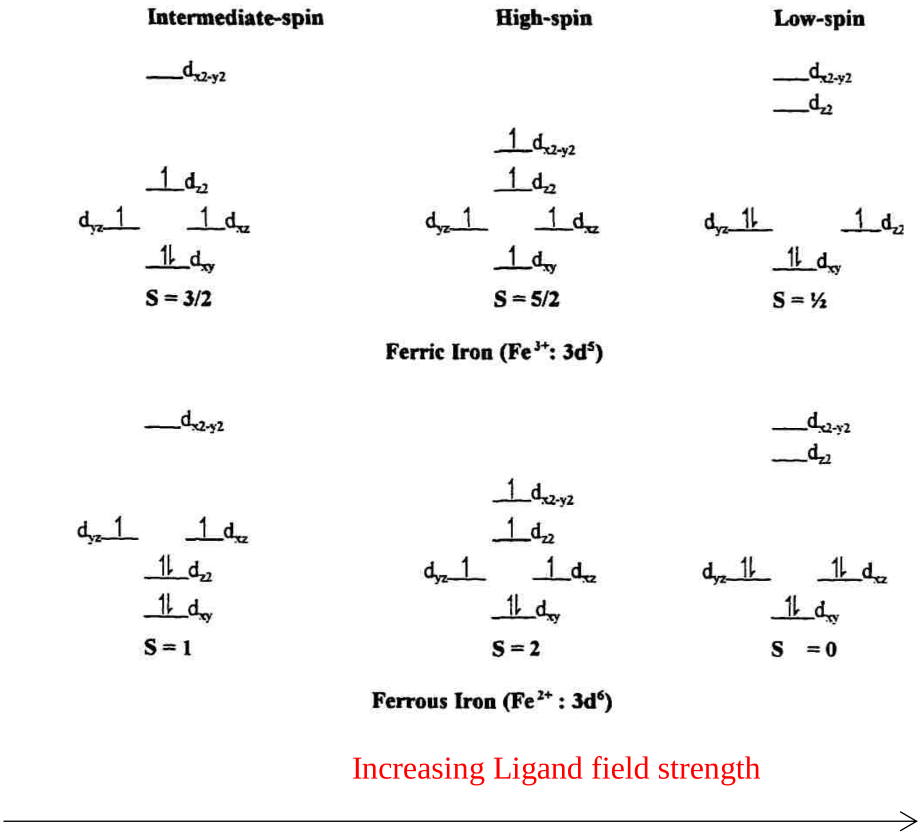

Figure 1-9. Energy levels and electron occupancy of *3d* orbitals in ferric and ferrous heme systems.[68]

1.7 Electrochemistry of Iron Porphyrin Nitrosyls

In general, metalloporphyrins might be oxidized or reduced at three different sites; at the porphyrin ring, the metal or at the axial ligand. Up to three reduction waves and three oxidation waves have been observed depending on the porphyrin macrocycles and solvents used. Voltammetry of Fe(TPP)(NO) and Fe(OEP)(NO) has been studied extensively in non-aqueous solvents.[52-55] The first reduction and oxidation for Fe(TPP)(NO) and Fe(OEP)(NO) were reversible in voltammetry time scale.[53, 55]

The bulk reduction in methylene chloride or pyridine did not lead to the isolation of $Fe(TPP)(NO)^-$ even though the reduced species is stable on the voltammetry and spectroelectrochemical time scale. The $Fe(TPP)(NO)^-$ was converted to Fe(TPP)(NO) by a catalytic process which was confirmed by the appearance of the visible spectrum of Fe(TPP)(NO) after the addition of 10 equivalent of electrons.[52] On the other hand, bulk oxidation of Fe(TPP)(NO) did not give $Fe(TPP)(NO)^+$, rather give $Fe(TPP)(ClO_4)$ or $Fe(TPP)_2O$.[53] The axial coordination by substituted pyridines and amines on the reduction of Fe(TPP)(NO) and Fe(TPC)(NO) have been examined.[51] A weak coordination of pyridine/amine have been observed. The ligands were lost upon further reduction. The pyridine binding constant of Fe(TPP)(NO) was 0.7 M^{-1}, which dropped to <0.03 M^{-1}in $Fe(TPP)(NO)^-$. This value indicates that the NO^- has a stronger trans effect than NO. Lehnert et al. [71] showed the same trans effect with a different porphyrin $Fe(To\text{-}F_2PP)(NO)$ using 1-methylimidazole as a model for His in proteins. The binding constant to $Fe(To\text{-}F_2PP)(NO)$ is 2055 M^{-1} which dropped to << 0.2 upon reduction.

The redox potential of one and two electron reduced species in organic solvents with a variety of models like Fe(OEP)(NO), Fe(TPC)(NO), Fe(MOEC)(NO), Fe(2,4-DMOEiBC)(NO), Fe(OEPone)(NO), Fe(2,4-OEPdione)(NO) and Fe(2,3-OEPdione)(NO) have been reported ((Figure 1-10).[69,70]

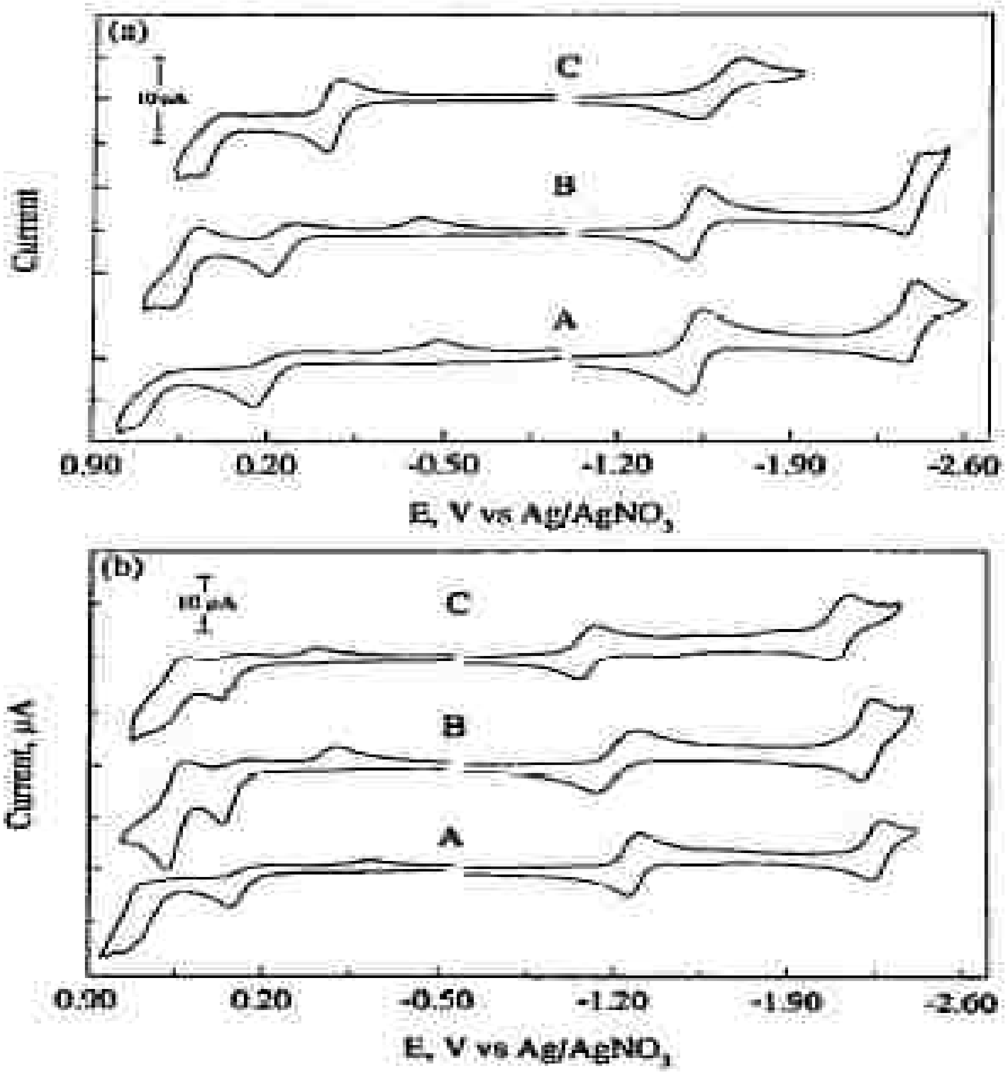

Figure 1-10. a) Cyclic voltammograms of Fe(OEP)(NO) (A) Fe(MOEC)(NO) (B) Fe(2,4-DMOEiBC)(NO) (C) in THF b) Cyclic voltammograms of Fe(OEPone)(NO) (A), Fe(2,4-OEPdione)(NO) (B), Fe(2,3-OEPdione)(NO) (C) in THF, Scan rate 100mV/s. Supporting electrolyte 0.10 M TBAP, Working electrode Pt.[70]

The polarographic and voltammetric of reduction of Fe(P)(NO), where P= TPP, OEP, TPC gave three waves. The first two waves were reversible and the third reduction showed reversible electron transfer followed by an irreversible chemical reaction based on the slope of the plot $E_{1/2}$ vs log[(id-i)/i] for polarographic wave, where the slopes were 59 mV, 55 mV and 60 mV for wave I , wave II and wave III respectively.

The Fe(OEP)(NO) and Fe(MOEC)(NO) complexes showed two reduction waves and both reactions were almost at same potential. The first reduction was reversible where the second reduction was reversible only at higher scan rate. At lower scan rate (less than 0.1 V/s), the $i_p/v^{1/2}$ values increased with the decrease of scan rate indicating a following reaction. The Fe(2,4-DMOEiBC)(NO) also showed a first reduction wave at a more negative potential (100 mV more) and the second reduction wave was 350 mV more negative than Fe(OEP)(NO) and Fe(MOEC)(NO). The first oxidation was irreversible for Fe(OEP)(NO) and Fe(MOEC)(NO) but was reversible for Fe(2,4-DMOEiBC)(NO). The second oxidation was irreversible for all the complexes. The porphinone and porphinedione iron nitrosyls showed two one-electron reductions and an oxidation. The reductions were reversible and the oxidation was irreversible. The iron porphinone nitrosyls were easier to reduce than methylated porphyrin nitrosyls.[69]

The reduction of iron porphyrin nitrosyls in the presence of acids was studied extensively by Liu et al.[72] The pulse polarography technique was used to obtain the kinetic parameters for the multi-electron reduction of Fe(P)(NO) in weak acids. The advantages of this technique were that the time window can be varied from 1-1000 ms and the kinetically important current could be obtained on the limiting current plateau which eliminates the effect of slow electron transfer interference. In addition, the reduction of acids was suppressed by the mercury electrode. The first wave was shifted in a positive direction without changing the limiting current (Figure 1-11) and a new wave was observed at a potential positive of the second electron reduction in the absence of acids. Examining the potential shift, it was observed that the shift was nonlinear and exceeded 59 mV slope which indicates more than single protonation. (Figure 1-12). Based on the potential shift following reaction scheme was proposed.

$$\mathbf{Fe(TPP)(NO) + e^- \rightarrow Fe(TPP)(NO)^-} \qquad \mathbf{(1\text{-}1)}$$

$$\mathbf{Fe(TPP)(NO)^- + PhOH \rightarrow Fe(TPP)(NHO) + PhO^-} \qquad \mathbf{(1\text{-}2)}$$

$$\mathbf{Fe(TPP)\ (NHO) + PhOH \rightarrow Fe(TPP)(NH_2O^+) + PhO^-} \qquad \mathbf{(1\text{-}3)}$$

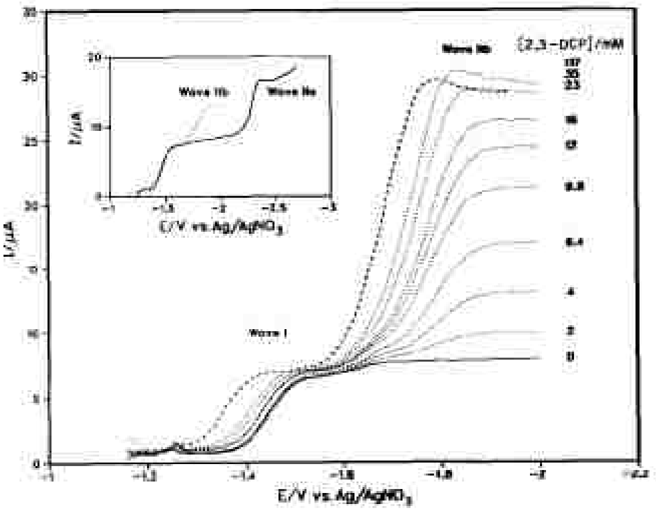

Figure 1-11. Normal pulse polarography of Fe(TPP)(NO) in the presenceof 2,3-dichlorophenol: -, [2,3-dcp] = 0; - - -, [2,3-dcp] =117 mM; . . . . , intermediate concentrations given on graph. Inset: ----, [2,3-dcp]=0 ......, [2,3-dcp] = 4.0 mM. Solvent THF, reference electrode 0.1 M Ag/AgNO$_3$, in acetonitrile, working electrode static mercury drop electrode, electrolyte 0.10 M TBAP, pulse time 80 ms, concentration of Fe(TPP)(NO) 0.60 mM.[72]

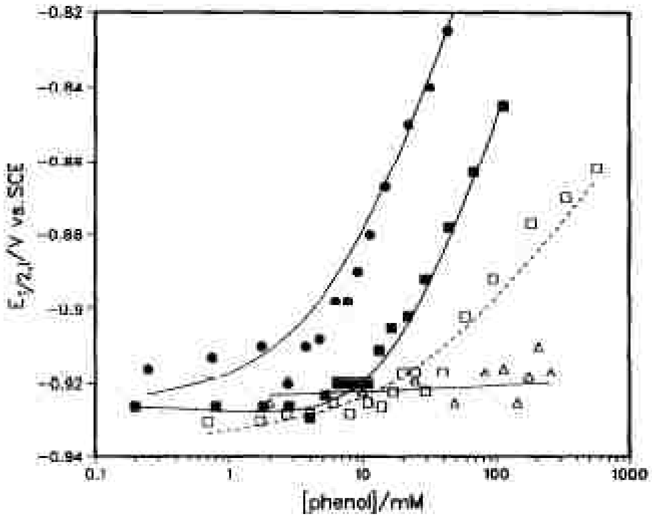

Figure 1-12. Effect of 2,3-dichlorophenol (■), 2,6-dichlorophenol (□), 3,4,5-trichlorophenol (●) and phenol (△) on the $E_{1/2}$ of the first wave of Fe(TPP)(NO) using d.c. polarography. The solid lines were constructed using eqn. (1-4). The dotted line is for 2,6-dichlorophenol where $K_1 = 0.018$ and $K_2 = 0$. Solvent THF, Fe(TPP)(NO) = 0.41 mM, supporting electrolyte 0.10 M TBAP, reference electrode SCE.[72]

$$E_{1/2,\,p} = E_{1/2,np} + 0.059 \log\left(1 + K_1[\mathrm{PhOH}]/[\mathrm{PhO}^-] + K_1K_2[\mathrm{PhOH}]^2/[\mathrm{PhO}^-]^2\right) \tag{1-4}$$

Rearranging Equation 1-4 and plotting the $E_{1/2}$ vs phenol concentration, a straight line should be obtained and the K_1K_2 can be obtained from the slope. But Figure 1-12 showed a weak dependence of potential shift with the phenol concentration. All the acids showed the same trend except for 2,6-dcp which never exceeded 59 mV. This indicated a single protonation of Fe(OEP)(NO)$^-$.

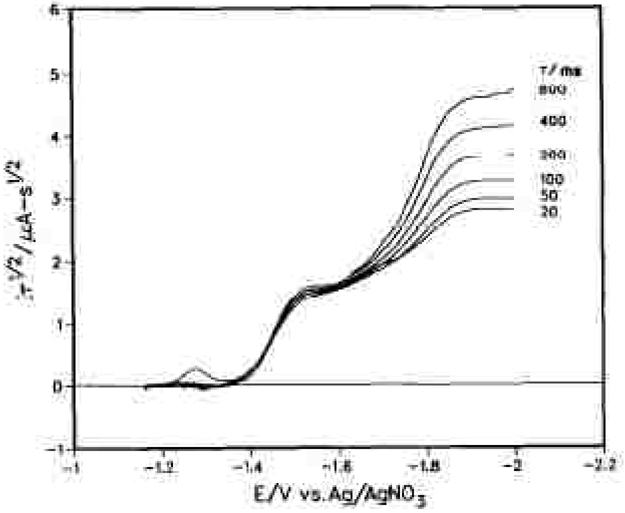

Figure 1-13. Normal pulse polarography of Fe(TPP)(NO) in the presence of 4.0 mM 2,3-dichlorophenol for a series of pulse times. Solvent THF, reference electrode 0.1 M Ag/$AgNO_3$, in acetonitrile, working electrode static mercury drop electrode, supporting electrolyte 0.10 M TBAP, concentration of Fe(TPP)(NO) 0.60 mM.[72]

The reversibility the electron transfer for wave I was confirmed by the independence of first wave on the phenol concentration and pulse time (Figure 1-13). In addition, the slope of the plot log[(I_L-I)/I)] vs potential maintained 59 mV for all acids. The square wave voltammetry showed the chemical reversibility for the first wave whereas the second wave was irreversible in the presence of acids. The second wave which involved a multielectron transfer was dependent on the pulse time, indicating a kinetically controlled reaction. The current depended on the pulse time and the acid concentration. At high acid concentration or long pulse times, the current was no longer kinetically controlled and was proportional to three electrons. But at lower acid concertation, the kinetic current was independent on pulse time (Figure 1-14).

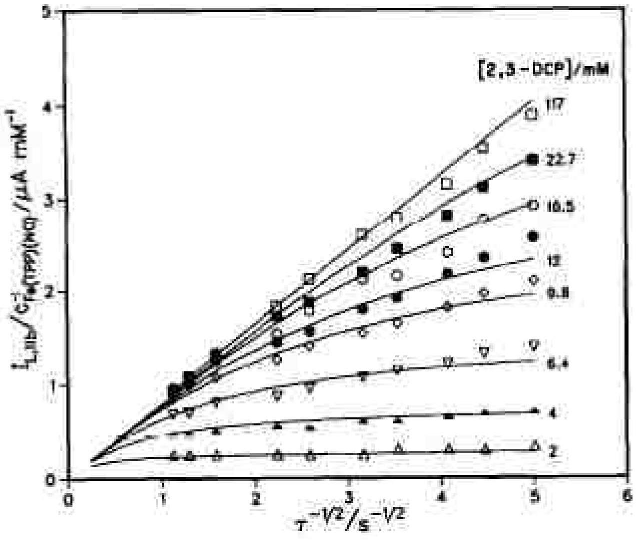

Figure 1-14. The limiting current of wave IIb as a function of $\tau^{-1/2}$ for Fe(TPP)(NO) for a series of concentrations of 2,3-dichlorophenol and pulse times τ. Solvent THF, reference electrode 0.1 M Ag/AgNO$_3$ in acetonitrile, Electrolyte 0.10 M TBAP.[72]

The behavior showed in Figure 1-13 and 1-14 and the potential shifts for first wave was consistent with a CE mechanism (Reactions 1-1, 1-2, and 1-5).

$Fe(TPP)(NH_2O^+) + 3e^- + 3PhOH \rightarrow Fe(TPP)^- + NH_2OH + PhO^-$ (1-5)

At higher concentrations of acids, the formation of Fe(P)NH$_2$O$^+$ is no longer rate limiting. At lower concentrations, the current was proportional to its rate of formation. For the second wave, the mechanism was considered EC$_{ir}$E mechanism because the reduction of Fe(P)NH$_2$O$^+$ was easier than Fe(P)NO$^-$. To observe the relationship between the phenol concentration and rate, the dependence of kinetic current on time was removed by Equation 1-6.

$$\lambda/\tau^{1/2} = (Kk_f)^{1/2} = \text{constant} \qquad \textbf{(1-6)}$$

The effect of chemical equilibrium on kinetic parameter was removed by averaging the constant ($\lambda/\tau^{1/2}$) for all pulse times at specific concentration of phenol. The k_f was estimated by the equation,

$$k_f = (\lambda/\tau^{1/2})_{ave}/K^{1/2} \tag{1-7}$$

Where K was determined from the potential shift as a function of acid concentration.

The value of k_f was found to vary linearly with the concentration of phenol, indicating that the reaction was pseudo-first order.

The kinetic current for the reduction in the presence of the phenolate base decreased as the phenolate concentration was increased. This indicated that the protonation step was reversible. With the addition of base, the $E_{1/2}$ shifted in a negative direction indicating less Fe(P)(HNO) was formed. The current for the second wave also decreased because of the formation of the double protonated species was suppressed.

After determining the kinetic parameters and plotting them against pK_a, the plot showed a slope near unity indicating that all variation in the kinetic parameters was due to the variations of equilibrium constants (Figure 1-15). In addition, there was no significant difference in the rates for different acids indicating the reactivities in the presence of acids due to the equilibrium effects.[72]

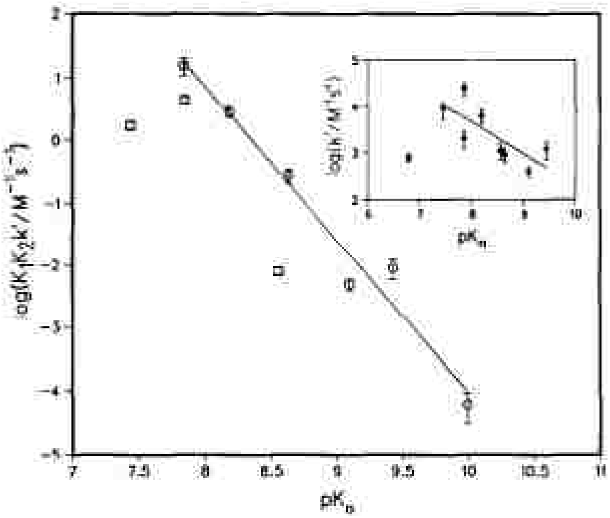

Figure 1-15. Variation in the K_1K_2k' values as a function of the pK_a of the substituted phenol: ○ phenols which are not 2-substituted, □ 2-substituted phenols; ---- least-squares fit line for the phenols that do not contain substitution at the 2-position. Inset: variation in log k' as a function of pK_a of the substituted phenol: ---- least-squares fit for all the data except 2,6-dcp; ■ 2-substituted phenols, ● 3- and 4-substituted phenols.[72]

The extent of protonation and the formation of Fe(TPP)(NH_2OH) could be controlled by the addition of phenolate base. The Fe(TPC)(NO) showed similar behavior in the presence of acids. The coulometric reduction of Fe(TPP)(NO) and Fe(TPC)(NO) at the wave IIb potential produced 90-100 % ammonia at higher concentration of acid (20 mM) where at lower concentration acids gave mixture of Fe(TPP) and Fe(TPP)(NO). The visible spectra were taken at low temperature to stabilize the protonated species but no change was observed in the spectra. The low temperature UV-visible spectroelectrochemical experiment showed the formation of ammonia rather than hydroxylamine characterized by Soret band at 424 nm and two other band at 531 and 562 nm (Figure 1-16). The formation of Fe(TPP)$(NH_3)^{2+}$ was confirmed by voltammetry with a one electron reduction wave at -0.54 V vs Ag/$AgNO_3$.[69]

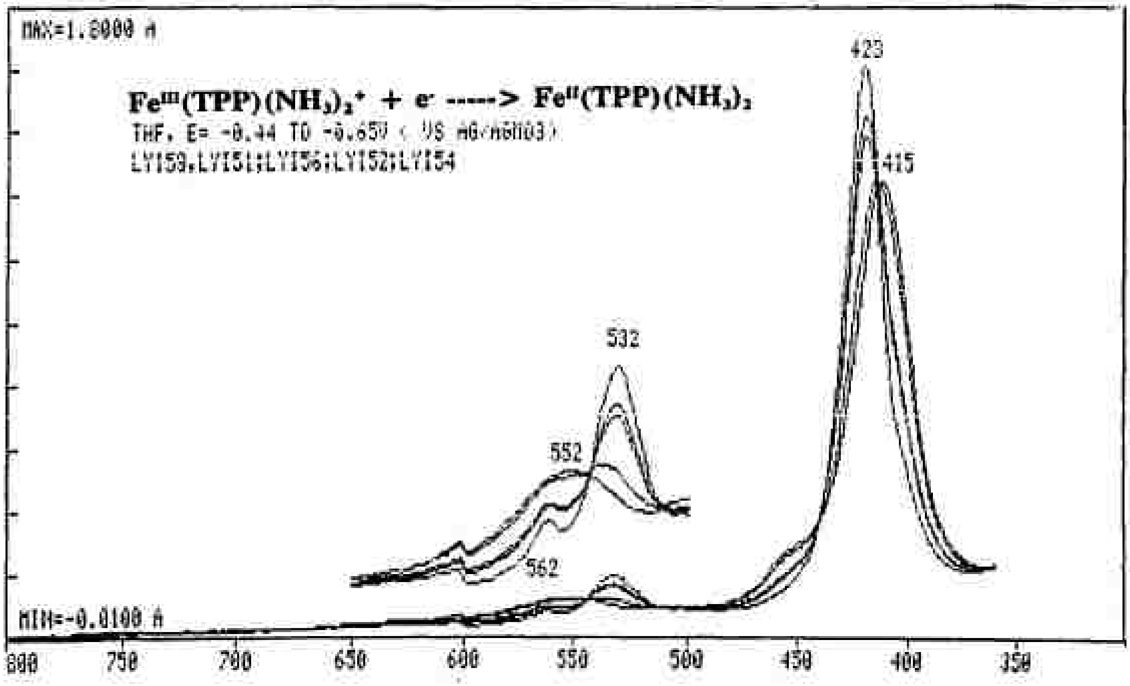

Figure 1-16. Visible spectra obtained during the reduction of Fe(TPP)$(NH_3)^{2+}$ in THF by OTTLE visible spectroelectrochemistry.[69]

The reduction and protonation reactions were also observed for Fe(OEP)(NO), Fe(MOEC)(NO), Fe(2,4-DMOEiBC)(NO), Fe(OEPone)(NO) and Fe(2,4-OEPdione)(NO).

In the presence of 2-chlorophenol (cp), Fe(OEP)(NO), Fe(MOEC)(NO) and Fe(2,4-DMOEiBC)(NO) showed similar polarographic behavior. The variation of the limiting current for Wave I and Wave IIb was studied as a function of the concentration of 2-cp.

The concentration needed to see wave IIb followed the order: Fe(2,4-DMOEiBC)(NO) < Fe(MOEC)(NO) ≈ Fe(OEP)(NO).

For Fe(2,4-OEPdione)(NO) , the current for wave I was independent of concentration of 2-cp and the wave shifted to positive potential with the increase in 2-cp concentration. The $E_{1/2}$ change with the concentration of 2-cp gave a slope 82 mv suggested the reduced species readily protonated and, when the concentration was greater than 10 mM even Fe(2,4-OEPdione)(NO) could be protonated to form Fe(2,4-OEPdione)$(NHO)^+$ which was then reduced. It also showed that the current for wave IIB increased with the increase in the concentration of acid, and produced ammonia at very high concentrations of acid.

There was no difference in the reduction mechanism for Fe(2,4-DMOEiBC)(NO) , Fe(MOEC)(NO) and Fe(OEP)(NO) but there was difference in the reaction rate . The $K_1K_2k_{2f}$ value for Fe(2,4-DMOEiBC)(NO) was 70 times greater than for Fe(MOEC)(NO) and Fe(OEP)(NO).

The basicity of the prosthetic group in nitrite reductase was the controlling factor to determine the fate of bound substrate. The iron isobacteriochlorin is a stronger base and favors reduction and protonation to produce ammonia while porphinedione is a weaker base which favors nitrous oxide gas through dimerization of HNO.[69]

1.8 UV-visible Spectroelectrochemistry of Iron Porphyrin Nitrosyls

The reduced species were characterized by UV-visible spectroelectrochemistry. The spectra of Fe(TPP)NO for the one and two electron reduction were shown in Figure 1-17.[62]

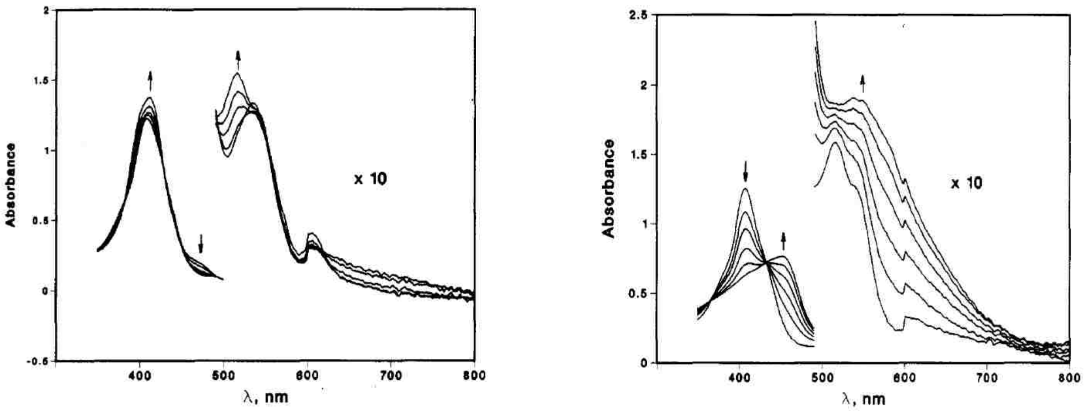

Figure 1-17. a) OTTLE spectroelectrochemical spectra reduction of Fe(TPP)(NO) to form Fe(TPP)(NO)$^-$; Solvent is THF.[73]

b) OTTLE spectroelectrochemical spectra reduction of Fe-(TPP)(NO)$^-$ to form Fe(TPP)(NO)$^{2-}$. Solvent is THF.[73]

Identification of the reduced species were done by UV-visible spectroelectrochemistry. The first electron reduction showed a new band at 512 nm with small changes in Soret region (Figure 1-17a) while a second electron reduction showed a dramatic change in the Soret and Q- band region. The Soret band shifted from 408 nm to 452 nm and a broad band at 545 nm for Fe(TPP)(NO)$^{2-}$ (Figure- 17b). This results indicated the first reduction was nitrosyl based and the second reduction more likely on the porphyrin macrocycle. The other two porphyrin complexes, Fe(TPC)(NO) and Fe(OEP)(NO), showed similar behavior. The one electron reduced species for those porphyrins was confirmed by chemical reduction by tetrabutylammonium borohydride, sodium anthracenide or sodium napthalide in THF. Coulometric reduction did not produce Fe(TPP)(NO)$^{2-}$ rather produced a σ- alkyl porphyrin, Fe(TPP)-Bu$^-$ (Figure 1-18).

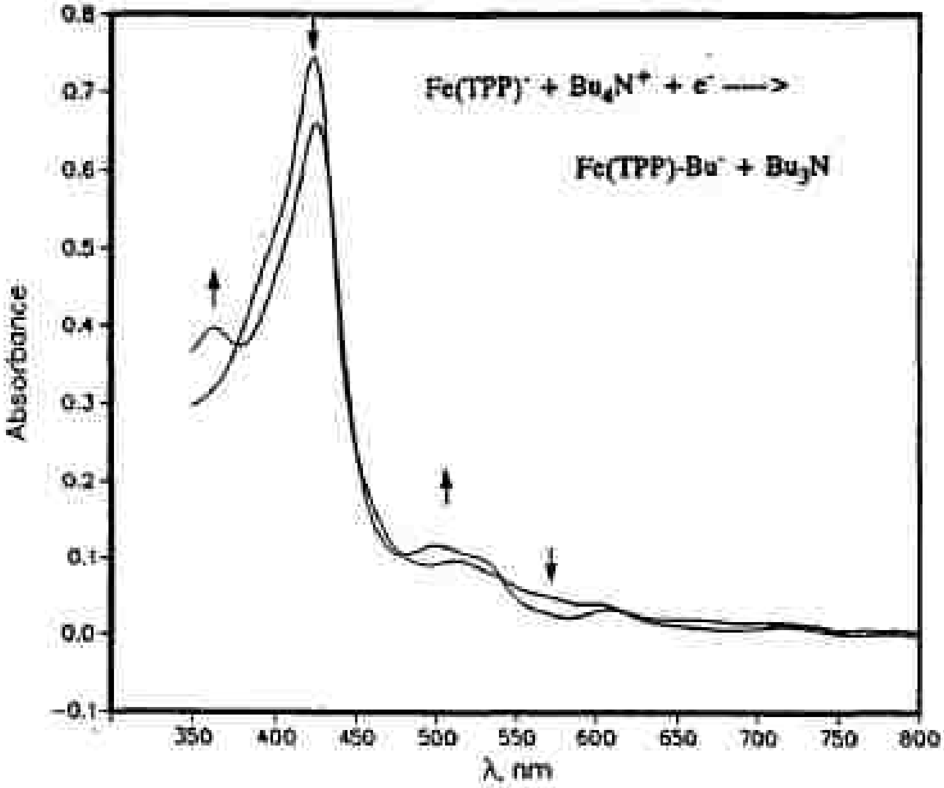

Figure 1-18. Visible spectra recorded during the first and second electron reductions of Fe(TPP) in THF in an OTTLE.[69]

The one and two electron reduced species in organic solvents with a variety of models like Fe(OEP)(NO), Fe(MOEC)(NO), Fe(2,4-DMOEiBC)(NO), Fe(OEPone)(NO), Fe(2,4-OEPdione)(NO) and Fe(2,3-OEPdione)(NO) were studied and identified by the UV-visible spectra for those reduced species(Figure1-19).[70]

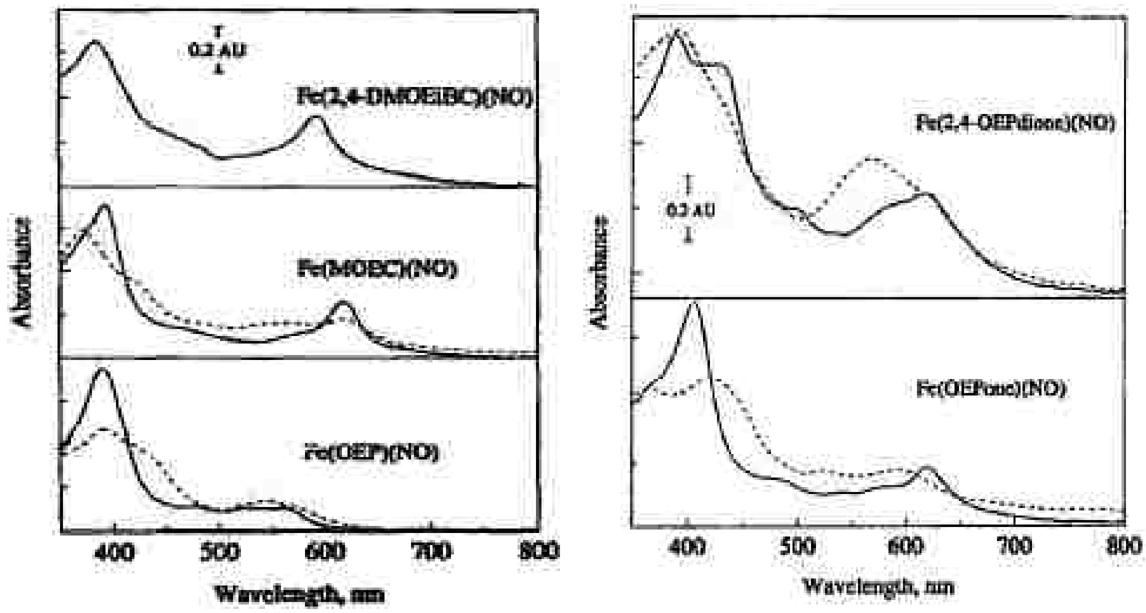

Figure 1-19. Left) Thin layer chromatograpgy of Fe(OEP)(NO), Fe(MOEC)(NO) and Fe(2,4-DMOEiBC)(NO). Right) Fe(OEPone)(NO) and Fe(2,4-OEPdione)(NO) in THF at a Pt gauze electrode. (-) Fe(P)(NO); (...) Fe(P)(NO)$^-$; (---) Fe(P)(NO)$^{2-}$. Supporting electrolyte: 0.10 M TBAP.[70]

Reduction of Fe(2,4-DMOEiBC)(NO) and Fe(2,4-OEPdione)(NO) showed a small increase of Soret band and a slight shift around 600 nm. For Fe(MOEC)(NO), a blue shift was observed (Figure 1-19). The 2nd reduction for Fe(MOEC)(NO) and Fe(OEPone)(NO) showed a decrease and broadening of the Soret and visible bands indicating a ring reduction to anion radicals. The 2nd reduction of Fe(2,4-OEPdione)(NO) resulted a blue shift with a slight increase in the Soret band (Figure 1-19).

The oxidation of Fe(OEPone)(NO) and Fe(2,4-OEPdione)(NO) was irreversible while it was reversible for Fe(MOEC)(NO) and Fe(2,4-DMOEiBC)(NO). The oxidation caused a decrease in the absorbance of the visible bands around 600 nm and a blue shift of the Soret bands which was consistent with the π-cation radical.

Recently, Goodrich et al.[74] synthesized some bis-picket fence porphyrin nitrosyls and used an OTTLE cell to characterize one electron reduction complex (Figure 1-20). The spectra displayed that the one electron reduction product for Fe(3,5-Me-BAFP)(NO) was stable in experimental time scale.[74]

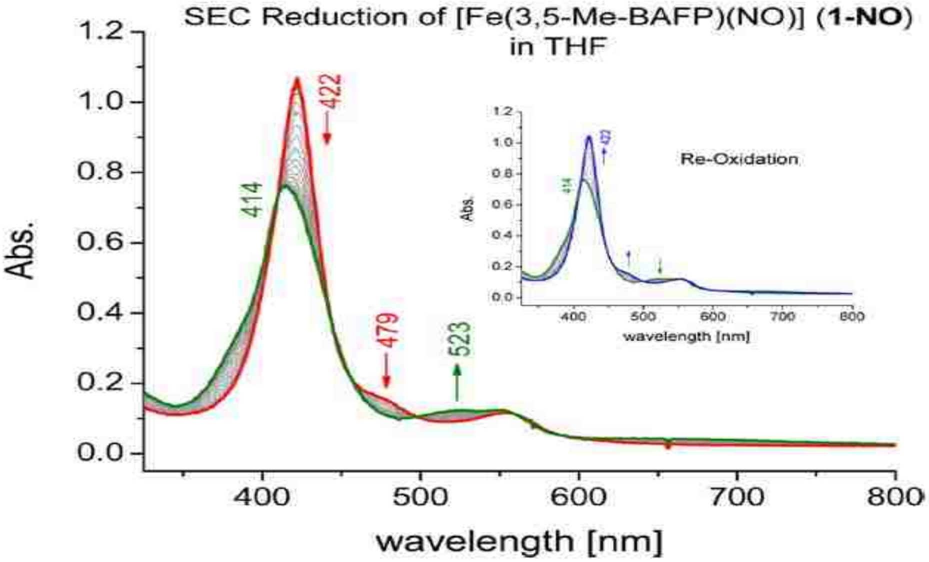

Figure 1-20. UV−visible absorption spectra for the spectroelectrochemical reduction of Fe(3,5-Me-BAFP)(NO) (1-NO, red to green), obtained by sweeping from −0.4 V to −1.8 V vs Ag wire at a rate of 10 mV/s in a 0.1 M TBAP solution in dry (top) 1,2-DCE and (bottom) THF. The reaction is chemically completely reversible upon sweeping from −1.8 V to −0.4 V vs Ag wire (inset).[74]

1.9 *In Situ* FTIR Spectroelectrochemistry of Iron Porphyrin Nitrosyls

Vibrational spectroscopy offers an advantage over many spectroscopic methodologies because much more detailed molecular structural information of the products, intermediates and reactants of the electrode process is attainable. EPR, Mossbauer and NMR techniques can also give detailed structural information, but it is very difficult to obtain these spectra during electrolysis.

UV- visible spectroelectrochemical methods can give information on electronic structure while vibrational (IR and Raman) spectroscopy can give information on functional groups. IR spectra of five coordinate iron porphyrin nitrosyls, Fe(P)(NO) (P= TPP, TMP, OEP) have a band around 1670 cm^{-1} for N-O stretching vibration.[52,53,58] The six coordinated Fe(TPP)(1-MeIM)(NO) displayed a band at 1625 cm^{-1} which is 35 cm^{-1} lower than the five coordinate complex Fe(OEP)(NO) indicating that axial coordination affects the N-O stretching vibration. Upon one electron oxidation of Fe(TPP)(NO), the N-O band shifted to higher wavenumbers ($\Delta\nu$ = 166-187 cm^{-1}) indicating that oxidation strengthened the N-O bond. The Fe-N(NO) stretch in Fe(TPP)(NO) shifts from 525 cm^{-1} to 549 cm^{-1} upon reduction.[73] For Fe(OEP)(NO), the N-O band shifted to 1440 cm^{-1} (1421 cm^{-1} for ^{15}NO) (Figure 1-21). The decrease of N-O band for Fe(OEP)(NO) (230 cm^{-1}) was larger than the Fe(TPP)(NO) (185 cm^{-1}) indicating less delocalization of extra electron to the ring. The vibrational bands for one electron reduced species for Fe(OEPone)(NO) and Fe(OEPdione)(NO) were also measured (Figure 1-22).[75]

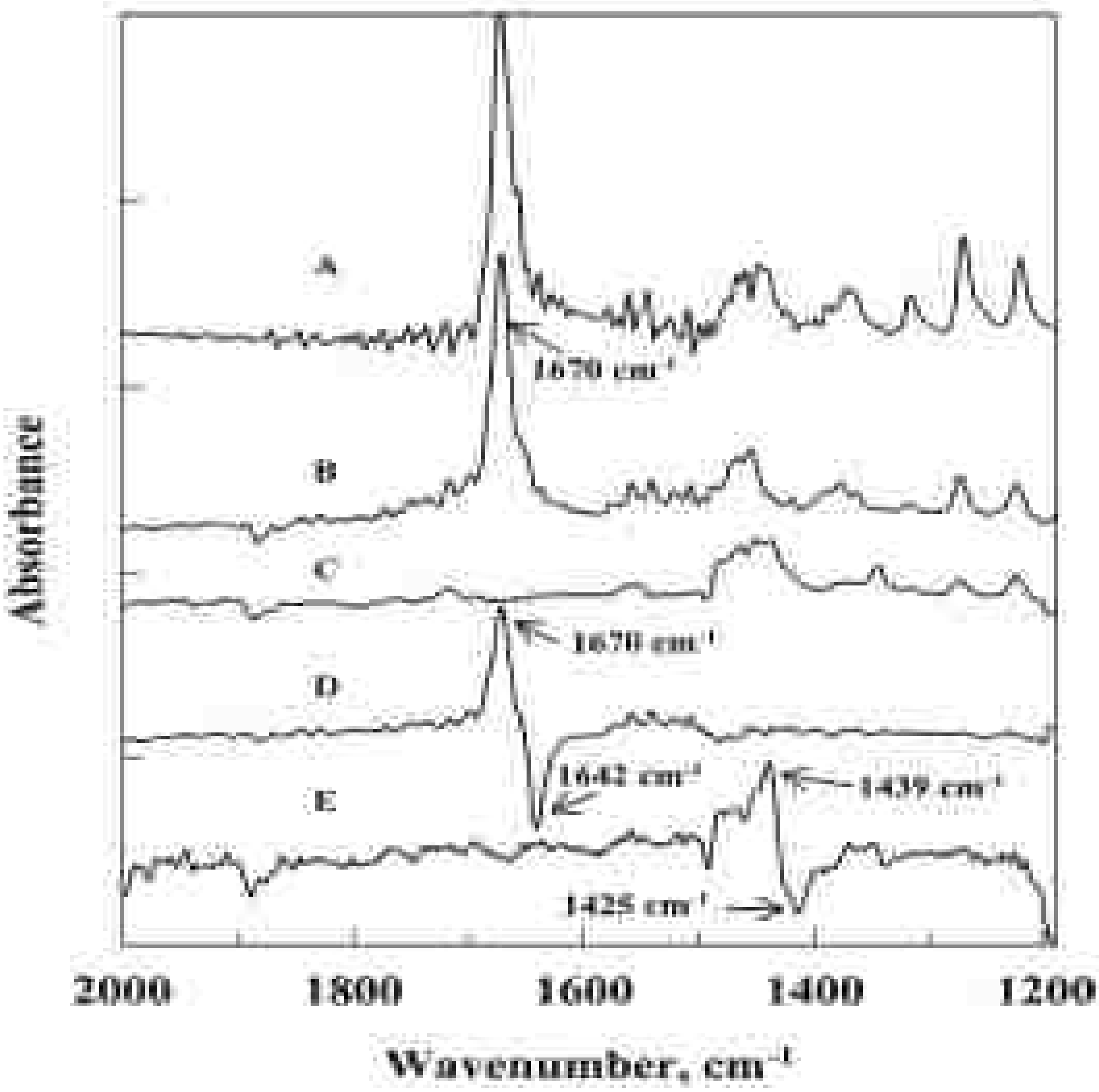

Figure 1-21. (A) FTIR spectrum of Fe(OEP)(NO) in KBr. (B) FTIR spectrum of Fe(OEP)(NO) in THF-*d₈*. (C) FTIR spectrum of Fe(OEP)(NO)$^-$ in THF-*d₈*. (D) Difference spectrum of Fe(OEP)(^{NA}NO) -Fe(OEP)(^{15}NO). (E) Difference spectrum of Fe(OEP)(^{NA}NO)$^-$ - Fe(OEP)(^{15}NO)$^-$. B/C solvent/electrolyte subtracte.[75]

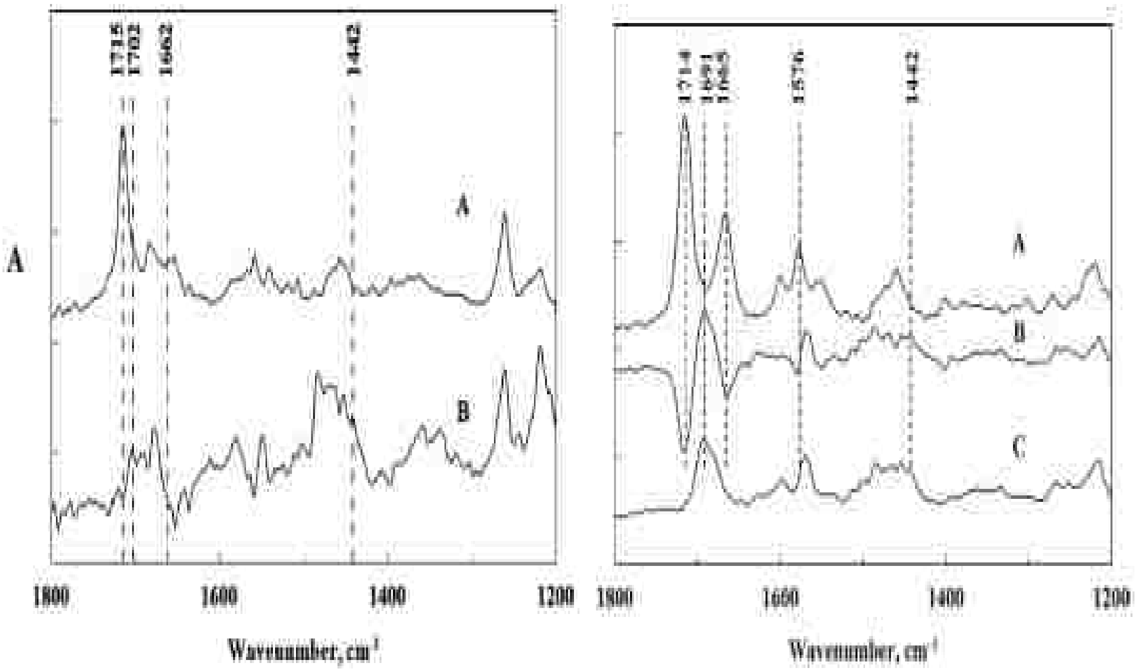

Figure 1-22. Left) FTIR spectrum of Fe(OEPone)(NO). (B) FTIR spectrum of Fe(OEPone)(NO)$^-$. Right) (A) FTIR spectrum of Fe(OEPdione)(NO). (B) Difference Spectrum of Fe(OEPdione)(NO)$^-$-Fe(OEPdione)(NO). (C) FTIR spectrum of Fe(OEPdione)(NO)$^-$. Spectra are solvent/electrolyte subtracted. Solvent: THF-*d*$_8$; electrolyte: 0.10M TBAP. [75]

Recently (2014), the Lehnert et al.[76] showed by DFT calculation that how the reduced electron distributed in low spin heme system and compared it with the non heme system (Figure 1-23). Reduction of low spin-(FeNO) results in double occupation of the Fe-NO bonding SOMO and the strengthening the Fe-N bond because of the increased π-back bonding between π* orbitals of nitric oxide and iron t_{2g} orbitals while increase the frequencies. At the same time, the N-O bond become weaker (because of back bonding) and the band decreases in wavenumbers. The resulting low spin (ls)-Fe{NO}^{8} complexes contains a bound singlet NO$^-$ ligand and are diamagnetic. This species is very stable and basic, fully protonated at pH=7.

For the heme system the reduction is ligand (NO) based whereas in nonheme high spin-FeNO complexes show that the reduction is metal based which is resulted in a decrease of the ν_{NO} band. The resulting Fe{NO}^{8} species have triplet NO$^-$ ligand which are very reactive and susceptible to decomposition. The ls-Fe(NO) complexes are very basic and easily protonated by weak acid. [74,76]

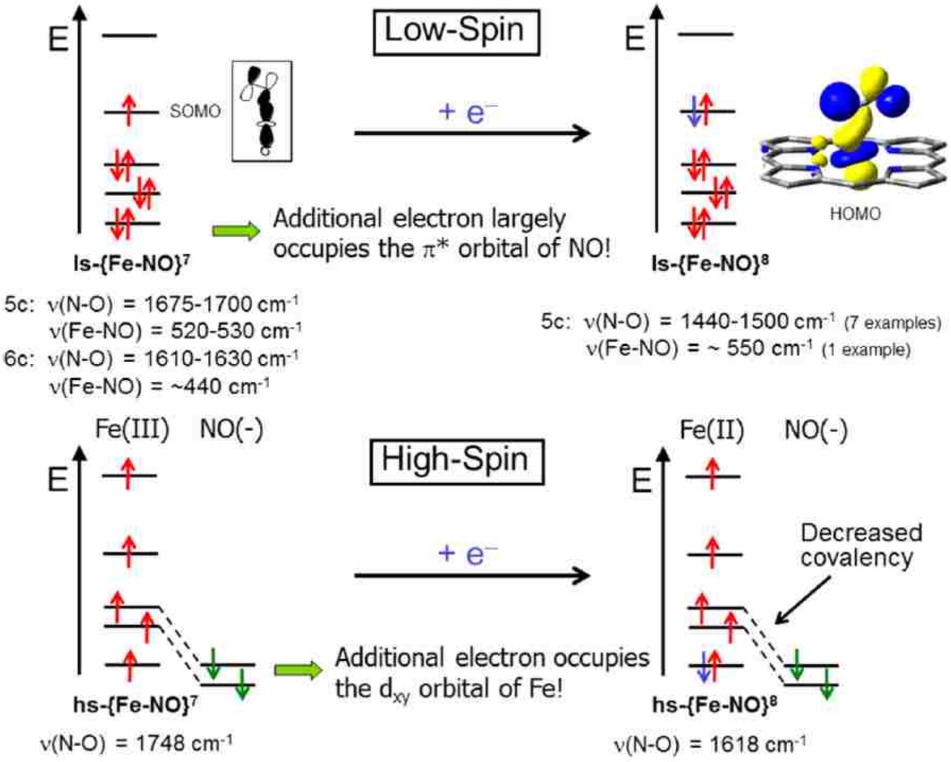

Figure 1-23. Illustration of the Differences in Electronic Structure between High-Spin and Low-Spin Nitroxyl Complexes.[76]

1.10 Iron Porphyrin Nitroxyls

The iron porphyrin nitroxyl is a proposed key intermediate in assimilatory nitrite reduction process.[26] The protonated form of one electron reduced nitrosyl has very high dimerization constant (8×10^6 $M^{-1}s^{-1}$) and generated N_2O and water.[42] When this HNO ligand binds to heme proteins showed a stability in solution.[77] This complex also has been implicated in numerous number of physiological and pathological processes such as cytochrome c nitrite reductase (ccNIR),[78-80] fungal cytochrome P450 nitric oxide reductase (P450nor),[81,82] and hydroxylamine oxidoreductase.[83]

The nitroxyl also considered as an important signaling molecule with extensive physiological activity as an inhibitor of aldehyde dehydrogenase and acts as a vasorelaxent and cardio protection in cardiovascular system.[76] The pK_a for free HNO is 11.6 indicating that at physiological pH, the nitroxyl anion exists in the protonated form.[42] The reduction potential of free NO to NO^- in aqueous solution is very negative $E^o = -0.76$ V vs NHE [42] while the pronated form (HNO) reduces more favorable redox potential, $E^o = -0.11$ V vs NHE and $E^o = -0.55$ V at pH= 7.[42,85] The change of redox potential upon reduction clearly indicated that reduction and protonation accelerated in the reduction of nitrite to ammonia or nitrogen. Even though the aqueous system contains free NO/HNO, we can expect the similar trend when it is coordinated to heme systems.

In 2000, Farmer and co-worker first synthesize HNO adduct of myoglobin by chemical reduction of Mb-NO.[86] The visible spectrum showed a slight shift of Soret absorbance from 421 to 423 nm with a minimal change in the Q band region (Figure 1-24). In proton NMR, a unique peak was seen at 14.8 ppm separated from protein peaks (Figure 1-25).

The stability of the complex was explained as an unusual protection of Mb-HNO within distal Mb pocket. Later, they provided the vibrational evidence from resonance Raman spectroscopy and bonding information by X-ray absorption spectroscopy.[87, 88]

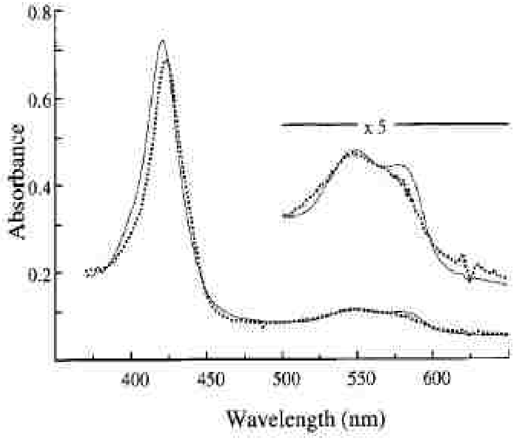

Figure 1-24. Absorbance spectra of NO-Mb, 1, (solid line) and HNO-Mb, 2, (dotted line) at 0.3 mM concentration in 50 mM borate buffer, pH 10.[86]

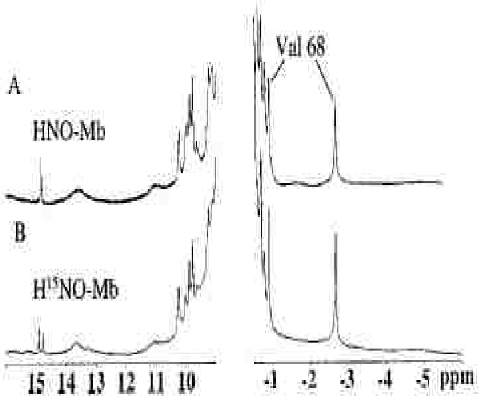

Figure 1-25. Water-decoupled ^{1}H NMR spectra of (A) natural abundance 2, (B) ^{15}N-labeled 2. Broad peaks are due to paramagnetic Mb impurities.[86]

The Fe-HNO unit was characterized by Fe-N and N-O stretching frequencies at 651 cm^{-1} and 1385 cm^{-1} respectively. The N-O value was lower than the free HNO value (1563 cm^{-1}).[89] The bonding information from XAFS showed that Fe-N and N-O bond distance increased in Mb-HNO as compared to Mb-NO. The bond angle of Fe-N-O decreased from 150° to 131° (for Mb-NO) in Mb-HNO. The Figure 1-26 represents bonding information for Mb-HNO, Mb(II)-NO and Mb(III)-NO.

Kincaid and Czarnecki provided vibrational evidence by resonance Raman spectroscopy in the lower wavenumber region.[90] The spectra showed the isotopic sensitive bands for

^{15}N, ^{18}O and ^{2}H (Figure 1-27). The band was seen at 647 cm^{-1} for Mb-HNO which was shifted to 628 cm^{-1} for Mb-H^{15}NO and to 606 cm^{-1} for Mb-DNO.[90]

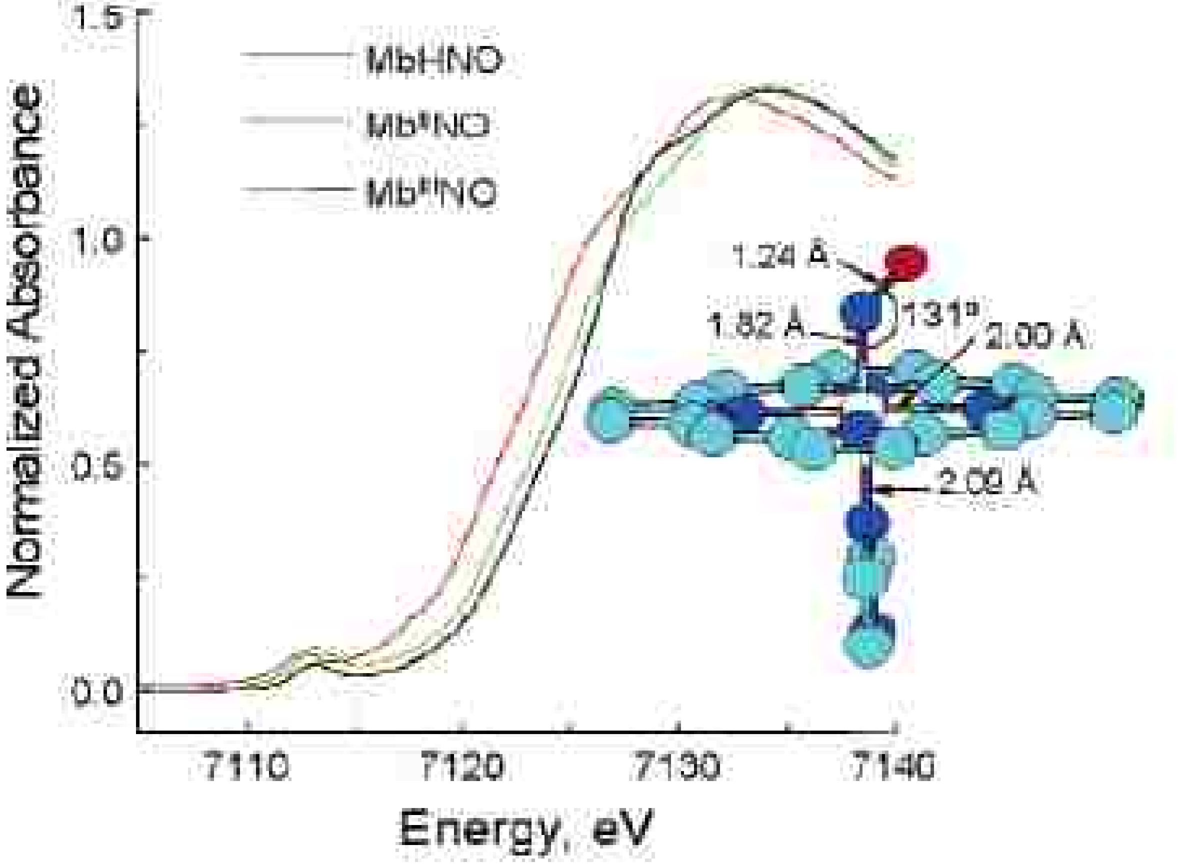

Figure 1-26. XANES spectra (10 K) of 40% aqueous glycerol solutions of 1 (inset: XAFS derived heme structure), and published spectra[88] of Mb(II)(NO) and Mb(III)(NO).[87]

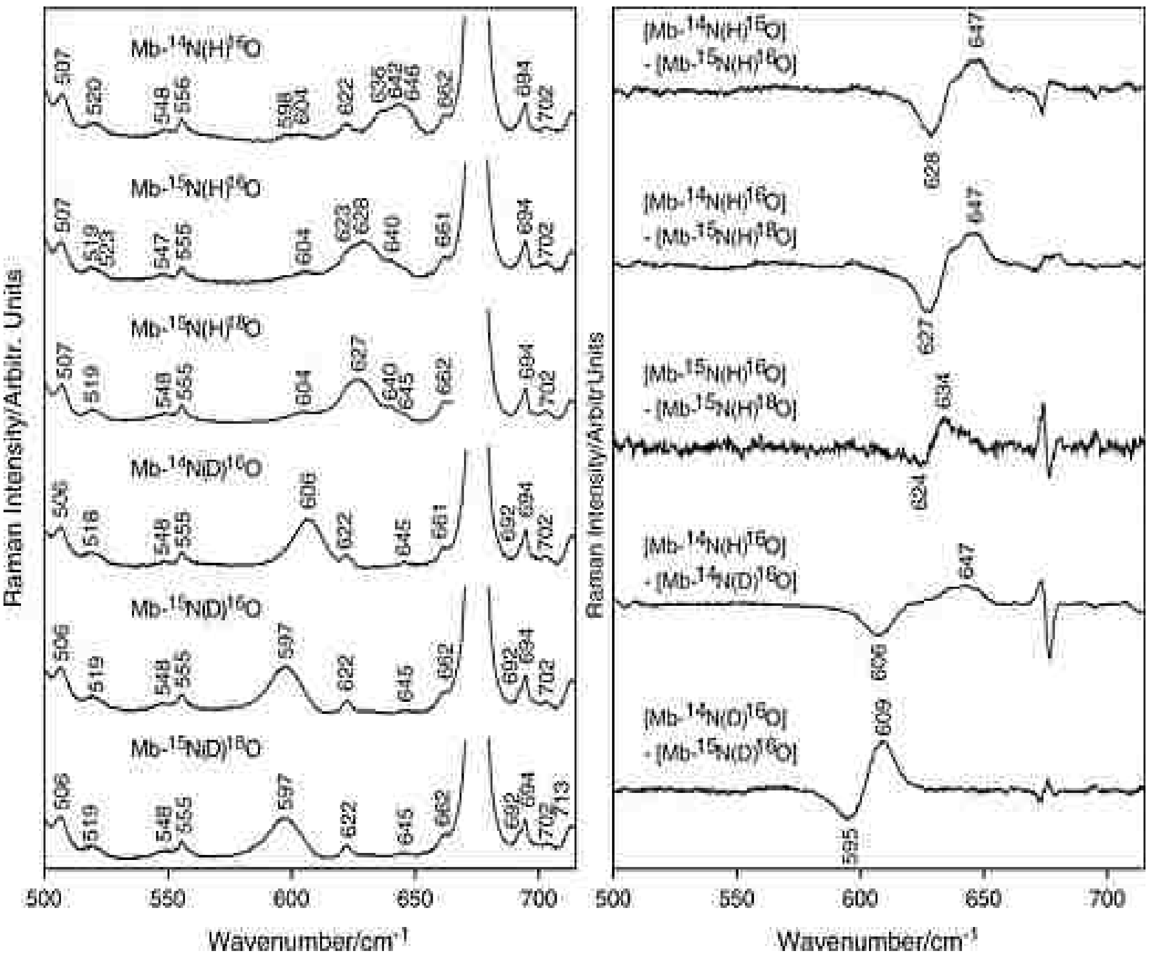

Figure 1-27. The low-wavenumber absolute (left-hand) and difference (right-hand) RR spectra of the products generated during cryoradiolysis of the ferrous nitrosyl myoglobin (Mb–NO).[90]

Goodrich et al. generated a Fe(P)(HNO) by adding a weak acid (acetic acid) to Fe(P)(NO)$^-$. The spectra showed that the protonated one electron reduction species was stable for 5 hours. (Figure 1-28). [74]

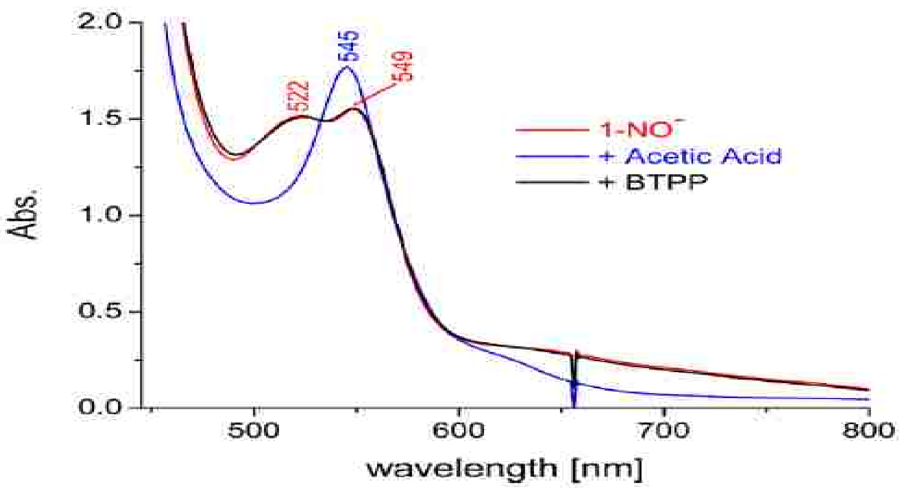

Figure 1-28. UV−visible spectrum for the reaction of 0.2 mM Fe(3,5-Me-BAFP)(NO)$^-$ (1-NO$^-$, red) with 1.4 equivalent of acetic acid (blue) to generate 1-NHO followed by deprotonation of 1-NHO with 2 equivalent of phosphazene base, P1-tBu-tris(tetramethylene) (BTPP, black) to regenerate 1-NO$^-$.[74]

The model complex, Fe-HNO had limited stability and regenerated the starting material by the following reaction. [73,74,76]

$Fe(Porph)(NO)^- + H^+ \rightarrow Fe(Porph)(NHO)$ (1-8)

$2Fe(Porph)(NHO) \rightarrow 2Fe(Porph)(NO) + H_2$ (1-9)

By using bis-picket fence porphyrin, a stable Fe(P)(HNO) was formed and the protonation was reversible in the presence of base.[74]

Lee et al.[91] identified photoexcited Mb-DNO by femtosecond vibrational spectroscopy in D_2O. Conradie and Ghosh carried out DFT calculations on metal porphyrin-HNO complexes and determined that Fe(P)(HNO) complex was a low spin ferrous complex. [92] The calculations were carried out using different basis sets (Figure 1-29), and all functional indicated that a low spin t_{2g}^6 configuration with Ms = 0 was formed. Comparing the DFT results with the experimental value,[88] they showed the Fe-N_{HNO} bond length matched with the theoretical value.

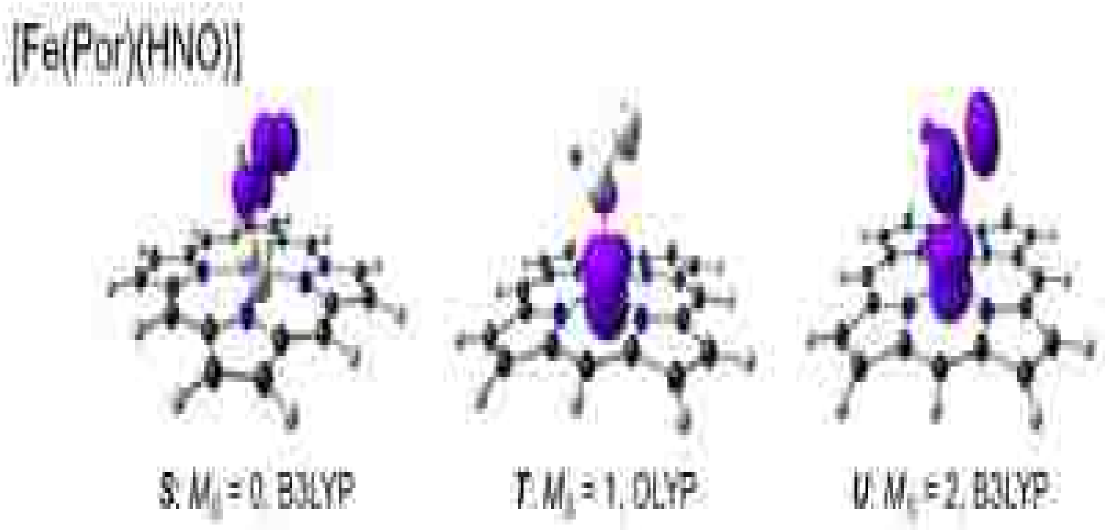

Figure 1-29. Spin density plots for the ground state and key low-energy states of M(Por)(HNO), The contour value chosen is 0.006 e/Å^3.[92]

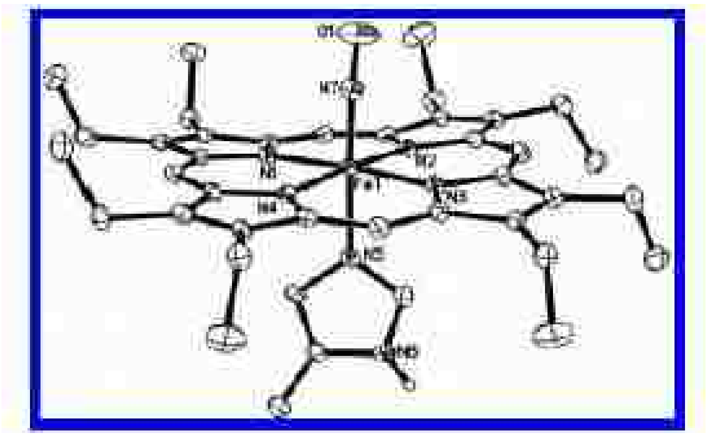

Figure 1-30. Ordered molecular structure of the cation of [(OEP)Fe-(NO)(5-MeIm)](OTf), with thermal ellipsoids shown at 50% probability. The hydrogen atoms (except for the imidazole N6 proton) and the anion have been omitted for clarity.[93]

In 2016, Abucayon et al. [93] reported a six coordinated Fe(P)(HNO) complex generated by hydride attack on ferric nitrosyl complex ([(OEP)Fe(NO)-(5-MeIm)](OTf) (Figure 1-30). An isotopically sensitive vibrational band at 1383 cm^{-1} was reported which was downshifted to 1360 cm^{-1} with ^{15}NO (Figure 1-31). The proton NMR (Figure 1-32) revealed a new resonance at 13.99 ppm and was assigned to a bound HNO which was split into a doublet with coupling constant 77 Hz by ^{15}N replacement. Hydrogen production from the disproportionation reaction was confirmed by proton NMR and gas chromatography. They also proposed a hydride attack on the ferric nitrosyl cation as the reaction mechanism using DFT calculation. (Figure 1-33). A larger positive charge on the nitrogen atom than on the oxygen atom induced hydride attack on nitrogen rather than oxygen, forming HNO rather than NOH.

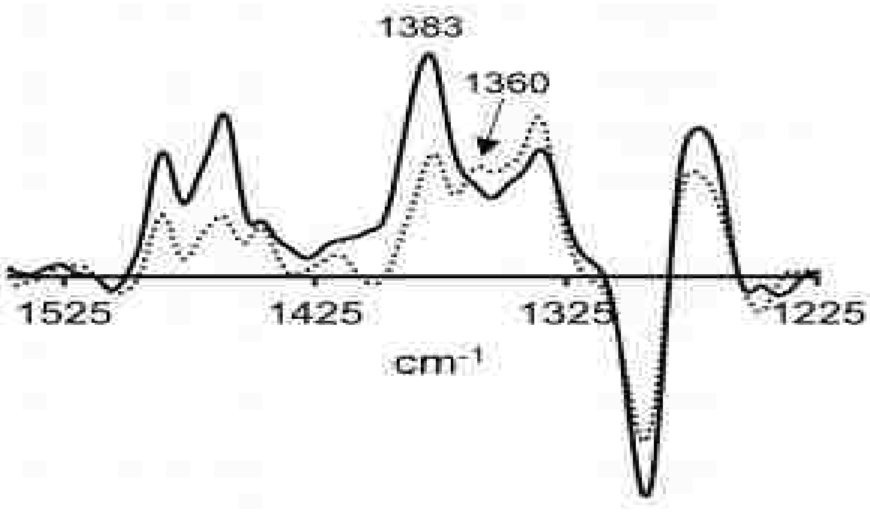

Figure 1-31. Difference spectra (product minus reactant) showing the new NO bands for (OEP)Fe(HNO)(5-MeIm) (solid line; 1383 cm^{-1}) and the H^{15}NO derivative (dashed line; 1360 cm^{-1}).[93]

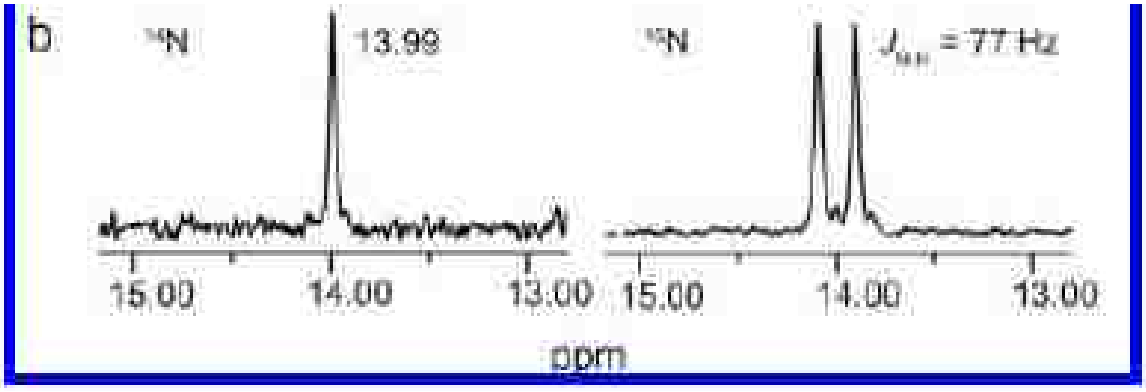

Figure 1-32. ^{1}H NMR spectrum showing the formation of the HNO ligand at δ = 13.99 ppm (left) and the $J_{N\text{-}H}$ coupling for the H^{15}NO derivative (right).[93]

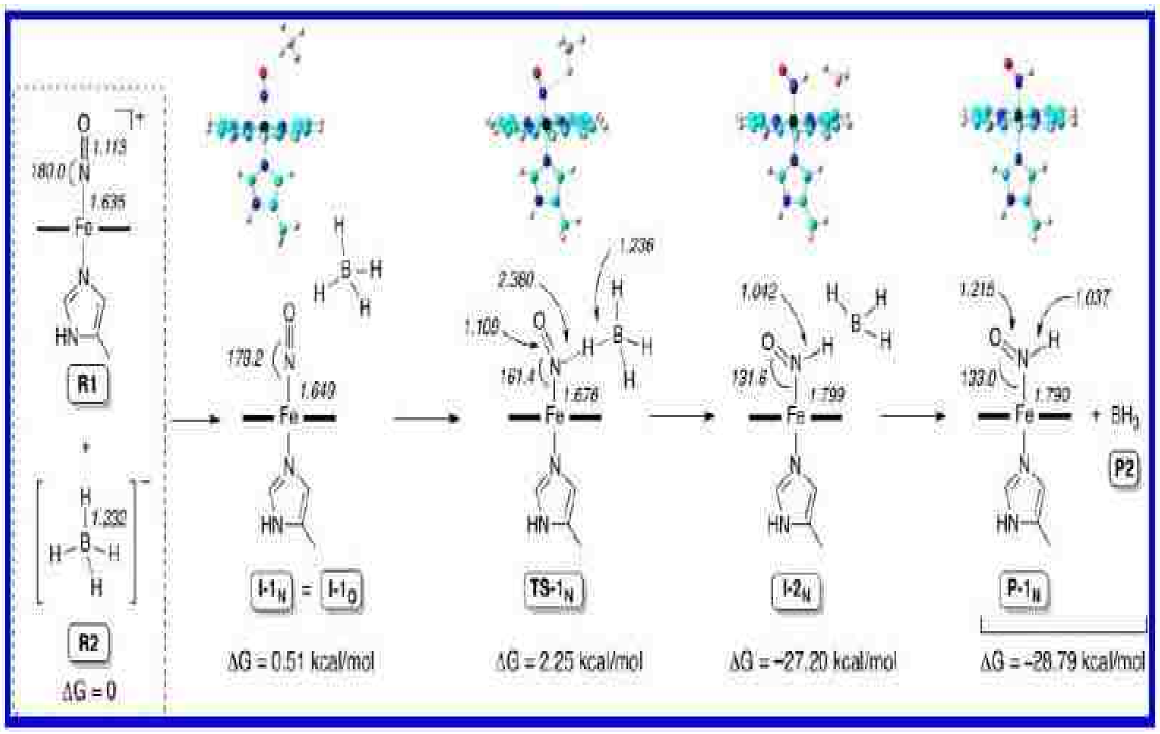

Figure 1-33. DFT-Calculated N-Pathway for Hydride Addition to the [(P)Fe(NO)(5-MeIm)]$^+$ Cation.[93]

1.11 Crystal Structure of Iron Porphyrin Nitroxyl Anion

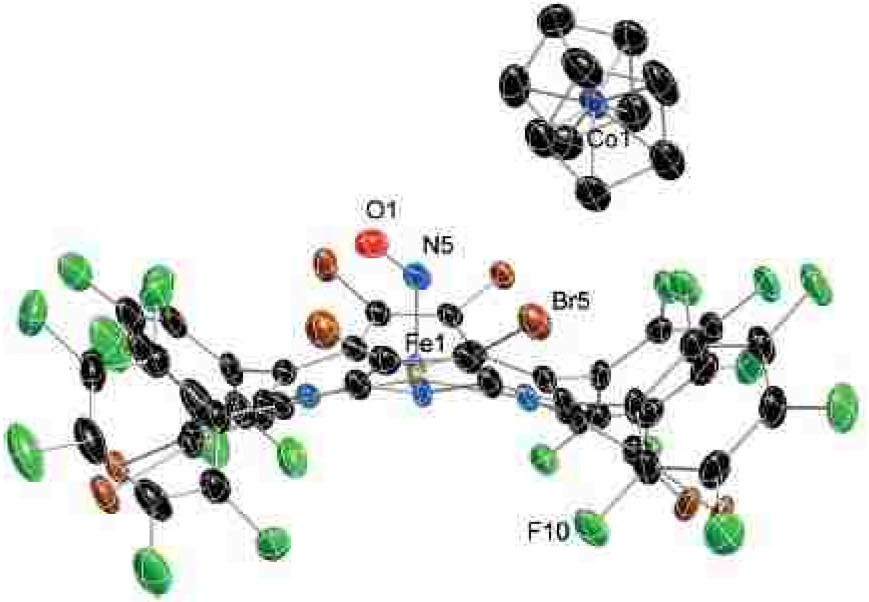

Figure 1-34. Thermal ellipsoid diagram of [Fe(TFPPBr$_8$)(NO)]. Ellipsoids are drawn at the 50% probability level. Solvent molecules are not shown for reasons of clarity. [94]

Recently Hu and Li reported the first crystal structure for a low spin iron(II) porphyrin nitroxyl as [Co(Cp)$_2$][Fe(TFPPBr$_8$)(NO)] where the asymmetric unit contains one Fe(TFPPBr$_8$)(NO)$^-$ anion, one [Co(Cp)$_2$]$^+$ cation and toluene solvent molecules (Figure 1-34).[94] The Fe-N-O$^-$ bond angle decreased to 122.4º from the starting Fe-N-O bond angle of 148.5º. This bond distortion was much smaller than Fe(NO)^7 analogs.[56,74,95,96] The bond distances for Fe-N and N-O$^-$ were 1.814 Å and 1.194 Å respectively, which were longer than the starting materials. The Fe-N(NO)$^-$ bond was almost perpendicular to porphyrin plane with tilt angle 1.8º while the porphyrin plane was more strongly saddled than the starting complex. The NO band dropped to 1540 cm^{-1} from starting NO vibration band 1718 cm^{-1}. The decrease of ν_{NO} 180 cm^{-1} upon reduction was consistent with the literature,[73] and with the extra electron occupying a mostly antibonding orbital. This resulted in the decrease of bond order, causing the downshift in the ν_{NO} band. The electronic transition was not significantly affected upon reduction with the bands at 430 and 582 nm changing little upon reduction.

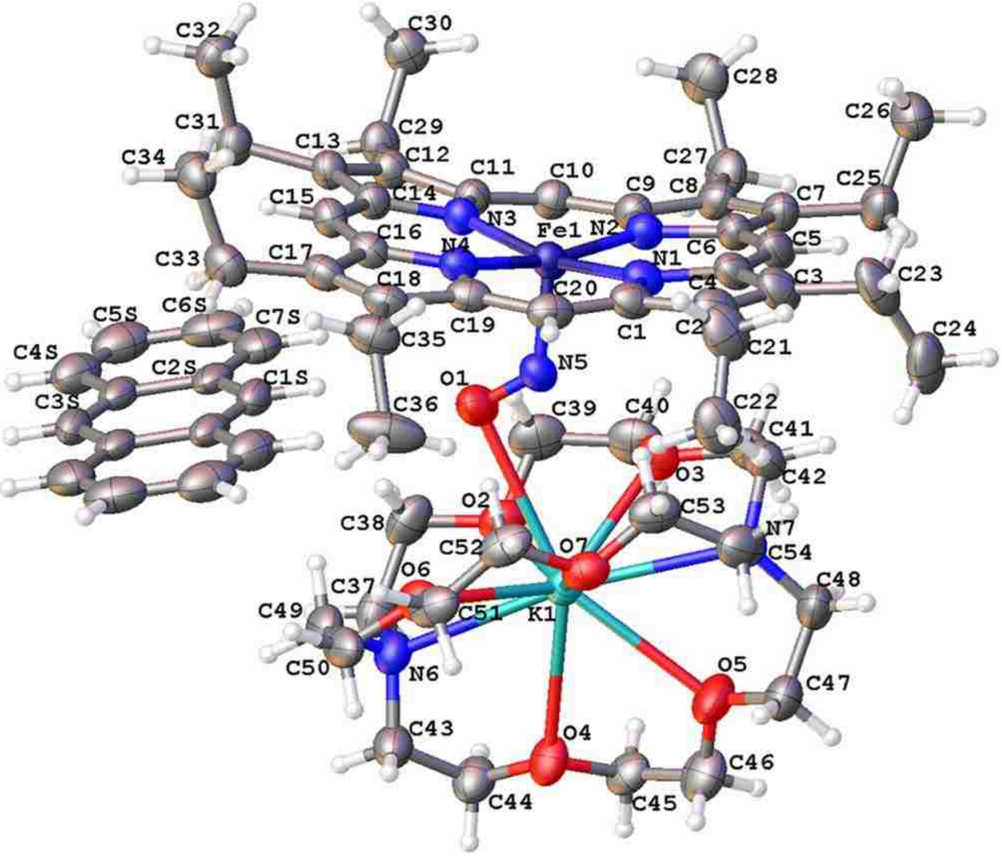

Figure 1-35. ORTEP diagram for one of the [K(2.2.2)][Fe(OEP)(NO)] units in the asymmetric unit. Ellipsoids are depicted at 50% probability. [97]

Recently our group was able to isolate the iron octaethylporphyrin nitroxyl ion, $Fe(OEP)(NO)^-$ as a potassium (2.2.2) cryptand salt (Figure 1-35),[97] which is more similar to the natural heme. The complex was synthesized by one electron reduction of Fe(OEP)(NO) using anthracenide reducing agent and the crystal was forming using anhydrous heptane. The key feature of the crystal was the Fe-N-O bond angle dropped from 142º (Fe-N-O before reduction) to 127º upon reduction. This decrease was a little larger than the Co(P)(NO) complexes[98-101] and also the reduced $Fe(TFPPBr_8)(NO)^-$. The FeN-O bond length increased upon reduction. The interaction between $Fe(OEP)(NO)^-$ and $[K(2.2.2)^+]$ was significant with a distance around 3.2 Å which indicated a contact ion pair formation.[102] No such interaction was observed between $Fe(TFPPBr_8)(NO)^-$ and $[Co(Cp)2]^+$.[94] The average Fe-Np bond distance decreased upon reduction and a significant increase in the nonplanarity of porphyrin ring. The average deviation of each atom from the 24-atom plane was larger than in Fe(OEP)NO, which made the porphyrin plane more saddled than starting complex. The UV- visible and FTIR spectra of the complex showed complete agreement with the literature.[70,75]

1.12 Fe(II)(protoporphyrin IX dimethyl ester)nitrosyl

Iron(II) porphyrinates (Figure 1-36) are one the critical targets for nitrosyls. Extensive work has been done to synthesize the complex and to elucidate their properties.[103-105] The protoporphyrin models are more similar to the natural nitrosyl heme proteins than Fe(OEP)(NO) or Fe(TPP)(NO). The value for the NO vibration (1655 cm^{-1}) is lower than the ν_{NO} for Fe(OEP)(NO) and Fe(TPP)(NO) (1670 and 1671 cm^{-1}). The carbonyl and nitrosyl vibrational bands were solvent dependent [103] and a coordination in the sixth position was observed with nitrogenous bases.[104] The solvent effect reflects considerable degree of polarization in Fe(PPDME)(NO) resulting from the delocalization of the unpaired electron of nitrosyl and metal to ligand back bonding. A previous crystal structure had a severe problem with disorder of the nitrosyl ligand.[56,95,106] Recently, Scheidt et al.[107] synthesized three five coordinated Fe(PPIX-DME)(NO) complexes. They also confirmed that the solvent or environmental effects did not come from the interaction between the nitrosyl and polar propionate side chain.

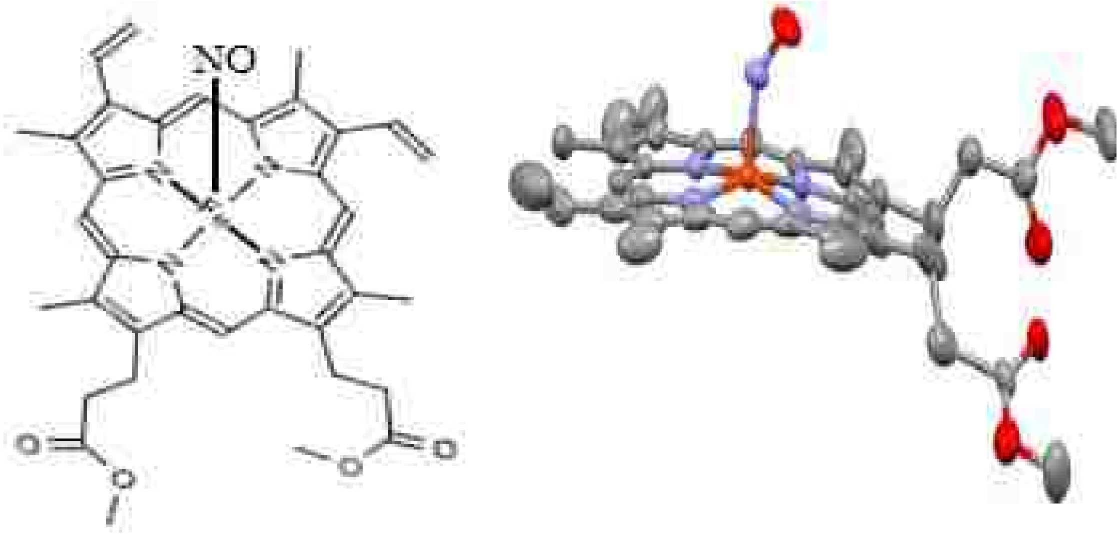

Figure 1-36. Thermal ellipsoid plot of the Fe(PPIX-DME)(NO) molecule. Ellipsoids are plotted at the 50% probability level. Hydrogen atoms have been omitted for clarity.[107]

1.13 Six Coordinated Iron Porphyrin Nitrosyls

Berto et al. synthesized a series of stable six coordinated iron porphyrin nitrosyl complexes in solution at room temperature.[108] They used pyridine or imidazole linker which weakly coordinated to iron center in the presence of only one equivalent of the N-donor ligand. The binding of linker ligand also depended on the character of porphyrin with an electron poor porphyrin can bind a sixth ligand effectively to the iron center.

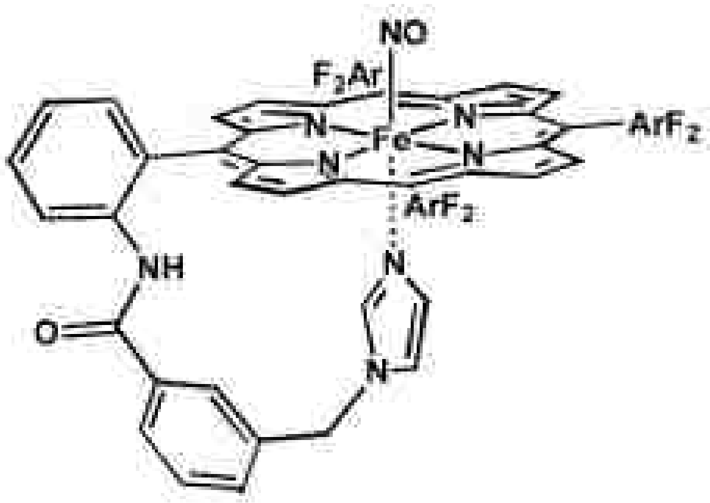

Figure 1-37. Drawing of the Structure of the 6C Complex Fe(T*o*-F2PP-BzIM)(NO).[108]

Figure 1-37 showed a complex in which a benzyl linker containing an imidazole ring which weakly bonded to the iron center. The UV-visible spectrum showed a band at 427 nm (Figure 1-38) which is more red shifted than the five coordinated iron porphyrin nitrosyls. All other six coordinated complexes with different N- donor ligands showed red shifted bands (Figure 1-39).

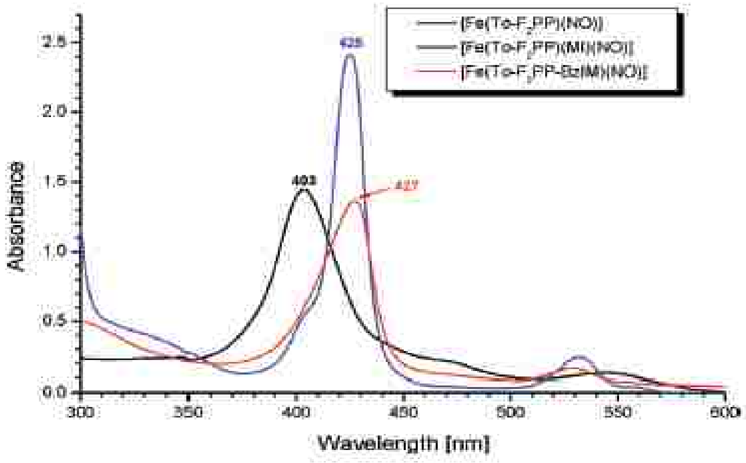

Figure 1-38. Electronic absorption spectra of Fe(T*o*-F$_2$PP-BzIM)(NO), (red), 5C Fe(T*o*-F$_2$PP)(NO) (black), and 6C Fe(T*o*-F$_2$PP)(MI)(NO)(MI) free 1-methylimidazole, blue).[108]

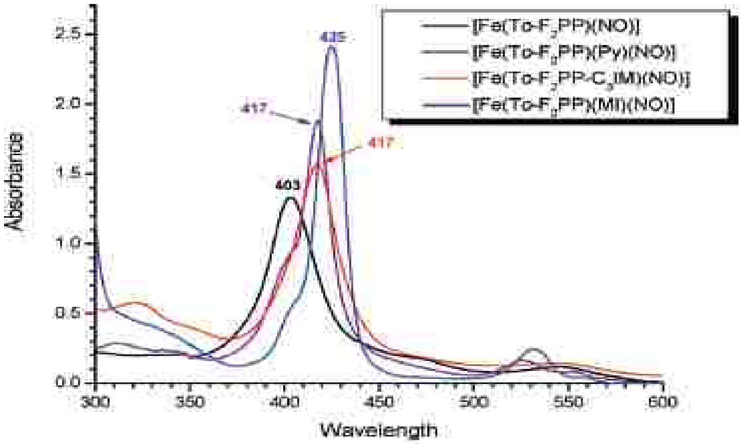

Figure 1-39. Electronic absorption spectrum of Fe(T*o*-F$_2$PP-C3IM)(NO) (2,red) in comparison to 5C Fe(T*o*-F$_2$PP)(NO) (black), and the 6C complexesFe(T*o*-F$_2$PP)(MI)(NO) (blue, MI) free 1-methylimidazole) and Fe(T*o*-F$_2$PP)(Py)(NO) (purple, Py) free pyridine). Spectra were recorded in CH_2Cl_2 or toluene solution at room temperature.[108]

The vibrational bands for the six coordinated complexes downshifted to a lower wavenumber than the five coordinated complexes. The benzyl linker six coordinated complex shifted a ν_{NO} band to 1644 cm^{-1} as compared to the 1680 cm^{-1} for the five-coordinate complex (Figure 1-40). This indicated a weakening of the N-O bond upon coordination at the sixth position. Six coordinated iron porphyrins were also observed with capped porphyrins in which the iron site was sterically shielded.[109]

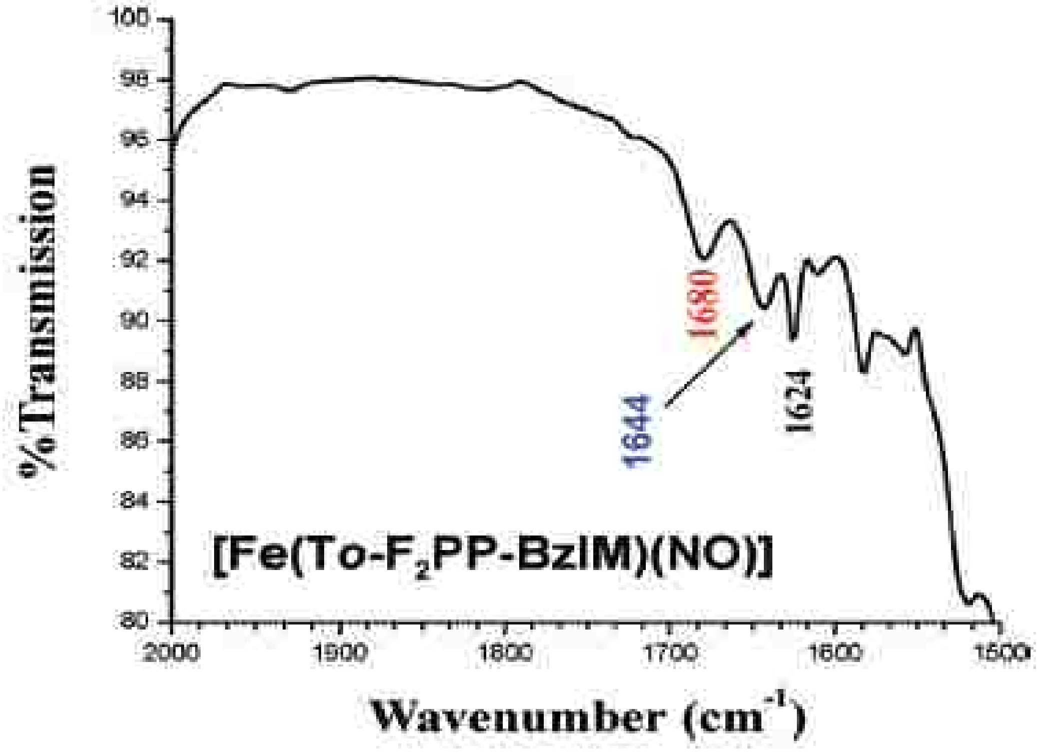

Figure 1-40. Solution IR spectrum of Fe(T*o*-F2PP-BzIM)(NO) showing the *ν*(N-O) stretching frequency at 1644 cm^{-1}.[108]

1.14 Iron Corrole Nitrosyls

Among the numerous porphyrin analogues, corroles have received a special attention because of its unique coordination chemistry and intriguing behaviors. These macrocycles contain 18 π electrons where two pyrrole rings were directly attached (Figure 1-41).

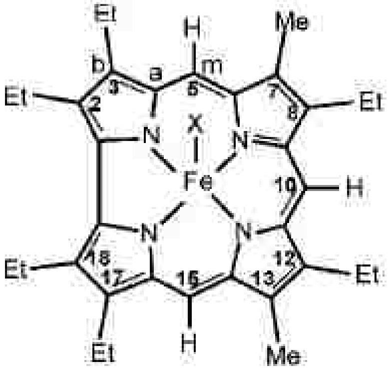

Figure 1-41. Chloroiron 7,13-dimethylhexaethylcorrolate, [FeCl(7,13-Me_2Et_6Corr)], X=Cl.[110]

When fully deprotonated, they are trianionic ligand.[110] Metallocorroles drew particular focus because the oxidation state of coordinated metal is sometimes higher than metals in porphyrin macrocyles.[111,112] Vogel, Ghosh, Walker and their coworkers synthesized a series of corrole complexes with different metals and various substituents on aryl group on meso position of macrocycles.[113-125] Extensive research has been done on corroles to elucidate the electronic configuration.[126-132] In 2001, Ghosh et al.[131] reported that high valent metals in corrole macrocycles led to oxidation of the corrole macrocycles. They characterized the corroles in this situation as non-innocent. The metallocorrole in these complexes are π- cation radical. The voltammetry data for Fe(IV)(Corrole)Cl (S=1) and Mn(IV)(Corrole)Cl (S=3/2) complexes showed a very high oxidation potential compared to Fe(IV)-O-Fe(IV)corrole (S=0) indicating the Fe(IV)(Corrole)Cl (S=1) and Mn(IV)Cl (S=3/2) complexes are already oxidized that means the corroles are non-innocent ligand and had some radical (π-cation) character and the one electron oxidation was significantly metal centered. They concluded that the Fe(III) (S=3/2) and Mn(III)(S=2) centers antiferromagnetically coupled with corrole ligand. The antiferromagnetic coupling was identified by Vogel and Cai et al.[126,128] previously. The chemical shift of chloroiron octaalkylcorrolates showed resonances at +170 and +190 ppm for meso proton. These shifts were much larger in magnitude and opposite in sign than the Fe(OEP)Cl, where meso proton shift was -56 ppm [133] and a low spin ruffled complex $[(OEP)Fe(t\text{-}BuNC)_2]^+$ where meso proton shift was -53 ppm.[134] This large positive chemical shift for corrolate complexes indicated the meso carbon contained a negative spin density. This negative spin did not arise from delocalization of the dπ electrons to the macrocycles rather indicated an antiferromagnetic coupling between an unpaired electron on the macrocycle and the unpaired electrons on the metal. The Fe(IV) complexes are proposed or detected intermediate for various heme and non heme iron enzymes.[135] In addition, with the high valent metal center, the Fe(IV)Cl and Mn(IV)Cl were strongly substituent dependent which were detected by distinct split of Soret band. [131] The split of band was attributed ligand to metal charge transfer. The electronic configuration of iron corroles was greatly affected with axial ligand depending on the nature of ligands. It shows non-innocent character of corrole macrocycles.[110] But with a strongly basic axial ligand such as Fe(IV)(Ph)Corrole, the corrole ligand did not show radical character. [121] In 2002, Zakharieva et al.[110] identified the iron corrole complexes such as chloroiron 7,13-dimethylhexaethylcorrolate, [FeCl(7,13-Me_2Et_6Corr)], and phenyliron 7,13-dimethylhexaethylcorrolate, [FePh-(7,13-Me_2Et_6Corr)] (Ph = C_6H_5) as a π- cation radical which involved the antiferromagnetic coupling between the S=3/2 Fe(III) and S= ½ π- cation radical centers resulted from symmetry allowed overlapping of d_{z^2} orbital out of plane of iron and the a_{2u}^- type orbital of the corrolate ring. Ferromagnetically coupling between porphyrin macrocycle and metal were seen in six coordinated Fe(III) porphyrinate π-cation radicals such as high spin Fe(III) S= 5/2 (Fe(OEP)(ClO_4) and mixed S=3/2, 5/2 Fe(TPP)(ClO_4) complexes where metal was in the plane of porphyrin macrocycle. [136,137] The five coordinated Fe(III) porphyrinate, a π-cation radical such as $FeCl(TTP)^+$-$(SbF_6)^-$ which is an analogue of FeCl corrole exhibited alternating sign ^{1}H-NMR phenyl H-shift indicated that the coupling of unpaired electron in the macrocycle with the iron electrons was antiferromagnetic.[138,139,141] In addition, the smaller macrocycle hole in corrole than porphyrin does not support a high spin Fe(III) electronic configuration which might be a possible source of macrocycle distortion and electron coupling.

Iron nitrosyl corroles are formed by the interaction of a FeNO center, which is strongly coupled to a corrole $^{\bullet 2-}$ radical. These compounds best be described as $\{FeNO\}^7$-(corrole$^{\bullet 2-)}$ with S= ½ for {FeNO} unit. [113,140]

Ghosh at el. have been done extensive work on the properties on iron corrole nitrosyl complexes. The crystal structure of Fe(Br_8TPFPC)(NO) showed (Figure 1-42) different electronic state $\{FeNO\}^6$ than porphyrin (tetraphenylporphyrin, octaethylporphyrin, tetra-p-methoxyphenylporphyrin, or picket fence porphyrin) complexes[136] with a Fe-N-O angle of 176.4º nearly linear. The Fe-N-O bond angle was also seen almost linear for cationic porphyrin complex, [(OEP)Fe-(NO)(5-MeIm)](OTf). [93] In spite of the dissimilarity with the proposed non-innocent radical character of corrole, a careful examination of the skeletal bond distances from crystal structure with the optimized structures (Figure 1-43) in DFT proved radical character for the corrole complexes.

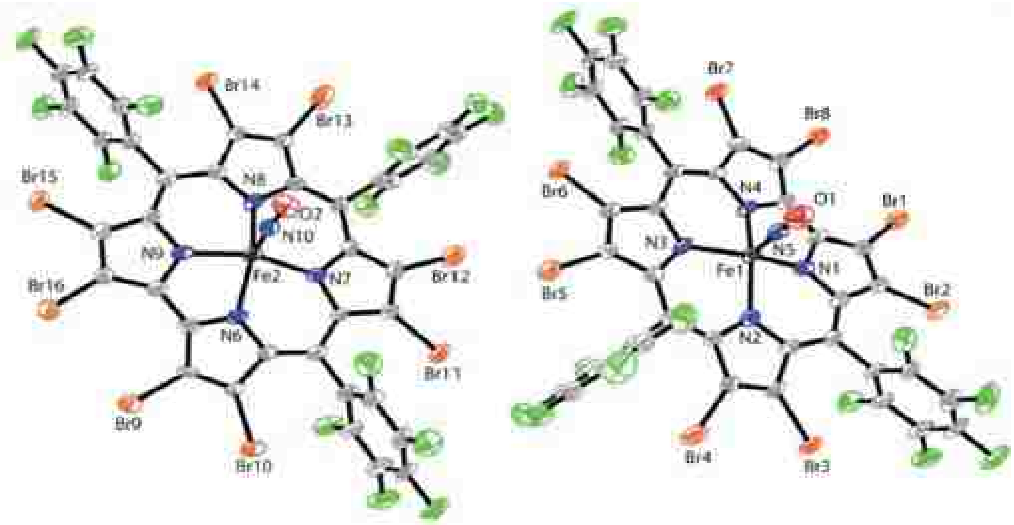

Figure 1-42. X-ray structure of Fe(Br$_8$TPFPC)(NO) thermal ellipsoid plot. [113]

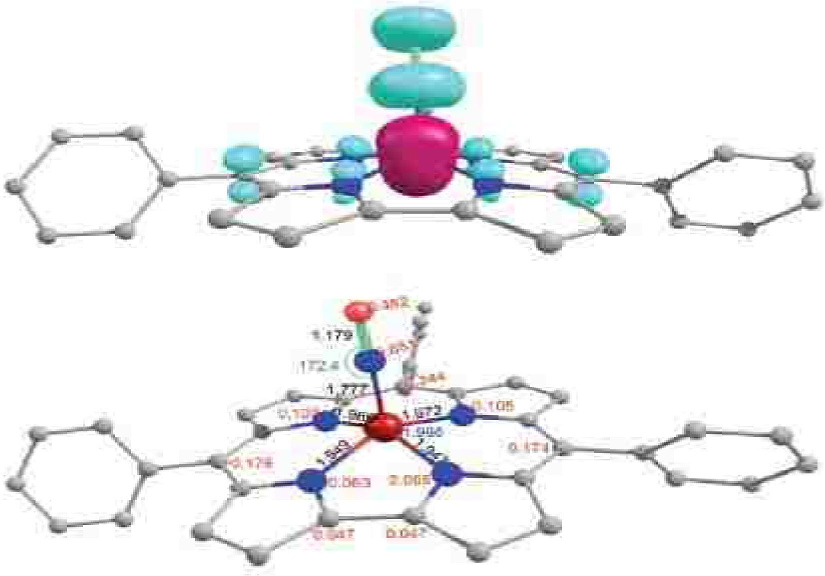

Figure 1-43. Selected BS-B3LYP/TZP results on Fe(TPC)(NO): BS spin density plot (top) and selected Mulliken spin populations (a in red, b in blue), distances(Å) and the FeNO angle.[140]

Ghosh at el.[114] classified the complexes in two groups based the shift of Soret maxima in electronic absorption spectra. In class I, the Soret maxima shifted to red upon substitution of electron donating group on para position (Figure 1-44) where in class II, the Soret maxima did not shifted to red. The shift arises from aryl to corrole charge transfer in certain transitions in the Soret region. Based on the Soret shift which was also seen previous studies,[118-120,140] they assumed that the complexes were non-innocent (radical character) and the electronic configuration are not $\{FeNO\}^6$-(corrole^{3-}) but $\{FeNO\}^7$-(corrole$^{\bullet 2-}$).

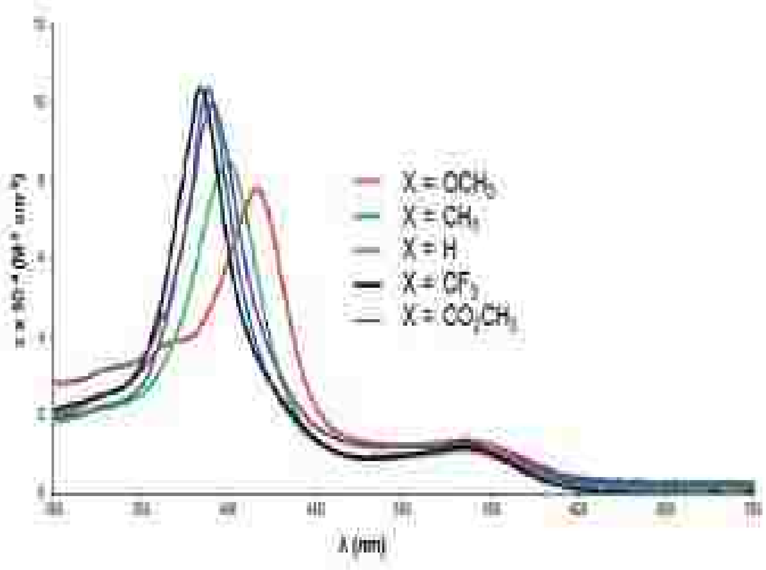

Figure 1-44. UV-visible spectra of Fe(TpXPC)(NO) complexes.[140]

The vibrational frequency also showed substituent effects where the ν_{NO} band shifted to higher frequency with electron withdrawing group and moved to lower frequency with electron donating group on para-aryl position. This trend was consistent with the porphyrin macrocycles where substituents influences the back bonding from macrocycles to antibonding orbitals of nitrosyl.

1.15 Fundamentals of Rotating Ring Disk Electrode Voltammetry

Rotating ring disk electrode (RRDE) voltammetry is a hydrodynamic technique where the electroactive solution is transported to the electrode surface either by diffusion and convection. Generally, the velocity of the solution is a function of geometric coordinates. When a cylindrical rotating electrode rotates, a cylindrical symmetry forms with important coordinates r and z (Figure 1-45A). The solution moves to the electrode surface by the rotation of the electrode, but the solution layer near the electrode will be stagnant which causes a diffusion layer. The thickness of diffusion layer

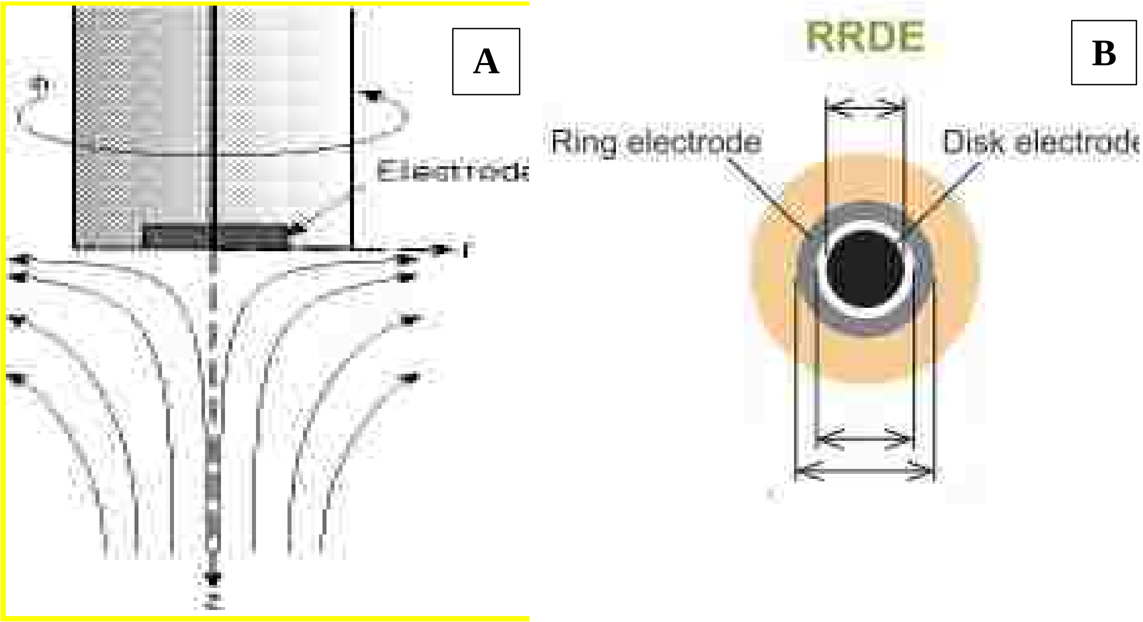

Figure 1-45. (A) Solution flow towards the electrode by rotation of electrode. (B) A typical Rotating Ring Disk Electrode.[142]

will be determine by hydrodynamic constants rather than diffusion coefficient. The current is proportional to the flux at the electrode surface. The stagnant layer thickness will decrease upon an increase of rotation rate which causes an increase in the current with an increase of rotation rate. For a given rotation rate the stagnant layer will be constant and not depend on time which give a steady state current in this technique.

The rotating ring disk electrode contains a disk electrode in the middle of cylinder which is separated by insulator from the ring electrode (Figure 1-45B). The potential of disk can differ from ring. In order to do this, four electrodes are needed to carry out a RRDE experiment. This problem was solved by using a bipotentiostat where the disk and ring potentials can be controlled independently (Figure 1-46A).

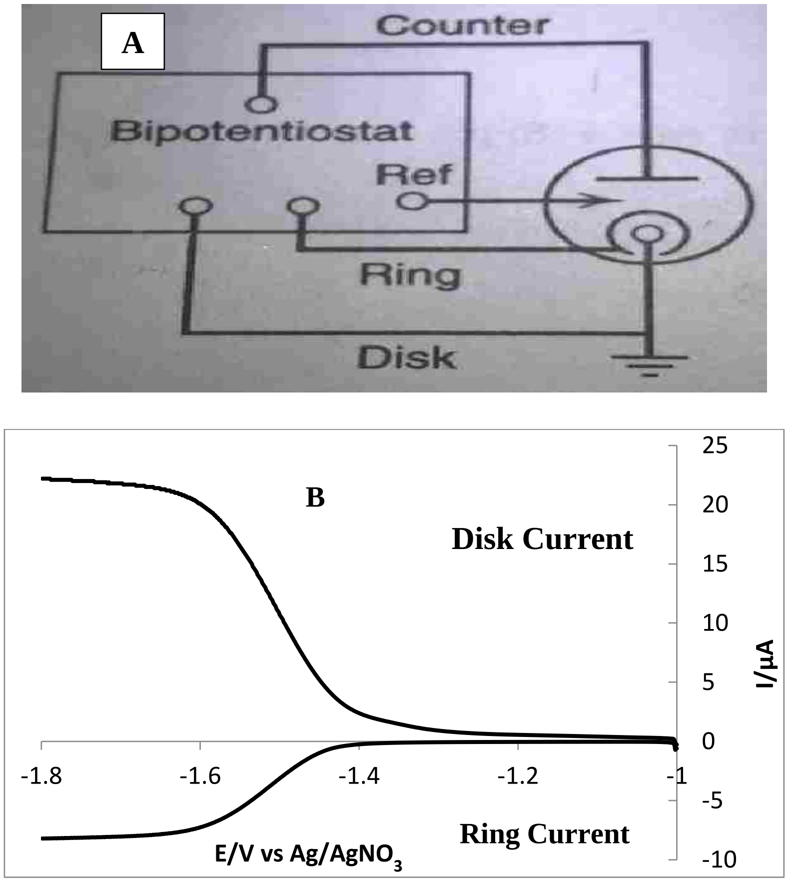

Figure 1-46. A) Block diagram of a bipotentiostat for RRDE experiment, [142] B) A typical RRDE voltammogram.

In the RRDE experiment, different electrode potentials are applied at the disk and the ring electrodes which give disk and ring currents. Usually, the electroactive species reduced at the disk will be swept to the ring by the rotation of electrode and re-oxidizes there if potentials maintain accordingly. As a result, two current will be displayed in the voltammogram, disk current (i_D) for reduction and ring current (i_R) for oxidation. The ring current lags slightly than the disk current because of the unavailability of the reduced species at the beginning of the scan. The two currents are mirror shape and opposite in sign (Figure 1-46B). The ring current is lower than the disk current because of the smaller surface area for ring electrode than the disk electrode and diffusion of the reduced species into the bulk. The important kinetic parameter, the collection efficiency (N_k), can be obtained from the ratio of absolute values of the two currents. The chemical reversibility of redox species can be determined from the ratio. Typical values from 0.25-0.45, which means 25%-45% of reduced species at disk will be oxidized back at the ring. The time scale of the RRDE experiment can controlled by changing the electrode rotation rate. Higher rotation rates lower experimental time scale. Thus, in this technique, important time parameter is the rotation rate not the scan rate. But slow scan rates are important so that the reaction can reach steady state at each potential.

The RRDE is very useful for the study of the kinetics of homogenous reaction in solution. [143] A coupled reaction causes perturbation in the limiting current and the $E_{1/2}$ for the disk and ring. This gives important information about reaction kinetics. In addition, with the RRDE techniques one can avoid issues involving slow electron transfer kinetics and the solution resistance. Double layer charging is also insignificant in this technique. Digital simulation can be carried out to determine the kinetic parameters with this technique.[143-145]

1.16 Goal of this work

The electrochemistry and spectroscopy of various iron porphyrin nitrosyls have been studied intensively but the reduction of nitrosyls in the presence of weak acids has not been examined in detail. The nitrosyl complexes are the model for the assimilatory and dissimilatory nitrite reduction intermediates which are stable and present in enzymatic turnover. The nitrosyl intermediate can be converted to ammonia or nitric oxide (and eventually to N_2O by another enzyme) via different intermediates such as nitroxyl Fe(P)(HNO) and hydroxylamine Fe(P)(NH_2OH). The conversion of nitrosyls to ammonia has been studied extensively but the kinetics of the formation of Fe(P)(HNO) and Fe(P)(NH_2OH) intermediates and their spectroscopic properties have not been examined extensively. Electrochemistry of nitrosyl porphyrins and porphinones will be studied in the presence of weak acids with various voltammetric techniques such as cyclic voltammetry (CV), rotating ring disk electrochemistry (RRDE) and square wave voltammetry (SWV) to determine the kinetics of the formation of Fe(P)(HNO) and Fe(P)(NH_2OH) intermediates. The voltammetric results will be fitted to a simulation program to determine the kinetic parameters. The intermediates (HNO and NH_2OH) will be characterized by UV-visible and FTIR spectroelectrochemistry. In addition, the spectroelectrochemical results will be verified by chemically produced species.

A comparative study of heme (iron porphyrin nitrosyl) and non heme iron corrole nitrosyl complexes will be carried out to monitor the formation of the Fe(C)(HNO) and Fe(C)(NH_2OH) intermediates by the above mentioned electrochemical and spectroscopic methods.

CHAPTER 2 EXPERIMENTAL MATERIALS AND METHODS

2.1 Chemicals

Fe(III)(OEP)Cl (OEP=Octaethylporphyrin), Co(II)(OEP)Cl, tetrabutylammonium perchlorate (TBAP), phenol, 2,3-dichlorophenol, 2,6-dichlorophenol and 3,5-dichlorophenol, 4,7,13,16,21,24-hexaoxa-1,10- diazobicyclo [8.8.8] hexacosan (2.2.2-cryptand), anthracene, D_2SO_4 were purchased from Sigma Aldrich Chem. Co. Fe(PPDME)Cl and H_2OEPone were obtained from Frontier Scientific. THF-d_8 and $^{15}NH_2OH.HCl$ were purchased from Cambridge Isotope Laboratory. 2,3-dcp-d_4, 2,3-dcp-d_3, 3,5-dcp-d_4, 3,5-dcp-d_3, 2,6-dcp-d_3, 4-cp-d_4 and 4-cp-d_5 were obtained from CDN Isotopes. All phenols were purified by sublimation. TBAP was dried at 90 ° C in a vacuum over night before use. Anhydrous THF and THF-d_8 were refluxed in the presence of sodium metal and benzophenone until the solution was a persistent blue color. After purification, the solvent was collected under nitrogen and stored in the glove box. All other solvents and reagents were spectrophotometric grade and were used without further purification. The iron corrole nitrosyls were obtained from Abraham Alemayehu, Department of Chemistry, The Arctic University of Norway.

2.2 Iron Insertion in H_2OEPone

Twenty-five mg of H_2OEPone was dissolved in 15 mL acetic acid containing 40 mg sodium acetate and 25 mg sodium chloride in 100 mL round bottle flask. The solution was degassed with nitrogen and then 50 mg ferrous acetate was added. The mixture was heated for one hour with gentle heat. The completion of the reaction was confirmed by quenching of the fluorescence from a UV lamp. Then the solution was cooled to room temperature and the solvent was removed under vacuum. The solid was washed several times with deionized water. The UV-visible and FTIR spectra of Fe(OEPone)Cl were consistent with the literature values. [146]

2.3 Synthesis of Fe(OEP)(NO), Fe(OEPone)(NO) and Fe(PPDME)(NO)

The nitrosyl complexes were synthesized by dissolving 50.0 mg of Fe(OEP)Cl , Fe(OEPone)Cl and Fe(PPDME)Cl in chloroform. A hydroxylamine solution was prepared by mixing 200.0 mg of hydroxylamine hydrochloride and 160.0 mg of sodium methoxide in 10.0 mL anhydrous methanol. The solution was filtered to remove NaCl salt. The hydroxylamine solution was mixed with the porphyrin solution and stirred for 5 minutes under argon. The solution sat for 30 minutes at room temperature and the precipitate was obtained by vacuum filtration. The solid was washed with methanol to remove solid hydroxylamine. The UV-visible and FTIR spectra for Fe(OEP)(NO) and Fe(OEPone)(NO) were consistent with the literature values.[69] The UV-visible and FTIR spectra for Fe(PPDME)(NO) was consistent with the literature values.[104,105] The ^{15}NO complex was synthesized using $^{15}NH_2OH$.

2.4 Synthesis of H_2OEP-d_4

The procedure of Bonnette et al.[147] was followed for the synthesis of H_2OEP-d_4. Normal abundance octaethylporphyrin (100 mg) was dissolved in a mixture of D_2SO_4/D_2O (9:1 w/v) and stirred for 24 hours at room temperature. Then the mixture was poured into icecold water (100 mL) in a separatory funnel. 100 mL of anhydrous chloroform was added to the funnel and shaken vigorously. The chloroform layer was separated then 100 mL of saturated aqueous $NaHCO_3$ solution was added and shaken vigorously. The same process was repeated with 2 portion of 100 mL of water. The resultant chloroform solution with $H_2OEP\text{-}d_4$ was chromatographed on MgO in benzene. The $H_2OEP\text{-}d_4$ was eluted with dichloromethane. The formation of $H_2OEP\text{-}d_4$ was confirmed by ^1H NMR and FTIR. The Fe(OEP-d_4)Cl showed no resonance at -55.00 ppm for the meso protons. In the FTIR, no band was observed at 835 cm^{-1} which was observed for H_2OEP.

2.5 Synthesis of $Co(OEP)(NH_2OH)_2^+$

Co(OEP)Cl (50.0 mg) was dissolved in 10.0 mL of anhydrous chloroform. A hydroxylamine solution was prepared by mixing 200.0 mg of hydroxylamine hydrochloride and 160.0 mg of sodium methoxide in 10.0 mL anhydrous methanol. The solution was filtered to remove NaCl salt. The hydroxylamine solution mixed with the Co(OEP)Cl solution and stirred for 5 minutes. The solvent then removed by rotary evaporator. The solid was re-dissolved in chloroform or acetonitrile to remove the excess solid hydroxylamine. The $Co(OEP)(NH_2OH)_2^+$ formation was confirmed by UV-Visible and FTIR spectroscopy. [69]

2.6 Synthesis of 3,5-dcp-d_1

100 mg of 3,5- dichlorophenol was dissolved in excess amount of D_2O (20 mL). The resultant solution was stirred for 2 hours. After stirring, the solution was poured into a separatory funnel, and very dry dichloromethane(DCM) was added and shaken

vigorously. The DCM portion was separated and the process was repeated for another 2 times to make sure that all the phenols in DCM layer. The solution was dried with Na_2SO_4 solid. The solvent was evaporated using rotary evaporator. The formation of deuterated phenol was confirmed by ^2H NMR. A resonance was seen at 9.3 ppm for the phenolic resonance.

2.7 Synthesis of Fe(OEP)(NO)$^-$

To reduce Fe(OEP)(NO), potassium cryptand anthracenide was prepared. Fifty-five mg (0.30 mM) of cryptand and 27 mg (0.30 mM) of anthracene were dissolved in 5 mL of double distilled THF in a 25-mL volumetric flask. A small piece of potassium metal was washed with hexane, dried and was added to the solution. The solution was stirred for 3-5 hours until the solution color turned to deep blue. The resultant solution was 0.03 mM K-cryptand reducing agent. [97]

Forty-five mg (0.06 mM) of Fe(OEP)NO was placed in 25 mL Erlenmeyer flask, and 3 mL of anthracenide reducing agent was added and was stirred for 30 minutes. UV-Visible and FTIR spectra were taken to confirm that a complete reduction occurred. A characteristic absorbance at 540 nm in UV-visible spectrum and a band at 1440 cm^{-1} for NO$^-$ vibration in FTIR spectrum were observed. After confirmation, 6 mL of anhydrous of heptane was added to the flask for precipitation. Sometimes the porphyrin was dissolved first in minimum amount of THF, then the reducing agent was added. To precipitate the nitroxyl complex, heptane was added to the solution, stirred and then was allowed to sit for 2-3 hours for precipitation to occur. For crystallization, heptane was added slowly to the flask and crystallization occurred after one day.

2.8 Synthesis of Fe(OEP)(HNO)

Five to ten mg of Fe(OEP)(NO)$^-$ was dissolved in double distilled THF. At least 10 mM of substituted phenols were added to the solution under an argon atmosphere in the glove box. The formation of Fe(OEP)(HNO) was confirmed by the UV-visible spectrum which had no sharp absorbance at 540 nm with a broadening of Soret band and a weak absorbance at 552 nm. The addition of excess acid did not affect the UV-visible spectrum. For further confirmation, a FTIR spectrum was taken and there was no band at 1440 cm^{-1}, indicating the reaction was complete. The Fe(OEP)(HNO) can also synthesize by direct mixing of acids in the Fe(OEP)(NO)$^-$ and cryptand anthracenide solution. For this synthesis, the solution must be oxygen free. The glove box was recycled with argon several times to make sure that the oxygen level was at a minimum before the synthesis of Fe(OEP)(HNO). Oxygen can form peroxynitrite (ONOO$^-$) reacting with NO$^-$ moiety of Fe(OEP)(HNO). The Fe(OEP)(HNO) solution was inserted in the spectroscopic cells (NMR tube, UV and FTIR cells) as early as possible after mixing with the acids to avoid dioxygen interference.

2.9 Equipment

Cyclic voltammetry was carried out by the potentiostat system (Cypress systems Instruments Lawrence KS, Model 2R, serial 1135) and by an electrochemical analyzer/work station (CHI version 12.06) model 600D series. The rotating ring disk electrode (RRDE) experiments were carried out using a bipotentiostat (CH Instrument, CHI 750E) and a BAS Instruments analytical rotator. The ring disk electrode made with platinum with the following dimensions: disk diameter: 0.20 cm; gap: 0.05 cm; outer ring: 0.35 cm. The boron doped diamond (BDD) electrode (0.3 cm) was purchased from Windsor Scientific Ltd.

For the UV-visible spectroelectrochemical experiments, the cell was made with a low volume thin layer quartz glass purchased from BAS Instruments (Figure 2-1). A platinum mesh was used as working electrode, a silver wire as auxiliary electrode and Ag/0.1 M $AgNO_3$ in acetonitrile as reference. UV-visible spectra were taken on HP 8452A diode array spectrophotometer.

The FTIR spectroelectrochemical cell was a modified Wilmad semi-permanent cell. The Teflon spacer between two CaF_2 windows was replaced by a polyethylene spacer in which the working (platinum mesh), pseudo reference (silver wire 0.05 mm diameter) and auxiliary (gold thin sheet 0.1 mm thickness) electrodes were melt-sealed. (Figures 2-2 and 2-3)

The infrared spectra were collected with a Thermo Nicolet-IR Spectrometer Model 670 Nexus with MCT detector. The MCT detector was cooled by liquid nitrogen for one hour before use. Solid FTIR spectra were taken in KBr salt and the solution FTIR spectra were taken using CaF_2 salt plates.

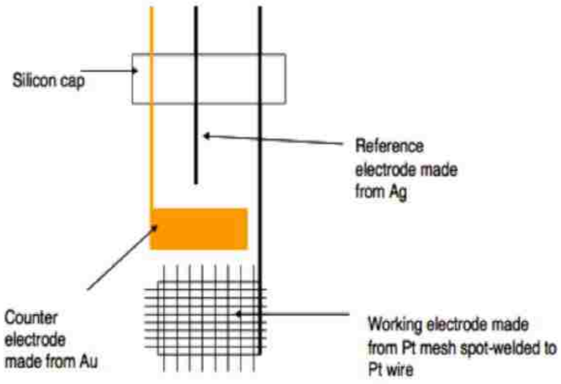

Figure 2-1. UV-visible Spectroelectrochemical cell.

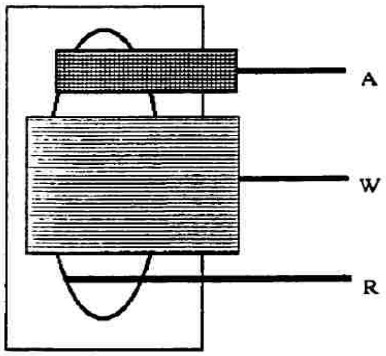

Figure 2-2. Front view of polyethylene spacer with melt-sealed electrodes. A= Pt gauze auxiliary electrode, W= Pt gauze working electrode, R= Ag wire, Pseudo reference electrode.

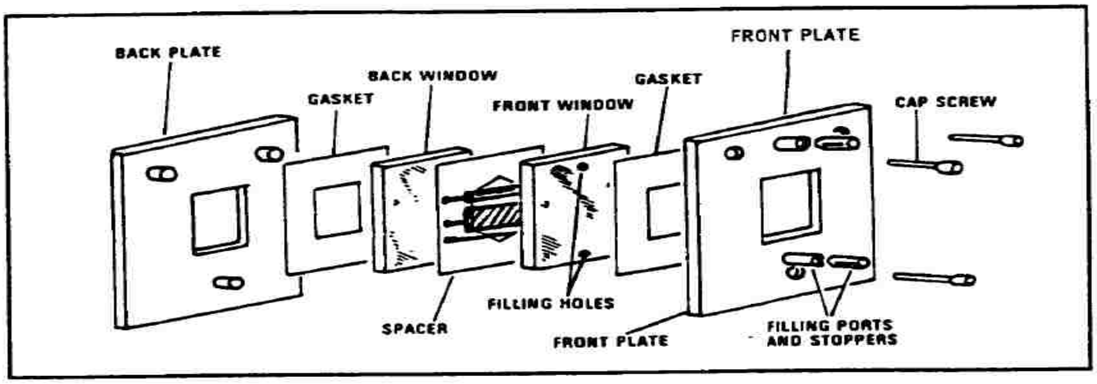

Figure 2-3. Schematic diagram of the IR OTTLE cell with three-electrode system.

The ^{1}H NMR and deuterated ^{2}H NMR were obtained using a Varian 400 MHz spectrometer. The spectra were analyzed with Spinwork3. The spectra were taken in THF-d_8. For ^{2}H NMR, one drop of normal THF was added in THF-d_8 to calibrate the spectra. Low temperature NMR were taken under nitrogen using liquid nitrogen.

X-ray crystal structures were obtained with Oxford Super Nova diffractometer using Cu (Kα) radiation.

2.10 Experimental Procedures

The cyclic voltammetry was carried out in a glove box with refluxed THF solvent and the reference electrode was Ag/$AgNO_3$ unless otherwise noted. For the UV-Visible spectroelectrochemical data, all the solutions were prepared and placed into an OTTLE cell in the glove box and parafilm was used to make the cell air tight. The FTIR cell was put into the glove box over night before use and the cells were filled in the glove box. Then the spectra were collected using 64 scans at a 2 cm^{-1} resolution in the absorbance mode with a range from 500 cm^{-1} to 4000 cm^{-1} . In all the electrochemical and spectroelectrochemical experiments, 0.1 M tetrabutylammonium perchlorate (TBAP) was used as supporting electrolyte.

2.11 RRDE Experiment Set up

Figure 2-4. RRDE experimental set up. The electrode connections 1) Green for disk electrode 2) Red for counter electrode 3) White for reference electrode 4) Yellow for ring electrode. 5) Two white tube, one for argon out and another for out.

For the RRDE experiment, 0.2-0.8 mM, iron porphyrin nitrosyl solution was prepared with doubly distilled THF in a glove box. The solution was transferred to the RRDE cell with an air tight Teflon cap. The cell was wrapped additionally with Teflon tape to prevent entry of oxygen. The reference and counter electrodes were wrapped with Teflon tape, and then tightly fitted to the holes on the Teflon cap. The large hole for the working electrode (ring-disk electrode) was sealed with a glass stopper to make sure the cell was perfectly sealed before being removed from the glove box.

To set up the cell with the rotator, the argon supply was pre-saturated with double distilled THF at least 10 minutes before the connection with the bubbler. The argon line connected first to the tiny hole on Teflon cap and then the electrode rotated for 10 minutes for degassing. The voltammetry was carried out under an argon atmosphere. The addition of acids was the most challenging part of the experiments. The acids were dissolved first into the THF then sealed with rubber septum in the glove box. The insertion of acids was done with a micro syringe through the tiny hole for the gas. The pressure of argon was high enough to prevent oxygen entry into the cell at the time of injection of the acid solution. Before carrying out the voltammetry, the system was degassed again for 5-10 minutes while rotating the electrode to make sure proper mixing of the acid and to prevent entry of oxygen in the cell solution.

Usually the ring potential was kept constant while the disk potential was scanned. To do the opposite, the working electrode connection was switched ring to disk and vice versa. The THF level in the bubbler was maintained by adding extra THF to prevent the decrease of solvent level in RRDE cell.

2.12 Computational Methods

To measure the limiting current accurately from rotating ring disk voltammetry, the rising portion of limiting disk current (i_D) was fitted to the classical rotating disk electrode equation:

$$E = E^0 - slope*\log\{(i_D - i)/i\} \qquad (2\text{-}1a)$$

The theoretical value for slope is 59 mV

The E^o, i_D and slope were adjusted to obtain the best fit of the RRDE data. Slope greater than 60 mV were due to uncompensated solution resistance.

The Levich equation was used to determine the diffusion coefficient of the systems

$$\mathbf{i_L = 0.61nFAD_o^{2/3}\,\omega^{1/2}\,\nu^{-1/6}\,C^*_o} \qquad (2\text{-}1b)$$

n = # of electron

F = Faraday constant

A = Area of electrode

D= Diffusion coefficient

ω = Rotation rate

ν = Kinematic Viscosity = η/d

C* = Initial concentration of the Fe(P)(NO)

The Koutecky- Levich equation was implemented to qualitatively examine the kinetics which are involved in the reaction mechanism. The equation is;

$$\frac{1}{i} = \frac{1}{iL} + \frac{1}{iK} \qquad (2\text{-}1c)$$

i_K = kinetic current and $i_L = 0.61nFAD_o^{2/3}\,\omega^{1/2}\,\nu^{-1/6}\,C^*_o$

2.13 Digital Simulation of EC Reversible Mechanism

The theoretical relationship between the collection efficiency and the kinetic parameter was obtained using the algorithm by Prater et al. [143-145] An alternate approach which has simplified the explicit method is the use of the heterogeneous equivalent method, first described by Ruzic and Feldberg.[148,149] In that case, they derived the equation for a fast reversible EC, and for the dimerization mechanism. For the EC mechanism described, the forward and reverse reactions were first-order (or pseudo-first order).

The EC mechanism for reductions in unbuffered solutions can be written as:

$$A + e^- \leftrightarrows B \tag{2-2}$$

$$B \leftrightarrows Y + P \tag{2-3}$$

The rate constants for Reaction 2-3 are k_f and k_b for the forward and reverse reaction, respectively. The equilibrium constant for Reaction 2-3, K, can be written as:

$$K = \frac{[Y][P]}{[B]} \tag{2-4}$$

In order to compare the simulated results to the experimental data, the concentrations need to be normalized. This will be done by dividing the simulated concentrations by the bulk concentration of A, C_A*.

$$C_A^* K_{sim} = \frac{[Y][P]}{[B]} \tag{2-5}$$

Leading to,

$$K = C_{A,sim}^* K_{sim} = K' \tag{2-6}$$

This formulation is sufficient for reductions in unbuffered aqueous solutions, where water is the reactant and does not appear in the equilibrium expression. If a reactant, X, is present, Reaction 2-3 becomes:

$$B + X \leftrightarrows Y + P \tag{2-7}$$

In this case,

$$K = \frac{[Y][P]}{[B][X]} \tag{2-8}$$

If [X] >> C_A*, its concentration will be constant during the experiment and can be combined with the equilibrium constant, *K*

$$K' = K[X] = \frac{[Y][P]}{[B]} \tag{2-9}$$

For the mechanism to be meaningful, *K'* must be greater than 1.

The explicit method, developed by Prater and Bard, [145,150] is useful for slow to moderate reactions, but fails for fast reactions that are required for a reversible mechanism. An alternative approach is to use the "heterogeneous equivalent" method developed by Ruzic and Feldberg. [148,149] The method combines the electron transfer process with the chemical step, in order to eliminate the intermediate (B) species.

$$A + e^- \rightarrow Y + P \tag{2-10}$$

The details of the rationale for this approach are given in the cited references. The derivation of the fluxes of A/Y/P for Reaction 2-10 is given in appendix. This approach can be applied in any explicit method, as it only concerns the concentrations at the electrode surface. The approach assumes that the concentration of B is at steady state, and the reaction layer is much smaller than the diffusion layer. To cover the full range of reaction rates, the explicit method without the heterogeneous equation was used for slow to moderate reaction rates.

Using the heterogeneous equivalent, the flux of Y at the reaction layer, μ, f(Y), is given by the following quadratic equation:

$$A f(Y)^2 + B f(Y) + C = 0 \tag{2-11}$$

where:

$$A = \frac{1}{\left(4K_{sim}D_P D_Y\right)} \tag{2-12}$$

$$B = \frac{1}{\sqrt{k_f D_B}} + \frac{P_1}{2K_{sim}D_Y} + \frac{Y_1}{2K_{sim}D_P} + \frac{\theta}{2D_A} + \frac{1}{k_{hf}} \tag{2-13}$$

$$C = \frac{Y_1 P_1}{K_{sim}} - \theta A_1 \tag{2-14}$$

Where A_1, P_1 and Y_1 are the concentrations of A, P and Y at the first volume element in the simulation, k_{hf} is the heterogeneous forward rate constant, and $\theta = k_{hf}/k_{hb}$. Because the homogeneous reaction is combined with the electron transfer, there is no need to use long simulation times in order to study fast reactions. The quadratic equation was solved for the flux of Y at each surface volume element on the ring, and the root that gave physically meaningful concentrations was used (positive concentrations; sum of the concentrations at the electrode surface cannot exceed the initial concentration). The flux of A at the disk assumed limiting current conditions. In order to verify the generality of this expression, the heterogeneous equation was also tested for cyclic voltammetry, and gave the correct voltammograms for limiting cases.

Figure 2-5A shows the results for the simulation of Reactions 2-2 and 2-3 for the relationship between *XKT* and collection efficiency, N_k, where:

$$N_k = -\frac{i_R}{i_D} \tag{2-15}$$

where i_R is the current at the ring and i_D is the current at the disk, and,

$$XKT = k\nu^{1/3} / \omega D^{1/3} (0.52)^{2/3} \tag{2-16}$$

where *k* is the rate constant, ν is the kinematic viscosity, D is the diffusion coefficient and ω is the rotation rate (rad/s). In this case, the heterogeneous equivalent was not necessary, as the rates are slow enough. The EC reversible mechanism can be divided into four zones (Figure 2-5B). In the first zone, k_b is not significant under the voltammetric conditions, and the voltammetry is controlled by k_f. The results are the same as the EC irreversible mechanism. Zone 2 starts from the point where N_k diverges from the EC irreversible curve due to the reverse reaction to the minimum value of N_k. The relationship between N_k and *XKT* are qualitatively the same for Zones 1 and 2 (e.g., N_k decreased as *XKT* increased) but is quantitatively different. Zone 3 begins at the minimum value of N_k for a given K_{sim} until N_k reaches the reversible value. In this region, N_k increases with *XKT*, which is the opposite of Zones 1 and 2. In Zone 4, N_k is the value for a reversible electron transfer and is independent of *XKT* (not shown in Figure 2-5B). In the limit where both k_f and k_b are fast, the voltammetric results will be the same as a reversible electron transfer, with the potentials shifted by Reaction 2-3. Between these two limits, the voltammetric results will depend upon *K* and k_f. For slow to moderately fast reactions (Zone 1), the explicit method of Prater and Bard is sufficient.[145] For the regions of interest (Zones 2-4), this method is too inefficient. The two regions that are of particular interest for the EC reversible mechanism are Zones 2 and 3. Diagnostically, we can differentiate Zone 2 from Zone 3 by the relationship between N_k and *XKT* (or ω^{-1}). In Zone 2, N_k decreases with *XKT* (or ω^{-1}), while in Zone 3, N_k increases with *XKT*. Using the results for Figure 2-5A, a generalized relationship between N_k and a new kinetic parameter, *XKTK*, can be obtained.

$$XKTK = \frac{\sqrt{XKT}}{K'} \tag{2-17}$$

where C^*_A is the bulk concentration of A. Using this new parameter and the data in Figure 1A, the relationship between N_k and *XKTK* is shown in Figure 2-5C. These results show that a general solution is possible for Zone 3 and 4.

For $K' > 1$, a single curve can be drawn for Zone 3 (Figure 2-6) for the relationship between N_k and *XKTK*. In Zone 3, the value of k_f or K' cannot be directly determined, but only the ratio $\sqrt{k_f}\,/\,K'$. K' must be determined independently. The following empirical equation can be fit for the data in Figure 2-6.

$$XKTK = \frac{2.085N_k + 0.001599}{N_k^2 - 0.8047N_k + 0.1604} \tag{2-18}$$

The constants in Eq. 2-18 have no physical significance, but this can be used to calculate *XKTK* from the experimental collection efficiency, N_k.

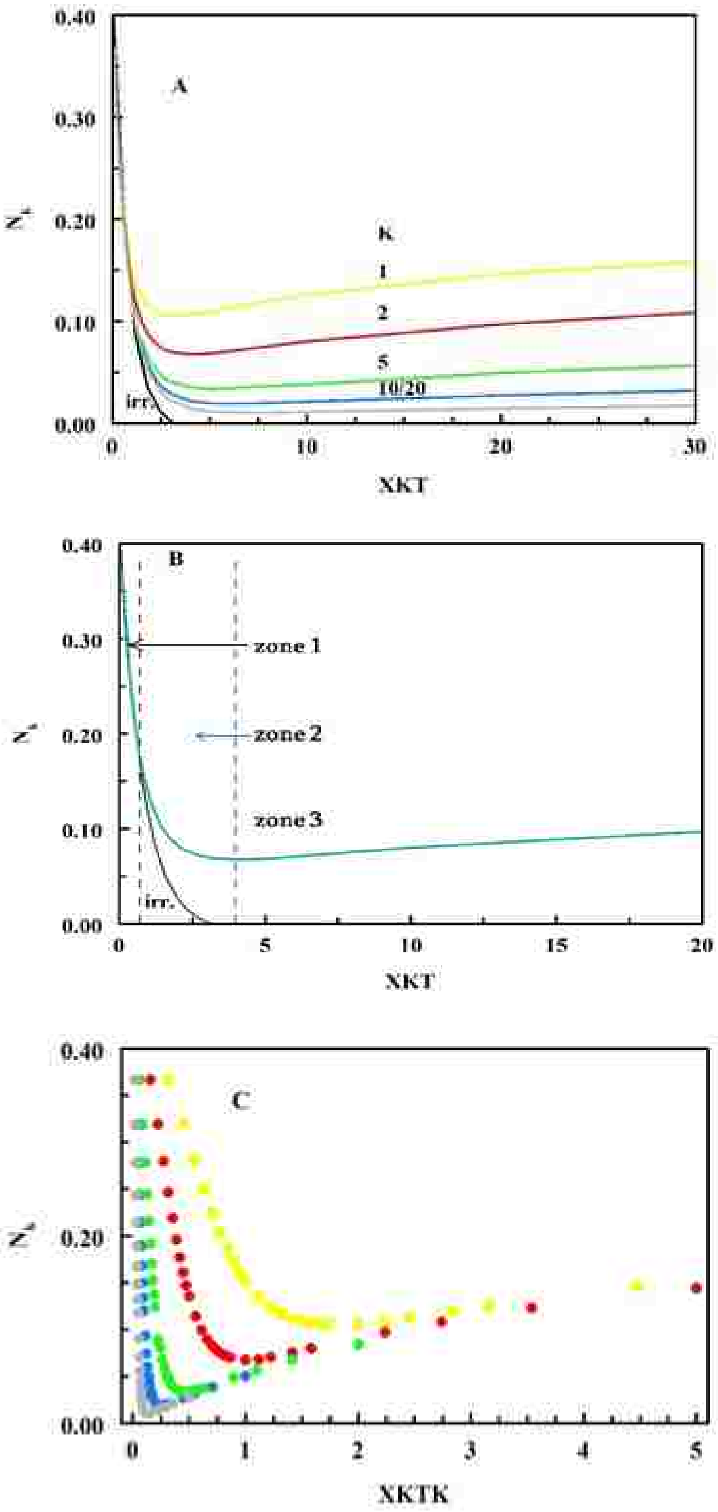

Figure 2-5. A. The collection efficiency, N_k, as a function of the kinetic parameter, *XKT*. B. The collection efficiency, N_k, for the irreversible case and for *K* = 7.5, indicating 3 of the 4 kinetics zones. C. The collection efficiency, N_k, as a function of *XKTK*. Values of C_A*K_{sim}: 1 (●); 2 (●); 5 (●); 10 (●); 20(●).

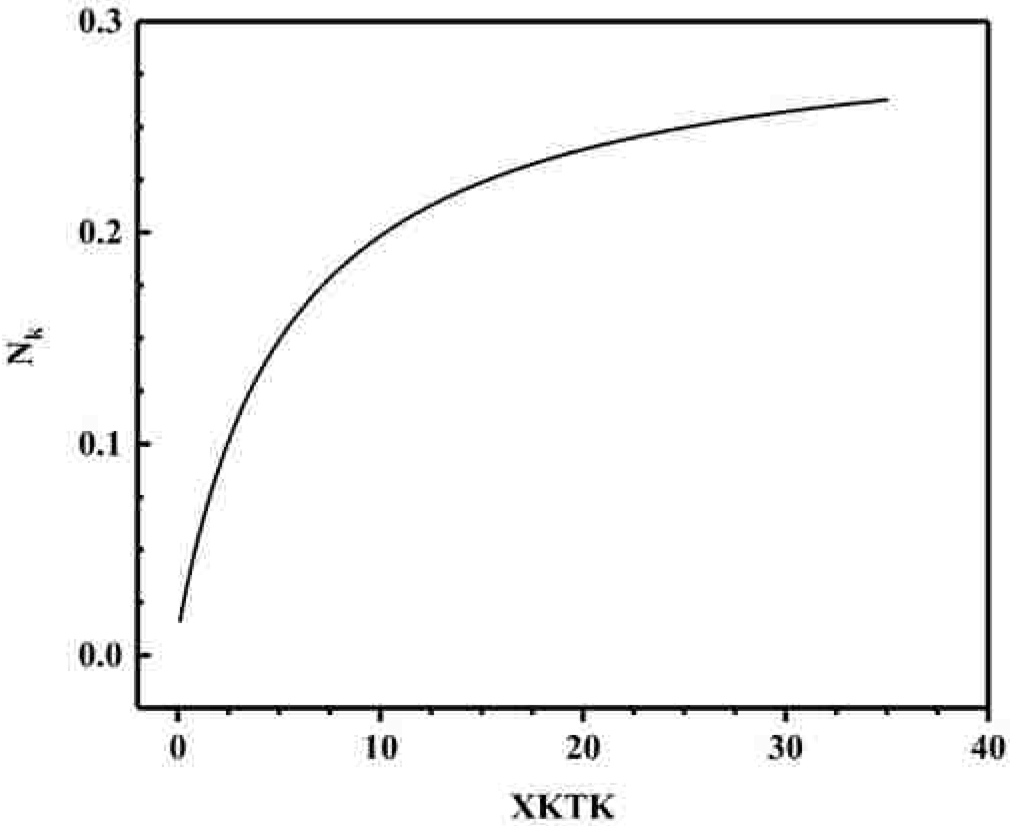

Figure 2-6. Relationship between *XKTK* and N_k, as derived by digital simulation of the EC reversible mechanism.

2.14 Factor Analysis

The spectra for redox species from the spectroelectrochemical data can be analyzed easily by the isobestic points if only two spectral species are present or if the potentials (E^0s) for multielectron transfers are clearly separated. But if these conditions are not fulfilled, the deconvolution of the spectra is difficult. In addition, the determination of number of species present in the solution is also tedious. These problems can be solved using the factor analysis method. [151]

In this methodology, a large set of data is reduced to its lowest dimensionality. The lowest dimensionality corresponds to the number of spectral species in solution. Usually spectroelectrochemical data are a bilinear data with the matrix row corresponding to absorbance and the columns corresponding to potential or time. This data matrix decomposes into two abstract matrices which have no physical significance.

$$D = R_{abs}C_{abs} \tag{2-21}$$

The R_{abs} and C_{abs} matrices are usually determined by singular value decomposition method. This method generates three matrices U, S and V^T .

$$D = USV^T \tag{2-22}$$

Where $R_{abs} = US$ and $C_{abs} = V^T$

The S matrix is a square diagonal matrix where the diagonal elements are the square of the eigenvalues. The eigenvalues, λ, decreases monotonically along the diagonal. For an $m\times m$ S matrix, the eigenvalues, λ_i, can be divided into two groups: λ_1 to λ_n where n= number of spectral species, and λ_{n+1} to λ_m which represent noise in the spectrum (ideally λ_{n+1} to λ_m should be zero). The aim of factor analysis is to find the value of n, which is equal to the number of spectral species. If the noise level is low, the real eigenvalues (λ_1 to λ_n) should be significantly larger than the noise eigenvalues (λ_{n+1} to λ_m), making it possible to determine the value of n. Once n is known, the order of the R and C matrices can be reduced to n.

The abstract matrices (both row and column) can be transformed into real concentration (C) and molar absorptivity (E) matrices when the number of species have been determined from the set of eigenvalues.

$$C = R'_{abs}\,T \tag{2-23}$$

$$E = C'_{abs}T^{-1} \tag{2-24}$$

Where R'abs and C'abs matrices have an order n.

T is a square transformation matrix which transforms the abstract to real matrices. Determination of the T matrix is a great challenge. Window factor analysis can be used to generate T matrix.[151]

Generating the T matrix is generally not needed if the primary aim is to determine the number of species and potential range where they appear. This can be done with evolving factor analysis.

In this method, each species can only appear once over a specific potential or time and has a concentration equal to zero for other potentials or time. This method consists of generating a series of eigenvalues matrices (S), starting with the first two spectra and then successively adding an additional spectrum with each step. As new species appears, the real eigenvalues will raise above the noise eigen values. This is called forward evolving factor analysis where eigenvalues calculation running from first spectrum to last spectrum (Figure 2-7).

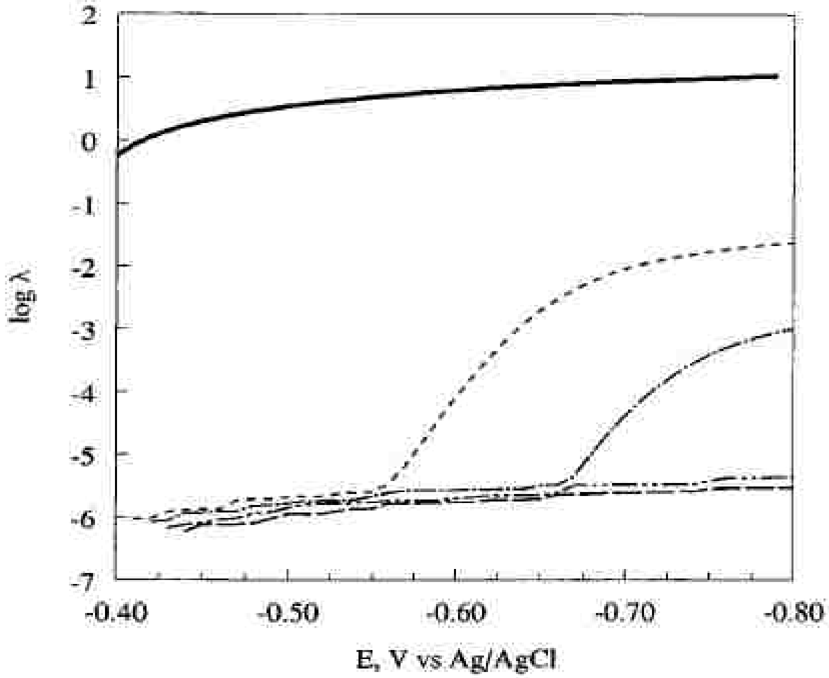

Figure 2-7. Forward EFA eigenvalues for the thin-layer spectroelectrochemistry of E. coli sulfite reductase hemoprotein: factors 1 (s), 2 (- - -), 3 (- â -), 4 (- â â -), and 5 (- -).[151]

This information is generally sufficient to deconvolute the spectra if there is enough time/potential difference in the appearance of the individual species. Similar process can be run starting from last spectrum to first spectrum which is called backward evolving factor analysis. The reverse EFA can also be done starting with the last two spectra, calculating S, and then progressively add additional spectra (Figure 2-8). The point where the eigenvalues raises above the noise is the point where a species has disappeared. Combining these two analyses, one can determine the appearance and the disappearance of the redox species in the specific potential range with concentration window.

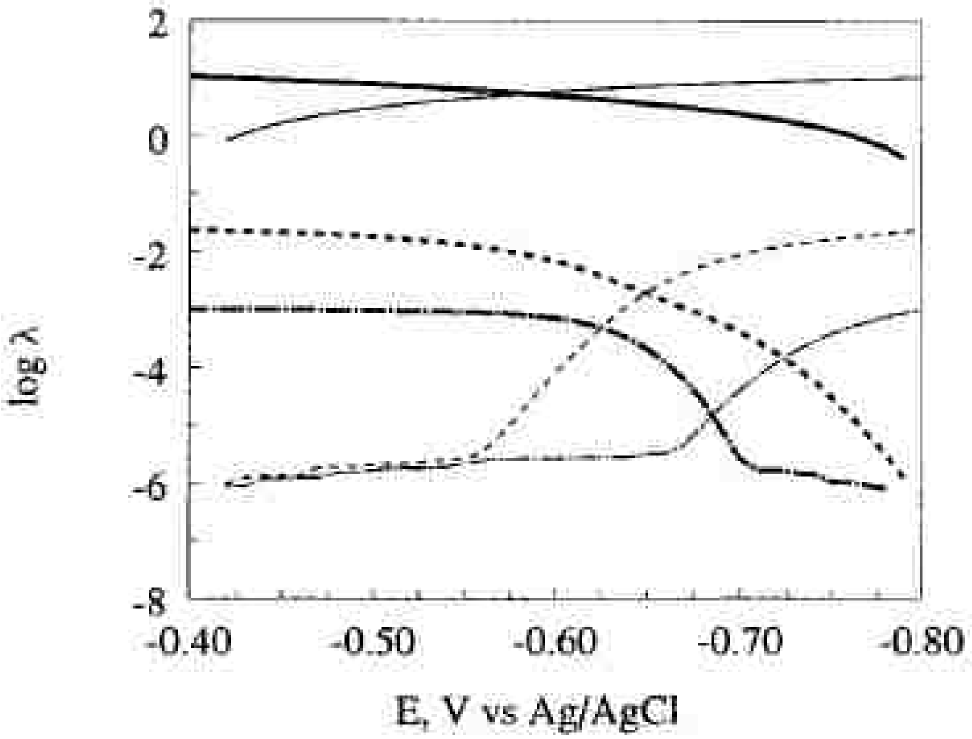

Figure 2-8. Forward and reverse EFA eigenvalues for the thin-layer spectroelectrochemistry of E. coli sulfite reductase hemoprotein: factors 1 (s), 2 (- - -), and 3 (- â -). Bolder lines are the reverse EFA eigenvalues.[151]

CHAPTER 3 VOLTAMMETRY OF IRON PORPHYRIN NITROSYLS

3.1 Cyclic Voltammetry of Fe(II)(OEP)(NO)

The cyclic voltammetry of Fe(OEP)(NO) was carried out in THF. The voltammograms are shown in Figure 3-1. The one electron transfer was reversible (Reaction 1/ Scheme 1) and the reduced species were chemically stable ($i_a/i_c \approx 1.0$) in voltammetric time scale. The potential difference between forward and reverse peak potential ((E_{pa}-E_{pc}) was found larger than 59 mV (2.3RT/nF) expected for Nernstian value which is attributed for high solution resistance of THF (≈ 220 mV). The peak current increased as a function of square root of scan rate (inset Figure 3-1) indicating a diffusion controlled process. Further reduction occurs at more negative potential.

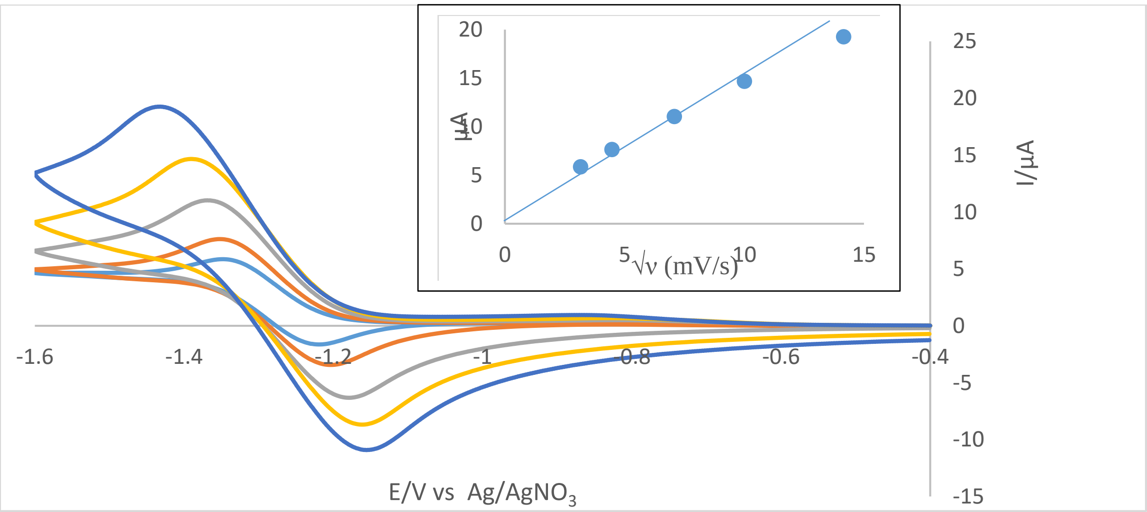

Figure 3-1. Cyclic voltammograms of 0.45 mM Fe(OEP)(NO) in THF with 0.1 M TBAP at different scan rates (10, 20, 50, 100 and 200 mV/s), working electrode Boron doped diamond electrode (BDD).

The voltammetry was also carried out in the presence of 2,6-dichlorophenol (dcp). With the addition of the acid, the wave was shifted to positive potentials which is characteristic of a following or EC (electron transfer then chemical reaction with acid) mechanism (Reaction 3-2/Scheme 1). With an increase in the acid concentration, the wave shifted to more positive potentials. The voltammograms are shown in Figure 3-2. The switching potential was chosen so that only the first electron reduction was observed. The peak current increased minimally in the presence of acid which indicated no further reduction of Fe(OEP)(HNO) occurred. The peak current ratio decreased as the scan rate increased. At slow enough scan rates, the wave was completely reversible (Figure 3-3). The increased chemical reversibility was consistent with an EC reversible mechanism (Reactions 3-1,3-2/ Scheme 1). Scheme 1 was proposed based on voltammetric results.

If the potential was scanned to more negative potentials, a second wave was observed (Figure 3-4). This was previously seen and led to the formation of hydroxylamine (on voltammetric time scale) and ammonia (on the coulometric time scale). These results were consistent with previously reported work using normal pulse polarography.[72]

Scheme 1

$Fe(OEP)(NO) + e^- \rightarrow Fe(OEP)(NO)^-$ (3-1)

$Fe(OEP)(NO)^- + PhOH \rightarrow Fe(OEP)(HNO) + PhO^-$ (3-2)

$Fe(OEP)(HNO) + 2\ e^- + 2PhOH \rightarrow Fe(OEP)(H_2NOH) + 2\ PhO^-$ (3-3)

$Fe(OEP)(HNO) + PhOH \rightarrow Fe(OEP)(H_2NO)^+ + PhO^-$ (3-4)

$Fe(OEP)(H_2NO)^+ + 3e^- + PhOH \rightarrow Fe(OEP)^- + H_2NOH + PhO^-$ (3-5)

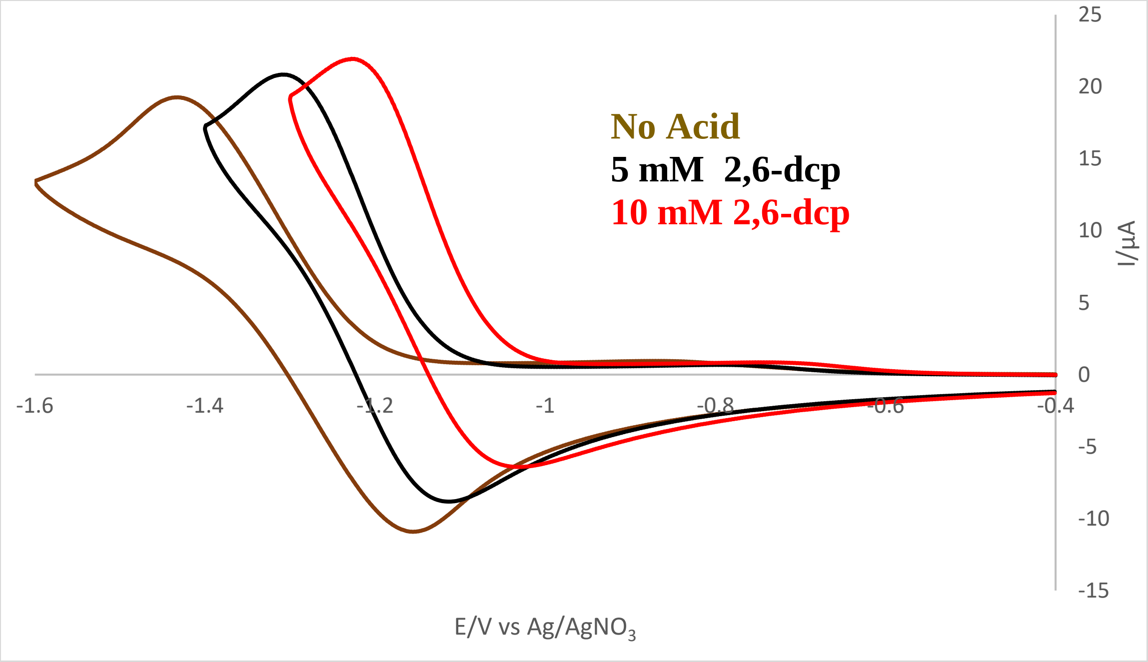

Figure 3-2. Cyclic voltammograms of 0.89 mM Fe(OEP)(NO) in THF with 2,6-dcp, 0.1 M TBAP at 50 mV/s, Working electrode BDD.

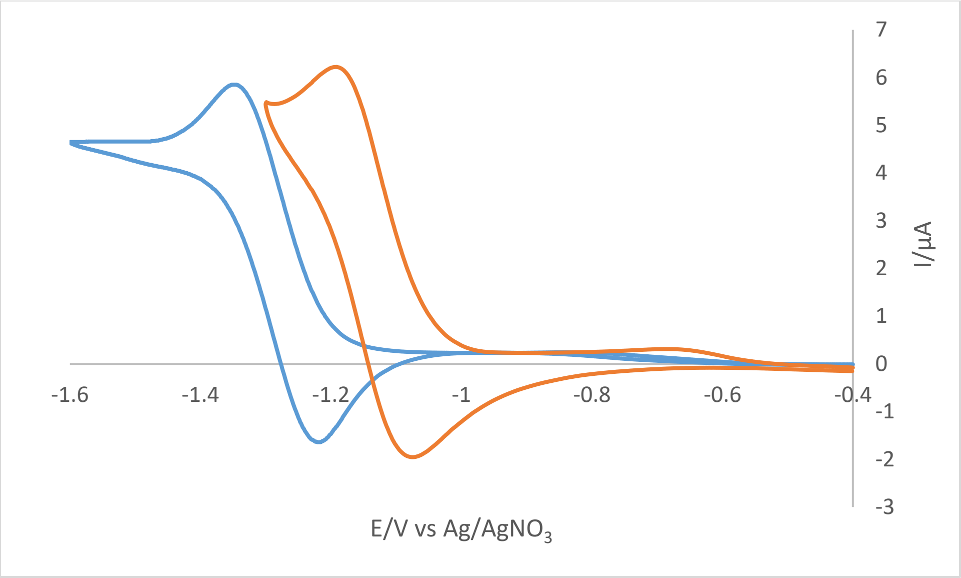

Figure 3-3. Cyclic voltammograms of 0.89 mM Fe(OEP)(NO) in THF with 0.10 M TBAP, Absence of 2,6 dcp (Blue); 10 mM 2,6-dcp (Orange). Scan rate: 10 mV/s, Working electrode BDD.

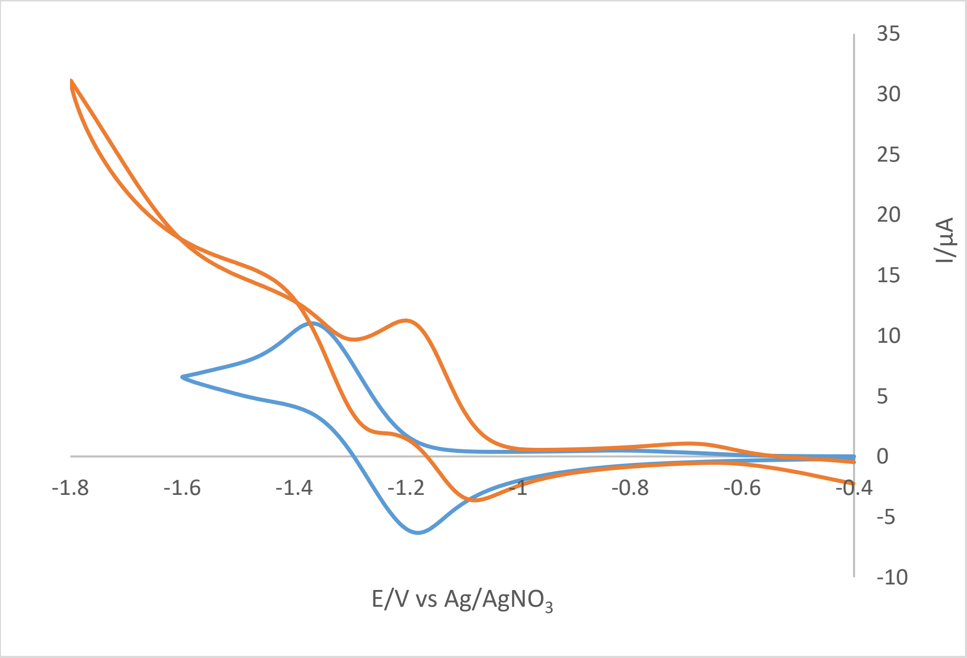

Figure 3-4. Cyclic voltammograms of 0.89 mM Fe(OEP)(NO)(Blue) in THF with 0.10 M TBAP in the presence of 10 mM 2,6-dcp (Orange), Scan rate: 50 mV/s, Working electrode BDD.

Another set of voltammetric data was obtained at low concentrations of 2,3-dcp which is shown in Figure 3-5 A. Two reduction waves were also observed within the potential range that was scanned. Using the semi derivative of the current, the ratio of the semi derivative of the second wave to that of the first wave was found about 2 at lower scan rate, indicating a multi electron (at least 2 electrons) reduction was occurring for the second wave (Figure 3-5A, Inset). To make sure that the wave was not due to the acid reduction, the experiment was repeated without Fe(OEP)(NO) (Figure 3-5 B). No wave was observed at the Fe(OEP)(NO) potential for the second wave. With the higher concentration of acid, these two-wave merged to form a broad peak (Figure 3-5C). The reverse peak was only observed at lower scan rate. These results were consistent with the behavior that was previously reported for normal pulse polarography using mercury electrode.[72] The kinetics of the second redox process was thoroughly examined in that work and corresponded to a kinetically controlled 3- electron process. The current for the three-electron process was strongly dependent upon scan rate and acid concentration. Three electrons were only observed at slow scan rate and with high acid concentrations. As the multi electron process (Reactions 3-4,3-5/ Scheme 1) has already been studied in detail, the focus will be mostly on the intermediate species, Fe(OEP)(HNO). Its formation kinetics, reactivity and characterization would be studied in detail.

Table 3-1. pK_a Values for Selected Phenols.

Compound	pK_a
2,6-dichlorophenol	6.79
2,3-dichlorophenol	7.76
3,5-dichlorophenol	8.18
phenol	10.00

A series of voltammetric experiments were performed with a variety of phenols depending on their pK_a values (Table 3-1). All the phenols showed a similar pattern but the shift of the wave was dependent on the pK_a of phenols. As the pK_a of the acid decreased, a higher concentration of acid (compared to higher pK_a of acids) was needed to shift the wave. While 5-10 mM 2,6-dcp and 2,3-dcp were needed to shift the E_1^o as shown in Figure 3-4 and 3-5A, much higher concentrations were needed for the weaker acids (0.2-0.5 M were needed for phenols itself). The height of the second wave was dependent on the concentration of phenols and on the structure of acids. In case of 2,6-dcp, the height of second wave was less than that of 2,3-dcp under the same conditions (Figure 3-4 and 3-5A). The reason might be the steric hindrance from 2,6-dcp which disfavored Fe(OEP)(NH_2OH) formation. This result indicated that there was an iron porphyrin nitroxyl-phenol intermediate formed at the transition state, then the phenolate dissociated to give Fe(OEP)(HNO).

From the shift in the E_1^o value, one can roughly estimate the concentration of substituted phenols needed to form Fe(OEP)(HNO) by plotting $E_{1/2}$ vs log[Acid] per Equation 3-6. A nonlinear curve could be generated and from the slope of the curve, one can find the minimum concentration of acid at which Fe(OEP)(HNO) formation was prominent. The concentration which is related to 59 mV slope, would give maximum single protonation. When the slope exceeded 59 mV value, doubly protonated species may be formed. This optimal concentration could be used to identify spectroscopic characteristics of the single protonated species. Because of the complications with cyclic voltammetry such as electron transfer kinetics and solution resistance, this technique was only used to identify the reaction mechanism. Extensive study was performed by rotating ring disk electrode (RRDE) voltammetry to determine kinetic parameters.

$$E_{1/2,\,p} = E_{1/2,np} + 0.059 \log(1 + K_1[\mathrm{PhOH}]/[\mathrm{PhO}^-]) \qquad (3\text{-}6)$$

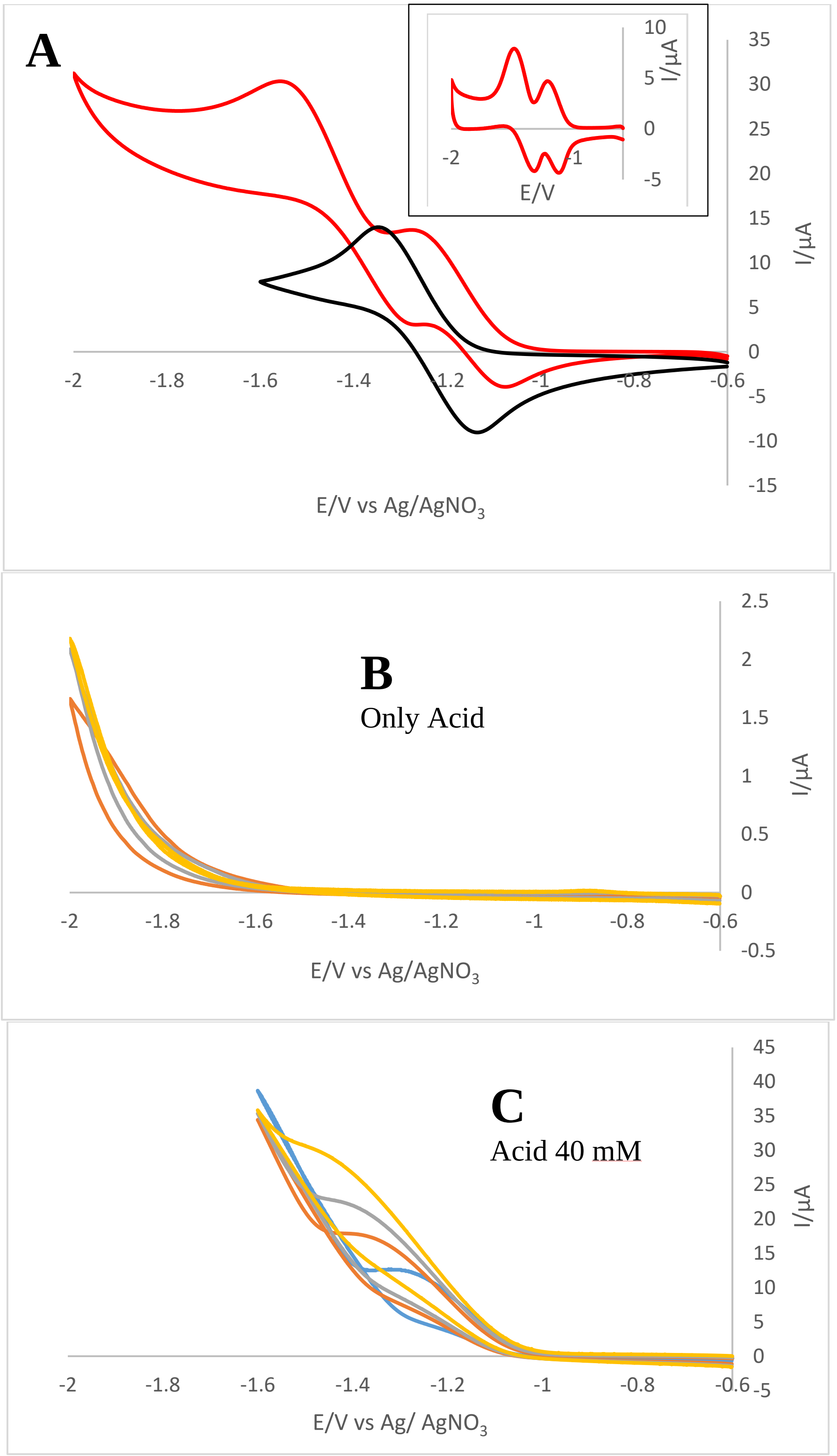

Figure 3-5. Cyclic voltammograms of 0.89 mM Fe(OEP)(NO) in THF with 0.1 M TBAP, A) With 5 mM 2,3-dcp (Red = Acid, Black = No acid) at 20 mV/s (Inset semi derivative wave) B) Only 2,3-dcp C) With 40 mM 2,3-dcp at different scan rate, Working electrode BDD.

3.2 Rotating Ring Disk Electrode (RRDE) Voltammetry

The characterization of the reaction mechanism using cyclic voltammetry is challenging because of the interplay among electron transfer kinetics, solution resistance and the homogenous protonation reaction with reduced species.

In order to overcome those challenge, an alternative voltammetry technique, rotating ring disk electrochemistry was chosen. In this technique, the current reaches at steady state and is measured at the limiting current plateau. The limiting current at steady state is not sensitive to the solution resistance and electron transfer kinetics. In this technique, the species which is formed at the disk due to electron transfer will move the ring by diffusion and convection. If the ring potential is set to a potential positive of the E^o, the reduced species will be re-oxidized. The purpose of this experiment is to observe the changes when the reduced species passed over the disk ring gap, during which the reduced species can undergo a chemical reaction. The important kinetic parameter is the collection efficiency, N_k, which is the absolute value of the ratio of the ring current to disk current. The maximum value can be calculated from the dimensions of the ring and disk electrodes. For a reversible system, the N_k is independent of rotation rate.

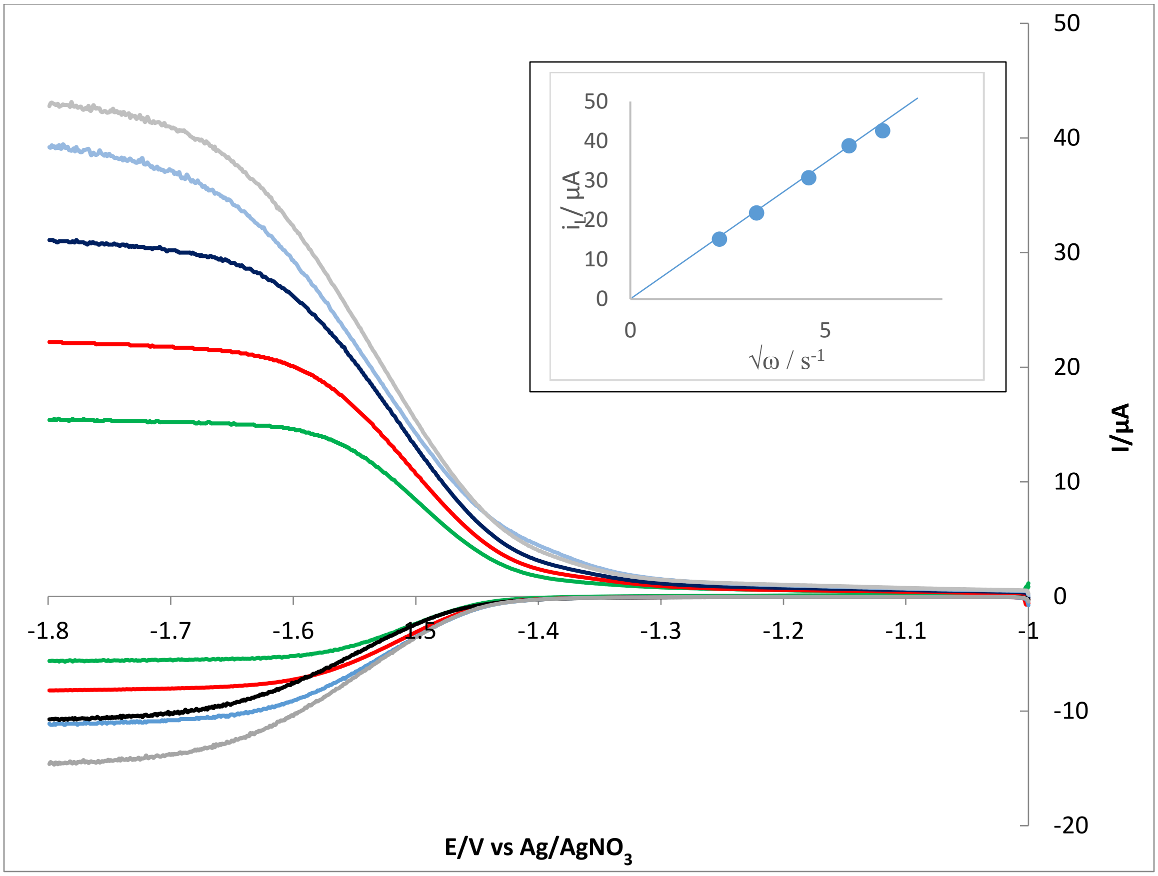

Figure 3-6. RRDE voltammograms of 0.5 mM Fe(OEP)(NO) in THF at different electrode rotating rates, scan rate 1 mV/s, working electrode Pt, 0.1 M TBAP, E_r = -0.8 V. (Top= higher rpm to bottom= lower rpm).

Table 3-2. Collection efficiency for Fe(OEP)(NO) in the absence of acids.

Rotation rate (rpm)	Collection efficiency 1^{st} wave	Collection efficiency 2^{nd} wave
50	0.364	0.260
100	0.369	0.256
200	0.371	0.254
300	0.369	0.256
400	0.358	

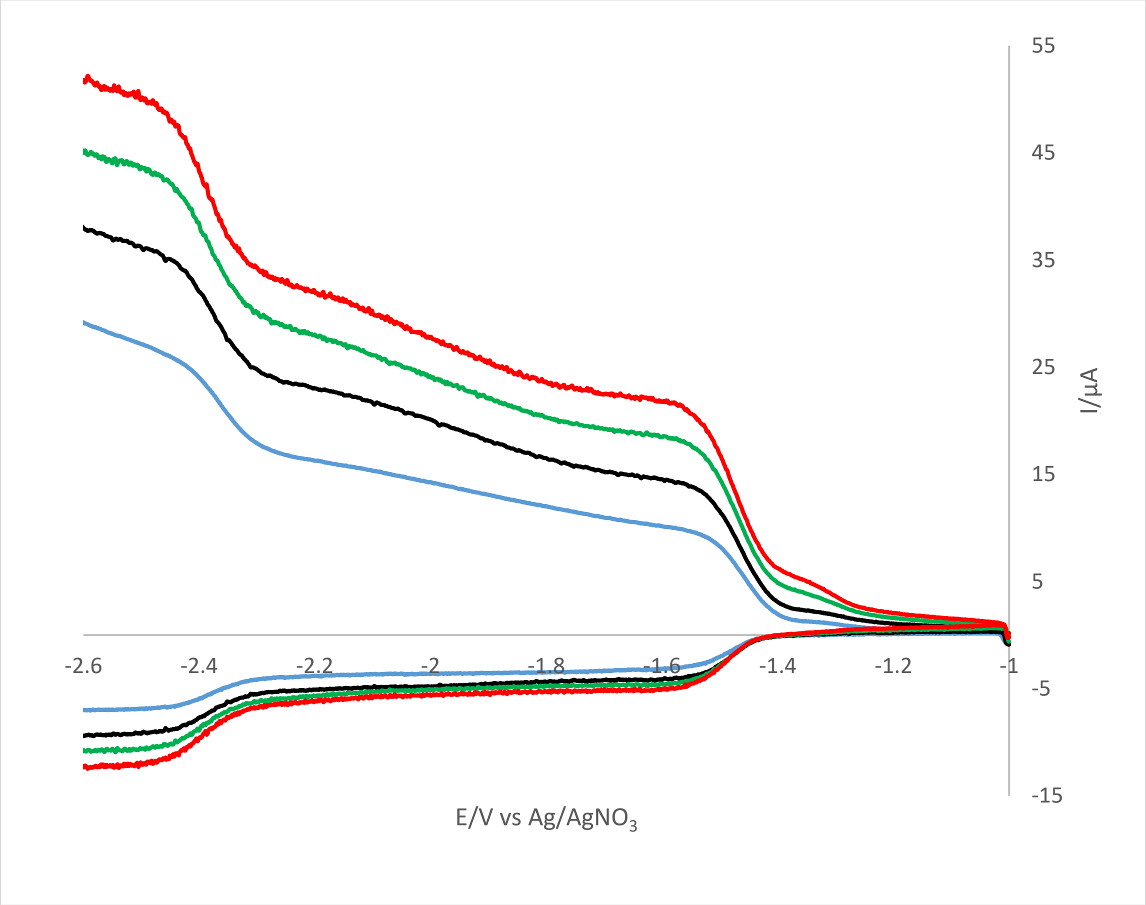

Figure 3-7. RRDE voltammograms of 0.25 mM Fe(OEP)(NO) in THF at different electrode rotating rates, scan rate 1 mV/s, working electrode Pt, 0.1 M TBAP, E_r = -0.8 V. (Top= higher rpm to bottom= lower rpm).

RRDE voltammetry of Fe(OEP)(NO) was carried out in the absence of substituted phenols. A typical set of data is showed in Figure 3-6. In the absence of acids, single reduction wave was observed up to -2.0 V, the second reduction wave was more negative than -2.0 V. The collection efficiency was consistent with a chemically reversible process (Table 3-2). The limiting current increases with square root of rotation rate (Figure 3-6 inset) which follows the Levich equation, indicating that the one electron reduction process was diffusion controlled. The potential was scanned up to -2.6 V, and a second reversible wave was observed (Figure 3-7). In the presence of acid, the one electron reduction wave shifted to positive potential (Figure 3-8). This indicated that the reduced species Fe(OEP)(NO)$^-$, reacted with the acid. The limiting disk current was the same both in the absence and presence of acid, indicating that there was no further reduction of the protonated species at this potential. Similar results were obtained for 2,3-dcp, 3,5-dcp and phenol (Figure 3-9 to 3-11). These results were consistent with the cyclic voltammetric results. An interesting phenomenon was observed for ring current. The ring current decreased in the presence of acid. Under the same conditions, it was independent of rotation rate. This behavior was symptomatic of a steady state condition for the reaction intermediate. All the acids showed the same behavior. These results were consistent with a slow chemical reaction prior to oxidation.

The potential shifts for all the acids (Figure 3-12) exceeded 59 mV which indicated at lower concentration of acid the reduced species was at least singly protonated. This increase in the slope might be due to an additional protonation or additional stabilization because of solvation due to hydrogen bonding. From the slope of the curve, the equilibrium constant can be estimated.

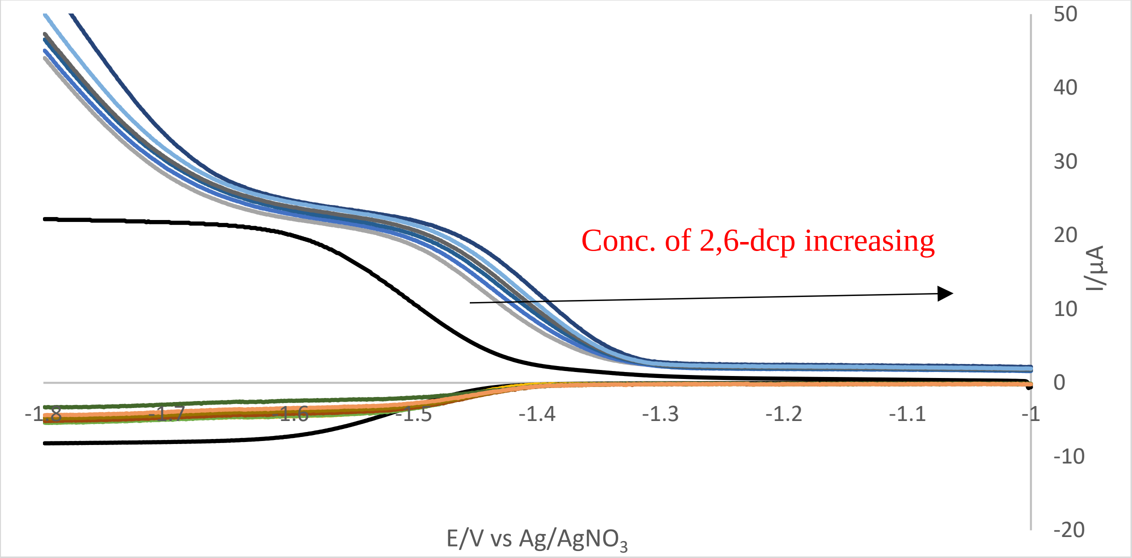

Figure 3-8. RRDE voltammograms of 0.5 mM Fe(OEP)(NO) in THF in the presence of 2,6-dcp at 100 rpm, scan rate 1 mV/s, working electrode Pt, 0.1 M TBAP, E_r = -0.8 V.

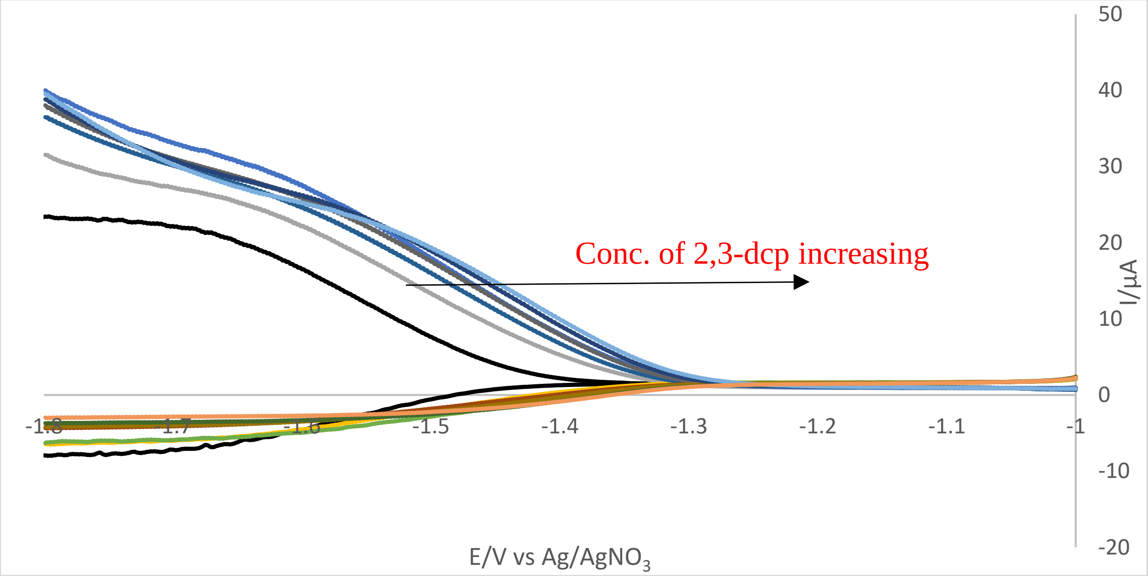

Figure 3-9. RRDE voltammograms of 0.5 mM Fe(OEP)(NO) in THF in the presence of 2,3-dcp at 100 rpm, scan rate 1 mV/s, working electrode Pt,0.1 M TBAP, E_r = -0.8 V.

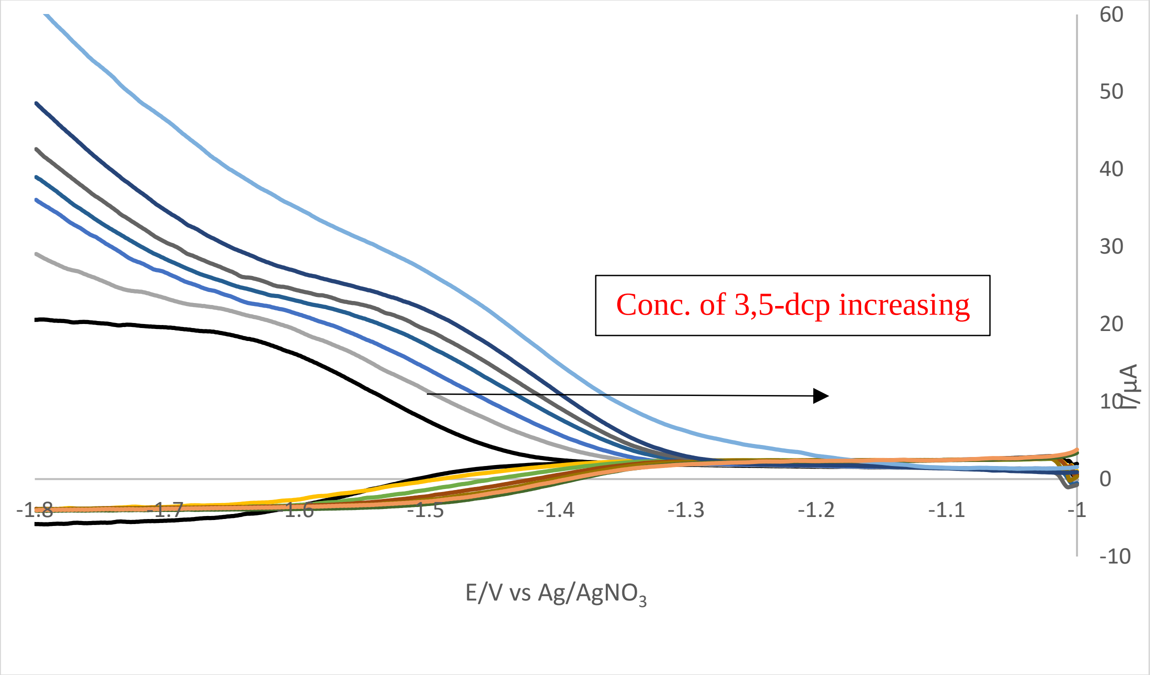

Figure 3-10. RRDE voltammograms of 0.5 mM Fe(OEP)(NO) in THF in the presence of 3,5-dcp at 100 rpm, scan rate 1 mV/s, working electrode Pt, 0.1 M TBAP, E_r = -0.8 V.

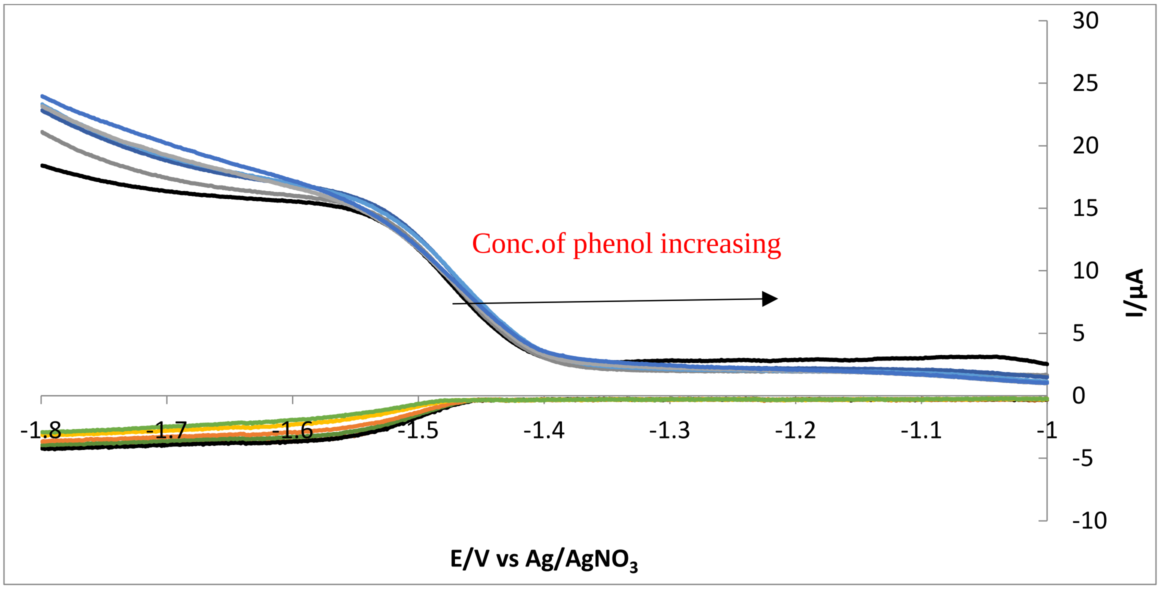

Figure 3-11. RRDE voltammograms of 0.45 mM Fe(OEP)(NO) in THF in the presence of phenol at 100 rpm, scan rate 1 mV/s, working electrode Pt, 0.1 M TBAP, E_r = -0.8 V.

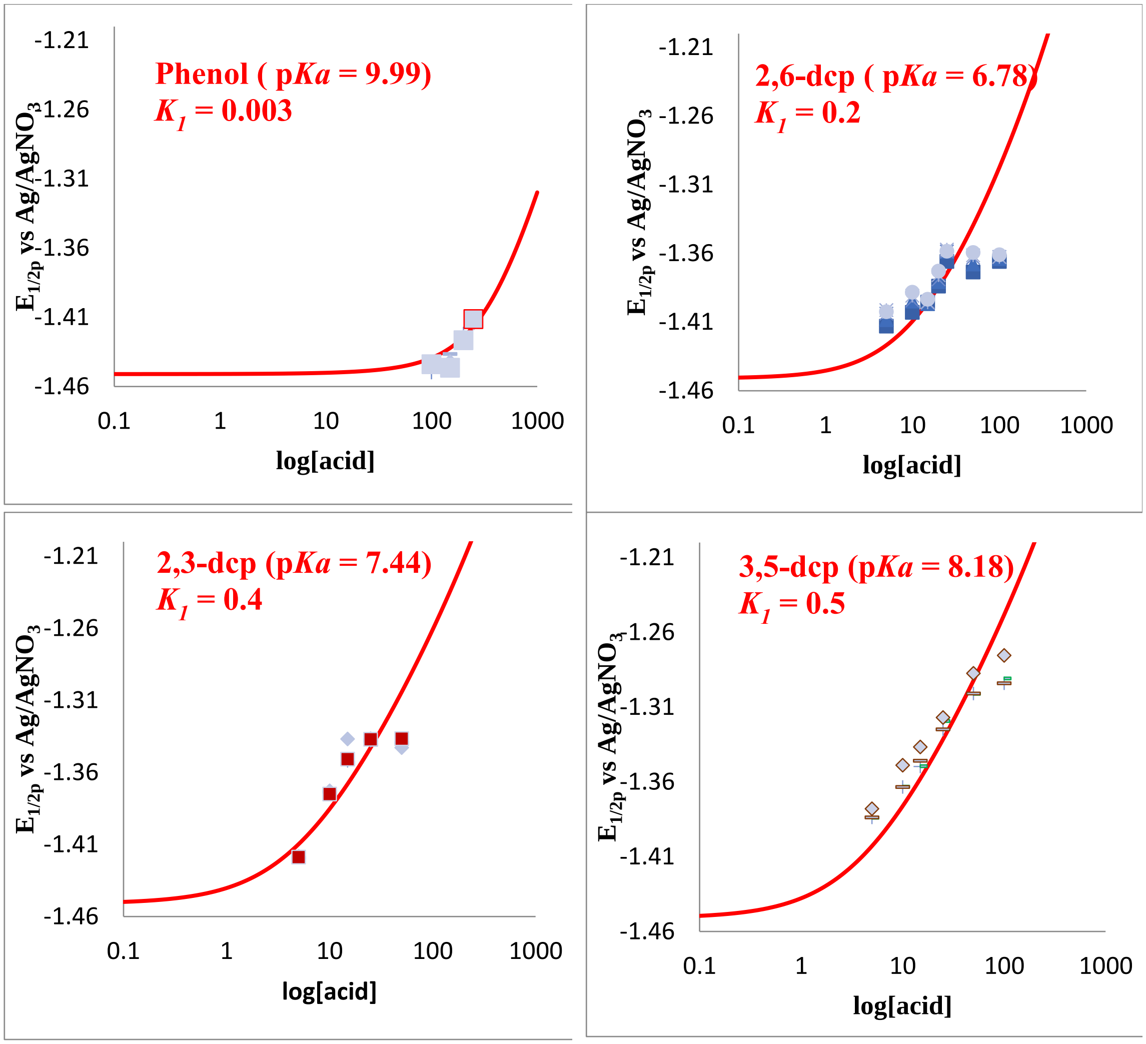

Figure 3-12. Effect on E½ of Fe(OEP)(NO) in the addition of phenol, 2,6-dcp, 2,3-dcp and 3,5-dcp.

As the reaction was not at equilibrium for the experimental time scale, the value of *K* cannot be accurately determined from the shift in the potential using Nernst equation. Thus, from the present experimental conditions, we can determine only the minimum value of *K* from potential shift using Nernst equation (Figure 3-12).

As mentioned in the experimental section, to obtain accurate disk current, the rising potion of the wave was fitted to the classical rotating disk equation (Figure 3-13,3-14).

The collection efficiency (Figure 3-15) decreased for all acids from the reversible value indicating that the ring current decreased with the concentration of acid. While there was a reaction between Fe(OEP)(NO)$^-$ and the acids was observed from the potential shift, there was no increase in the limiting current of Fe(OEP)(HNO) which indicated on further reduction of Fe(OEP)(HNO). The re-oxidation rate of Fe(OEP)(HNO) to Fe(OEP)(NO) was slow.

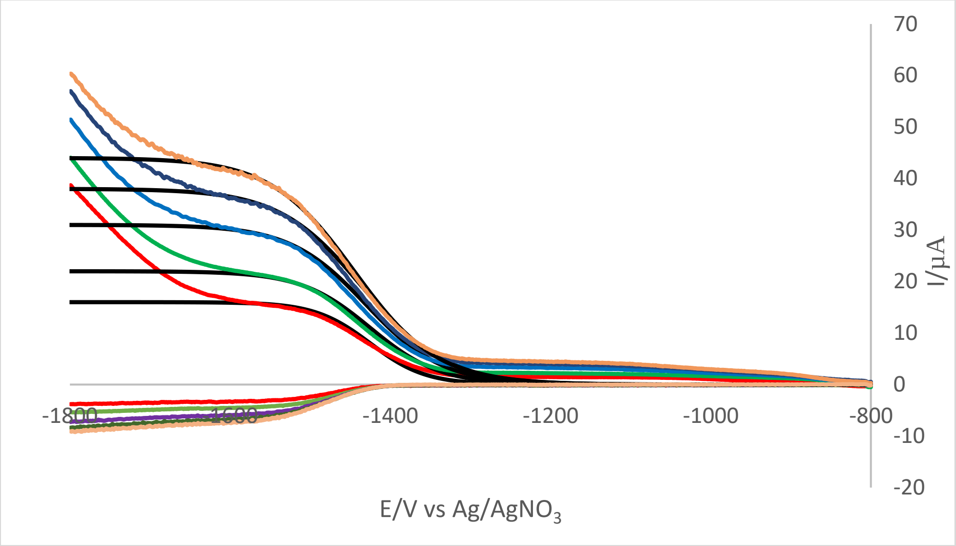

Figure 3-13. RRDE voltammograms of 0.5 mM Fe(OEP)(NO) 5 mM 2,6-dcp in THF at different electrode rotating rates, scan rate 1 mV/s, working electrode Pt, 0.1 M TBAP, E_r = -0.8 V. (Top=higher rpm to bottom= lower rpm, black line = theoretical line).

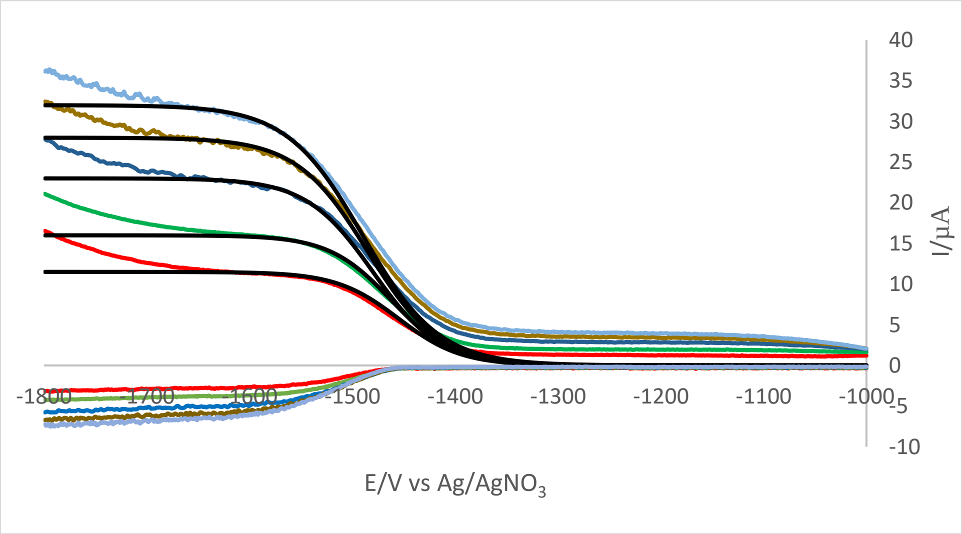

Figure 3-14. RRDE voltammograms of 0.5 mM Fe(OEP)(NO) with 100 mM phenol in THF at different electrode rotating rates, scan rate 1 mV/s, working electrode Pt, 0.1 M TBAP, E_r = -0.8 V. (Top=higher rpm to bottom=lower rpm, black line= theoretical line).

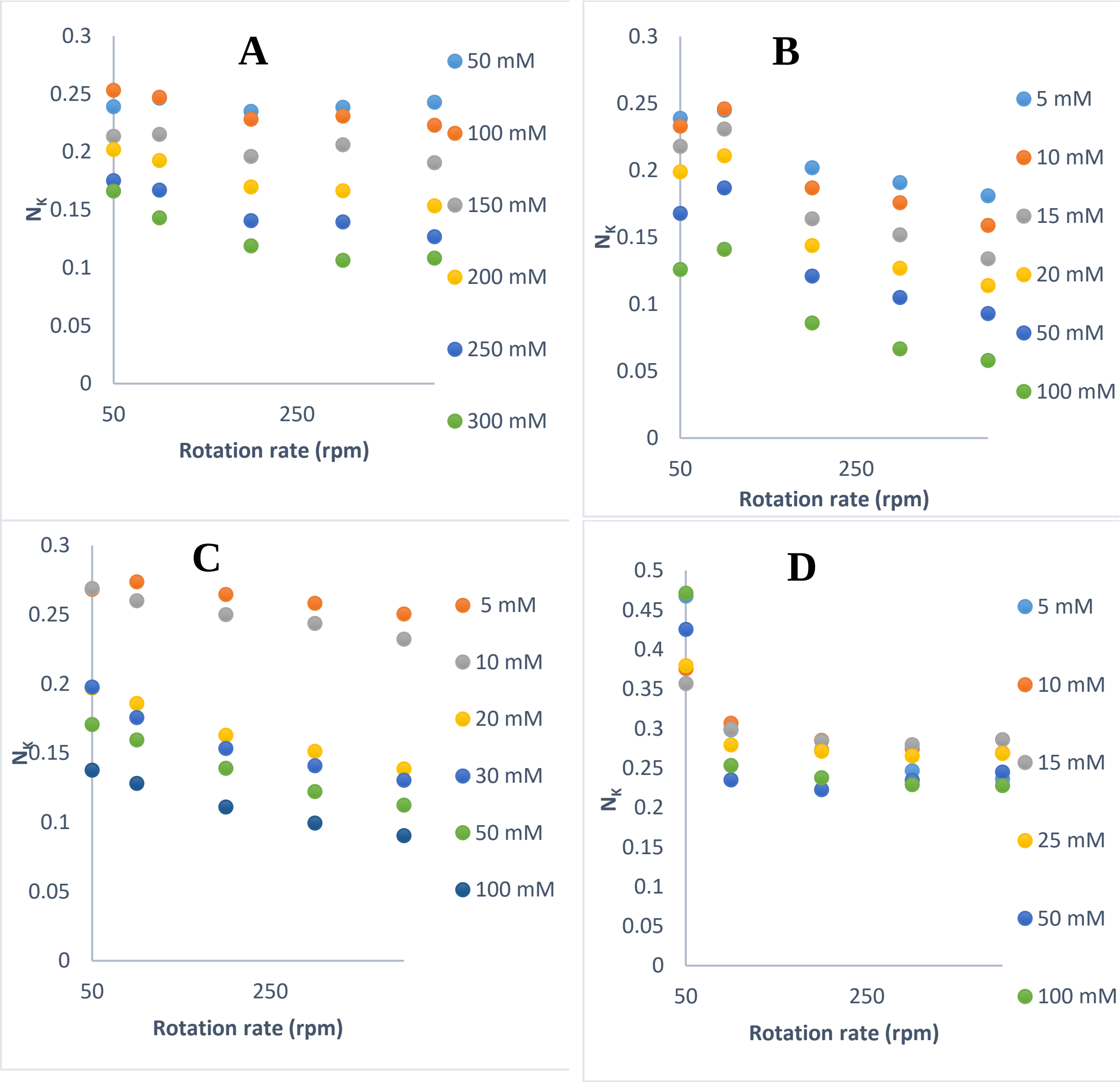

Figure 3-15. Change of collection efficiency for Fe(OEP)(NO) with rotation rates for A) phenol, B) 2,6-dcp, C) 2,3-dcp, D) 3,5-dcp.

The reduction and protonation of the reduced species occurred at disk, (Reaction 3-1, 3-2/Scheme 1) and by convection the protonated species were swept to ring and re-oxidized. The homogeneous reaction (Reaction 3-2/Scheme 1) was rate limiting at the ring. As can be seen in Figure 3-16, the collection efficiency decreased as the acid concentration increased for a given rotation rate. This was consistent with slower observed oxidation rate at higher acid concentration. Another interesting observation that the collection efficiency decreased as the rotation rate increased. This was also consistent with a reversible mechanism because at lower rotation rates the protonated species had more time to deprotonate before re-oxidation. For an irreversible reaction, the collection efficiency would increase as the rotation rate was increased.

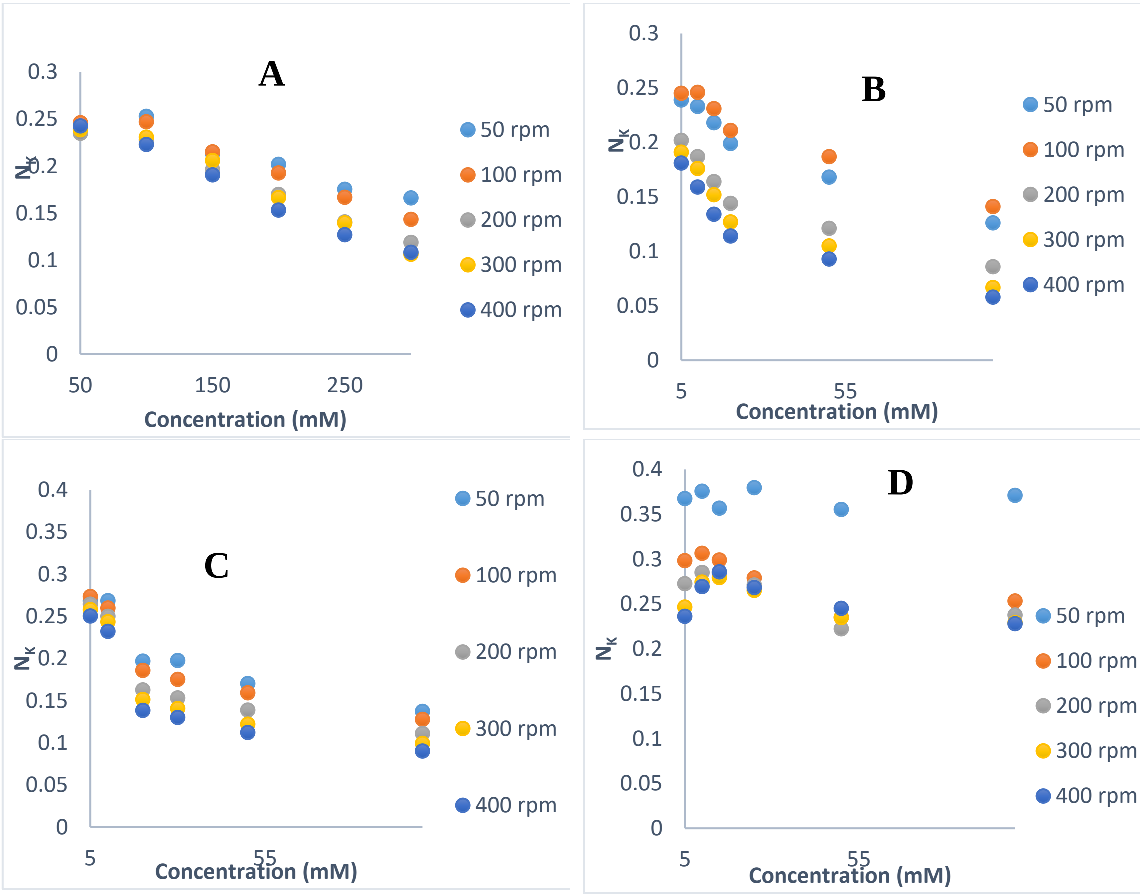

Figure 3-16. Change of collection efficiency for Fe(OEP)(NO) with concentrations for A) phenol, B) 2,6-dcp, C) 2,3-dcp, D) 3,5-dcp.

The Koutecky- Levich plot showed that the deprotonation reaction was controlled by both mass transfer and kinetics. The lower kinetic current for stronger acids (Figure 3-17) indicates that the equilibrium lies toward product side (HNO) and (H_2NOH).

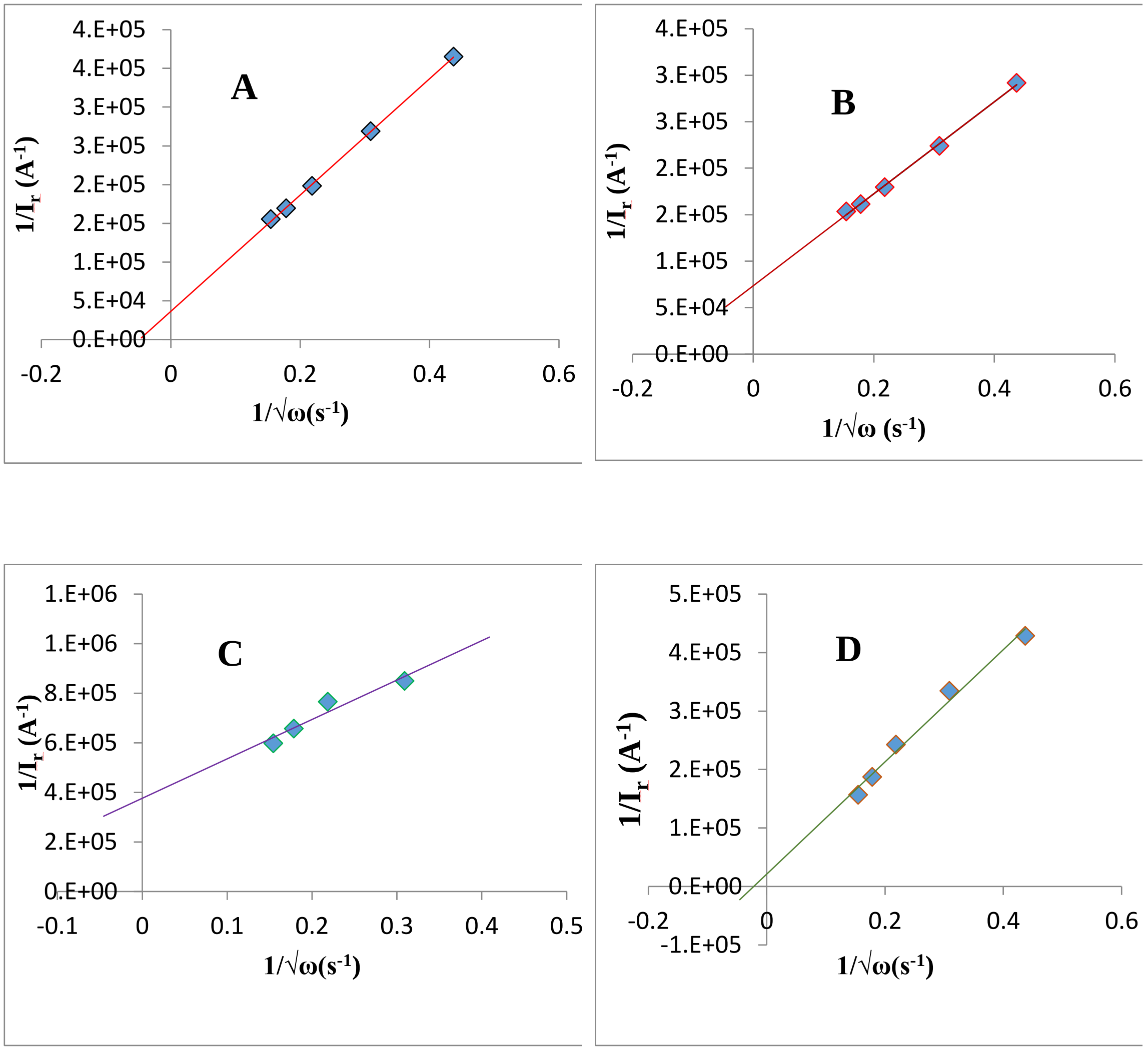

Figure 3-17. Koutecky – Levich plots for Fe(OEP)(NO) with different acids, A) Phenol (pK_a = 9.99), B) 2,6- dcp (pK_a = 6.78), C) 2,3-dcp (pK_a = 7.44), D) 3,5-dcp (pK_a = 8.18).

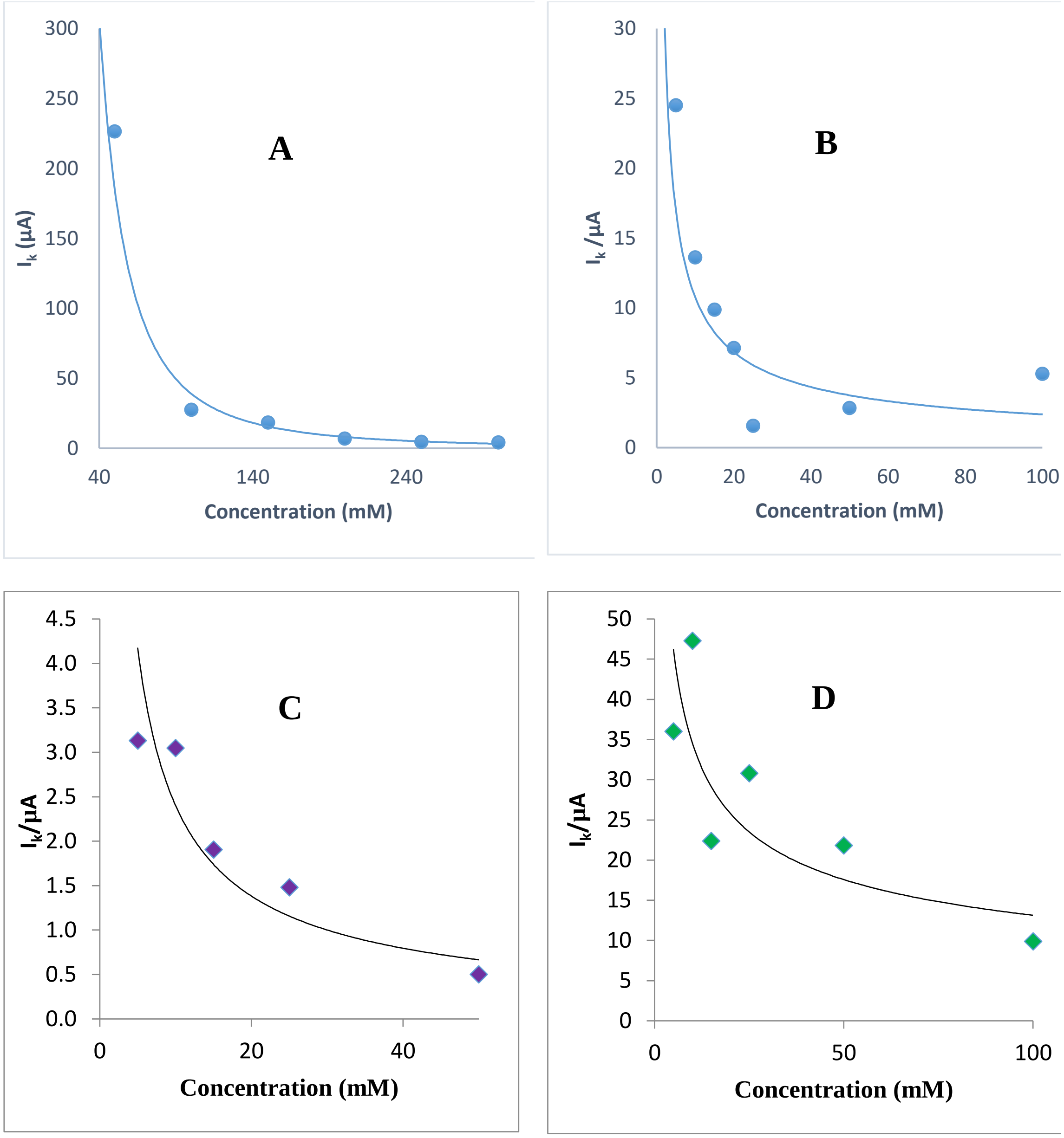

Figure 3-18. Concentration dependence of kinetic current obtained from Koutecky – Levich plots for Fe(OEP)(NO) with A) Phenol (pK_a = 9.99) , B) 2,6- dcp (pK_a = 6.78), C) 2,3-dcp (pK_a = 7.44), D) 3,5-dcp (pK_a = 8.18).

The concentration dependence of ring kinetic current showed in Figure 3-18. As the concentration of acid increased, the ring current decreased for all acids. The inverse dependence on concentration indicates the reverse reaction was inverse order. A plot of kinetic current vs inverse concentration gave a straight line which passed through the origin, indicates the reaction was inverse first order (Figure 3-19). This was followed by phenol and 2,6-dcp. In contrast, the 2,3-dcp and 3,5-dcp followed the inverse half order. The possible reason for the difference in order of the reaction was that phenol was very weak acid and in this acid, the reduced species barely doubly protonated. For 2,6-dcp double protonation was not possible because of steric hindrance and the hydrogen bond which was formed between 2,6 positioned chlorine atoms with hydroxyl group of phenol.[72]

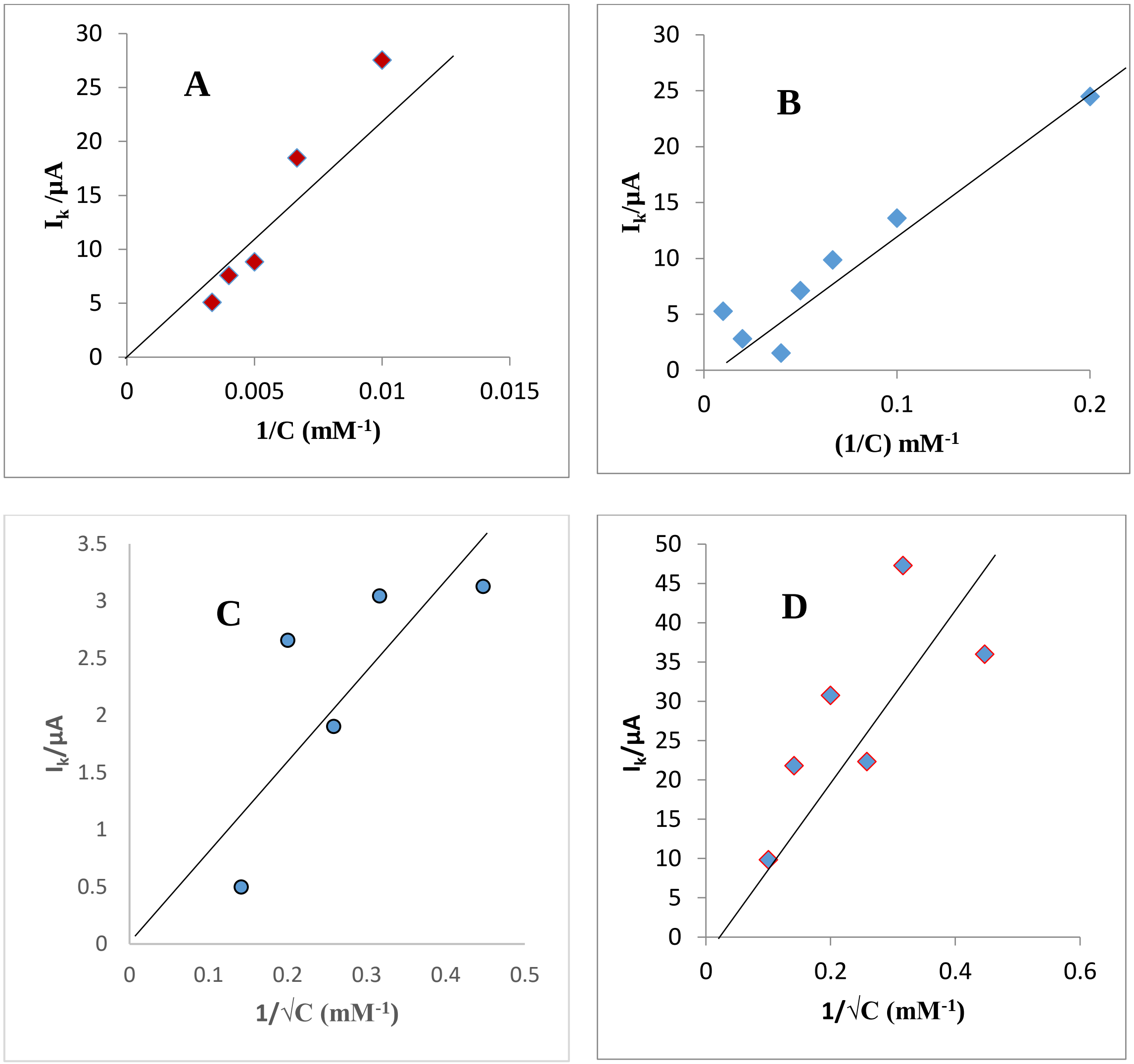

Figure 3-19. Determination of the order of deprotonation reaction for Fe(OEP)(NO) with A) Phenol (pK_a = 9.99) , B) 2,6- dcp (pK_a = 6.78), C) 2,3-dcp (pK_a = 7.44), D) 3,5-dcp (pK_a = 8.18).

In order to confirm that the protonation and deprotonation reaction was reversible, the RRDE voltammetry of Fe(OEP)(NO) was carried out in the presence of the conjugate base. Another purpose is to verify the rate limiting step in the oxidation of Fe(OEP)(HNO). The voltammetry is shown in Figure 3-20. As we expected, the wave was shifted to positive with 50 mM acid. The wave shifted to negative potentials with the addition of the conjugate base which clearly indicated the equilibrium was shifted towards Fe(OEP)(NO)$^-$/PhOH with the increase in base.

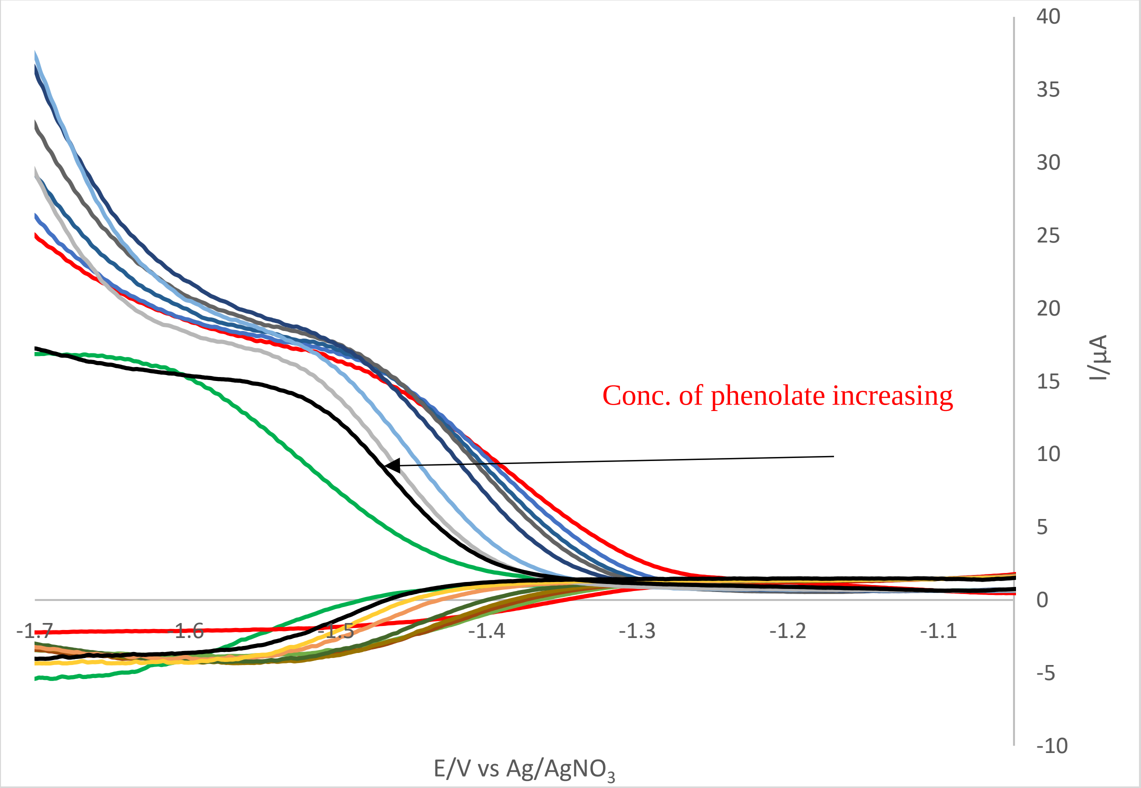

Figure 3-20. RRDE voltammograms of 0.45 mM Fe(OEP)(NO) (Green) with 50 mM 3,5-dcp (Red) and different concentration of base (Black highest conc. of base) in THF at 50 rpm, scan rate 1 mV/s, working electrode Pt, 0.1 M TBAP, E_r = -0.8 V.

With constant base concentration (Figure 3-21), a similar effect was observed. At lower concentration, the rising portion after one electron reduction wave suppressed because of base, this portion arising more at higher concentration of acid. It was assumed that the rising portion attributed from phenol reduction and some second redox process.

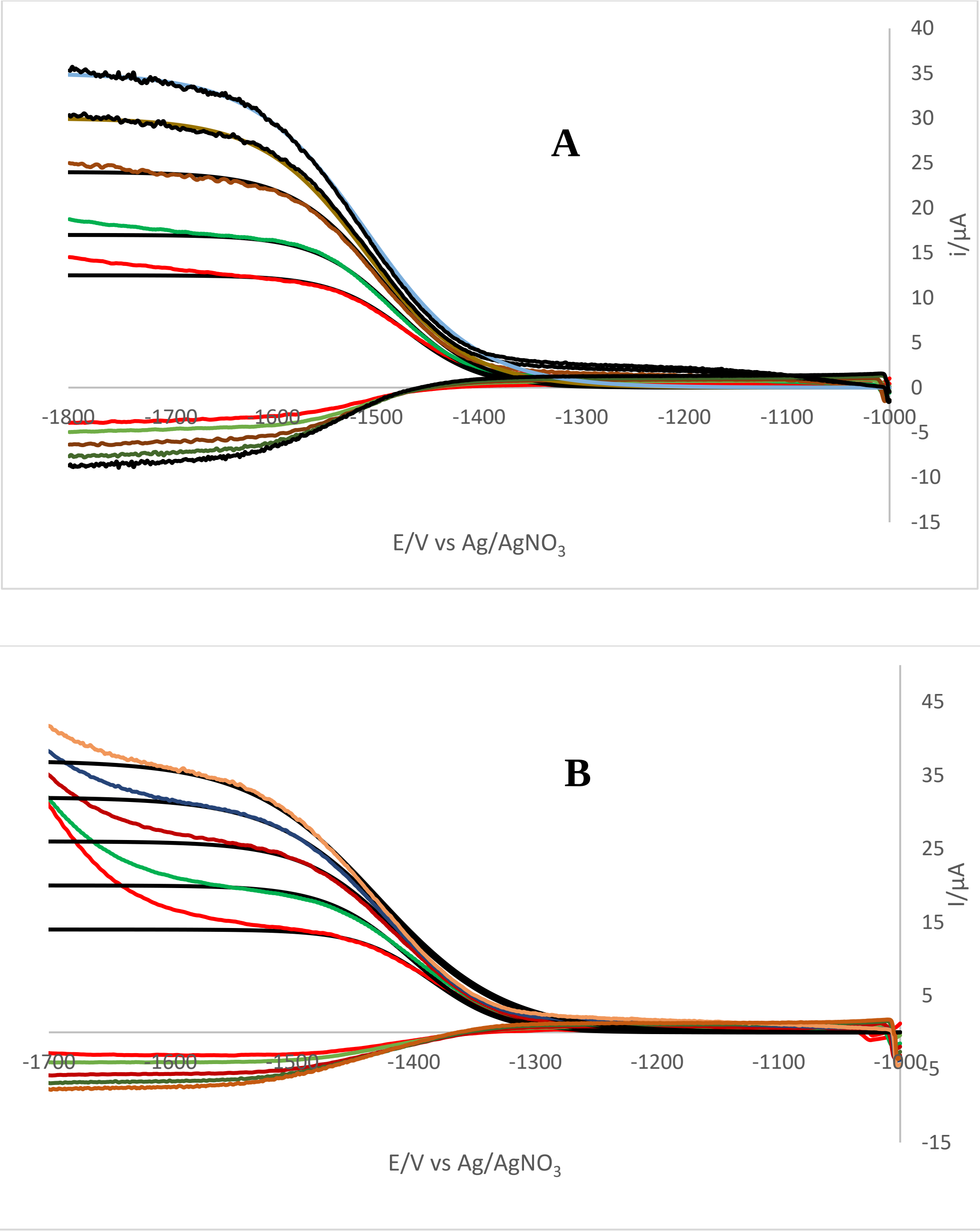

Figure 3-21. RRDE voltammograms of 0.8 mM Fe(OEP)(NO) with 4 mM base A) 5 mM 2,3-dcp B) 100 mM 2,3-dcp in THF at different electrode rotating rates, scan rate 1 mV/s, working electrode Pt, 0.1 M TBAP, E_r = -0.8 V. (Top=higher rpm to bottom= lower rpm, black = theoretical line).

The collection efficiency showed more interesting phenomena (Figure 3-22 to 3-24), for the experiment where a constant acid (50 mM) was use. The collection efficiency was dropped to lower values (Figure 3-22, 3-23), and then the collection efficiency increased with addition of base. Another set of data (for constant base concentration 4mM) showed that collection efficiency did not dropped as much was seen for only acid system (Figure 3-24). All acid showed the same pattern. This results further confirmed the reversibility of Reaction 2 (Scheme 1). The calculation of rate constant with phenolate concentration by digital simulation was very complex, as the results depended on the value of *K*.

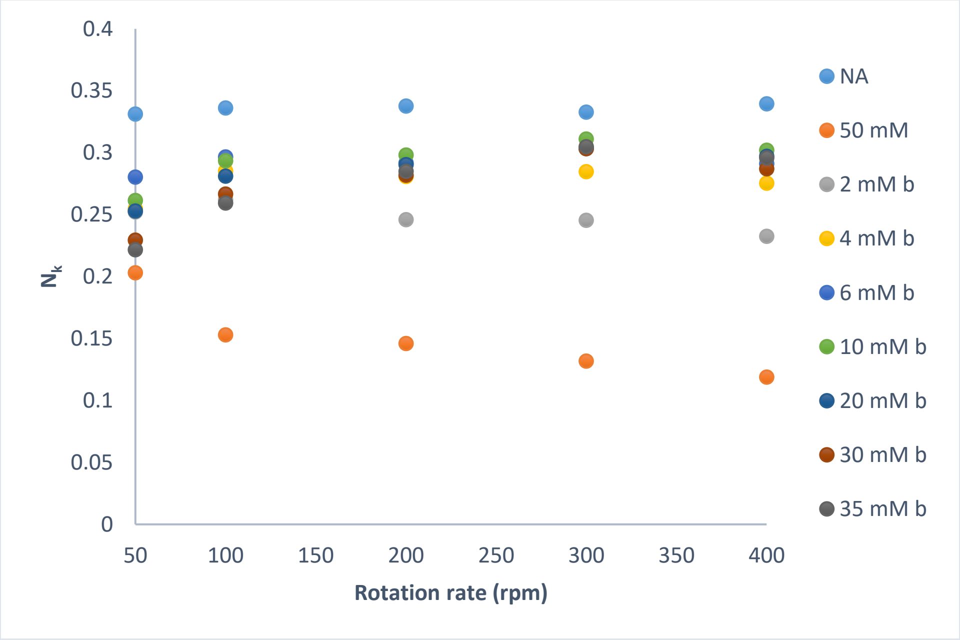

Figure 3- 22. Change of collection efficiency for Fe(OEP)(NO) with 2,3-DCphenolate (NA = No Acid, b = base).

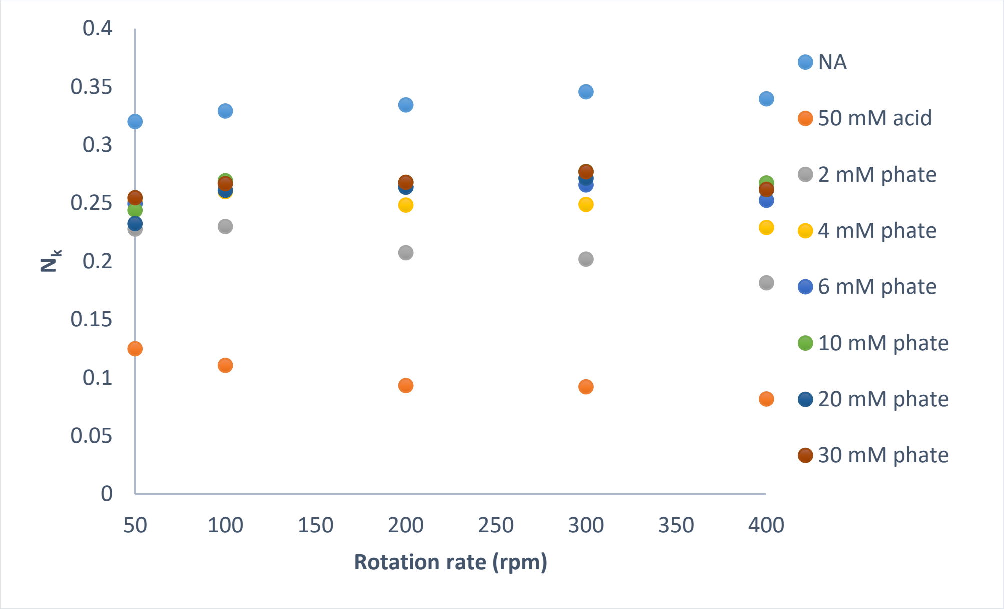

Figure 3-23. Change of collection efficiency for Fe(OEP)(NO) with 3,5-DCphenolate (NA = No Acid, phate = base).

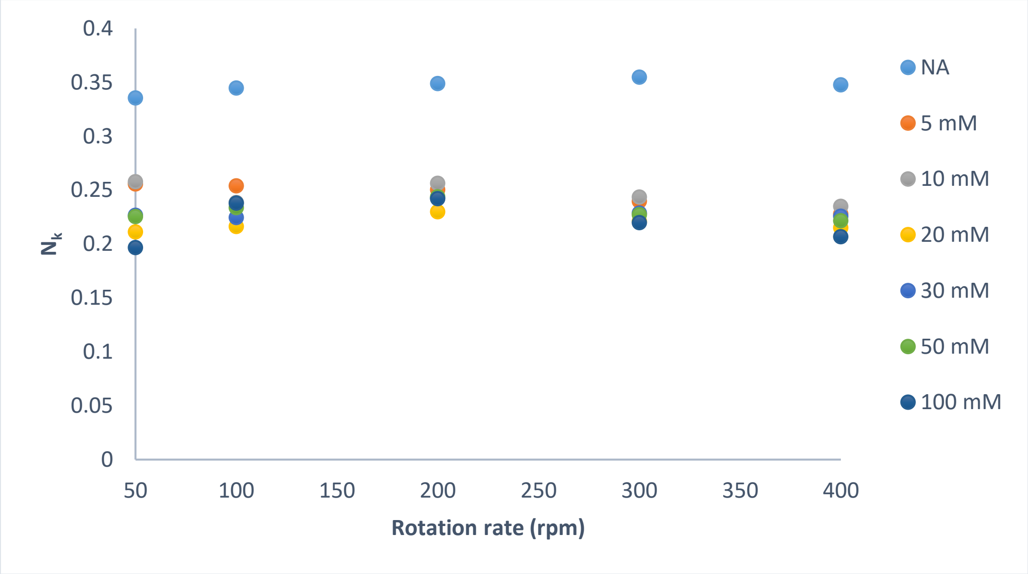

Figure 3-24. Change of collection efficiency for Fe(OEP)(NO) with 4 mM 2,3-DCphenolate with different concentration of acid (NA = No Acid).

A closer look to figure 3-22 and 3-23 showed that for 0 to 4 mM of phenolate, the collection efficiency increased with phenolate concentration increased and it decreased as the rotation rate increased which was expected. For lower concentrations of phenolate, the change of collection efficiency was observed but for higher concentration of phenolate there was no observable change in it. At higher concentrations of phenolate, the reverse reaction became more competitive with the forward reaction and the N_k vs *XKT* became shallower. Depending on the *K* value, N_k was independent of rotation rate (4mM) or increased with rotation rate as the kinetic zone shifted to the left of the minimum (Figure 2-5A in experimental section).

To investigate this further, digital simulation was carried out for reversible EC mechanism for Reactions 3-1,3-2/Scheme 1 (reduction and protonation). The details of the digital simulation described in the experimental section. The relationship between *XKTK* and N_k for values of *XKTK* beyond the minimum in Figure 2-5A is shown in Figure 2-6. The curve in Figure 2-6 can be fitted to the following equation,

$$XKTK = \frac{2.085N_k + 0.001599}{N_k^2 - 0.8047N_k + 0.1604} \tag{3-7}$$

For each value of N_k, the *XKTK* value be obtained. The collection efficiencies are shown in Table 3-3, and the *XKTK* values are shown in Table 3-4. The simulated collection efficiencies are shown in Figure 3-25. Expanding *XKTK*,

$$XKTK = \frac{\sqrt{XKT}}{Ksim} = \frac{\sqrt{XKT}}{K[PhOH]} = \frac{[(0.51)^{2/3}kC^{*}\nu^{1/3}D^{-1/3}\omega^{-1}]^{1/2}}{K[PhOH]} \tag{3-8}$$

Rearranging and solving for √*k/K*,

$$\frac{\sqrt{k}}{K} = XKTK[PhOH][\frac{\omega}{(0.51)^{2/3}C^{*}\nu^{1/3}D^{-1/3}}]^{1/2} \tag{3-9}$$

All the terms on the right side determined experimentally. In this work, D = 6.47×10^{-6} cm^2/s and ν = 0.0091 cm^2/s. Concentration must be in molarity and ω in rotation rad/s. Using these factors, the values of $\sqrt{k_f}/K$ are given in Table 3-5.

Table 3-3. Experimental collection efficiencies for 2,6-dcp.

[PhOH], M	50 rpm	100 rpm	200 rpm	300 rpm	400 rpm
0.005	0.239	0.245	0.202	0.191	0.181
0.01	0.233	0.246	0.187	0.176	0.159
0.02	0.218	0.231	0.164	0.152	0.134
0.03	0.199	0.211	0.144	0.127	0.114
0.05	0.168	0.187	0.121	0.105	0.093
0.1	0.126	0.141	0.086	0.067	0.058

Table 3-4. The XKTK values for the collection efficiencies.

[PhOH],M	5.24 rad/s	10.5 rad/s	20.9 rad/s	31.4 rad/s	41.9 rad/s
0.005	19.90	22.0	10.90	9.27	7.98
0.01	17.90	22.40	8.73	7.41	5.77
0.02	14.0	17.40	6.21	5.21	3.99
0.03	10.50	12.60	4.63	3.59	2.93
0.05	6.59	8.73	3.27	2.54	2.08
0.1	3.53	4.43	1.84	1.27	1.05

Table 3-5. The √k/K values for different rotation rate and concentrations.

[PhOH],M	5.24 rad/s	10.5 rad/s	20.9 rad/s	31.4 rad/s	41.9 rad/s	Average √*k/K* for diff. rpm	Final √*k/K* s^{-1}
0.005	3.80	5.96	4.19	4.34	4.32	4.52	
0.01	6.86	12.14	6.680	6.95	6.25	7.78	
0.02	10.80	18.80	9.51	9.77	8.63	11.49	10.94
0.03	12.00	20.40	10.63	10.10	9.52	12.53	
0.05	12.60	23.60	12.50	11.90	11.24	14.380	
0.1	13.50	24.0	14.1	11.90	11.340	14.95	

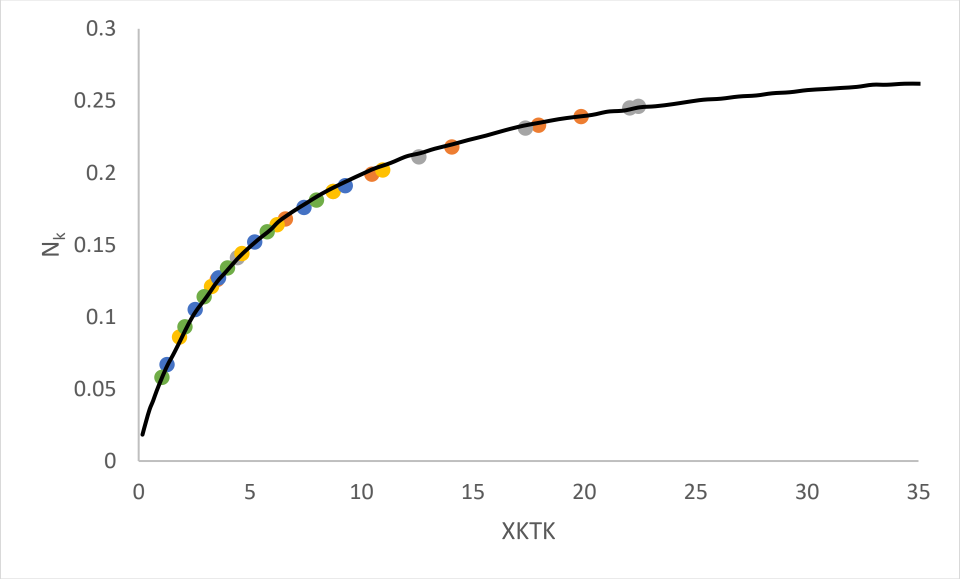

Figure 3-25. Collection efficiency for the RRDE voltammetry of Fe(OEP)(NO) in the presence of 2,6-dcp. Filled circles are experimental data; solid lines are simulated collection efficiencies for $\sqrt{k_f}$ / K = 10.94. (Colors represent concentrations).

Table 3-6. The √k/K values for different phenols.

Acid	$k_f^{1/2}/K$ **(s^{-1})**
2,6-DCP(pKa=6.78)	10.90
2,3-DCP (pKa= 7.44)	14.20
3,5-DCP(pKa=8.18)	18.20
2,3-DCPOD(pKa=7.44)	21.60
2,3-DCP with Fe(OEPone)(NO)	11.00

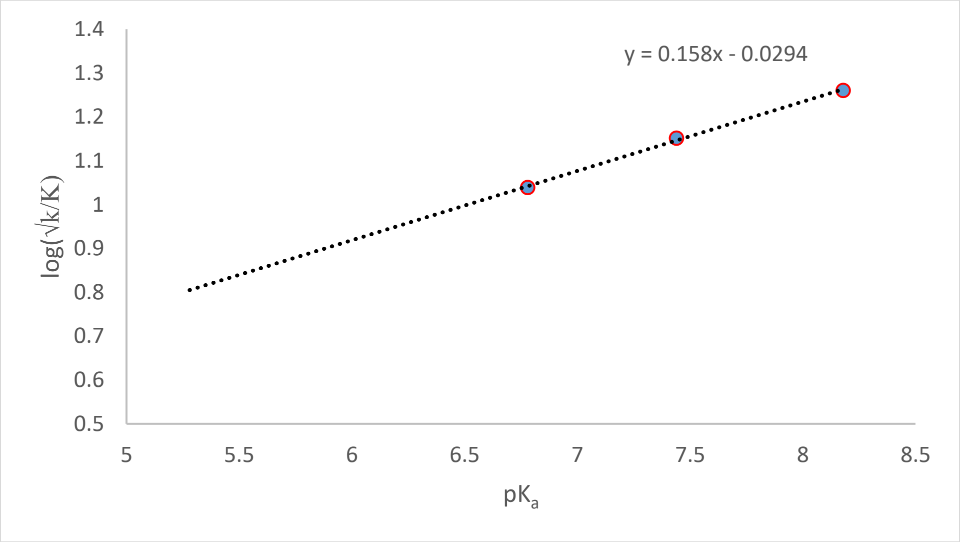

Figure 3-25b. Variation in the $\sqrt{k_f}/K$ values as a function of pK_a of substituted phenols.

With the digital simulation, the $\sqrt{k_f}/K$ values were determined for different acid (Table 3-6). The values showed an interesting behavior. With the decrease of steric hindrance of acids, the $\sqrt{k_f/K}$ values increased. The 2,6-dcp showed a lower value than 2,3-dcp and 3,5-dcp. The possible reason might be the steric hindrance which might arise from the chlorine at 2 and 6 position. In case of 2,3-dcp, the chlorine at 2 position sterically interact when protonation on Fe(OEP)(NO)$^-$ occurred. This steric interaction less pronounced for 3,5-dcp where the chlorine atoms comparatively far from phenol hydroxyl group. This result indicated that there was an activated complex formed between phenols and the nitroxyl anion and the activated complex formation favored with less sterically hindered acids. The easier formation of the activated complexes, the more protonation occurred. As the pK_a values for acids were close, then it was possible not to observed a difference in rates. The steric effect might be a prominent factor to accelerate the protonation reaction compared to the slightly different acids strength. It was difficult to find K or k_f independently at this experimental time scale. Only at very lower rotation rate those kinetic parameters could be determined. But at the lower rotation rate, the hydrodynamic layer mixed with diffusion layer which makes the system more complex. The variation in the $\sqrt{k/K}$ values as a function of pK_a of the substituted phenols was shown in Figure 3-25b. A linear relationship was observed with a slope 0.158. As the pK_a was increased, the $\sqrt{k/K}$ was increased. This effect was bigger as for $\sqrt{k}$ than K. The smaller slope showed a weak relationship between the acidity of phenols and the $\sqrt{k/K}$ values. This indicated that differences in reactivities in the presence of various phenols were due to a combination of kinetic and equilibrium effects (K).

To verify the protonation on the reduced species, deuterated phenols were used to observe the primary kinetic isotopic effect on the kinetic parameters. We were limited in this case due to the convolution of K and k_f. For this purpose, the RRDE voltammetry was carried out with 2,3-dcp-d_4 (Figure 3-26). It also showed the similar behavior like normal abundance acids such as the potential shifted to positive potentials the concentration of 2,3-dcp-d_4 increased (Figure 3-27). But from the potential shift, it was difficult to observe the reaction condition as it slower or faster. Comparative shifts for 2,3-dcp and 2,3-dcp-d_4 (Figure 3-30) showed the shifts were more for normal abundance acid than deuterated acid, indicating a smaller K value. The collection efficiency changes with respect to rotation rate and concentration of the deuterated acid showed trend similar to normal abundance acids (3-27, 3-28). For all rotation rates, the collection efficiency was lower for 2,3-dcp than for the 2,3-dcp-d_4 (Figure 3-31). The $\sqrt{k_f/K}$ values for 2,3-dcp and 2,3-dcp-d_4 were calculated from digital simulation (Table 3-6). The $\sqrt{k_f/K}$ value was higher for the deuterated acid than normal abundance acids. The larger value of $\sqrt{k_f/K}$ could be due to a smaller K or a larger k_f. An increase in k_f is unlikely. The smaller K is probably the source of increase. This would be consistent with the smaller shift in the E^o values when 2,3-dcp-d_4 was used. This is possible if the Fe(OEP)(^{2}HNO) was not stabilized by hydrogen bonds with the phenolate and phenols. As we know, the hydrogen bonds with OH are stronger than the OD group. Consequently, when Fe(OEP)(HNO) was formed with normal abundance substituted phenols, the complexes were stabilized by a strong hydrogen bonds between complex and phenols, and the equilibrium favored to right. On the other hand, when Fe(OEP)(^{2}HNO) was formed, because of the weaker hydrogen bonds between complex and phenols, the equilibrium shifted to the left. This phenomenon indicated the protonation reaction dependent on equilibrium rather than reversibility.

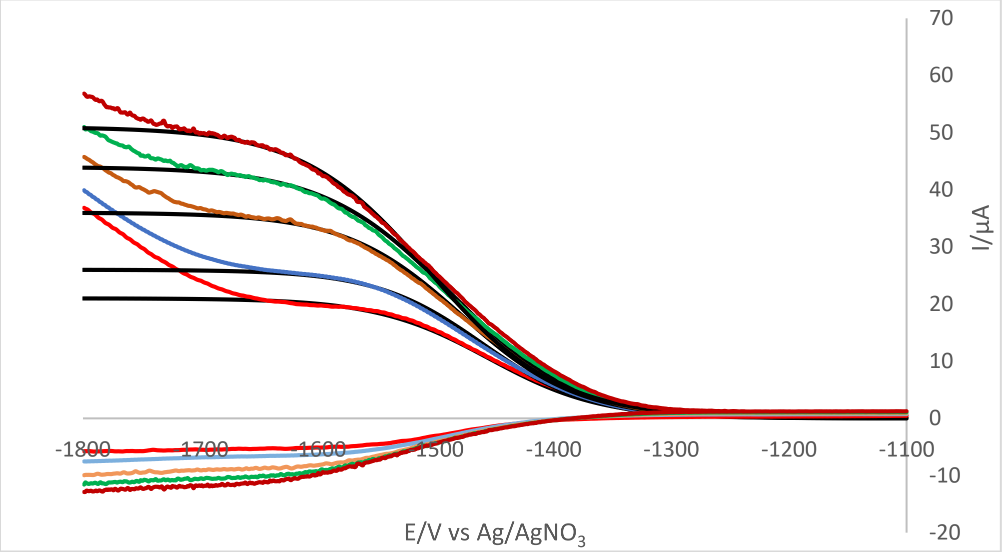

Figure 3-26. RRDE voltammograms of 0.56 mM Fe(OEP)(NO) with 50 mM 2,3-dcp-*d₄* in THF at different electrode rotating rates, scan rate 1 mV/s, working electrode Pt, 0.1 M TBAP, E_r = -0.8 V. (Top=higher rpm to bottom=lower rpm, black= theoretical line).

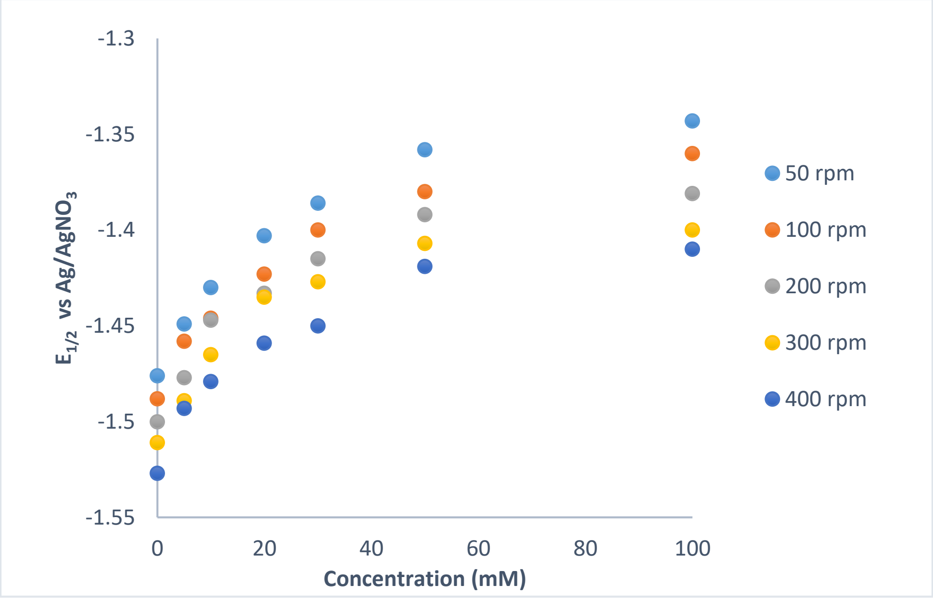

Figure 3-27. Shift of $E_{1/2}$ for Fe(OEP)(NO) in the addition of 2,3-dcp-*d₁*.

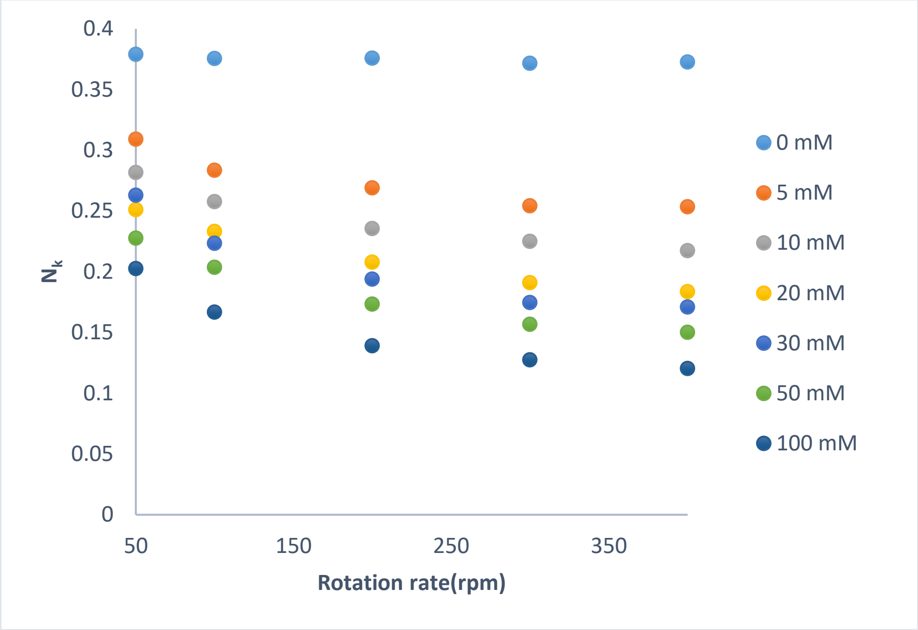

Figure 3-28. Change of collection efficiency for Fe(OEP)(NO) with rotation rates.

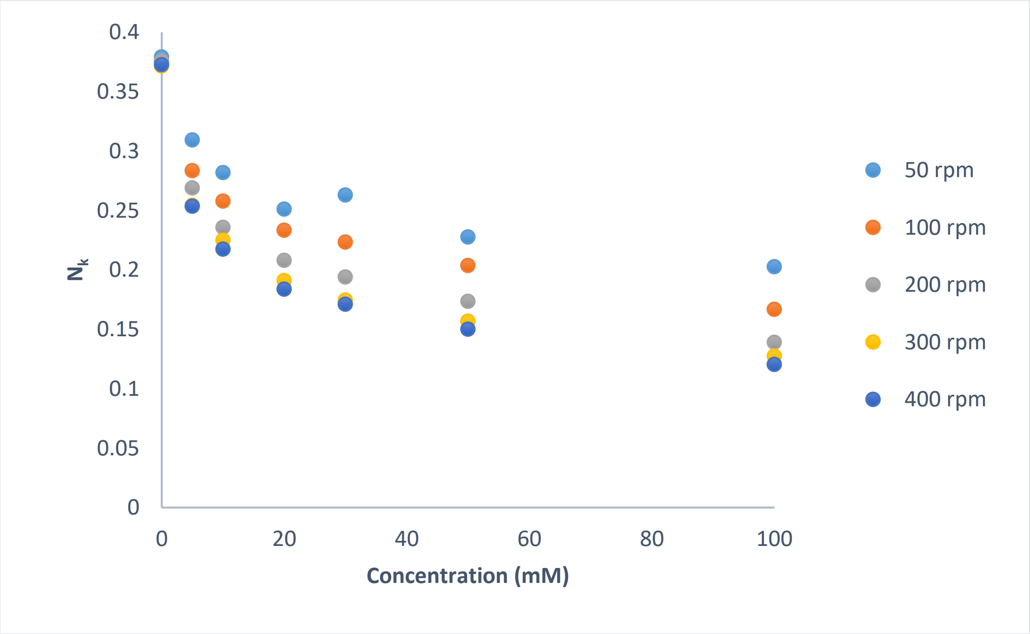

Figure 3-29. Change of collection efficiency for Fe(OEP)(NO) with concentrations.

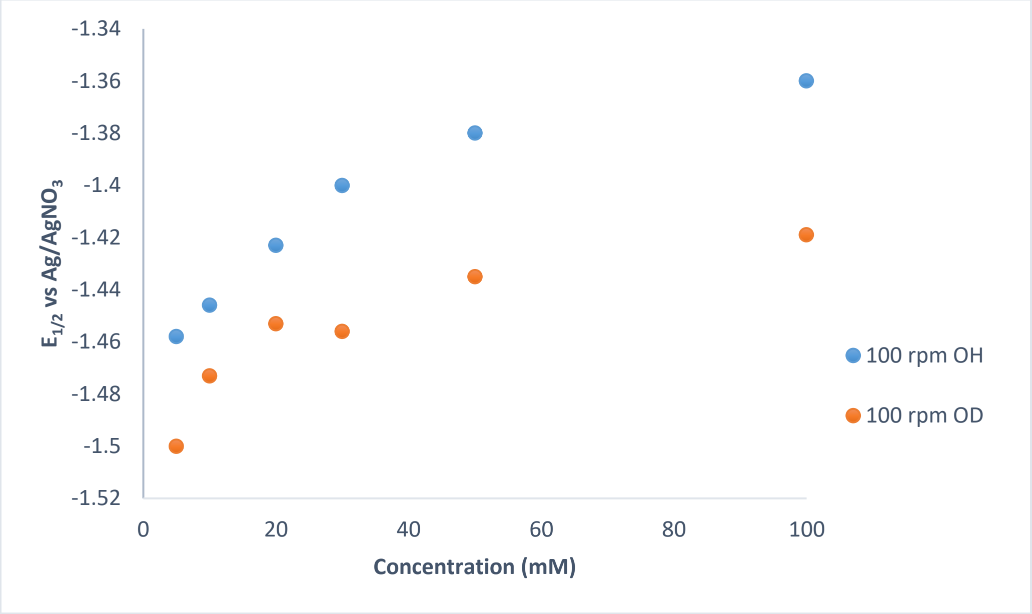

Figure 3-30. $E_{1/2}$ shifts for Fe(OEP)(NO) in the presence of 2,3-dcp and 2,3-dcp-*d_4*

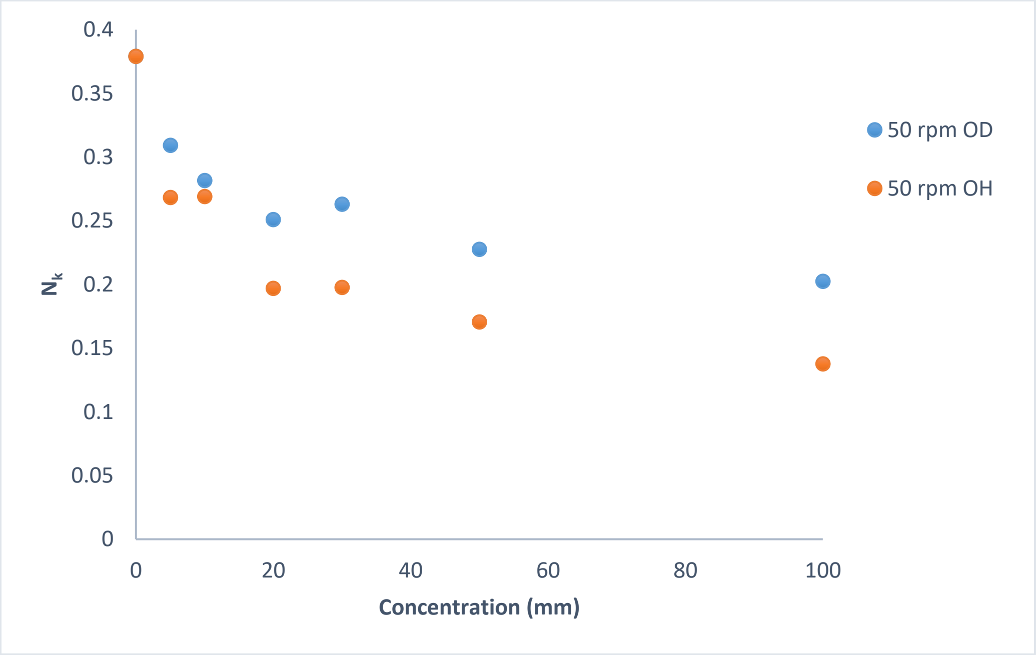

Figure 3-31. Change of collection efficiency for Fe(OEP)(NO) in the addition of 2,3-dcp and 2,3-dcp-*d_1*.

3.3 Cyclic Voltammetry of Fe(II)(OEPone)(NO)

Fe(OEPone)(NO) was reduced by one electron scanning from 0 mV to -1600 mV versus Ag/$AgNO_3$ (Figure 3-32). The potential difference of forward peak current and reverse peak current was more than the Nernstian value (59 mV) which is around 200 mV due to high solution resistance of THF. The peak current increased as a function of square root of scan rate which implied a diffusion controlled process. Further reduction occurred at more negative potentials. The Fe(OEPone)(NO) complex was easier to reduce than the Fe(OEP)(NO) complex. The $E_{1/2}$ for Fe(OEPone)(NO) was about 220 mV easier than the OEP complex. The reason for that was, in Fe(OEPone)(NO) an electron withdrawing group (carbonyl) which could stabilize the reduced species.

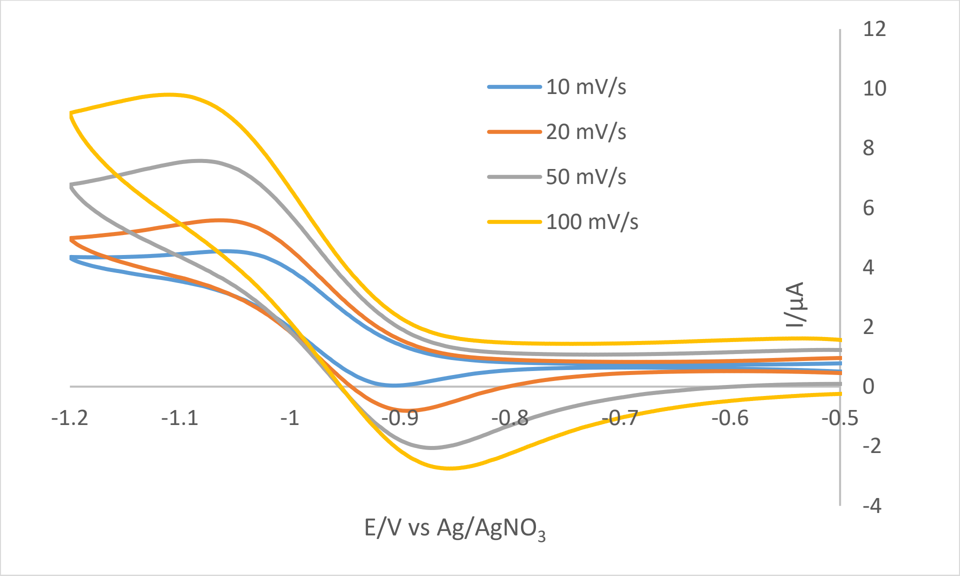

Figure 3-32. Cyclic voltammograms of 0.2 mM Fe(OEPone)(NO) in THF at different scan rate, 0.1 M TBAP, Working electrode BDD.

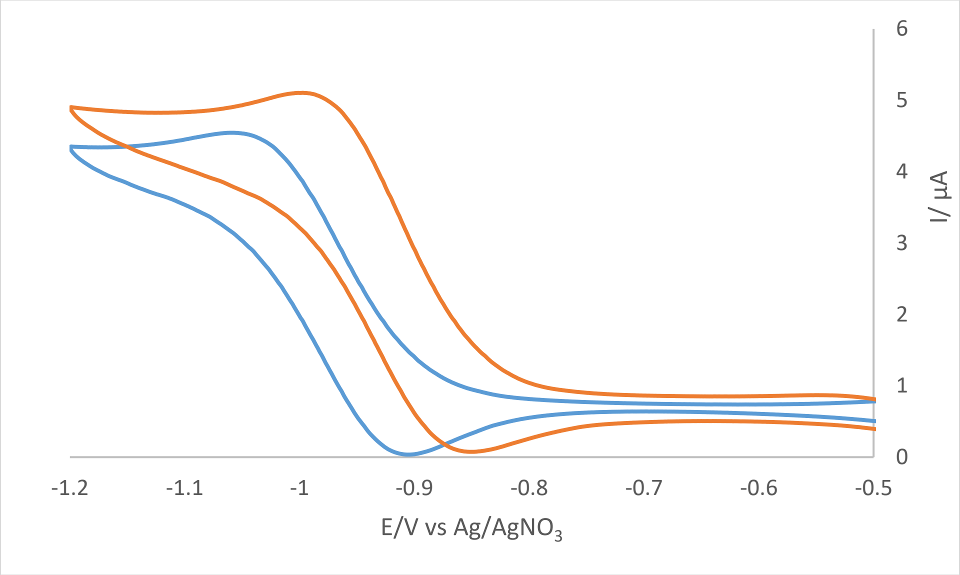

Figure 3-33. Cyclic voltammograms of 0.2 mM Fe(OEPone)(NO) (Blue) in THF at 10 mV/s with 10 mM 2,3-dcp (Orange), 0.1 M TBAP, Working electrode BDD.

Cyclic voltammetry was carried out in the presence of 2,3- dichlorophenol. The wave was shifted in a positive direction without changing the peak current indicating the EC (electron transfer then protonation) mechanism. The reverse current was less than what was in the absence of acid. At very slow scan rate, (Figure 3-33) the reverse current was close to value expected for a chemically reversible process. This porphinone required more acid concentration to cause the same change as Fe(OEP)(NO), indicating it was a less reactive species. When the potential was scanned to more negative potentials, the multi electron reduction peak was not as prominent was seen with Fe(OEP)(NO) even though the reverse peak for the multi electron reduction was observed. This corresponded to a less reactive iron nitrosyl complex.

3.4 RRDE Voltammetry of Fe(OEPone)(NO)

RRDE voltammetry of Fe(OEPone)(NO) was carried out in the absence and presence of 2,3-dcp phenol (Figure 3-34 and 3-35). In the absence of acid, a single reduction wave was observed up to -1.6 V. The collection efficiency was consistent with a chemically reversible process (Table 3-7). The limiting current increases with square root of rotation rate (Figure 3-34 inset) which follows Levich equation, which indicated that the one electron reduction process was diffusion controlled. In the presence of acid, the one electron reduction wave shifted to more positive potentials (Figure 3-35) which showed that the generated reduced species Fe(OEPone)(NO)$^-$ reacted with acid. The disk current was at same as those measured in the absence of acid, indicating no further reduction at this potential. The trend of the potential shift was almost similar to Fe(OEP)(NO) with the addition of substituted phenols (Figure 3-36A). The change in collection efficiency with rotation rate was not significant, the collection efficiency remained same with the rotation rate change indicating a slow homogenous reaction (Figure 3-36B, C). The reaction pattern was same as Fe(OEP)(NO). The kinetic parameter was identified by digital simulation process. The ratio $\sqrt{k_f/K}$ was 11.4 s^{-1} for 2,3-dcp which was smaller than the Fe(OEP)(NO) (14.18 s^{-1}) indicating this porphinone was less reactive towards acids than Fe(OEP)(NO).

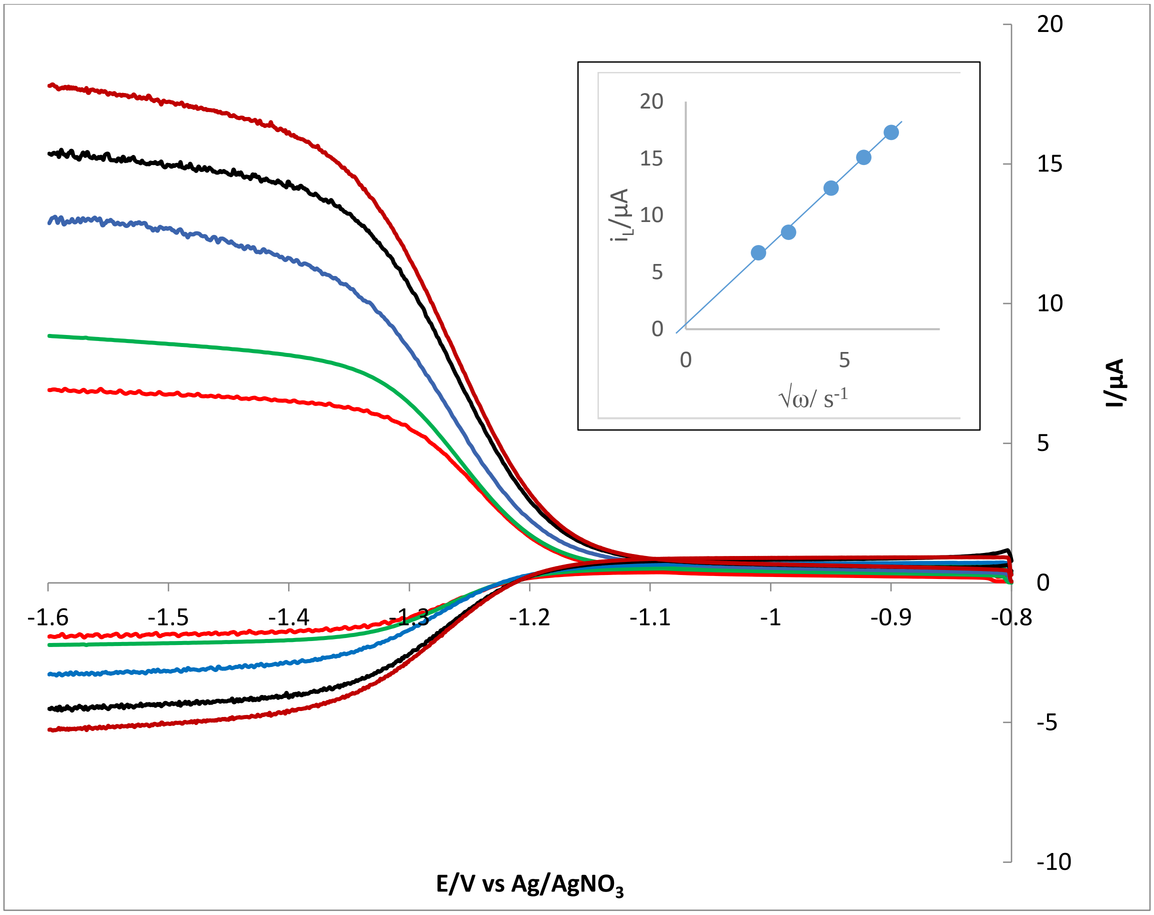

Figure 3-34. RRDE voltammograms of 0.45 mM Fe(OEPone)(NO) in THF at different electrode rotating rates, TBAP = 0.1 M, Working electrode Pt. (Top= higher rpm to bottom =lower rpm).

Table 3-7. Collection efficiency for Fe(OEPone)(NO) in the absence of acids.

Rotation rate (rpm)	**Collection efficiency**
50	0.321
100	0.316
200	0.304
300	0.310
400	0.311

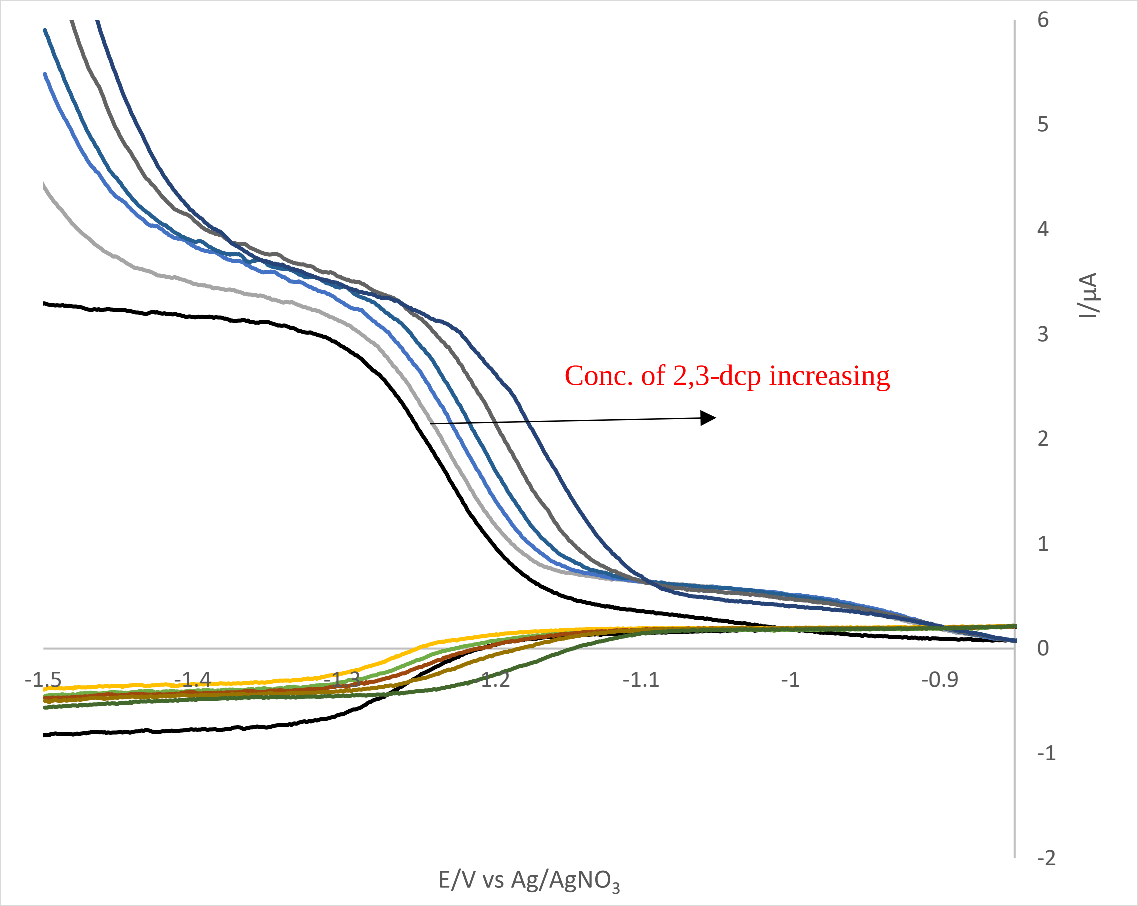

Figure 3-35. RRDE voltammograms of 0.5 mM Fe(OEPone)(NO) in THF in the presence of 2,3-dcp at 100 rpm, scan rate 5 mV/s, working electrode Pt, reference electrode Ag/AgNO$_3$, 0.1 M TBAP, E$_r$ = -0.6 V.

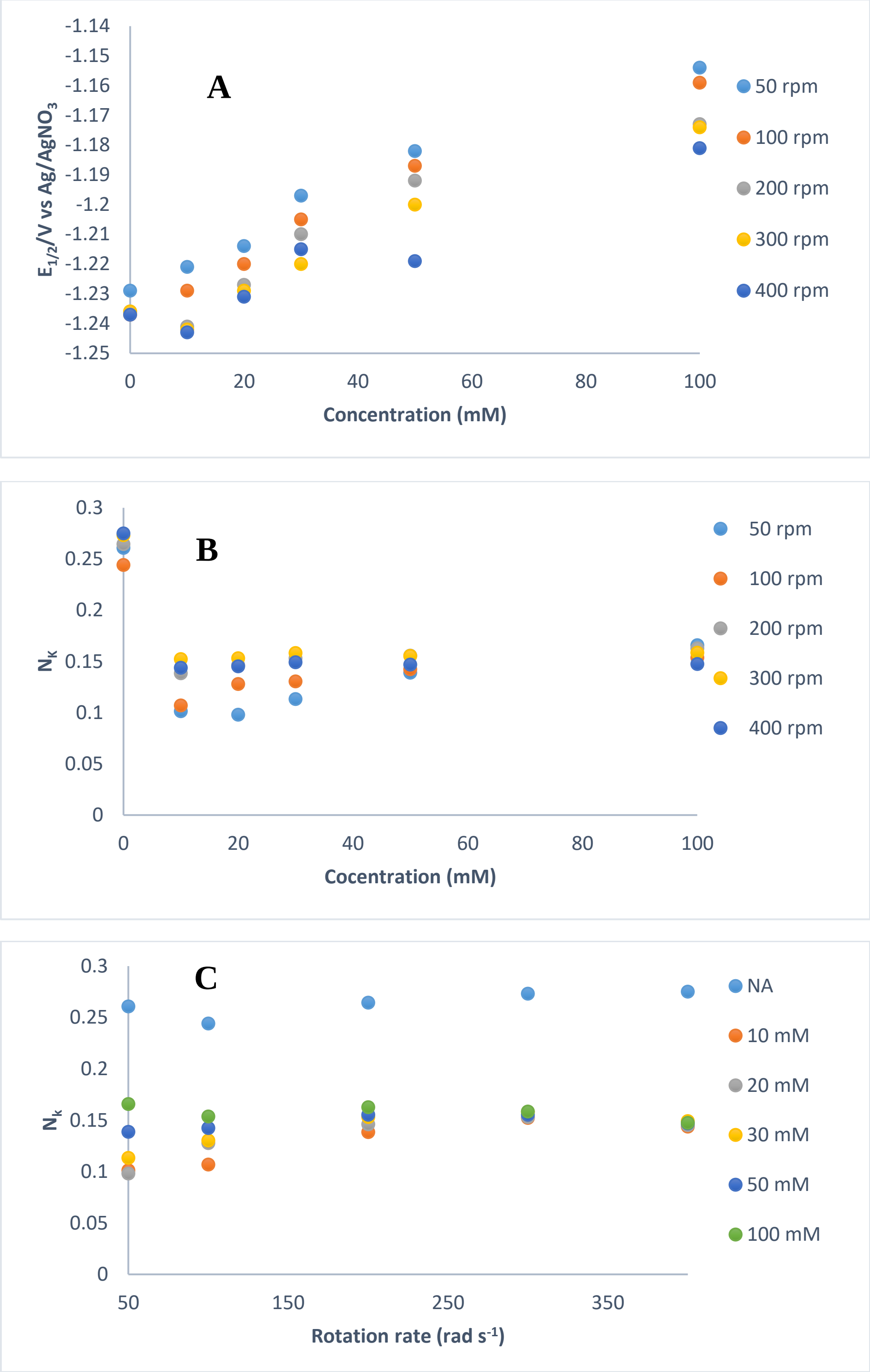

Figure 3-36. Change of A) $E_{1/2}$ with concentrations, B) Collection efficiency with concentrations, C) Collection efficiency for Fe(OEPone)(NO) with rotation rates for Fe(OEPone)(NO), (NA = No Acid).

CHAPTER 4 UV-VISIBLE SPECTROELECTROCHEMISTRY

4.1 UV-visible Spectroelectrochemistry of Fe(OEP)(NO)

The visible spectroelectrochemistry of Fe(OEP)(NO) was carried out to obtain spectroscopic evidence for the protonated species. The spectra for the reduction of Fe(OEP)(NO) while the potential was being linearly scanned from -1.0 V to -2.0 V showed a minimal change in Soret region and a new band was observed at 541 nm (Figure 4-1) which was consistent with the previous study.[70] A set of isobestic points were observed, indicating only two spectral species were present. The initial Fe(OEP)(NO) spectrum was almost completely regenerated by re-oxidation, indicating that the one electron reduction product was stable on the time scale of the experiment.

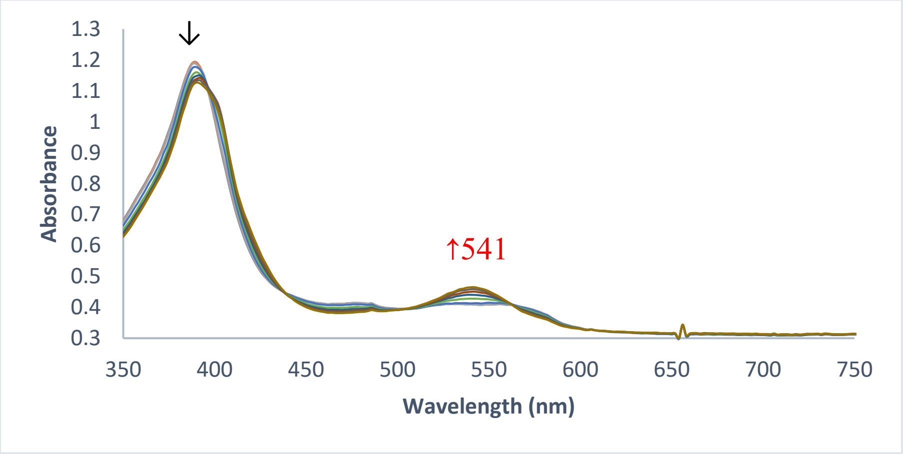

Figure 4-1. UV-visible spectroelectrochemistry of 0.19 mM Fe(OEP)(NO) in THF, E_i = -1.0 V, E_f =-2.0 V, scan rate 1 mV/s, Reference electrode Ag/$AgNO_3$, Working electrode Pt.

The experiment was then repeated in the presence of 2,6-dcp (Figure 4-2). A close observation of the spectra revealed that initially, the Soret band was slightly red shifted with decrease in the absorbance and was broadened then when potential going to more negative new band at 402 nm, and 523, 556 nm in Q band region appeared. The reduction of Fe(OEP)(NO) in the presence of 2,6-dcp occurred at a more positive potential than was observed in the absence of acids. This was consistent with the voltammetric data in the presence of acid. It was observed that the re-oxidation of the reduced species was very slow (Figure 4-3). The complete reduction occurred 100 s, while the re-oxidation needed 2000 s. This was consistent with the RRDE data which showed a slow re-oxidation reaction. Surprisingly, when the potential was reversed, the band at 402 nm continued to grow. This indicated that the formation of species at 402 nm controlled by kinetic factors. From the spectra (Figure 4-2) it was seemed as if there were more than two species. To verify this, evolving factor analysis was carried out with the spectral data which showed clearly that there were three species present during electrolysis (Figure 4-4). Deconvolution of the spectra was straightforward as the initial and final spectra were known. Comparison of the spectra (Figure 4-5) extracted from Figure 4-1 showed that the second and third species differed significantly from the initial reduction product, $Fe(OEP)(NO)^-$, indicating that the reaction of $Fe(OEP)(NO)^-$ with acid was fast in the spectroelectrochemical timescale. It should be noted that the timescale for the experiment was significantly longer than the RRDE experiment. Thus, for RRDE data shown, only species 2, Fe(OEP)(HNO) was present.

The third species was considered to be $Fe(OEP)(NH_2OH)$ because the potential was maintained positive enough to avoid the formation of ammonia upon successive reduction and protonation.[72] The sharp Soret band indicated that the reduction was on the nitrosyl moiety. If a π- anion radical was formed, then significant bleaching of Soret band would be observed. In addition, the sharp Soret band at 402 nm was similar to other ferrous porphyrin complexes such as 410 nm for Fe(OEP)$(py)_2$,[152] 409 nm for Fe(OEP)(CO)(py) and 410 nm for Fe(OEP)$(O_2)(CH_3CN)$.[153] These complexes all are six coordinate. In our case, might be THF might acts as the sixth ligand for Fe(OEP)(NH_2OH). DFT calculation were done for the Fe(OEP)(NH_2OH)(THF) complex (Figure 4-2A). The bond distance for Fe-N(NH_2OH) was 1.992(4) Å and for Fe-O(C_4H_8O) was 2.082(2) Å. According to the bond distances, the Fe-N bond was stronger than the Fe-O bond. These two bonds weaker than the Fe-N(NO) and Fe-N$(NO)^-$ bonds where the bond distances were 1.7307(7) Å and 1.812(3) Å respectively.[97] Overall, though, the distances were consistent with a Fe-O covalent bond. A 6-coordinate complex is clearly possible.

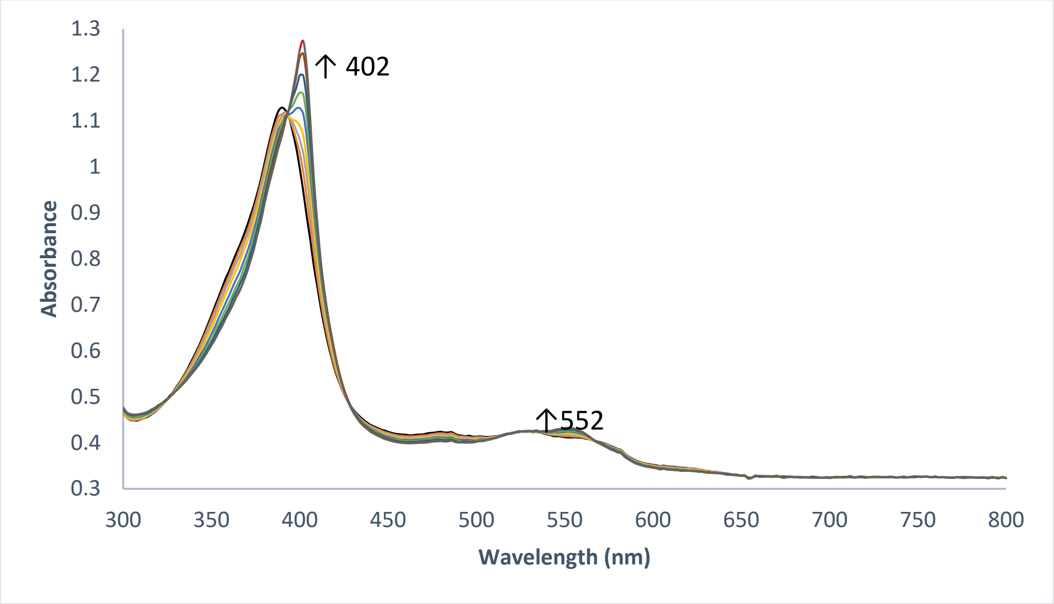

Figure 4-2. UV-visible spectroelectrochemistry of 0.20 mM Fe(OEP)(NO) in THF with 20 mM 2,6-dcp, 0.1 M TBAP, potential step from -1.00 to -1.35 V, scan rate 1 mV/s, Reference electrode Ag/AgNO$_3$, Working electrode Pt.

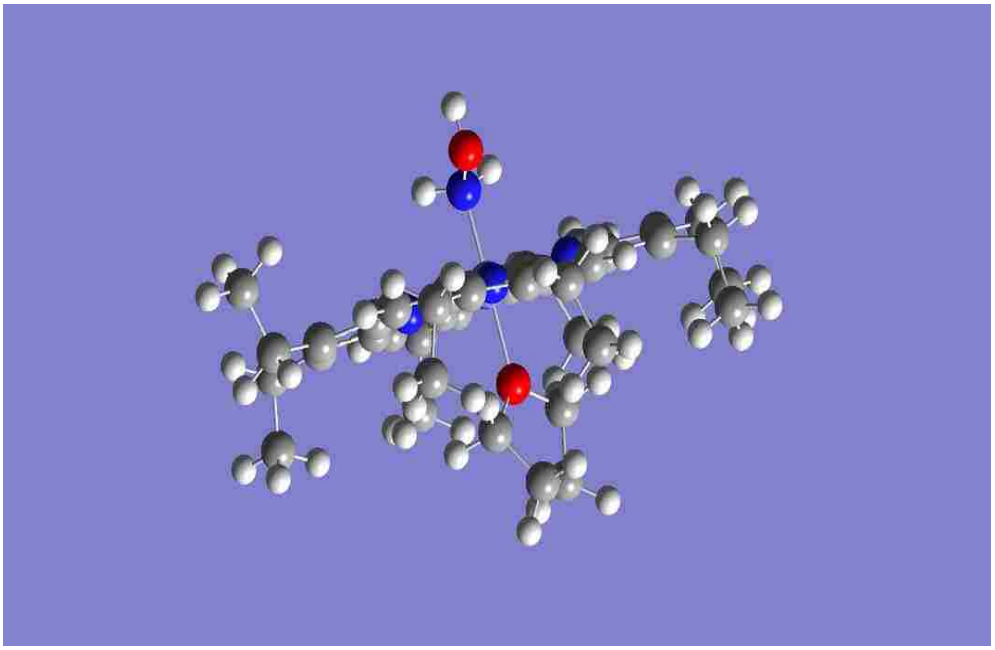

Figure 4-2A. Fe(OEP)(NH$_2$OH)(THF) complex.

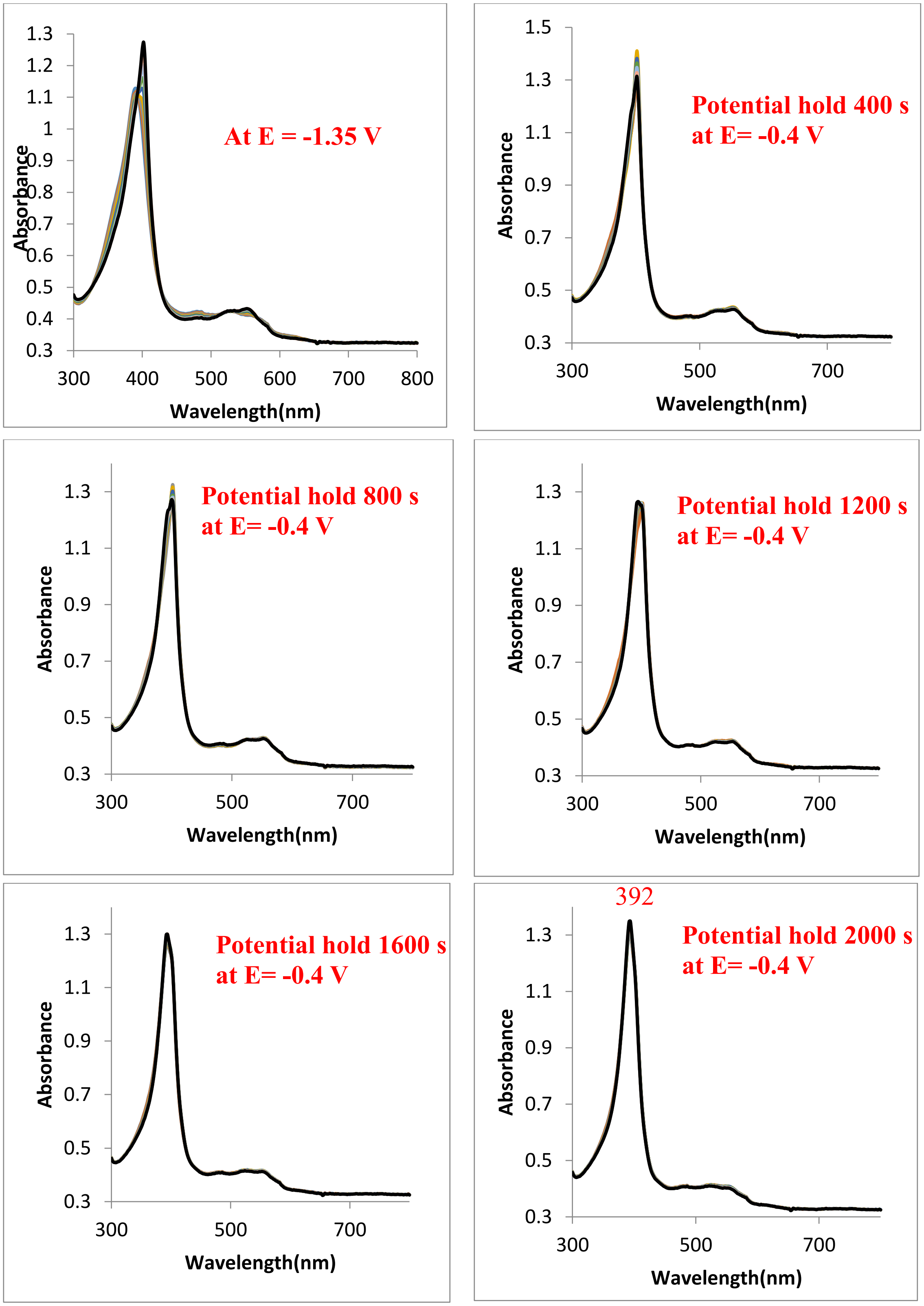

Figure 4-3. UV-visible spectroelectrochemistry of 0.20 mM Fe(OEP)(NO) in THF with 20 mM 2,6-dcp, 0.1 M TBAP, potential step from -1.00 to -1.35 V, potential hold at -0.4 V, scan rate 1 mV/s, Reference electrode Ag/AgNO$_3$, Working electrode Pt.

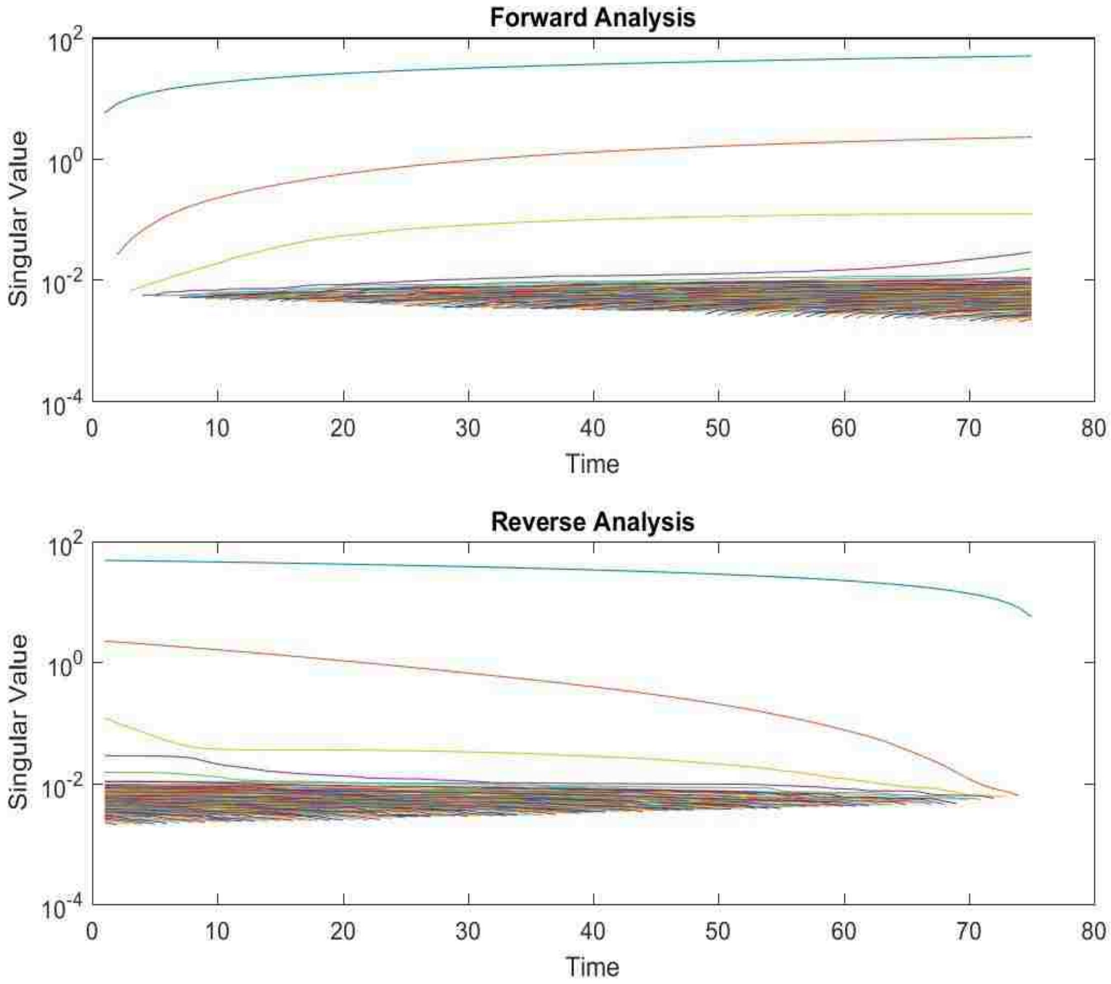

Figure 4-4. Evolving factor analysis of UV-visible spectroelectrochemistry of Figure 4-2 to determine the number of species.

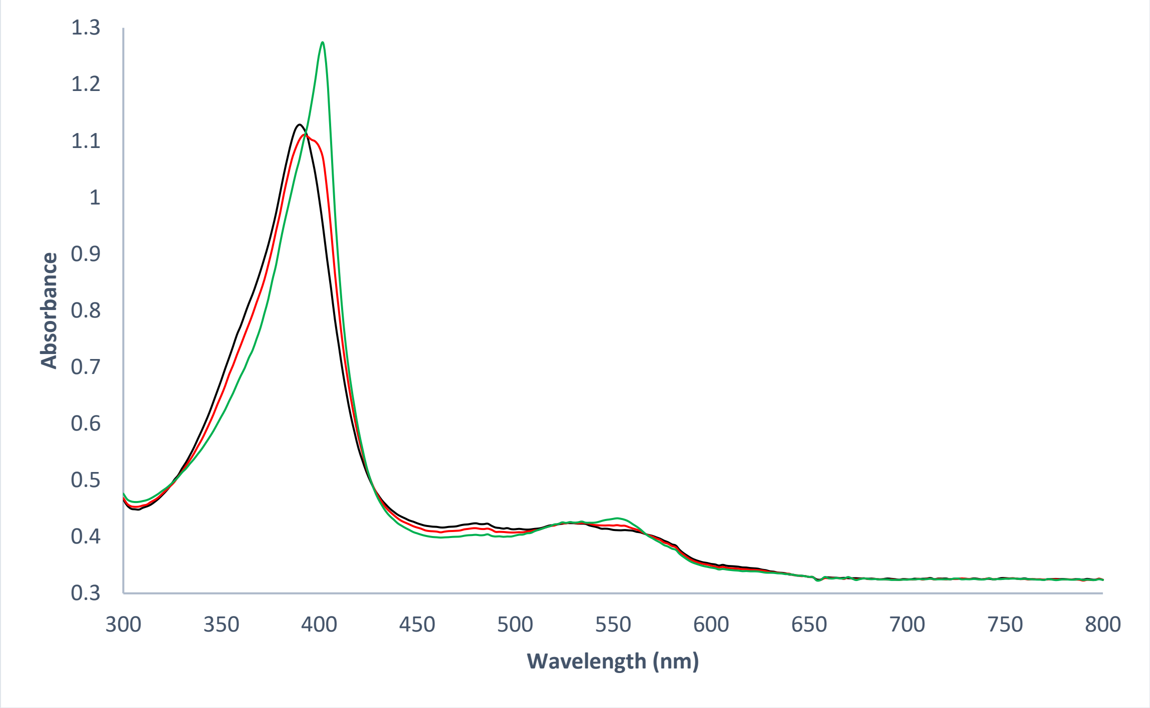

Figure 4-5. UV-visible spectra of Fe(OEP)(NO) black trace, Fe(OEP)(HNO) red trace, Fe(OEP)(NH_2OH) green trace, extracted from Figure 4-2.

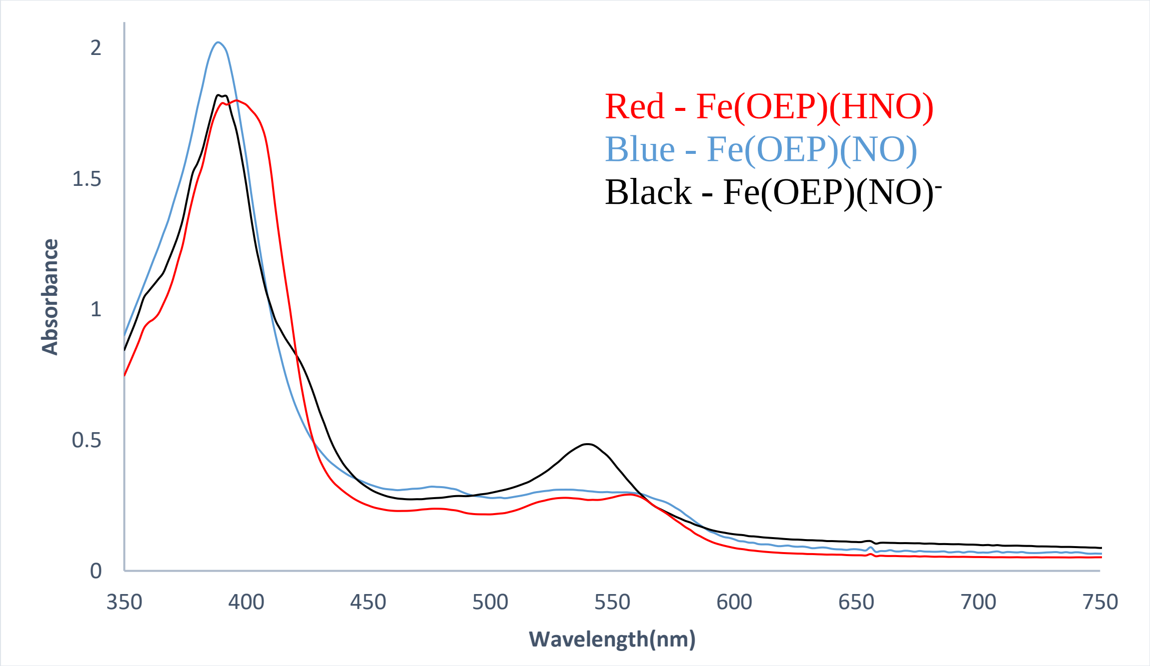

Figure 4-6. UV-visible spectra of chemically generated Fe(OEP)(HNO) in THF.

The initial product was presumably Fe(OEP)(HNO) (no Fe(OEP)(NO)$^-$ was observed). To verify this assessment, Fe(OEP)(NO)$^-$ was generated by chemical reduction of Fe(OEP)(NO) by the anthracenide reducing agent. The UV-visible spectrum of chemically reduced Fe(OEP)(NO)$^-$ (Figure 4-6) was consistent with spectroelectrochemically generated spectra (Figure 4-1). With the addition of 2,6-dcp, the bands for Fe(OEP)(NO)$^-$ was disappeared and new spectrum generated. A comparison of spectra generated electrochemically (Figure 4-7) with the chemically produced protonated species spectrum showed that the species were the same. Addition of more acid to that solution did not lead any change of the spectrum. This indicated that the protonated species was not further protonated with excess acids though doubly protonated species might not be different spectrally. The spectrum for Fe(OEP)(NO)$^-$ re-appeared by the addition of 2,6-dichlorophenolate base which further confirmed the chemical reversibility of protonation reaction. This was consistent with the voltammetric data.

The spectra of Fe(OEP)(NO) and Fe(OEP)(HNO) were quite similar except that the Soret band for Fe(OEP)(HNO) was red shifted and there was little change in the Q band region. Similar spectroelectrochemical and chemical data were obtained with 2,3-dcp and 3,5-dcp.

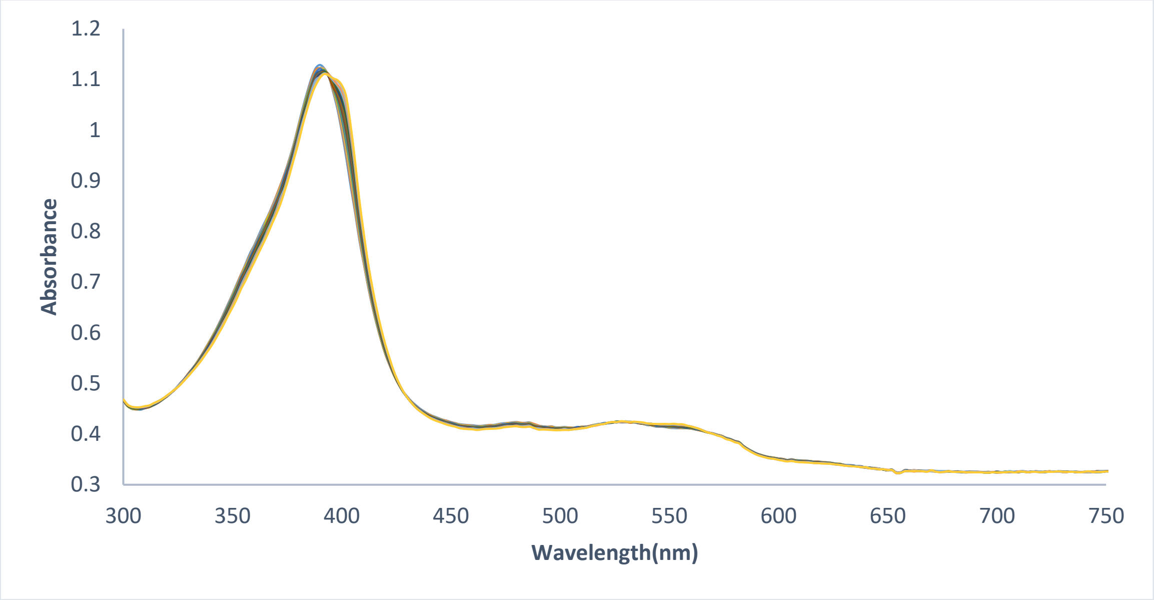

Figure 4-7. UV-visible spectra of 0.2 mM Fe(OEP)(NO) in THF, electrochemically generated Fe(OEP)(HNO), potential step from -1.0 V to -1.1 V, extracted from Figure 4-2.

As was already observed in the RRDE experiment, the protonation reaction was reversible and the extent of protonation could be controlled by the addition of phenolate. While the protonation reaction between iron nitroxyl, $Fe(OEP)(NO)^-$ and the substituted phenols was fast on the spectroelectrochemical time scale, the reverse reaction was slow. Using the normal scan rates of 1-5 mV/s, no re-oxidation was observed for Figure 4-2. In fact, continued reduction of Fe(OEP)(HNO) to $Fe(OEP)(NH_2OH)$ could be observed at the end of scan. This indicated the thermodynamic E^o of Fe(OEP)(HNO) to $Fe(OEP)(NH_2OH)$ was equal to or positive of $Fe(OEP)NO^{(0/-1)}$ wave at that concentration of acid. Kinetic factors prevented the multi-electron reduction of Fe(OEP)(NO) in the presence of acid at the first wave. To observe the effect of the conjugate base, cyclic spectroelectrochemistry scan was carried out in the presence of 2,6-dcp (20 mM) and 2,6-

dichlorophenolate (50 mM). In the Figure 4-8, Fe(OEP)(HNO) was the major product unlike what was observed in Figure 4-2. Small amounts of Fe(OEP)(NH_2OH) eventually formed at the end of the scan. Comparing Figure 4-2 and 4-8A, one can see that Fe(OEP)(NH_2OH) formation was significantly suppressed in the presence of base. The reverse scan showed (Figure 4-8B), the re-oxidation was accelerated and reached to initial spectrum within 500 s when the potential held at final potential. This was again demonstrated that the reaction was reversible and re-oxidation was accelerated by the addition of corresponding phenolate.

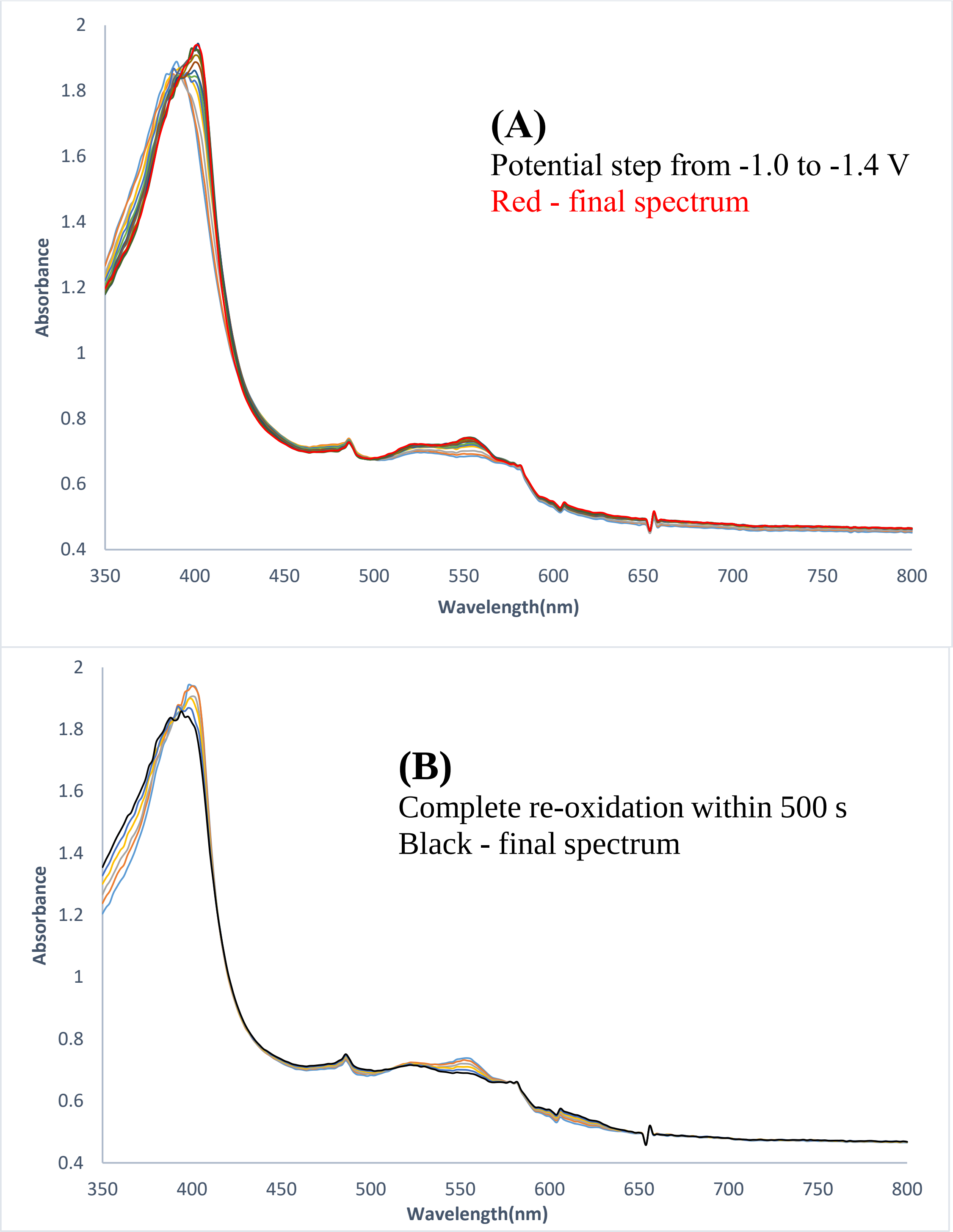

Figure 4-8. UV-visible spectroelectrochemistry of 0.32 mM Fe(OEP)(NO) with 2,6-dcp acid and the conjugate base in THF, 0.1 M TBAP, Reference electrode Ag/$AgNO_3$, A) Forward scan B) Reverse scan.

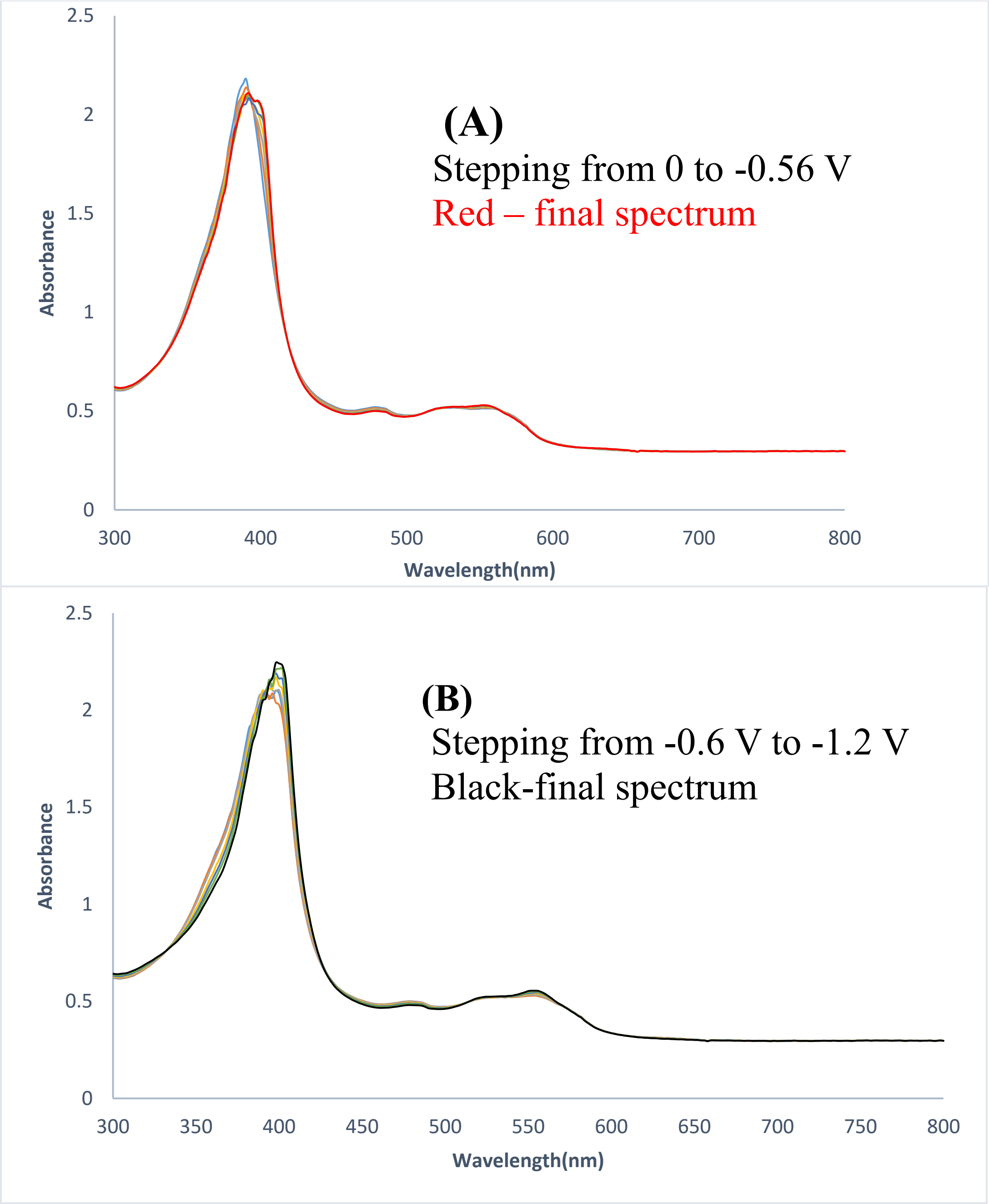

Figure 4-9. UV-visible spectroelectrochemistry of 0.30 mM Fe(OEP)(NO) with 4 mM 2,6-dcp acid and the conjugate base in THF, 0.1 M TBAP, Reference electrode Ag/AgNO$_3$, A) Potential step from 0 to -0.56 V B) From -0.6 to -1.2 V.

An alternative approach was then used for the spectroelectrochemistry. Rather than scanning the potential, as was normally done previously, the experiment was carried out by stepping the potential through the first wave, allowing species to come to steady state at each potential. At lower concentrations of acid (4 mM) and at lower (more positive) potentials, Fe(OEP)(HNO) was the product of the reduction (Figure 4-9A). As the potential was stepped more negatively, Fe(OEP)(NH_2OH) was formed (Figure 4-9B). The re-oxidation was also faster at lower concentrations of 2,6-dcp. As the concentration of 2,6-dcp increased (10 mM), Fe(OEP)(HNO) was still the prominent solution species with some Fe(OEP)(NH_2OH) being formed at more negative potential (Figure 4-10A). At this concentration both species could be observed. But at much higher concentrations of 2,6-dcp (100 mM), Fe(OEP)(NH_2OH) was generated progressively even at lower potential. As a result, it was difficult to observe Fe(OEP)(HNO) in the reduction (Figure 4-10B). This result confirmed the voltammetric observation that, at lower concentration of acid, the two reduction waves could be observed as was seen in the previous spectroelectrochemistry experiment. But at higher concentrations of acid the two waves merged (if the potential scan was slow enough). Under these conditions, it was difficult to see the Fe(OEP)(HNO) species. These results confirmed that the two waves observed in voltammetry were due to kinetic (acid concentration) rather than a thermodynamic factors (potential).

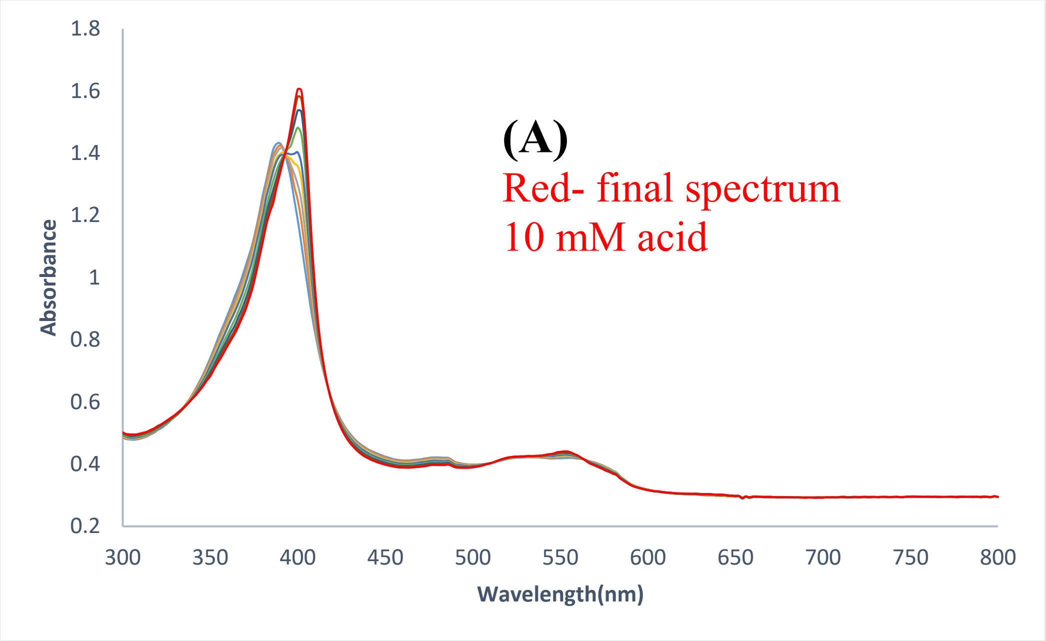

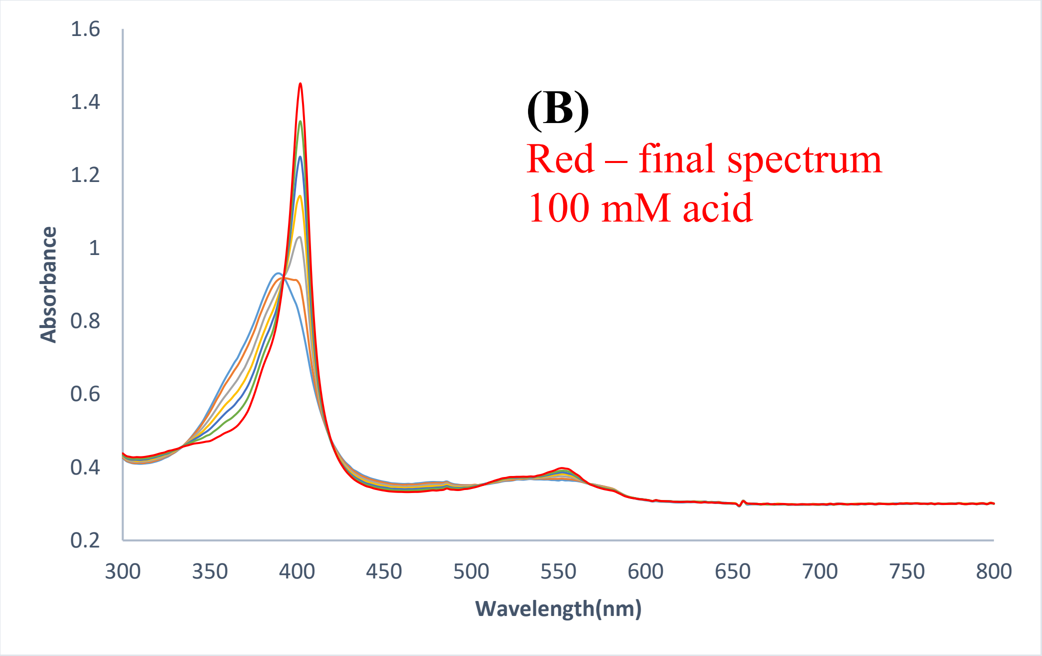

Figure 4-10. UV-visible spectroelectrochemistry of 0.25 mM Fe(OEP)(NO) in THF, Potential step from -0.6 V to -1.2 V, 0.1 M TBAP, Reference electrode Ag/AgNO$_3$, A) 10 mM 2,6-dcp B) 100 mM 2,6-dcp.

To confirm the electrolysis was need to form Fe(OEP)(NH_2OH) from Fe(OEP)(HNO), the spectroelectrochemistry of Fe(OEP)(HNO) itself was studied. The Fe(OEP)(HNO) complex was generated by the one electron chemical reduction of Fe(OEP)(NO), followed by the addition of 2,6-dcp (20 mM). The solution containing Fe(OEP)(HNO) was then reduced electrochemically and the visible spectra were monitored. The initial spectrum of Fe(OEP)(HNO) was consistent with previously generated Fe(OEP)(HNO). Upon reduction of the complex, a band at 402 nm appeared, indicative of the Fe(OEP)(NH_2OH) species (Figure 4-11A). No evidence was observed for the formation of the bis-hydroxylamine complex, Fe(OEP)($NH_2OH)_2$.[154]

With the addition of very high concentrations of 2,3-dcp (300-500 mM) with chemically generated Fe(OEP)(NO)$^-$, it was possible to produce hydrogen within half an hour by the analysis of head space of the reaction.

On the reverse scan, little re-oxidation was observed. If the potential was then held at -0.2 V, complete re-oxidation from Fe(OEP)(NH_2OH) to Fe(OEP)(NO) would occurred slowly. This indicated that the Fe-N bond to ligand remain intact throughout the redox process. The production of Fe(OEP)(NH_2OH) further confirmed by comparing with chemically produced bis-hydroxylamine species which was stable at -20.0º C. The spectrum was consistent with the spectroelectrochemically produced Fe(OEP)(NH_2OH) even though the chemically produced was bis-hydroxylamine complex in solution (Figure 4-11B). Both spectra were typical of low spin ferrous porphyrin complexes.

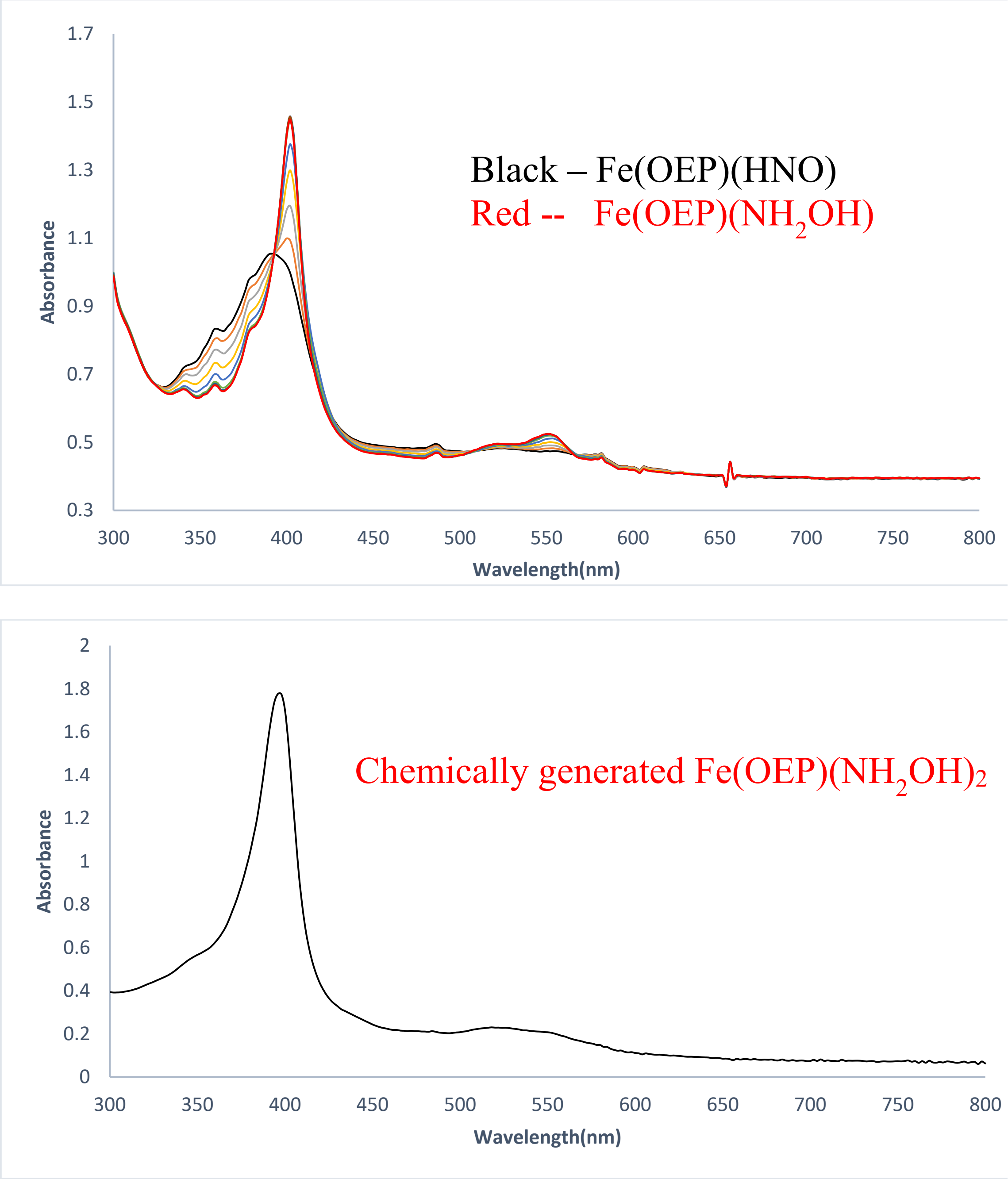

Figure 4-11. (A)Visible spectroelectrochemistry of 0.15 mM Fe(OEP)(HNO) in THF with 20 mM 2,6-dcp, 0.1 M TBAP, potential step from -0.6 to -1.0 V, Reference electrode Ag/AgNO$_3$ (B) Chemically generated Fe(OEP)(NH$_2$OH) at -20.0^o C.

There were two reasons that Fe(II)(OEP)(NH_2OH) continued to be observed during the reverse scan. First, the sluggishness of deprotonation reaction which removes Fe(OEP)(HNO) from the equilibrium. This probably due to the participation of phenolate in the rate limiting step. Based on the concentration of phenol, the protonation reaction was first order. The reverse reaction was second order as the porphyrin and phenolate concentrations were roughly equal. Secondly, the formation of Fe(OEP)(NH_2OH) was probably controlled by kinetic rather than thermodynamic factors. The formation of Fe(OEP)(NH_2OH) was time dependent which was observed in UV-visible spectroelectrochemical experiments. Even when the potential was reversed, Fe(OEP)(NH_2OH) band continued to grow at the end of the scan. Only at very positive potentials, the reaction was reversed. The formation of Fe(OEP)(NH_2OH) was dependent on the kinetics of the protonation reactions. The faster the protonation reaction, more the Fe(OEP)(NH_2OH) that was formed. In RRDE, the time scale was proportional to the rotation rate which was significantly shorter than UV-visible spectroelectrochemistry experiments. Therefore, in the UV-visible experiment, there was enough time to form Fe(OEP)(NH_2OH).

Cyclic voltammetry and normal pulse polarographic data both showed a multi-electron reduction at more negative potentials. The spectroelectrochemical data were most consistent with the formation of Fe(OEP)(NH_2OH) complex. The potentials were kept positive of the Fe(II/I) potential, unlike what was done in pulse polaroghraphy.[72] The following reduction was consistent with the spectroelectrochemical data.

$$\mathrm{Fe(II)(OEP)(HNO)} + 2\ \mathrm{PhOH} + 2e^- \rightarrow \mathrm{Fe(II)(OEP)(NH_2OH)} + 2\mathrm{PhO}^- \qquad (4\text{-}1)$$

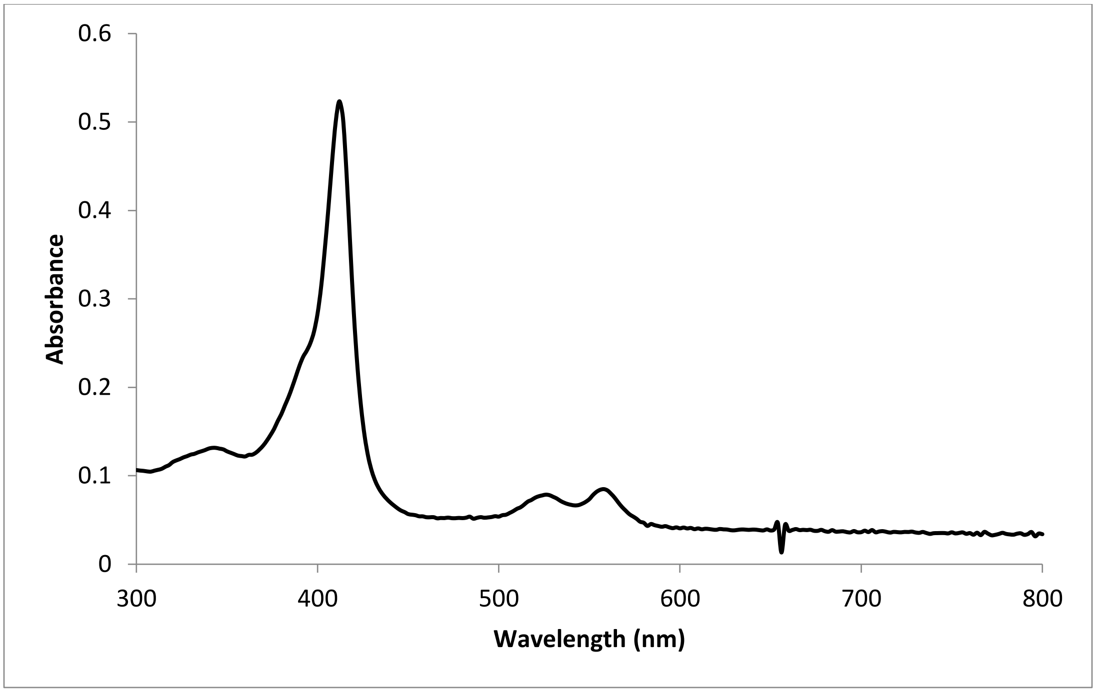

Figure 4-12. Co(III)(OEP)(NH_2OH)$_2$$^+$ in dichloromethane at room temperature.

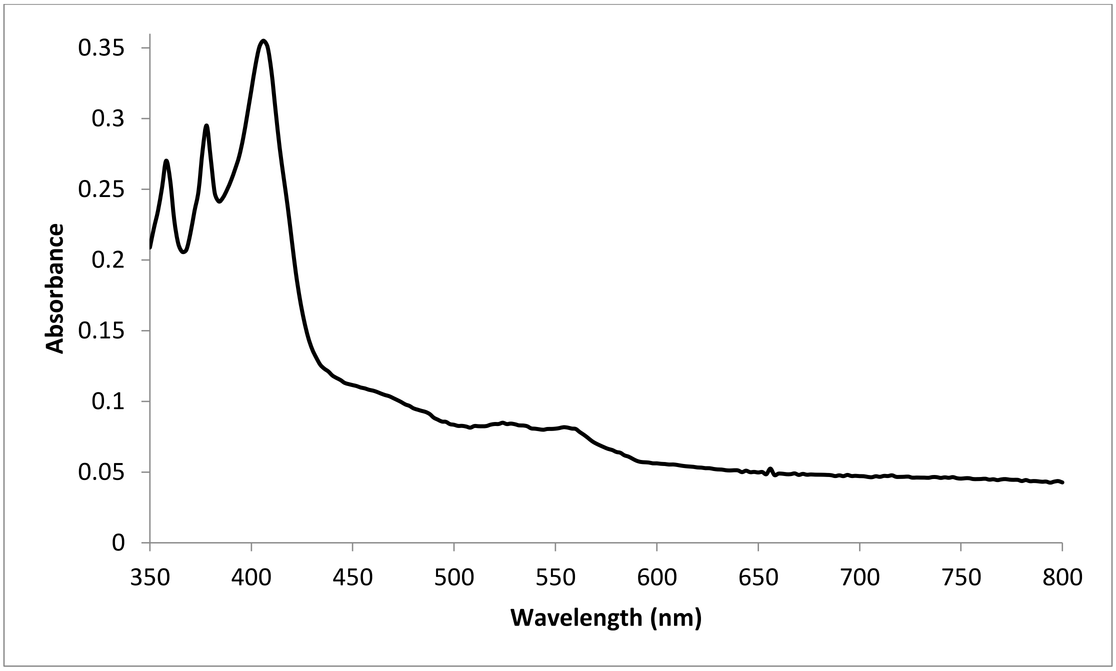

Figure 4-13. Chemically generated Fe(OEP)(NH_2OH) with tenfold excess anthracenide reducing agent with Fe(OEP)(HNO) and 4-cp-*d₄* solution at room temperature.

To confirm the formation of Fe(OEP)(NH_2OH) in spectroelectrochemistry experiments, Co(III)(OEP)$(NH_2OH)_2^+$ was synthesized at room temperature. The UV-visible spectrum gave a sharp band at 412 nm which is similar to the Soret band, observed in the spectroelectrochemistry experiments at more negative potential or at the higher concentration of acids.

Another set of experiments were carried out to synthesize Fe(OEP)(NH_2OH) chemically in solution by using excess anthracenide reducing agent in Fe(OEP)(HNO) and 4-cp-d_4 solution. The purpose of using excess reducing in the Fe(OEP)(HNO) solution was to reduce the Fe(OEP)(HNO) complex to form Fe(OEP)(NH_2OH). The UV-visible spectrum (Figure 4-13) showed the same spectrum (with the addition of anthracene bands from reducing agent) as that generated in spectroelectrochemical experiments. At lower concentration of reducing agent (2 times than Fe(OEP)(NO) concentration), the solution contained a mixture of Fe(OEP)(HNO) and Fe(OEP)(NH_2OH) complexes, after 2-3 hours, the Soret band at 390 nm appeared for Fe(OEP)(NO). With the higher concentration of reducing agent, solution containing only Fe(OEP)(NH_2OH) complex, which was only stable for 90 minutes.

Addition of phenolate to the iron porphyrin nitrosyls would lead to Fe(OEP)$(OPh)^-$ which could be a possible final product. In order to determine its spectral properties, Fe(OEP)$(OPh)^-$ was synthesized by mixing Fe(OEP)Cl with 3,5-dichlorophenolate in THF then crystallized by the addition of anhydrous heptane. (Figure 4-14B). The visible spectrum (Figure 4-14A) showed a unique band at 620 nm in the Q region. The band was never seen in the spectroelectrochemical experiments of Fe(OEP)(NO) in the presence of substituted phenols. This confirmed that there was no ligation of phenolate ligand to iron center. In the above experimental reaction conditions with phenols, there was no evidence of the production of H_2 from the reaction Fe(OEP)(HNO) with substituted phenols other than at high concentration of substituted phenols. If this were to happen, the visible spectrum for Fe(OEP)(NO) would be observed. However, isolation of Fe(OEP)(HNO) from the solution which was attempted by removing the solvent did lead to the formation of Fe(OEP)(NO), probably with the H_2 evolution. This is consistent with the head space analysis of the reaction of Fe(OEP)(HNO) and high concentration of phenols.

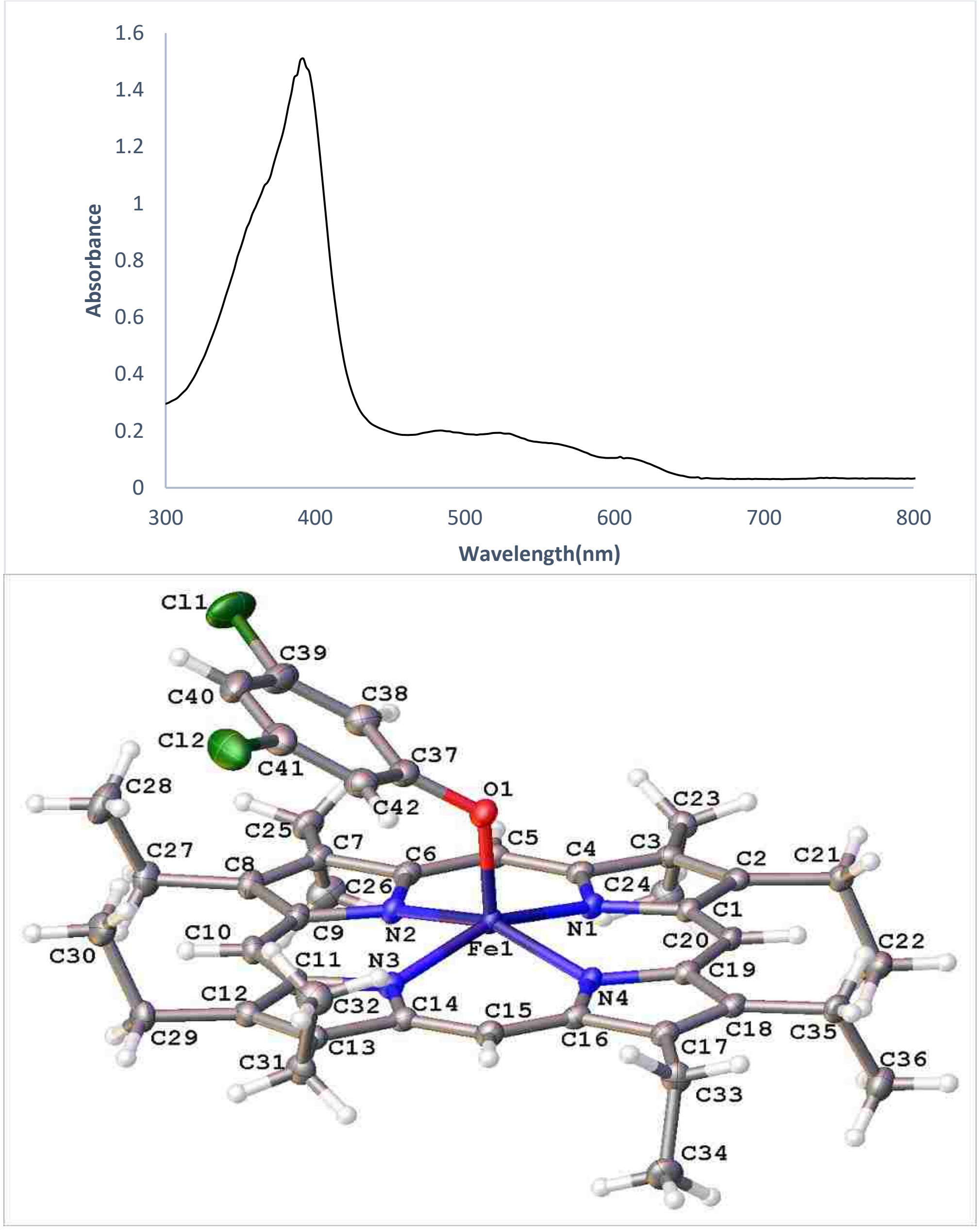

Figure 4-14. A) UV-visible spectrum of Fe(OEP)(PhO)$^{-}$ B) Crystal structure of Fe(OEP)(PhO)$^{-}$.

4.2 UV-visible Spectroelectrochemistry of Fe(OEPone)(NO)

To identify the reduced species, UV-visible spectroelectrochemistry of Fe(OEPone)(NO) was performed in THF. The reduction potential for Fe(OEPone)(NO) was more positive than the Fe(OEP)(NO), and the potential was scanned from -0.5 V to –1.5 V against Ag/AgNO$_3$ reference electrode. Significant changes observed in Q band region as the band at 618 nm shifted to 608 nm and new band at 533 nm were observed with the increase Soret band. The initial spectrum was regenerated upon the potential scanning to initial potential, indicating the reduced species was stable in the experimental timescale. A set of isobestic points in the spectra (Figure 4-15) indicated only two spectral species were present.

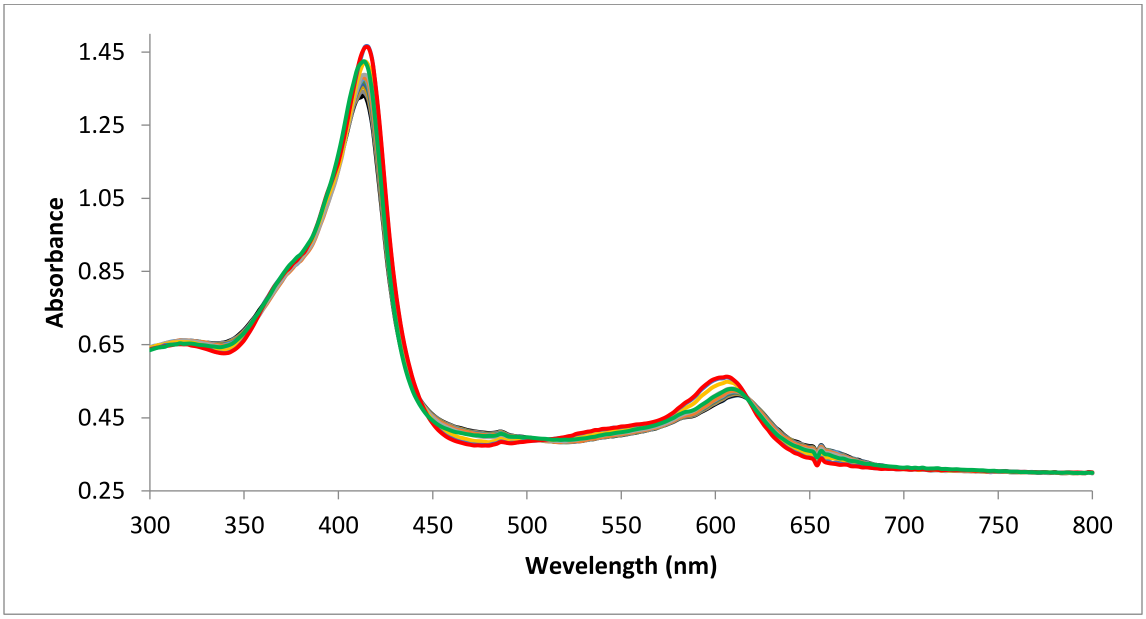

Figure 4-15. UV-visible spectroelectrochemistry of 0.23 Fe(OEPone)(NO) in THF, 0.1 M TBAP, E_i = -0.5 V, E_f = -1.5 V, scan rate 1 mV/s, Reference electrode Ag/AgNO$_3$, Working electrode Pt.

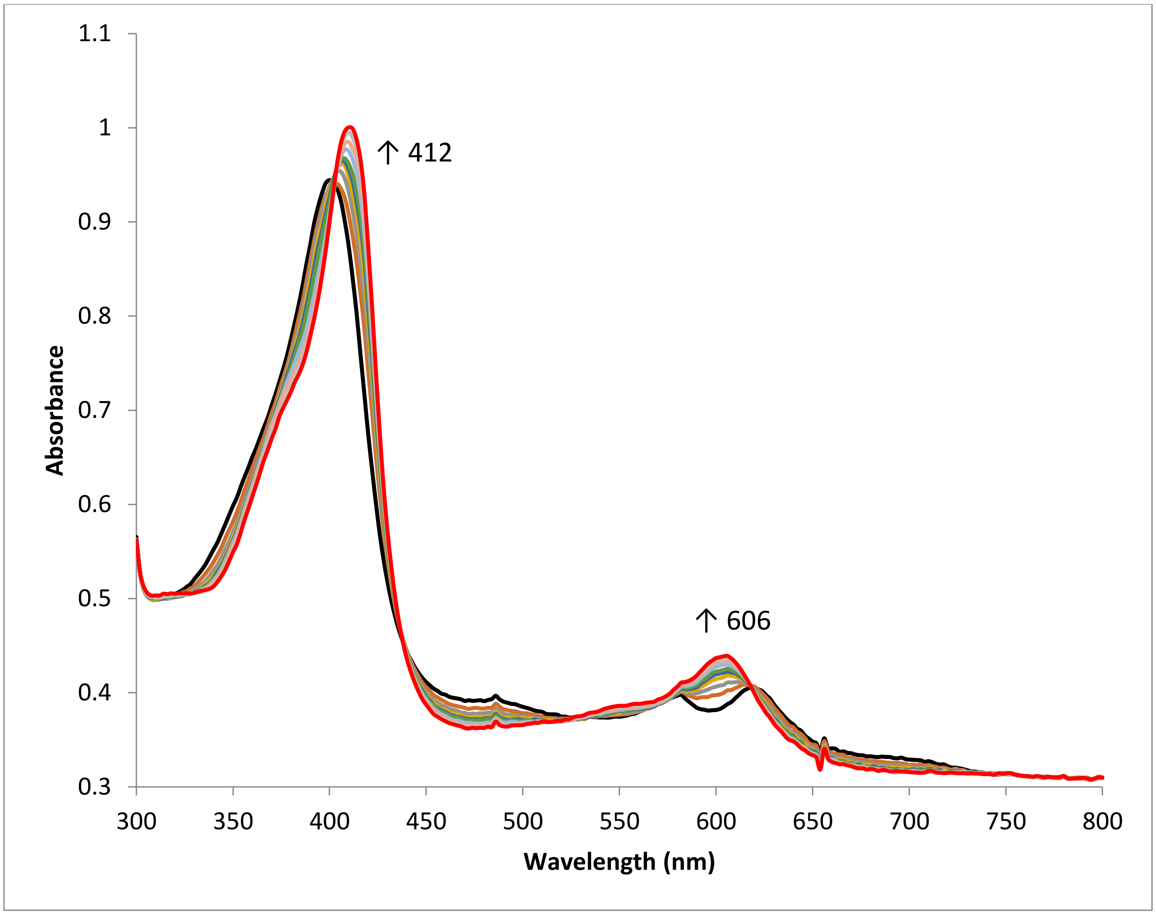

Figure 4-16. UV-visible spectroelectrochemistry of 0.15 mM Fe(OEPone)(NO) with 100 mM 2,3-dcp in THF, 0.1 M TBAP, E_i = -0.5 V, E_f = -0.9 V, scan rate 1 mV/s, Reference electrode Ag/AgNO$_3$, Working electrode Pt.

A similar experiment was carried out in the presence of 2,3-dcp. In this case, a high concentration of 2,3-dcp (100 mM) was used. We have already seen that this porphinone was less reactive than Fe(OEP)(NO). The change of spectra was seen at less negative potential than in the absence of acid. This indicated that the reduced species reacted with acids. A set of isobestic points indicated that only two spectral species were present in the experimental time scale. The significant change of spectra was seen in the presence of acid. In the Soret region, a band shifted to 412 nm and in the Q region, the band at 608 nm shifted to 604 nm (Figure 4-16). If the potential scanned to more negative, the bands in Soret and Q region were increased as was observed for Fe(OEP)(NO). To determine the number of species, present in the solution, the data were treated by evolving factor analysis (Figure 4-17). The analysis showed that at least three species were present in the experimental time scale. This results consistent with at least three species perhaps four. We can expect the three of the species were Fe(OEPone)(NO), Fe(OEPone)(HNO) and Fe(OEPone)(NH_2OH). The band at 412 nm clearly indicated a Ferrous hydroxylamine complex. This band was similar to 402 nm for Fe(OEP)(NH_2OH), 410 nm for Fe(OEP)$(py)_2$,[152] 409 nm for Fe(OEP)(CO)(py) and 410 nm for Fe(OEP)(O_2)(CH_3CN).[153]

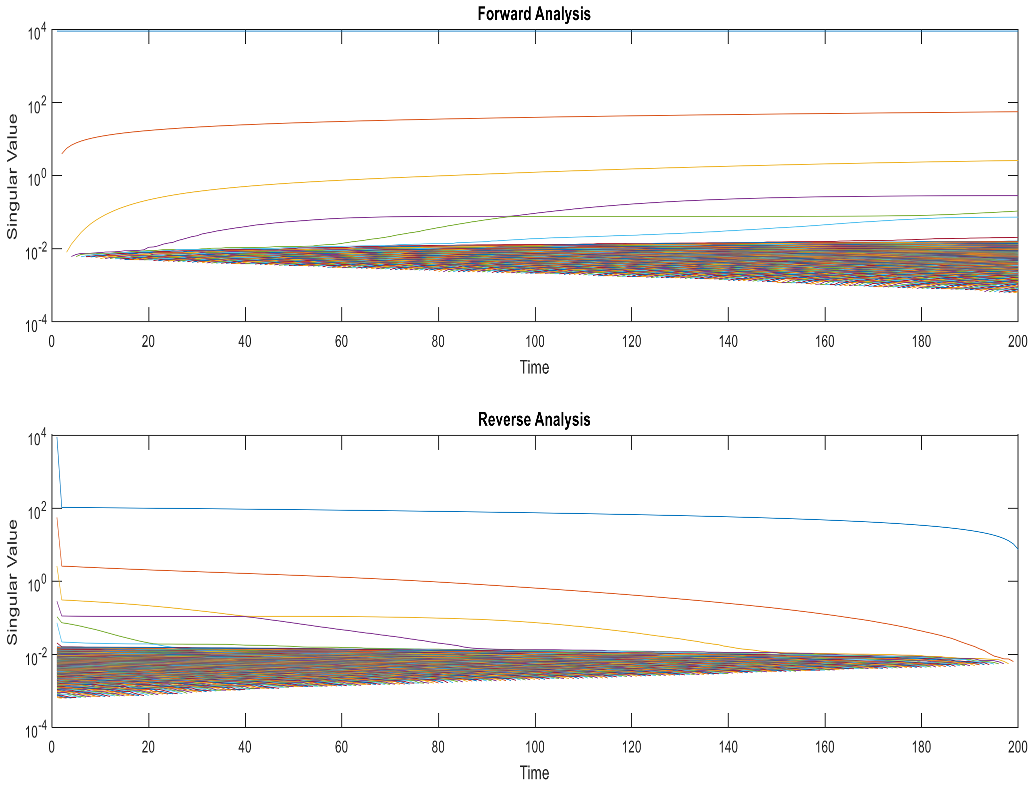

Figure 4-17. Evolving factor analysis of UV-visible spectroelectrochemistry of Figure 4-16 to determine number of species.

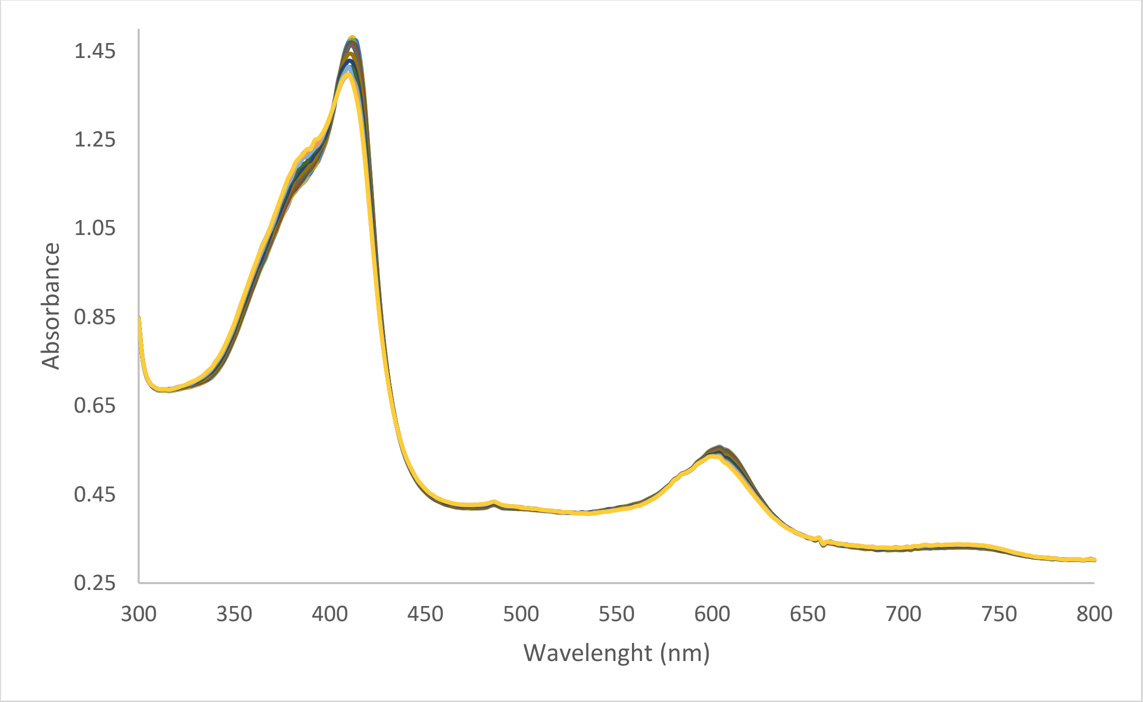

Figure 4-18. UV-visible spectroelectrochemistry of 0.23 mM Fe(OEPone)(NO) with 120 mM 2,3-dcp in THF, 0.1 M TBAP, Potential at 0.0 V for 3000 s, scan rate 1 mV/s, Reference electrode Ag/AgNO$_3$, Working electrode Pt.

The reverse scan showed an unusual behavior that the band 604 nm shifted to 600 nm with the decrease of Soret band and two new bands at 386 and 732 nm (Figure 4-18). The possible reason might be the concentration of acid was too much which strongly inhibited the reverse reaction. Another possibility was the protonation species dissociated and then reduction happened on the porphinone macrocycle which changed in the Soret band. Because the bands at 386 and 730 nm band were seen for Fe(OEPone)Cl. If HNO or NH$_2$OH released, we should see bands for N$_2$O or NH$_2$OH in IR. Extensive study on Fe(OEPone)(NO) with different substituted phenols in the presence of corresponding phenolate was not done.

CHAPTER 5 NUCLEAR MAGNETIC RESONANCE (NMR)

5.1 NMR of Fe(OEP)(NO)$^-$ and Fe(OEP)(HNO)

The ^{1}H NMR of the starting complex, Fe(OEP)(NO) cannot be obtained due to the paramagnetism of the complex. Fe(OEP)(NO)$^-$ though is a S= 0 complex, and it should be possible to obtain its spectrum. The Fe(OEP)(NO)$^-$ complex was obtained by the chemical reduction of Fe(OEP)(NO). The resonances observed for Fe(OEP)(NO)$^-$ complex were 7.4, 7.5, 7.57, 7.77, 7.95 and 8.4 ppm. Among those resonances 7.4, 7.95 and 8.4 ppm were identified as anthracene resonances. The remaining resonances 7.50, 7.57 and 7.77 ppm were attributed to Fe(OEP)(NO)$^-$ complex. The compound was a S=0 complex but the ^{1}H NMR was significantly different from other S=0 metalloporphyrin complexes. Typical values for meso-protons for Mg(II)(OEP) and Fe(II)(OEP)(Py)$_2$ are 10.0 ppm. This compound did not show any resonances at 10.0 ppm. In order to confirm the meso-protons for the complex, Fe(OEP-d_4)(NO)$^-$ was synthesized where the

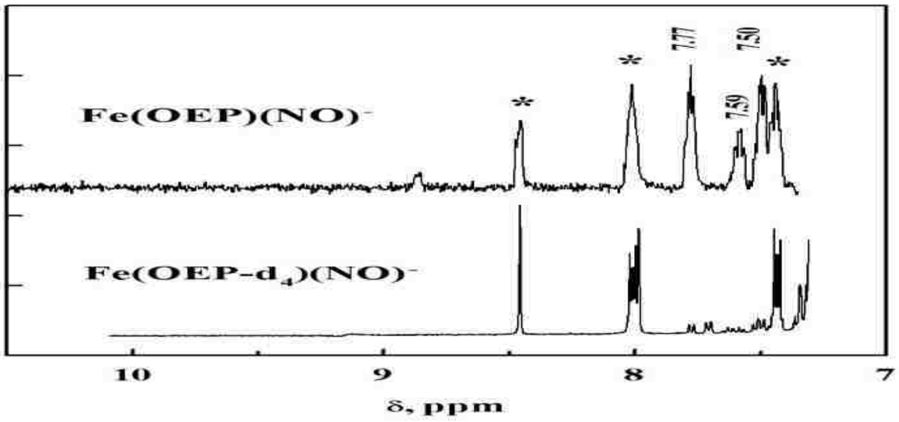

Figure 5-1. ^{1}**H NMR of 7.0 mM Fe(OEP)(NO)$^-$ and Fe(OEP-d_4)(NO)$^-$ in THF-d_8.**

meso protons were replaced by deuterium atoms. From Figure 5-1, resonances that were observed at 7.50, 7.57 and 7.77 ppm for normal abundance Fe(OEP)(NO)$^-$ were missing or highly attenuated for Fe(OEP-d_4)(NO)$^-$. This confirmed that those three resonances came from meso protons. This ^{1}H NMR was unusual than in comparison to those for other S=0 complexes. The splitting for meso-protons is also unique, this might be due to the displacement of iron atom from the porphyrin plane. To test the splitting for meso protons, DFT calculations for Fe(OEP)(NO)$^-$ were carried out where the iron atom into and out of the porphyrin plane.[97] The results showed splitting of the meso protons. The source of splitting of meso protons most likely due to slow rotation of NO$^-$ ligand around the iron atom.

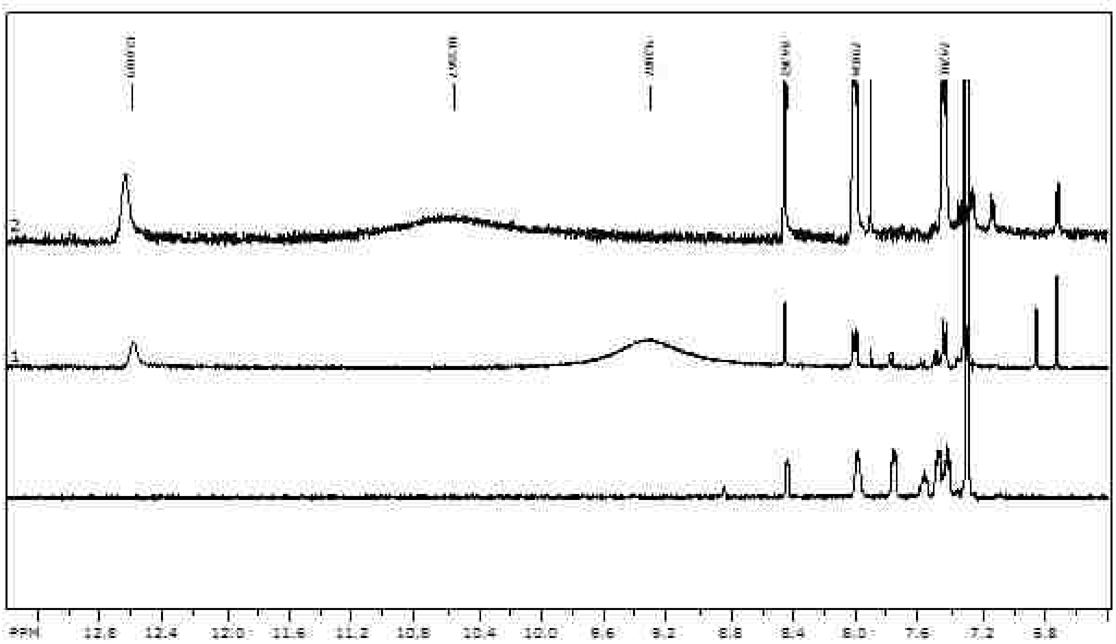

Figure 5-2. ^{1}H NMR of only 7.0 mM Fe(OEP)(NO)$^-$ (Lower most) and 7 mM Fe(OEP)(NO)$^-$ (Middle), 8.6 mM Fe(OEP)^{15}NO$^-$ (Upper most) complexes with 10 mM 3,5- dcp in THF-d_8.

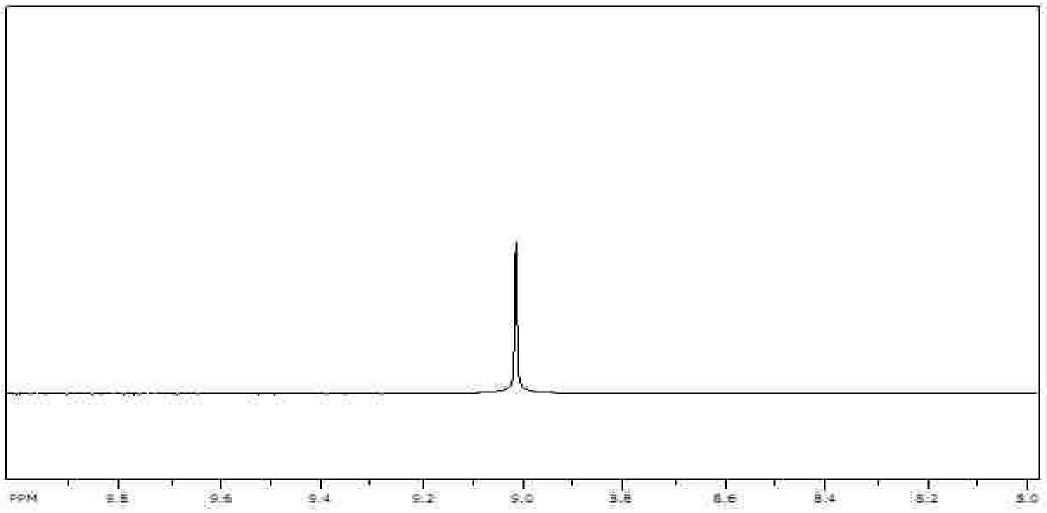

Figure 5-3. ^{1}H NMR for 3,5-dcp-*d*$_3$ in CDCl$_3$.

In order to obtain the protonated species, 3,5-dcp was added to the solution of Fe(OEP)(NO)$^-$. New resonances were now observed at 9.30 and 12.60 ppm (Figure 5-2). The resonance at 9.0 ppm was due to the acid which was confirmed by ^{1}H NMR of only 3,5-dcp-*d*$_3$ in CDCl$_3$ (Figure 5-3). The resonance at 12.60 ppm came from Fe(OEP)(HNO) which was consistent with literature values. [93] The HNO proton in the Fe(OEP)(5-MeIm)(HNO) complex was 14.0 ppm. The small upfield shift may due to the lack of trans-coordination and hydrogen bonds between the excess acids and the complexes. The meso protons shifted to 7.76, 7.78 and 7.90 ppm (Figure 5-2). We already observed that the addition of acids to Fe(OEP)(HNO) solution did not lead to Fe(OEP)(NH$_2$OH). Irradiation the peak at 12.60 ppm led to attenuation of 9.3 ppm peak (Figure 5-4), indicating that the two protons were in an exchange reaction. When 3,5-dichlorophenolate was added to the solution, the 12.6 ppm resonance disappeared. With the addition of 3,5-dcp to Fe(OEP)(NO)$^-$, the resonances for meso protons disappeared for Fe(OEP)(NO)$^-$ but then reappeared when 3,5- dichlorophenolate was added (Figure 5-5). The ^{1}H NMR for Fe(OEP)(^{15}NO)$^-$ with 3,5-dcp did not show $J_{N\text{-}H}$ coupling for H^{15}NO probably due to rapid proton exchange with excess acids in solution. The ^{1}H NMR of Fe(OEP-d_4)(NO)$^-$ with acid showed the resonance at 9.30 and 12.6 ppm. This confirmed that those resonances did not come from meso-protons (Figure 5-6).

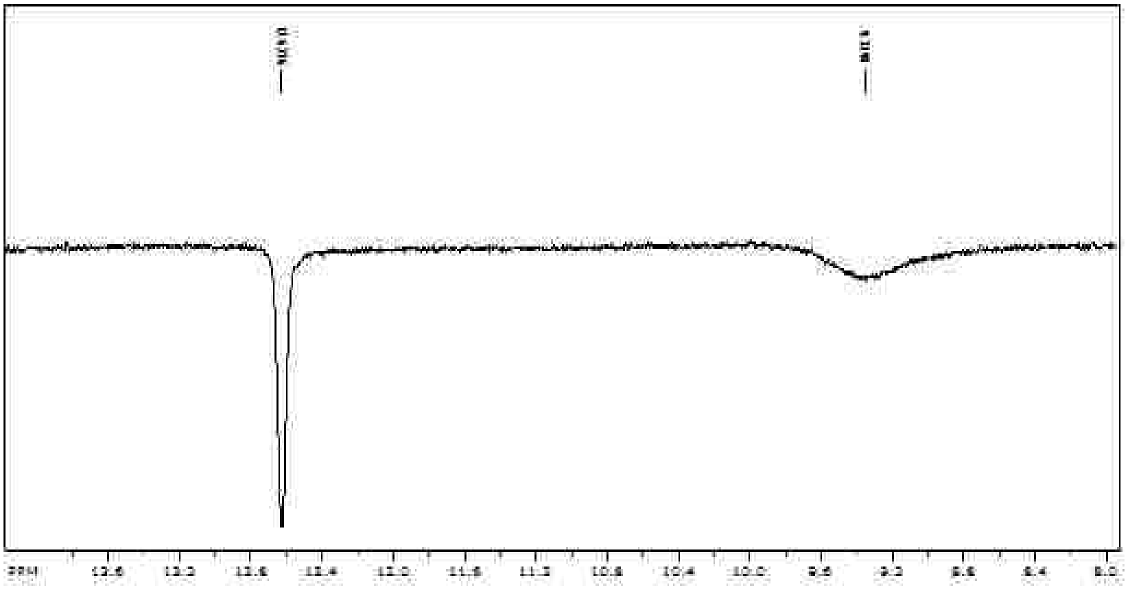

Figure 5-4. NOE difference ^{1}H NMR of 7 mM of Fe(OEP)(^{15}NO)$^-$ with 10 mM 3,5-dcp in THF-d_8.

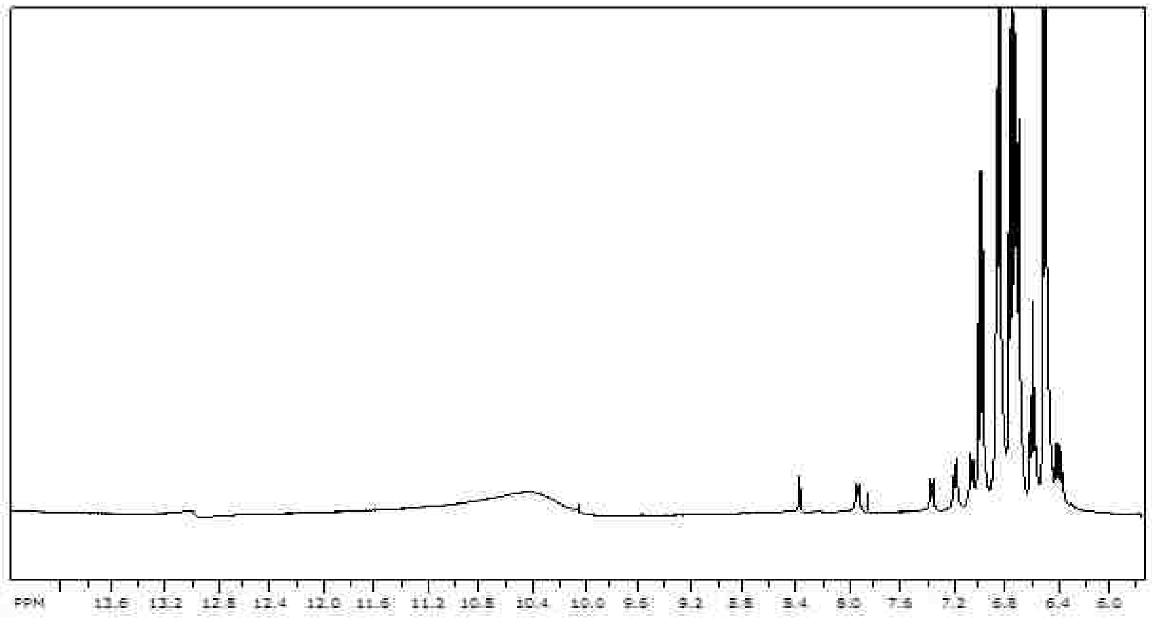

Figure 5-5. ^{1}H NMR of Fe(OEP)(NO)$^-$ with 2,3-dcp and 2,3-dichlorophenolate in THF-d_8.

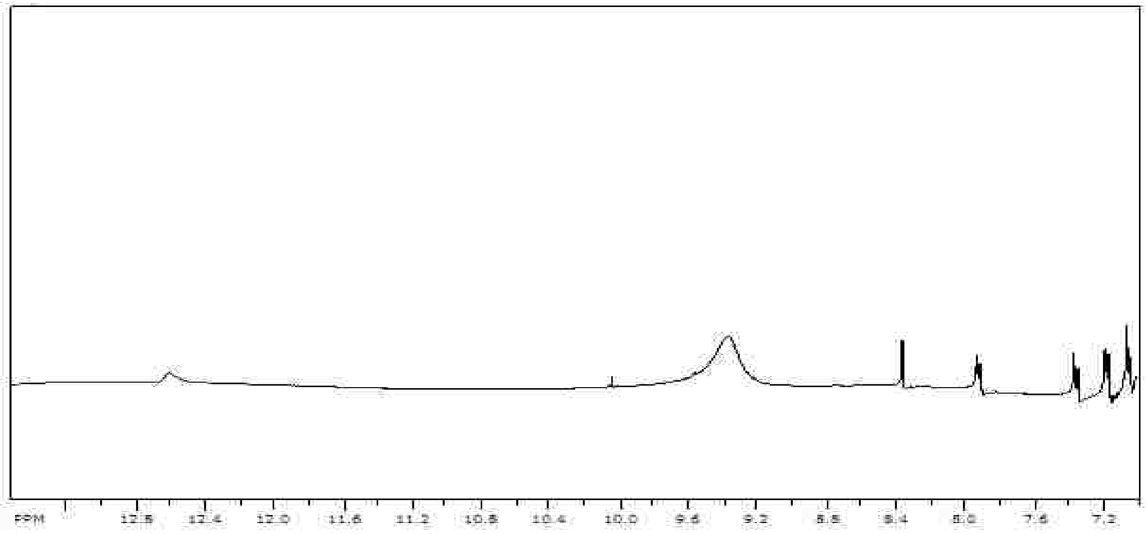

Figure 5-6. ^{1}H NMR of Fe(OEP-d_4)(NO)$^-$ with 2,3-dcp in THF-d_8.

To slow the proton exchange, low temperature ^{1}H NMR was performed. The result (Figure 5-7) showed a very interesting phenomenon. As the temperature was reduced, the peak for HNO was attenuated and the peak for the acid became sharper with the resonances approached each other. At the same time the peak for HNO meso-proton at 7.9 ppm disappeared and reappeared from room temperature to low temperature. This type of phenomena was observed previously. [155,156] This unusual phenomenon might be due to hydrogen bonding or multiple exchange of proton at different sites (Figure 5-8A/B).

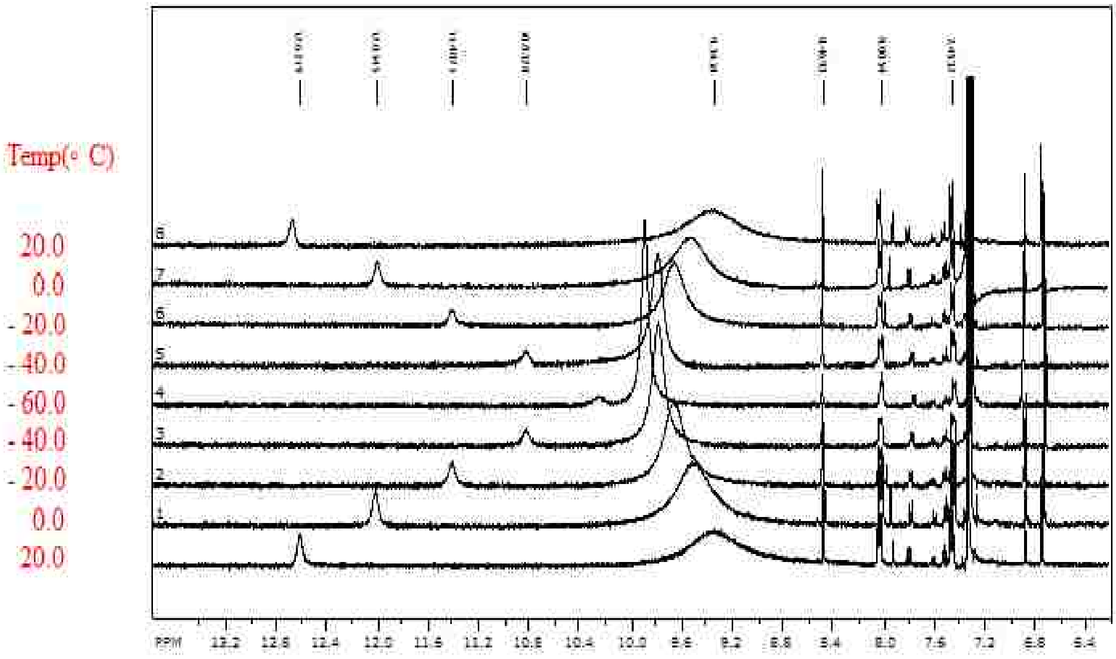

Figure 5-7. ^{1}H NMR of 8 mM of Fe(OEP)(^{15}NO)$^-$ complex with 10 mM 3,5-dcp in THF-d_8 at different temperature.

Two resonances were seen previously, one of them was for hydrogen bonded complex and other one was for free protons. [156] The two resonances were shifted with the variation of temperature. In case of our system, two resonances were observed, one for Fe(OEP)(HNO) and other for substituted phenols (Figure 5-7). Earlier Golubev et al.[155] proposed two mechanism for the hydrogen bonded complexes at room and lower temperature. Based on the assumption, the reactions were,

$$\text{Fe(OEP)(HNO)} + \text{PhOH} \leftrightarrow \text{Fe(OEP)(HNO)}\ldots\ldots\text{HOPh} \qquad (5\text{-}1)$$

$$\text{Fe(OEP)(HNO)}\ldots\ldots\text{HOPh} \leftrightarrow \text{Fe(OEP)(NO)}^{-}\ldots\ldots{}^{+}\text{H}\ldots{}^{-}\text{OPh} \qquad (5\text{-}2)$$

At low temperature, the reaction (5-1) was slow which attributed for hydrogen bond formation at room temperature and the reaction (5-2) was fast which attributed for the formation of ion pair. At lower temperature, the reaction (5-1) was slow which was consistent our spectra (Figure 5-7). When the temperature was decreased, the protonated complex formation was suppressed because of slow hydrogen bonding process which was observed by the decrease of intensity for mobile proton from the Fe(OEP)(HNO) complex. As at lower temperature, the ion pair formation reaction was fast which might change the K value by a shift between H-bonding and protonation. This might attribute the decrease of the intensity of Fe(OEP)(HNO) and the shift toward acid resonance. The sharpness of acid resonance at lower temperature also indicated a decrease of mobility of protons. At lower temperature, the acids aggregated more into themselves than the room temperature acids which attributed slow hydrogen bonding. These phenomena indicated at lower temperature the protonation reaction was controlled by thermodynamic rather than kinetic factors.

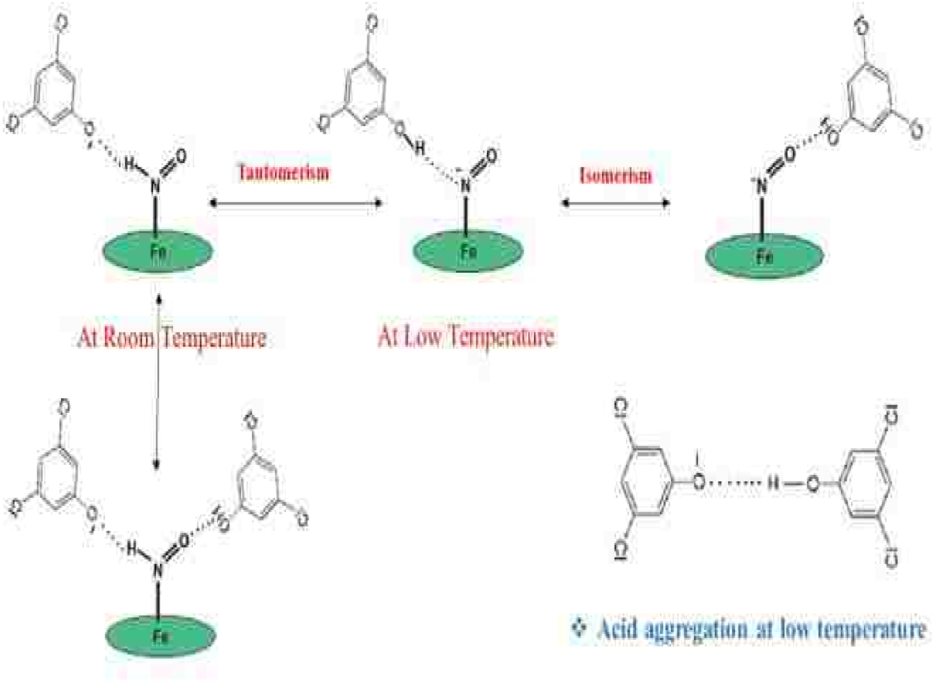

Figure 5-8. Possible hydrogen bonding and proton transfer among Fe(OEP)(HNO), phenol and phenolate.

^{2}H NMR was also taken for Fe(OEP)(NO)$^{-}$ with 3,5-dcp-d_4 to observe ^{2}HNO moiety. The resonance was not seen, which might be due to exchange reaction or insensitivity of deuterium (Figure 5-9). A low temperature, ^{2}H NMR was also run to slow the exchange reaction. At -40.0^{o} C, a peak 11.0 ppm observed for ^{2}HNO which was confirmed the presence of HNO peak at the same position and at the same temperature (Figure 5-10).

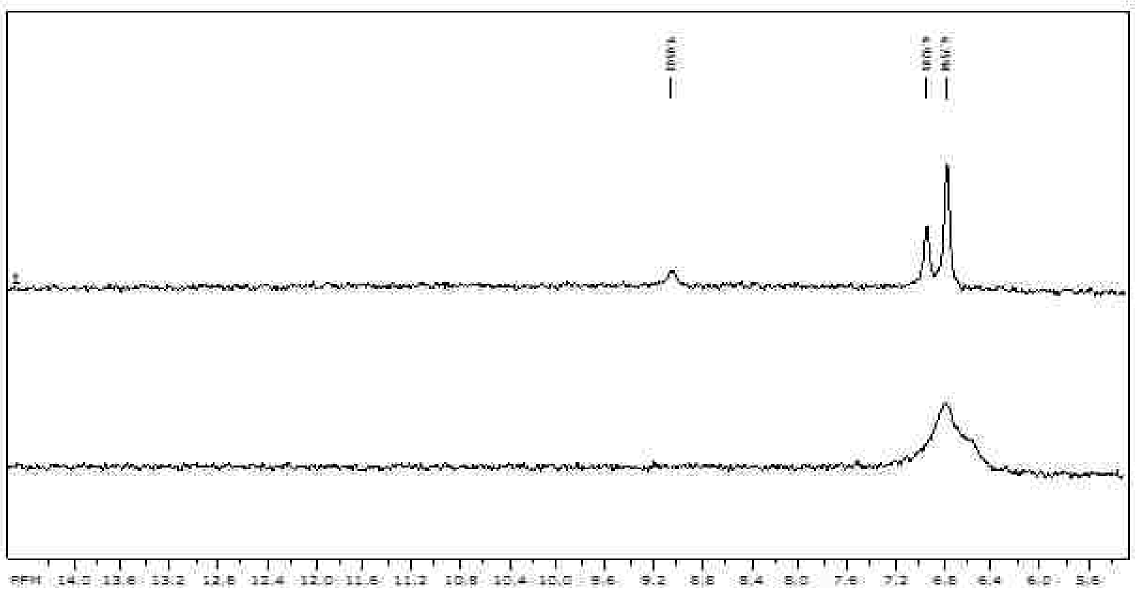

Figure 5-9. ^{2}H NMR of 7.0 mM Fe(OEP)(^{15}NO)$^-$ with 10 mM 3,5-dcp-d_4 (Bottom) in THF with 0.2 mM of THF-d_8, (Top), only 3,5-dcp-d_4.

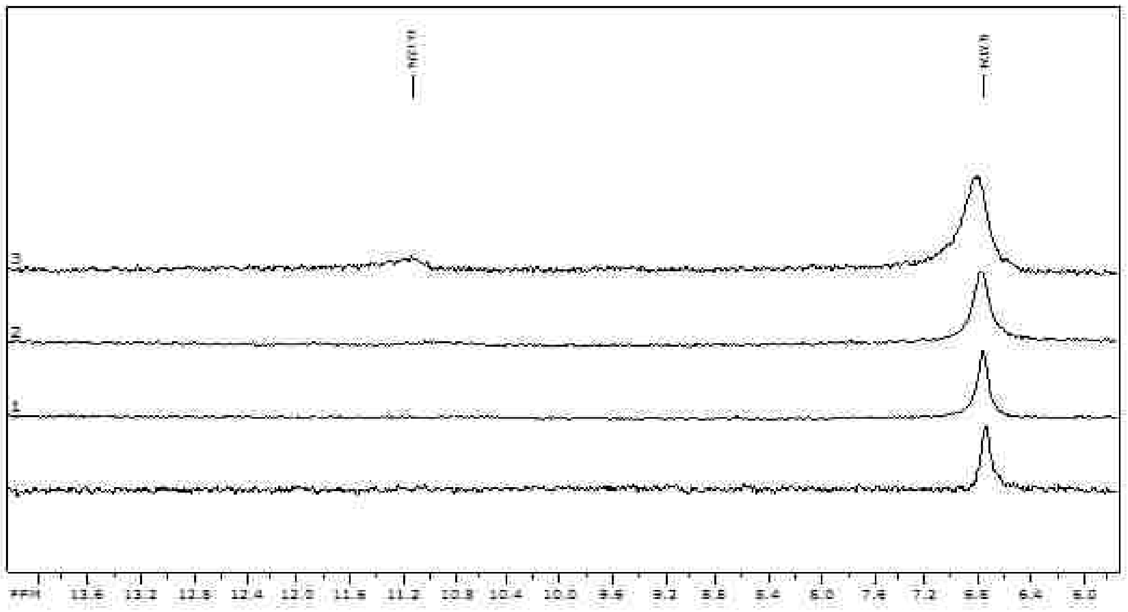

Figure 5-10. ^{2}H NMR of 7.0 mM Fe(OEP)(^{15}NO)$^-$ with 10 mM 3,5-dcp-d_4 in THF with 0.2 mM of THF-d_8 at different temperature. (20°, 0 °, -20° and -40 ° C bottom to top).

The formation of Fe(OEP)(HNO) complex by the reaction of Fe(OEP)(NO)$^-$ with substituted phenols was observed which was previously seen (Chapter 3 & 4) in the voltammetric and UV-visible spectroelectrochemistry experiments. The proton resonance for HNO moiety was far from meso protons from macrocycle and acid protons. The paramagnetic Fe(OEP)(NO) complex was transparent in the above-mentioned regions (30.0 to -5.0 ppm), but the diamagnetic Fe(OEP)(NO)$^-$ complex showed unique resonances for the complex. Fortunately, the meso protons did not obscured the HNO protons. The reversibility of the protonation reaction was also observed in NMR experiment. The reducing agents (potassium cryptand and anthracene) and phenolate (potassium 18-crown-6- ether) sometimes made the spectra more complex, then identification of resonances became difficult. The stability of HNO complex was difficult because of disproportionation reaction which generated hydrogen.[73] The stability of HNO complexes were observed (2-3 hours) in all the experiments (Chapter 3,4 & 5) even at room temperature. The unusual stability might be come from exchange reaction and hydrogen bonds among HNO, phenols and phenolate. Low temperature ^{1}H NMR showed the loss of HNO character (decrease of resonance) at low temperature and that was reversible. This phenomenon indicated, might be Fe(II)(OEP)(NHOH) formed because of strong hydrogen bonding among phenols and phenolates. The room temperature NMR showed, the HNO complex was more free at room temperature than at low temperature. If the phenolate was bonded to the iron, the resonances for the phenolate should have been observed in the NMR.

CHAPTER 6 FTIR SPECTROELECTROCHEMISTRY

6.1 FTIR Spectroelectrochemistry of Fe(OEP)(NO)

Infrared spectroscopy can give us more detailed structural information on the redox products. Fe(OEP)(NO) has a strong nitrosyl band at 1670 cm^{-1}, which was shifted to a broad band upon reduction at 1440 cm^{-1} in THF.[75] But the region from 1350 cm^{-1} to 1380 cm^{-1} and from 1430 cm^{-1} to 1500 cm^{-1} was blocked by C-H stretching bands from THF. The use of THF-d_8 solved this problem and made the region from 1200 cm^{-1} to 1800 cm^{-1} transparent.

6.2 Fe(OEP)(NO) in THF-d_8

Thin layer FTIR spectroscopic data were collected during the electro-reduction of Fe(OEP)(NO) while the potential was being scanned from -400 mV to -1500 mV. A series of difference spectra for the reduction of Fe(OEP)(NO) was obtained between the spectrum at each potential and the initial spectrum. The positive bands were due to new bands that appeared from electrolysis or from the increase in absorbance of bands in the starting complex while negative bands represent disappearance of bands or the decrease in absorbance of Fe(OEP)(NO) bands.

In the spectral region between 1800 cm^{-1} and 1200 cm^{-1}, the band at 1670 cm^{-1} was the strongest one and was negative, because it decreased during the reduction. New bands appeared as positive bands. The bands are 1558 cm^{-1}, 1440 cm^{-1}, 1383 cm^{-1}, 1373 cm^{-1}, 1346 cm^{-1} and 1343 cm^{-1} (for ^{15}NO) indicated a new species appearing upon the addition of an electron into the compound. The band at 1440 cm^{-1} disappeared when the potential was scanned to more negative potentials. This band due to the one electron reduction product, $Fe(OEP)(NO)^-$. The IR band at 1670 cm^{-1} is due to the N-O stretching vibration which has been confirmed from literature.[75] Upon ^{15}N substitution in NO ligand the 1670 cm^{-1} band was shifted to 1640 cm^{-1}. Upon reduction of NO and ^{15}NO compound the bands at 1670 cm^{-1} and 1640 cm^{-1} were shifted to 1440 cm^{-1} and 1421 cm^{-1} respectively. The bands at 1440 cm^{-1} and 1421 cm^{-1} were from the reduction species of $Fe(OEP)(NO)^-$ and $Fe(OEP)(^{15}NO)^-$ and this is confirmed from the derivative peak (Figure 6-1). Other bands (1383 cm^{-1},1373 cm^{-1}, 1228 cm^{-1}) appeared which indicated those bands were appeared from porphyrin macrocycle. The 1346 cm^{-1} band was downshifted to 1343 cm^{-1} for $Fe(OEP)(^{15}NO)$, due to coupling of the NO vibration with macrocycle. With the re-oxidation, the band at 1670 cm^{-1} reappeared indicating the redox species was chemically stable in the FTIR spectroelectrochemical time scale (Figure 6-2).

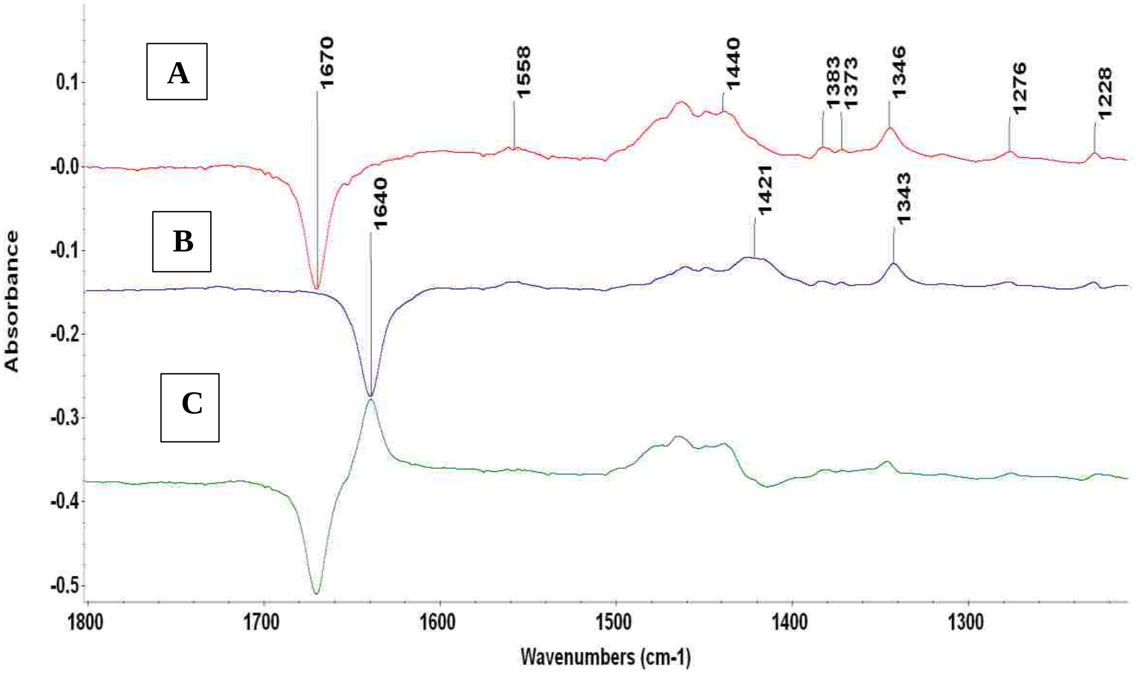

Figure 6-1. FTIR difference spectra for the reduction of A) Fe(OEP)(NO)$^-$ B) Fe(OEP)(^{15}NO)$^-$ C) difference spectrum from Fe(OEP)(^{15}NO)$^-$ - Fe(OEP)(NO)$^-$ in THF-d_8 with 0.1 M TBAP; E$_i$= -400 mV; E$_f$ = -1500 mV vs Ag wire ; scan rate = 1 mV/s; 64 scans, 2 cm^{-1} resolution.

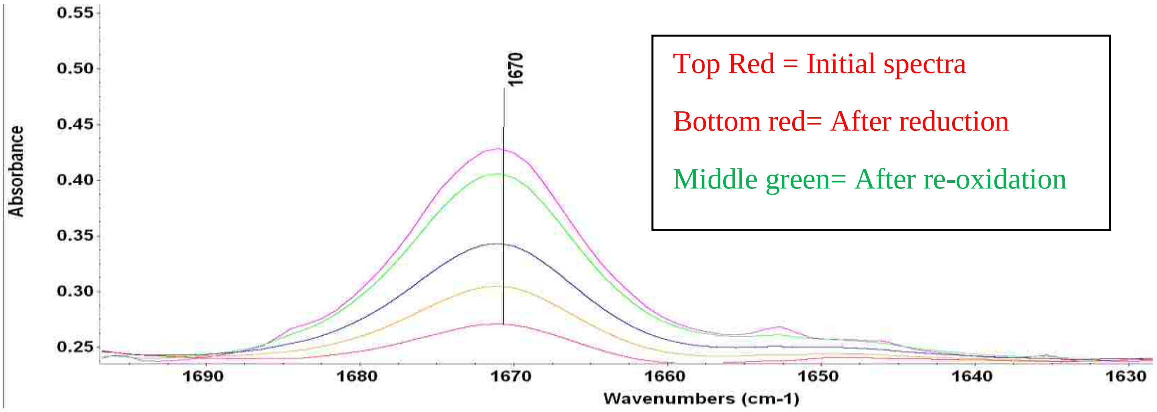

Figure 6-2. FTIR spectra for the reduction and re-oxidation of 6.0 mM Fe(OEP)(NO) in THF-d_8 with 0.1 M TBAP, E$_i$= -400 mV ; E$_f$= -1500 mV vs Ag wire ; scan rate = 1 mV/s; 64 scans, 2 cm^{-1} resolution.

6.3 Reduction of Fe(OEP)(NO) in the Presence of Phenol

In situ FTIR spectroelectrochemical measurements were carried out to investigate the reduction of Fe(OEP)(NO) in the presence of phenol and substituted phenols. Before investigating the reduction of Fe(OEP)(NO) in presence of phenol, the reduction of TBAP and phenol were performed to determine which bands were due to phenolate.

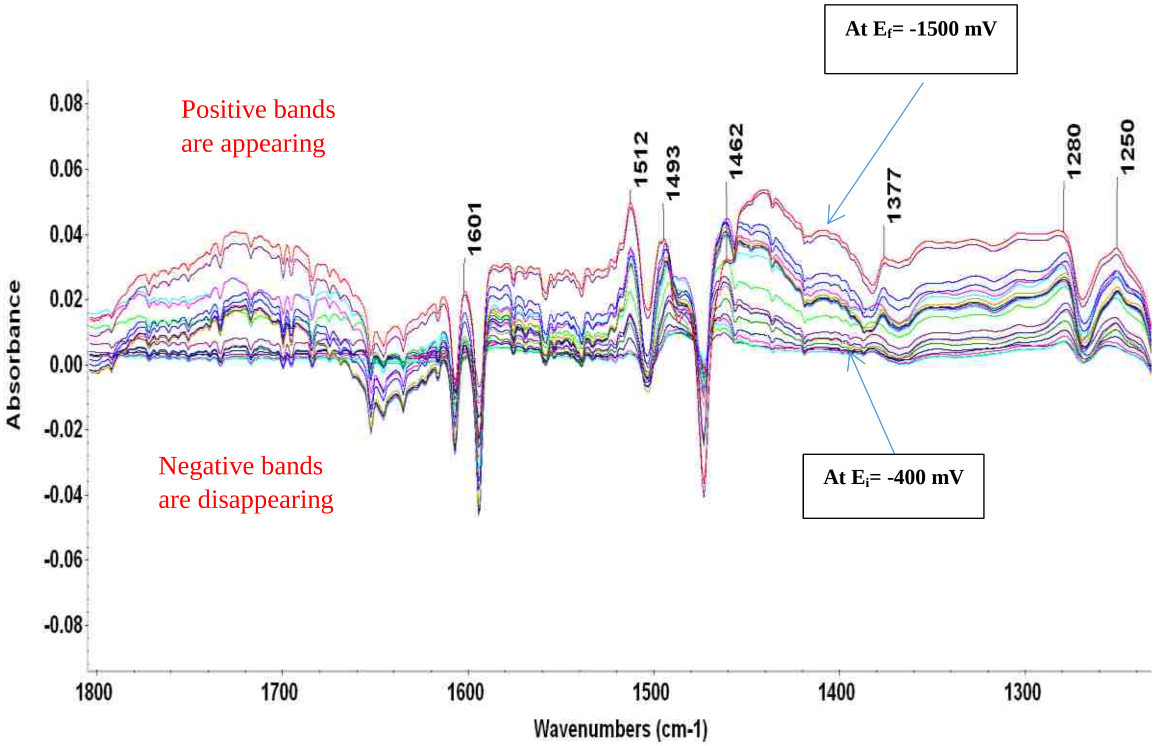

Figure 6-3. FTIR difference spectra for the reduction of 0.1 M TBAP and 4 mM of phenol in THF-d_8; E_i= -400 mV; E_f= -1500 mV vs Ag wire ; scan rate = 1 mV/s; 64 scans, 2 cm^{-1} resolution.

Figure 6-3 shows that bands at 1601 cm^{-1}, 1512 cm^{-1}, 1493 cm^{-1}, 1462 cm^{-1}, 1377 cm^{-1}, 1280 cm^{-1} and 1250 cm^{-1} appeared upon reduction and are probably due to the phenolate. The bands at 1612 cm^{-1}, 1593 cm^{-1}, 1580 cm^{-1}, 1448 cm^{-1}, 1440 cm^{-1} and 1260 cm^{-1} increased when the concentration of phenol was increased. The bands from 1377 cm^{-1} - 1607 cm^{-1} are due to aromatic C=C stretching vibration in phenol, ethyl from macrocycle and the bands from 1100 cm^{-1} to 1300 cm^{-1} might be for the O-H deformation and C-O stretching combination.

6.4 Potential Step Experiment

Initially, the potential was scanned through a long range usually from -400 mV to -1500 mV. The ^{15}N isotopomer was frequently used because the nitrosyl band at 1421 cm^{-1} was easier to observe as it avoided overlap with porphyrin bands around 1450 cm^{-1}. The spectral changes due to that electrolysis showed some peaks that appeared at the beginning of the potential sweep but those peaks disappeared as the potential became more negative (Figure 6-4). Specifically, the band at 1421 cm^{-1} [from Fe (OEP)(^{15}NO)$^{-}$] related to one electron reduction product disappeared at more negative potential. The absorbance of band at 1421 cm^{-1} increased as the potential increased but then decreased after some potential while the 1640 cm^{-1} band continued to decrease (Figure 6-5). This indicated that the one electron reduction product might be converted to a two electron or more reduced product.

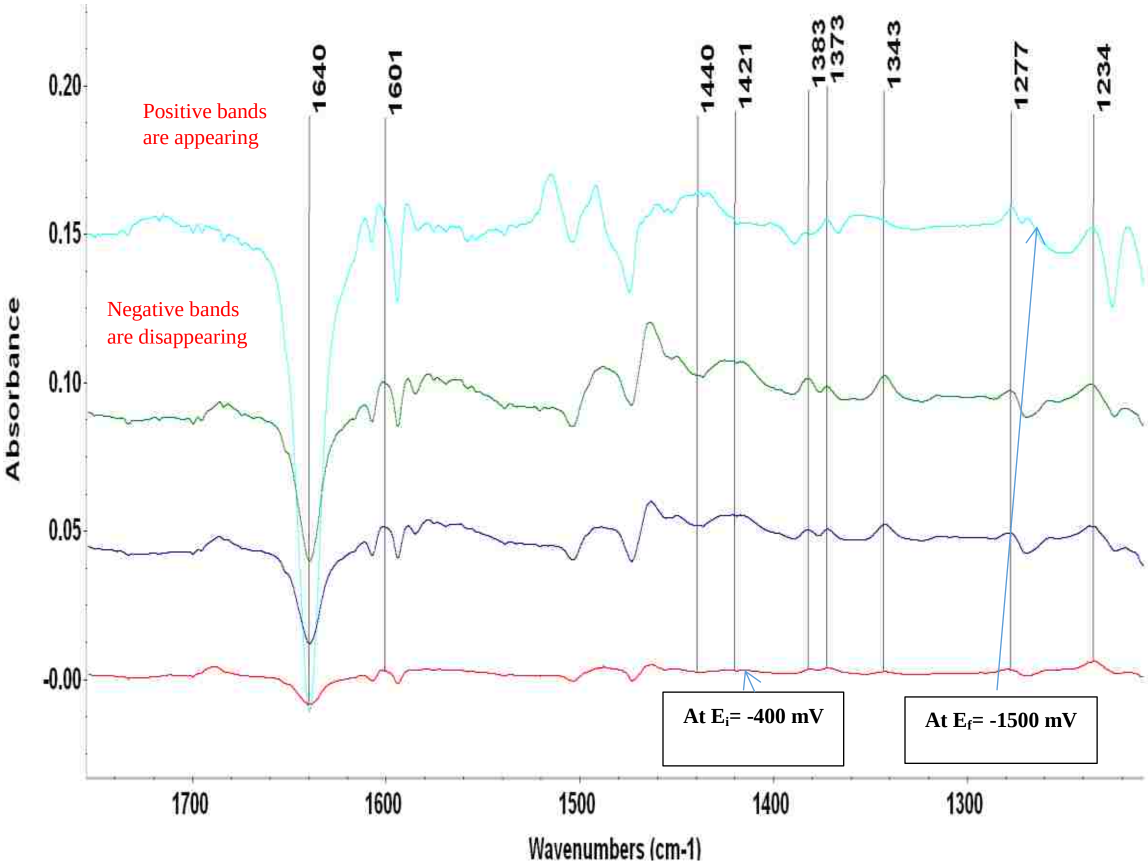

Figure 6-4. FTIR difference spectra for the reduction of Fe(OEP)(^{15}NO) in presence of 2 mM phenol in THF-d_8 with 0.1 M TBAP; E_i= -400 mV; E_f= -1500 mV Vs Ag wire; scan rate = 1 mV/s; 64 scans, 2 cm^{-1} resolution.

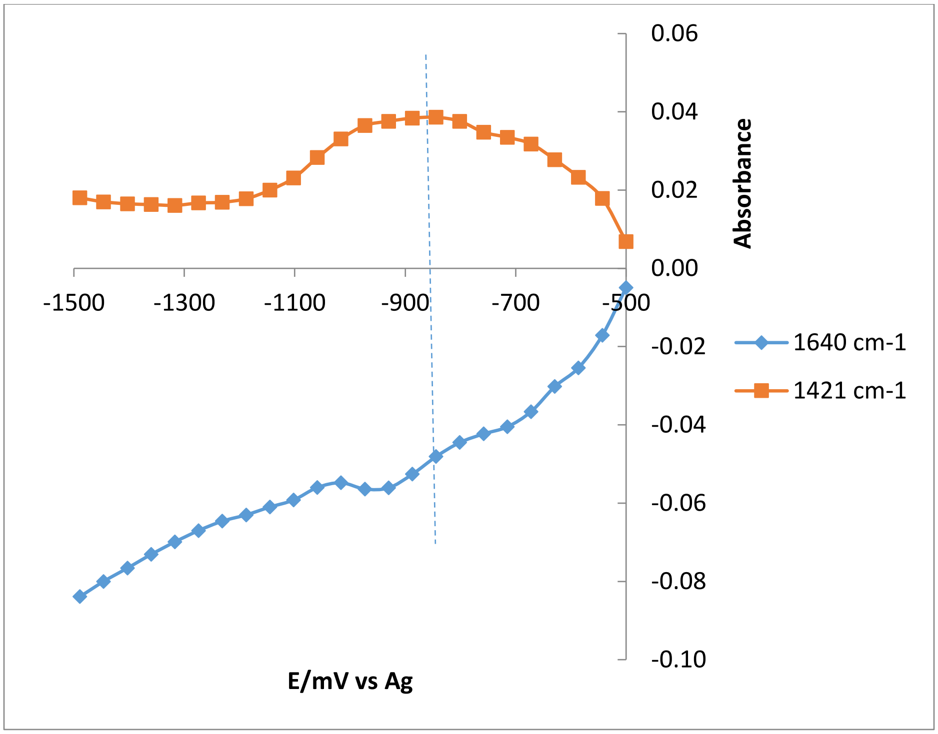

Figure 6-5. The change of absorbance at 1421 cm^{-1} for Fe(OEP)(^{15}NO), E_i= -500 mV E_f = -1500 mV, reference electrode Ag wire.

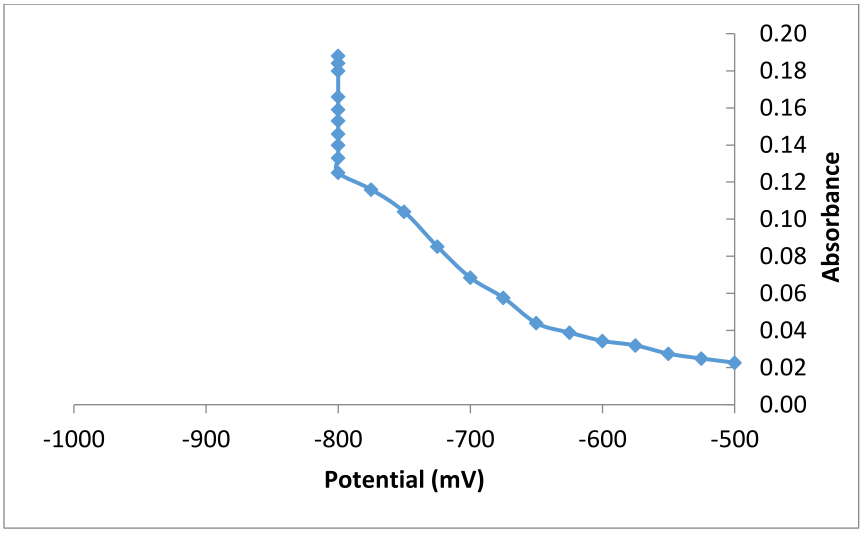

Figure 6-6. The change of absorbance at 1421 cm^{-1} for Fe(OEP)(^{15}NO), E_i= -500 mV E_f= -800 mV, reference electrode Ag wire, Hold time= 400 s.

By holding the potential at -800 mV, the absorbance for the one-electron reduction product is at the maximum (Figure 6-6). This potential was chosen for potential step because further reduction of the complex did not occur.

6.5 Phenols with Different Concentrations

Based on the previous voltammetric data, the following scheme has been proposed.[69]

$Fe(OEP)(NO) + e^- \rightarrow Fe(OEP)(NO)^-$ (6-1)

$Fe(OEP)(NO)^- + HA \rightarrow Fe(OEPP)(HNO) + A^-$ (6-2)

$Fe(OEP)(HNO) + 2e^- + 2HA \rightarrow Fe(OEP)^- + NH_2OH + 2 A^-$ (6-3)

$2Fe(OEP)(HNO) \rightarrow Fe(OEP) + N_2O + H_2O$ (6-4)

$Fe(OEP)(HNO) + HA \rightarrow Fe(OEP)(NO) + H_2 + A^-$ (6-5)

Where HA is a weak acid.

Other possible reactions can be written,

Cross reaction $Fe(OEP)(HNO) + Fe(OEP)(NO)^- \rightarrow Fe(OEP)(HNO)^- + Fe(OEP)NO$ (6-6)

In above mechanisms, Fe(OEP)(HNO) and $Fe(OEP)(NH_2OH)$ are possible intermediate, which we hoped to observe.

The FTIR spectroelectrochemistry was repeated at different concentrations. At lower concentrations of phenol (2 mM Figure 6-7, 4mM Figure 6-8), all the bands related to $Fe(OEP)(NO)^-$ were clearly visible even in the presence of phenol. In addition, 1315 cm^{-1} (from porphyrin), 1361 cm^{-1} (Ethyl wagging) and 1236 cm^{-1} (from phenolate) were observed. There was a band at 1336 cm^{-1} (for 4 mM phenol) which was not seen for other concentrations. This band might have appeared at the expense of 1346 cm^{-1}. At lower concentration of phenol, the presence of bands for $Fe(OEP)(NO)^-$ indicated that the reaction between reduced species and phenols did not occur. At higher concentrations of acid, bands at 1558 cm^{-1}, 1440 cm^{-1}, 1383 cm^{-1}, 1373 cm^{-1} and 1346 cm^{-1} were attenuated which indicated the reaction between phenols and reduced species occurred. Unfortunately, a band for H-N (in HNO) was not observed.

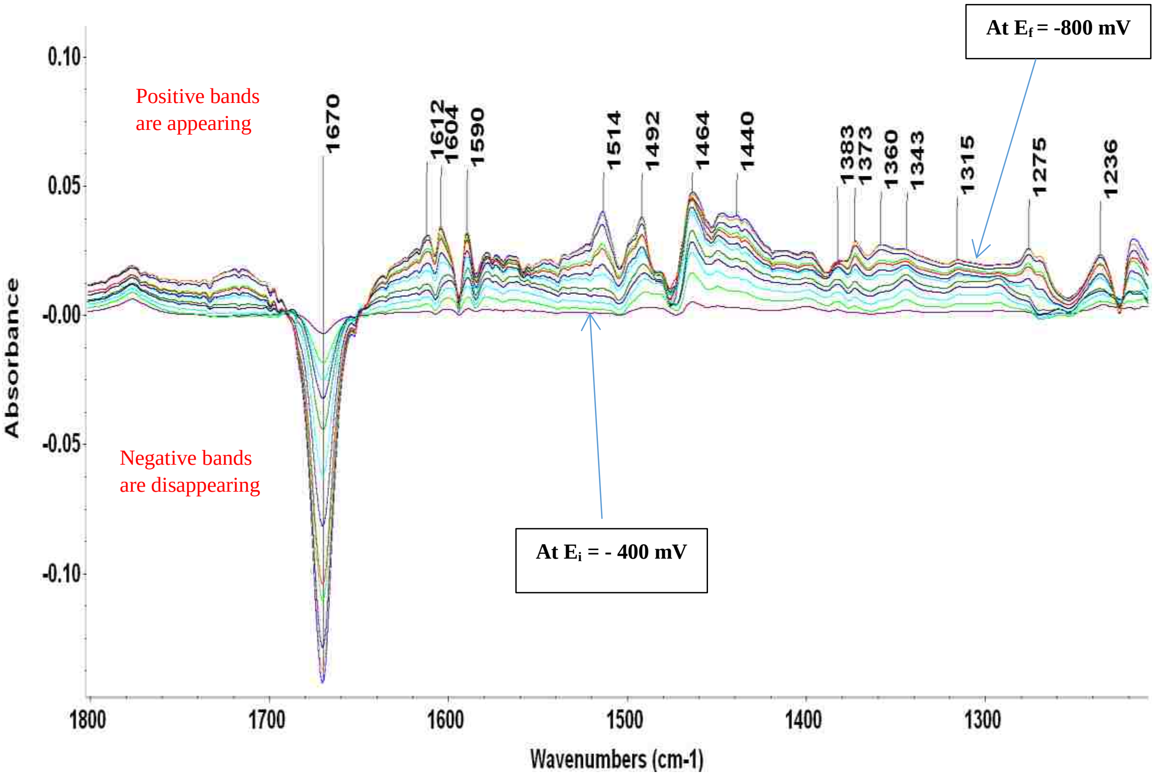

Figure 6-7. FTIR difference spectra for the reduction of 3.0 mM Fe(OEP)(NO) in presence of 2 mM phenol in THF-*d*$_8$ with 0.1 M TBAP; E_i= -400 mV ; E_f= -800 mV vs Ag wire ;hold time=400 s; scan rate = 1 mV/s; 64 scans, 2 cm^{-1} resolution.

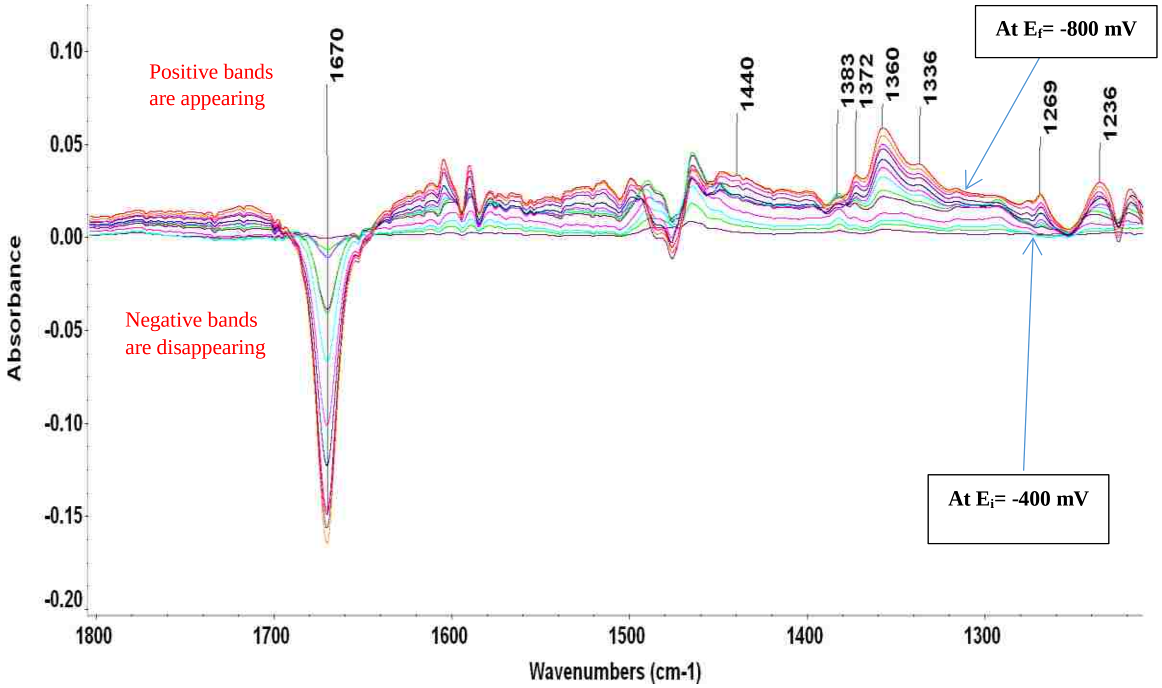

Figure 6-8. FTIR difference spectra for the reduction of 3.0 mM Fe(OEP)(NO) in presence of 4 mM phenol in THF-d_8 with 0.1 M TBAP; E_i= -400 mV; E_f= -800 mV vs Ag wire; hold time= 400 s; scan rate = 1 mV/s; 64 scans, 2 cm^{-1} resolution.

Higher concentrations of phenol were supplied to observe the vibration related to the protonated species. The FTIR spectroelectrochemical spectra for Fe(OEP)(^{15}NO) were collected (Figure 6-9 to 6-11) at different concentration, 2 mM, 4 mM, 6 mM, 8 mM, 25 mM and 30 mM (Table 6-1). The band at 1400 cm^{-1} appeared for Fe(OEP)(NO) was found as a shoulder with band at 1421 cm^{-1} from Fe(OEP)(^{15}NO)$^-$. This band did not shift upon isotopic substitution which confirmed that the band was not related to the HNO vibration. With an increase of concentration, the band at 1421 cm^{-1} and 1343 cm^{-1} became more prominent and the band at 1421 cm^{-1} became broader.

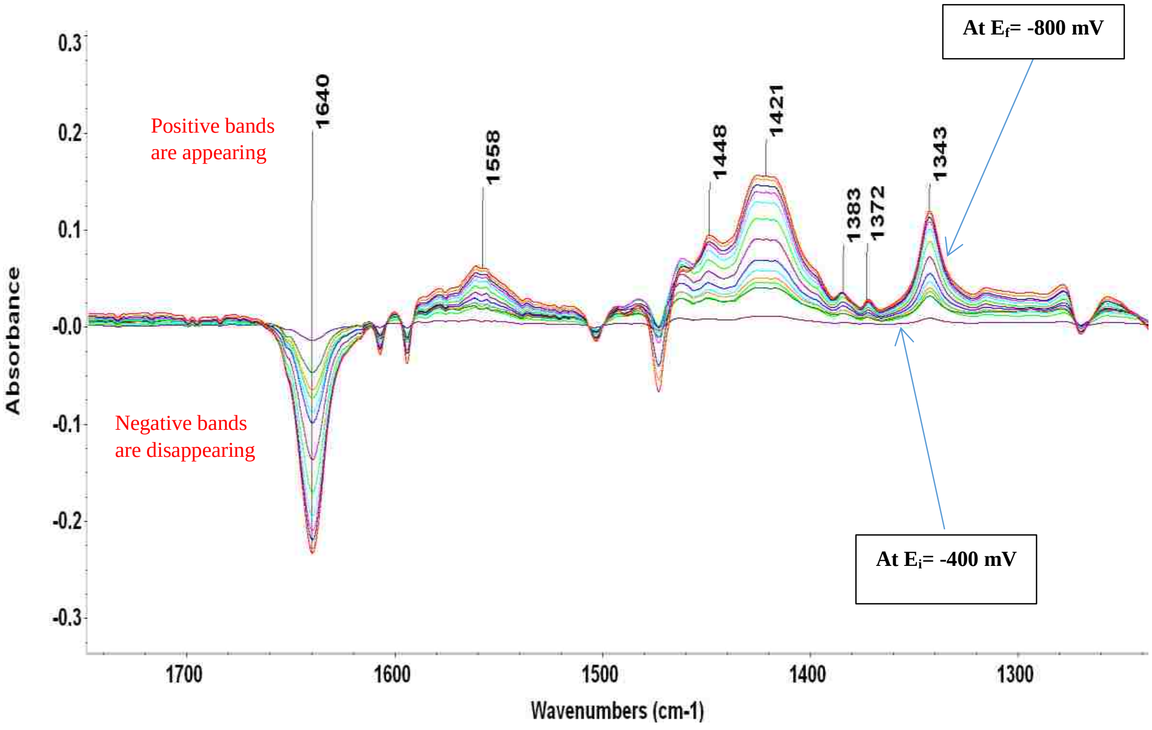

At E_f= -800 mV

Positive bands are appearing

Negative bands are disappearing

At E_i= -400 mV

Figure 6-9. FTIR difference spectra for the reduction of 5.2 mM Fe(OEP)(^{15}NO) in presence of 6 mM phenol in THF-d_8 with 0.1 M TBAP; E_i = -400 mV; E_f = -800 mV vs Ag wire; hold time= 400 s; scan rate = 1 mV/s; 64 scans, 2 cm^{-1} resolution.

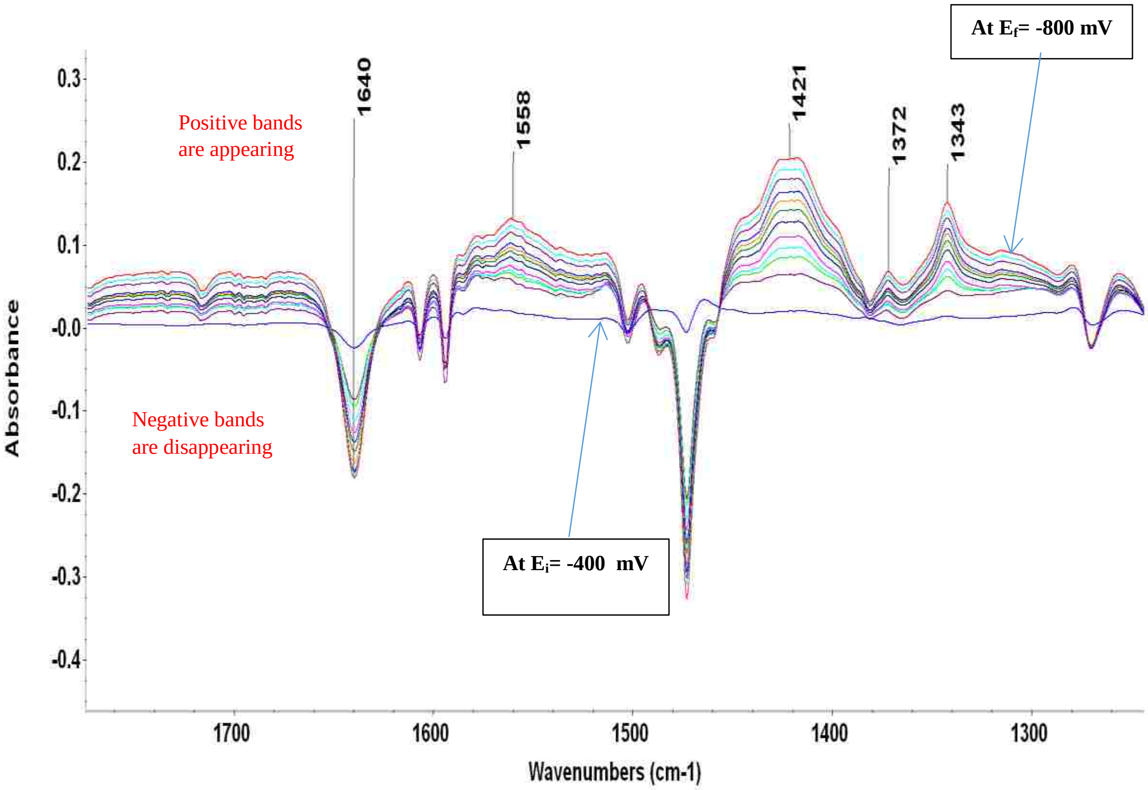

Figure 6-10. FTIR difference spectra for the reduction of 5.63 mM Fe(OEP)(^{15}NO) in presence of 25 mM phenol in THF-*d$_8$* with 0.1 M TBAP; E$_i$= -400 mV; E$_f$= -800 mV vs Ag wire; hold time= 400 s ; scan rate = 1 mV/s; 64 scans, 2 cm^{-1} resolution.

As the concentration of phenol increased (from 20 mM) the regions 1430 to 1500 cm^{-1} and 1570- 1610 cm^{-1} were dominated by phenolate bands. At 40 mM (Figure 6-11) the band at 1421 cm^{-1} and 1343 cm^{-1} were attenuated, indicating the reaction of reduced species with acids but there was no new bands observed for protonated species. All other bands from phenol and phenolate became prominent. The bands for different concentrations of phenol are recorded in Table 6-1.

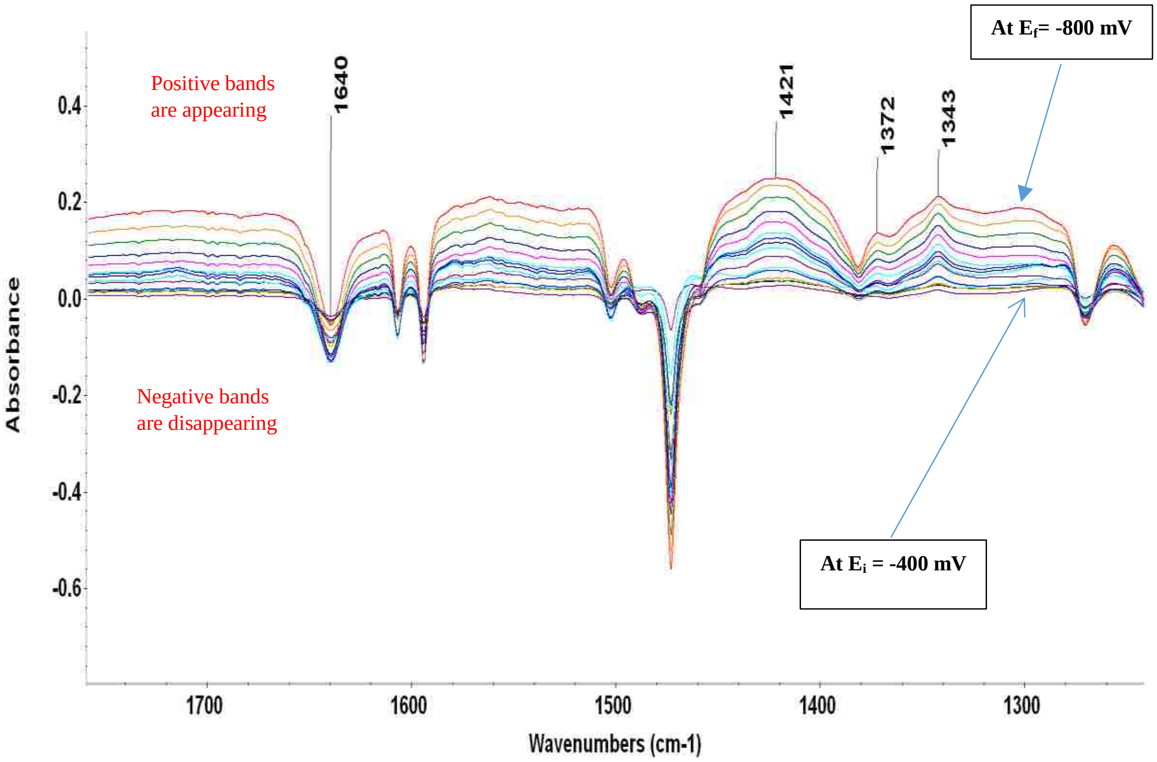

Figure 6-11. FTIR difference spectra for the reduction of 5.6 mM Fe(OEP)(^{15}NO) in presence of 40 mM phenol in THF-d_8 with 0.1 M TBAP; E_i= -400 mV; E_f= -800 mV vs Ag wire; hold time= 400 s ; scan rate = 1 mV/s; 64 scans, 2 cm^{-1} resolution.

Table 6-1. Appearance and disappearance of FTIR bands for Fe(OEP)(NO) and Fe(OEP)(^{15}NO) complexes upon electrolysis in the presence of phenols.

Compound	Disappeared bands	Appeared bands
Phenol and TBAP	1612, 1601, 1593,1580, 1512, 1493, 1462, 1448, 1440,1377, 1280, 1250	
Fe(OEP)((NO)	1670	1558,1440,1383,1373,1346,1276,1228
Fe(OEP)(NO) in 2 mM phenol	1670	1612,1604,1590,1559,1514,1493,1462,1440, 1400,1383,1373,1360,1346,1315,1275,1236, 1215
4 mM	1670	1612, 1602, 1590, 1559, 1512, 1492, 1462, 1440, 1383, 1372, 1360, 1275, 1268, 1236, 1215.
6 mM	1640	1612,1602,1590,1559,1512,1492,1462,1448, 1421,1400,1383,1372,1343,1315,1215.
Fe(OEP)(^{15}NO)	1640	1558,1421,1383,1373,1343,1228
Fe(OEP)(^{15}NO) 2 mM phenol	1640	1612,1602,1590,1558,1512,1492,1462,1448, 1421,1400,1383,1372,1343,1315,1215.
4 mM	1640	1612,1602,1590,1558,1512,1493,1480,1462, 1448,1421,1400,1383,1372,1343,1315,1260, 1230.
6 mM	1640	1612,1602,1590,1558,1512,1493,1480,1448, 1421,1400,1383,1372,1343,1315,1230
8 mM	1640	1612,1601,1558,1493,1480,1448,1421,1400, 1383,1372,1343,1315, 1275, 1260, 1230.
25 mM	1640	1612,1601,1558,1512, 1421, 1400,1372,1343,1280.
30 mM	1640	1601,1580,1558,1512,1448,1421,1400,1383, 1372,1343,1280, 1260
40 mM	1640	1601, 1558, 1493, 1421, 1372, 1343, 1258.

At high concentrations of phenol, the electrogenerated phenolate might inhibit the formation of HNO. As a result, the protonation of Fe(OEP)(NO)$^-$ was less favorable. Buffering the solution with phenolate would prevent changes in acidity during the electrolysis. But, that would have required higher concentrations of phenol, which would have dominated in the IR spectrum. During the spectroelectrochemical reduction, the band for N=O (from N_2O) was not found in the 2200- 2300 cm^{-1} (Reaction 6-4). Reaction 6-5 can be ruled out because the one electron reduction bands were present, and the Fe(OEP)(NO) was not regenerated.

Voltammetric data indicated that more than 0.1 M phenol was needed to shift the first wave. This concentration was too high to obtain reliable Fe(OEP)(HNO) spectrum. As a result, stronger acids 2-chlorophenol, 2,3-dcp, 2,6-dcp and 3,5-dcp were used.

6.6 Reduction of Fe(OEP)(NO) in the Presence of 2-Chlorophenol

In order to observe a reaction between Fe(OEP)(NO)$^-$ and acid, a stronger acid, 2-chlorophenol (2-cp) was used (pK_a = 8.5). The thin layer FTIR spectroelectrochemistry data were collected as the potential was being scanned linearly from -400 mV to -1500 mV with very slow scan rate (0.5 mv/s) in the presence of 2-chlorophenol. The difference spectra are shown in Figure 6-12. The region 1440 cm^{-1} to 1520 cm^{-1} and 1575 cm^{-1} to 1625 cm^{-1} are totally blocked because of the 2-chlorophenol C-H stretching and some bands arouse from the phenolate. The region from 1300 cm^{-1} to 1400 cm^{-1} was not usable. A band for HNO could not be identified for the system which contains 2-chlorophenol even though a reaction between 2-cp and Fe(OEP)(NO)$^-$ was reported.[72]

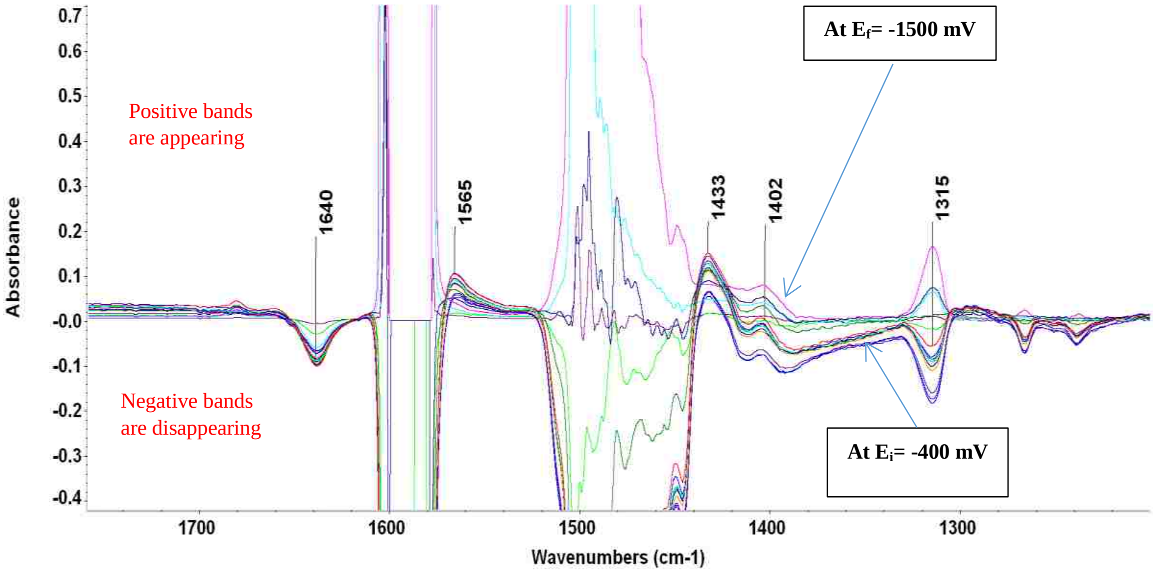

Figure 6-12. FTIR difference spectra for the reduction of 2.5 mM Fe(OEP)(^{15}NO) in presence of 4 mM 2- chlorophenol in THF-d_8 with 0.1 M TBAP; E_i= -400 mV; E_f = -1500 mV vs Ag wire ; scan rate = 1 mV/s; 64 scans, 2 cm^{-1} resolution.

6.7 Reduction of Fe(OEP)(NO) in the Presence of 2,6-Dichlorophenol

From the literature,[72] it was known that 2,6-dcp was involved in single protonation step and it was also a stronger acid than 2-cp and phenol. The FTIR spectroelectrochemistry experiments carried out with 2,6-dcp.

The IR spectroelectrochemical spectra were taken for 4 mM 2,6-dcp and 0.1 M TBAP in the absence of Fe(OEP)(NO). The potential range was -400 mV to -1000 mV. The difference spectra are shown (Figure 6-13).

The bands at 1568 cm^{-1}, 1501 cm^{-1}, 1454 cm^{-1}, 1433 cm^{-1}, 1263 cm^{-1} and 1228 cm^{-1} were generated because of 2,6-dcp reduction. At higher concentrations, the band at 1300 cm^{-1} and 1383 cm^{-1} were observed. There are peaks from 1600 cm^{-1} – 1300 cm^{-1} due to aromatic C=C and ethyl vibration for different modes and the band at 1263 cm^{-1} might be from C-O stretching vibration. FTIR spectroelectrochemical investigation with the same potential range was carried out in the presence of various concentrations (Figure 6-14, 6-15) of 2,6-dcp with Fe(OEP)(NO). The bands are given in Table 6-2. The bands for one electron reduction species were observed as 1558 cm^{-1}, 1440 cm^{-1}, 1383 cm^{-1} and 1346 cm^{-1}. A band at 1400 cm^{-1} appeared which was also seen in the phenolic system might be generated from reduction of 2,6-dcp. The band at 1434 cm^{-1} become prominent upon the increase of concentration of substituted phenols. The band for reduce species Fe(OEP)(NO)$^{-}$ at 1440 cm^{-1} was masked by phenol band but the band at 1346 cm^{-1} still present indicating that the concentration was not sufficient to react with all the reduced species.

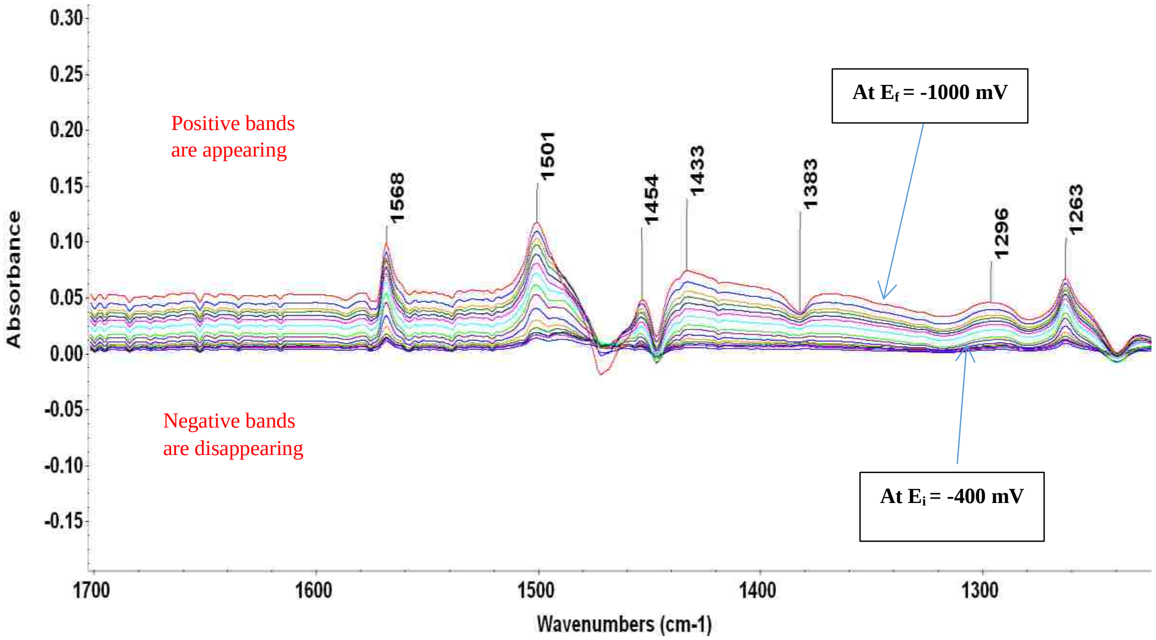

Figure 6-13. FTIR difference spectra for the reduction of 0.1 M TBAP and 4 mM 2,6-dcp E_i= -400 mV; E_f= -1000 mV vs Ag wire; scan rate = 1 mV/s; 64 scans, 2 cm^{-1} resolution.

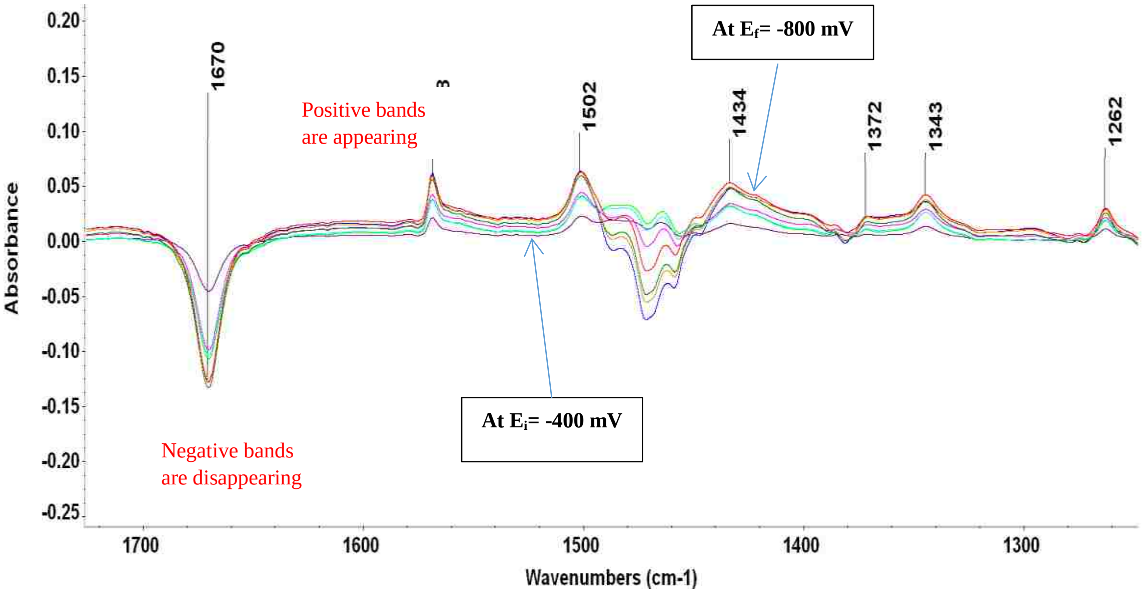

Figure 6-14. FTIR difference spectra for the reduction of 2.8 mM Fe(OEP)(NO) in presence of 2 mM 2,6-dcp in THF-d_8 with 0.1 M TBAP; E_i= -400 mV; E_f = -800 mV vs Ag wire; hold time= 400 s; scan rate = 1 mV/s; 64 scans, 2 cm^{-1} resolution.

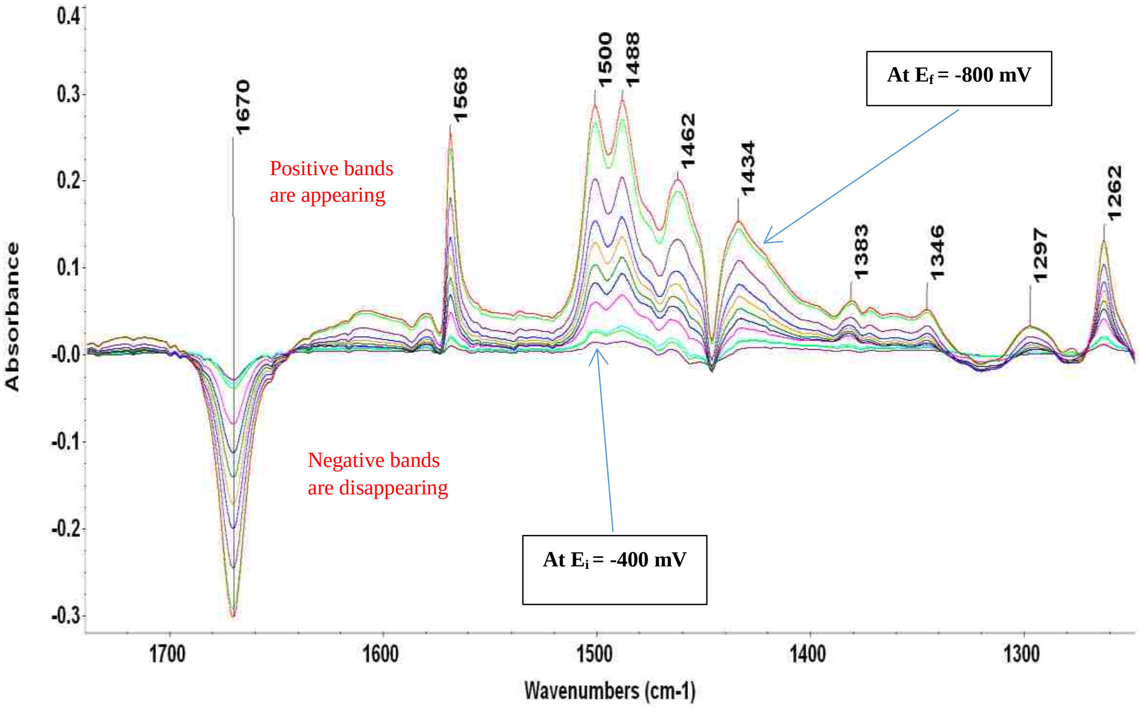

Figure 6-15. FTIR difference spectra for the reduction of 4.5 mM Fe(OEP)(NO) in presence of 6 mM 2,6-dcp in THF-*d₈* with 0.1 M TBAP; E$_i$= -400 mV; E$_f$= -800 mV vs Ag wire; hold time= 400 s ; scan rate = 1 mV/s; 64 scans, 2 cm^{-1} resolution.

The isotope substituted complex gave a clear band at 1421 cm^{-1} at low concentrations of 2,6-dcp (Figure 6-16). But at higher concentrations, the band from 2,6-dcp became dominant and the reduced species band (1421 cm^{-1}) was totally gone (Figure 6-17) indicating again a complete reaction with acids. The region from 1365-1390 cm^{-1} became obscure as the concentration of 2,6-dcp increased which was the region where we expected to see the N-O vibration (from HNO). This limited our ability to use higher concentrations. The reaction with 2,6-dcp was expected according to literature.[72] The bands for different concentrations of 2,6-dcp are shown in Table 6-2.

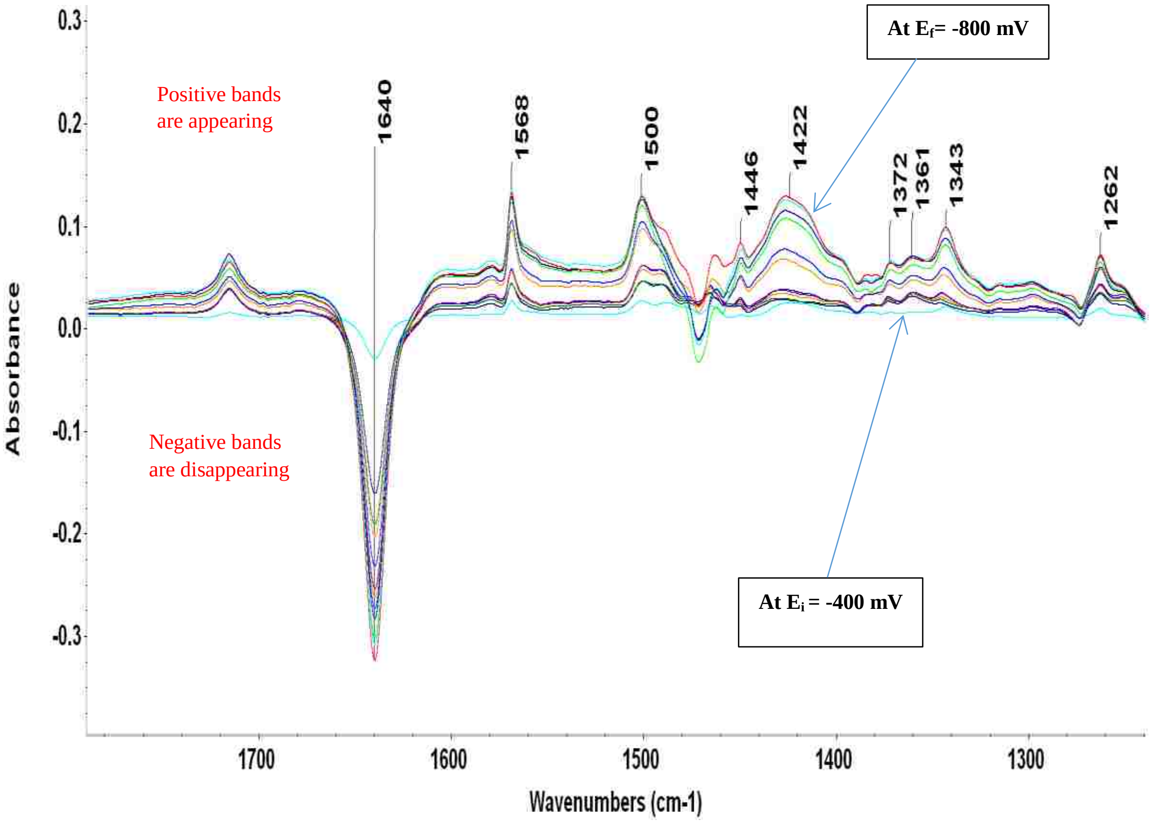

Figure 6-16. FTIR difference spectra for the reduction of 4.6 mM Fe(OEP)(^{15}NO) in presence of 2 mM 2,6- dcp in THF-*d_8* with 0.1 M TBAP; E_i= -400 mV; E_f= -800 mV vs Ag wire; hold time= 400 s; scan rate = 1 mV/s; 64 scans, 2 cm^{-1} resolution.

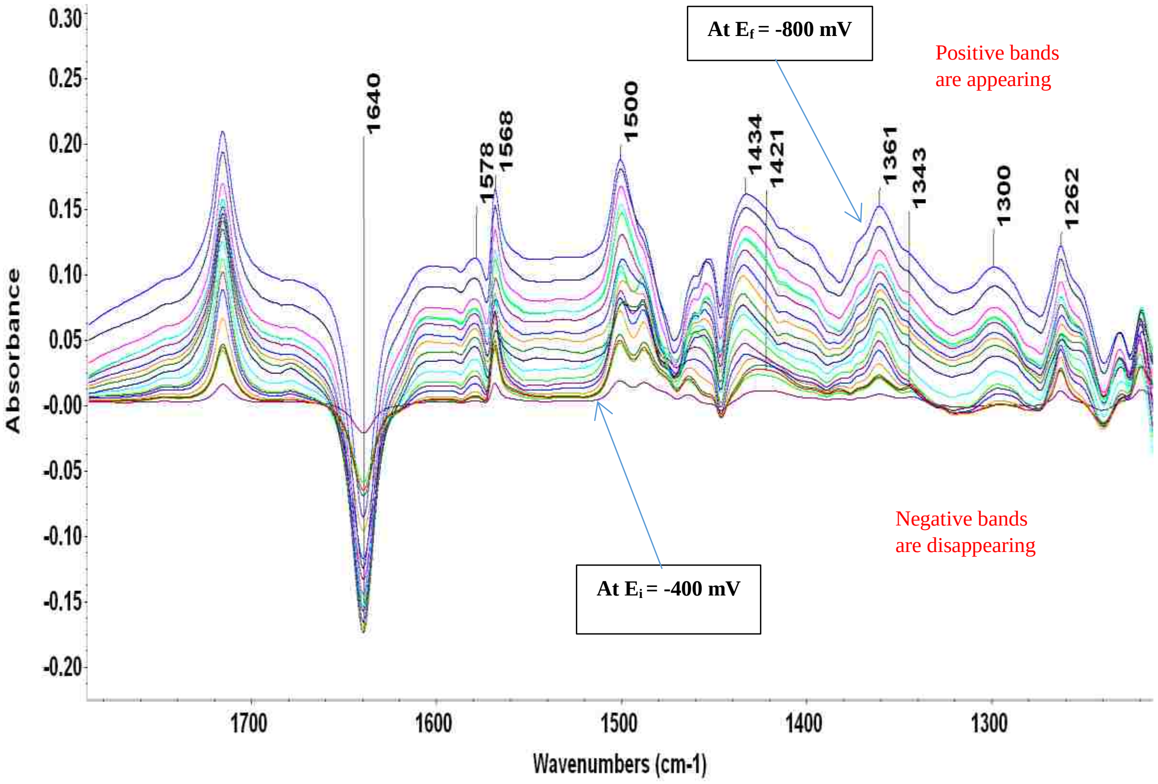

Figure 6-17. FTIR difference spectra for the reduction of 2.8 mM Fe(OEP)(^{15}NO) in presence of 6 mM 2,6- dcp in THF-d_8 with 0.1 M TBAP; E_i= -400 mV ; E_f= -800 mV vs Ag wire ; hold time= 400 s ; scan rate = 1 mV/s; 64 scans, 2 cm^{-1} resolution.

Table 6-2. Appearance and disappearance of FTIR bands for Fe(OEP)(NO) and Fe(OEP)(^{15}NO) complexes upon electrolysis in the presence of 2,6-dcp.

Compound	**Disappeared bands**	**Appeared bands**
2,6-dcp and TBAP		1568, 1501, 1454, 1433, 1296, 1263, 1228
Fe(OEP)(NO)	1670	1558,1440,1383,1373,1346,1276,1228
Fe(OEP)(NO) in 2 mM	1670	1568, 1559, 1502, 1434, 1372, 1343, 1262
4 mM 2,6-dcp	1670	1568, 1500, 1440, 1343, 1262
6 mM 2,6-dcp	1670	1568, 1500, 1462, 1453, 1434, 1383, 1372, 1346, 1297, 1262
Fe(OEP)(^{15}NO)	1640	1558,1421,1383,1373,1343,1228
Fe(OEP)(^{15}NO) in 2 mM 2,6-dcp	1640	1568, 1500, 1462, 1446, 1422, 1372, 1361, 1343, 1262
4 mM 2,6-dcp	1640	1568, 1500, 1434, 1421, 1372, 1343, 1300,1262
6 mM 2,6-dcp	1640	1578, 1568, 1500, 1434, 1421, 1361, 1343, 1300, 1262

As Liu et. al already mentioned earlier, the acid concentration that was used for FTIR spectroelectrochemistry experiment was based on the strength of acids (pK_a values).[75] As we know from the voltammetric data that the potential shifted with the addition of acids related to the extent of the reaction of reduced species with acids. And the acid concentration which was related to 59 mV shift could be considered as at that concentration (roughly) the single protonated species would be prominent according to Nernst equation for the system even though Nernst equation was not applicable for our system. Taking the optimal condition from RRDE data, cyclic FTIR spectroelectrochemical experiments were carried out for different acids (2,3-dcp, 3,5-dcp). The spectra (Figure 6-18) showed the complete reduction of species with complete reaction with acids. No band for Fe(OEP)(HNO) was observed in the region from 1450 to 1200 cm^{-1} and no isotope sensitive bands were observed within the region. Only weak bands due to the porphyrin vibration were observed. Re-oxidation of Fe(OEP)(HNO) to Fe(OEP)(NO) was observed in the FTIR spectroelectrochemistry experiments.

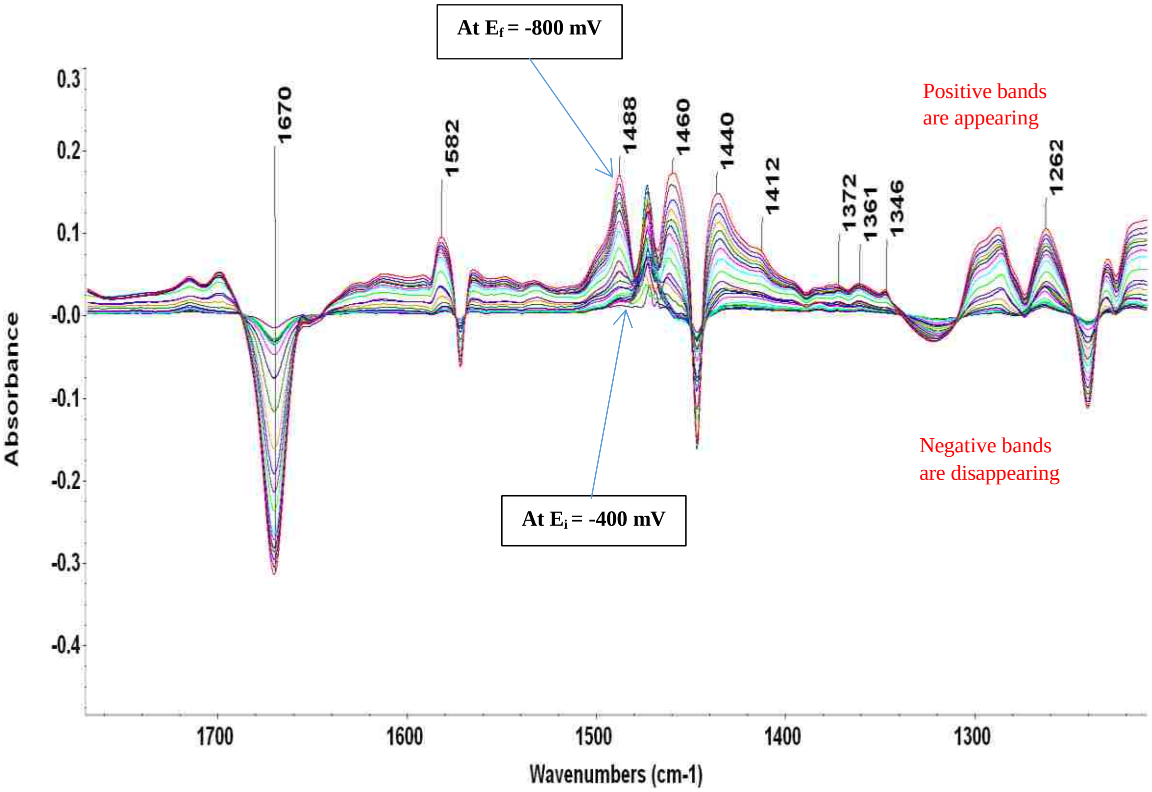

Figure 6-18. FTIR difference spectra for the reduction of 5.0 mM Fe(OEP)(NO) in presence of 10 mM 2,6-dcp in THF-d_8 with 0.1 M TBAP; E_i= -400 mV ; E_f= -800 mV vs Ag wire ; hold time= 400 s ; scan rate = 1 mV/s; 64 scans, 2 cm^{-1} resolution.

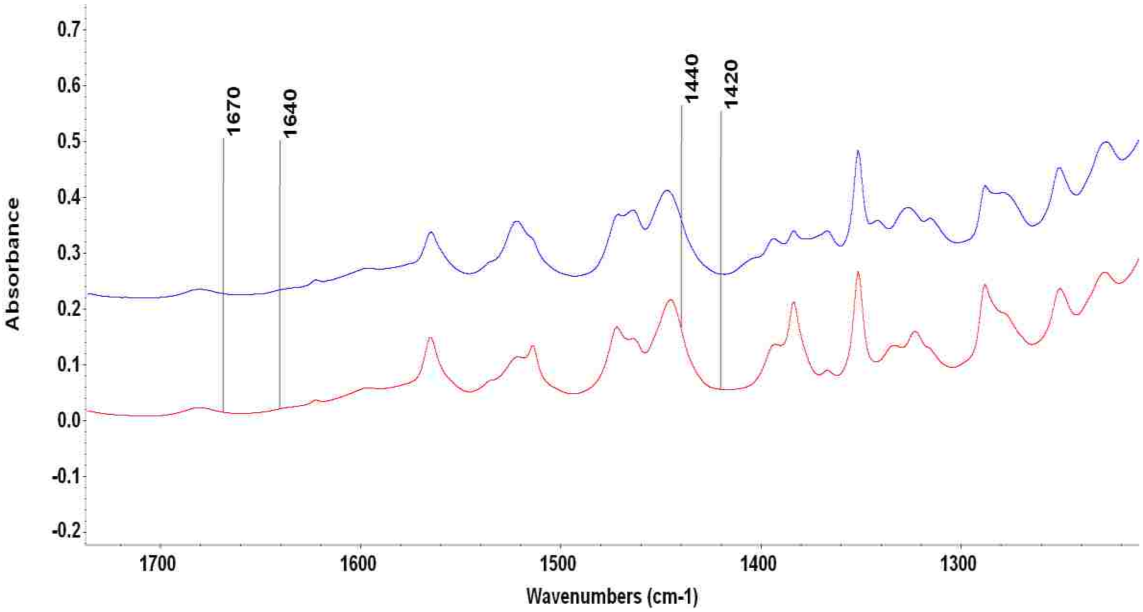

Figure 6-19. FTIR spectra of Fe(OEP)(HNO) generated from the reaction of $Fe(OEP)(NO)^-$ (Bottom) and $Fe(OEP)(^{15}NO)^-$ (Top) with 2,3-dcp.

In order to confirm the spectroelectrochemical data, FTIR spectra of $Fe(OEP)(NO)^-$ and $Fe(OEP)(^{15}NO)^-$ with higher concentration of acid (50 mM 2,6-dcp) was taken (Figure 6-19). The band for NO^- in both cases were disappeared indicating the reaction occurred. The spectra for Fe(OEP)(HNO) were quite similar to the spectra obtained from spectroelectrochemistry. No isotopically shifted bands were observed.

Attempts were also made to observe vibration for NH in 3000- 3500 cm^{-1} region. There was no new vibration was seen for NH. Another experiment with 3,5-dcp-d_4 was also carried out to see the ND vibration. No new isotope sensitive band was observed. DFT calculations for Fe(OEP)(HNO) showed that a HNO band in that region would be weak and would overlap with other vibrations.

Previous studies on Fe(OEP)(HNO) and related complexes have involved six coordinated species.[86-88,93] Farmer et al. observed a NO vibration for Mb-HNO at 1385 cm^{-1} using resonance Raman spectroscopy,[87] Abucayon et al.[93] observed a band at 1383 cm^{-1} in IR which they considered as due to HNO. In our work, we did not observe similar bands in either the chemical or electrochemical experiments. This might due to the difference in coordination number (6 versus 5). The DFT calculation done our group for Fe(OEP)(HNO) showed that the 5- coordinated HNO yielded NO vibration upshifted from the six coordinated complexes. The comparison of 5-coordinated complex with 6-coordinated complex was difficult. As a result, the HNO band for Fe(OEP)(HNO) may be in the congested region between 1450-1500 cm^{-1} where there are other phenolate and porphyrin bands. It is also possible that this Fe(OEP)(HNO) complex was six coordinated with THF as a ligand.

To see the multi-electron reduced species, Fe(OEP)(NH_2OH) the FTIR spectroelectrochemistry was carried out by scanning to more negative potential than the first electron reduction potential. The spectra (Figure 6-20) showed a broad band with two peak at 3566 and 3500 cm^{-1}, which indicated the Fe(OEP)(NH_2OH) was generated at more negative potential. No such band was observed when the potential scanned from 0.0 V to -800 mV. The same experiment was carried out with 2,3-dcp which showed the same bands in the higher wave number region. (Figure 6-21)

To verify the ND_2OD band, FTIR spectroelectrochemistry with 2,3-dcp-d_1 was carried out. A new broad band with two peaks was observed at 2688 and 2654 cm^{-1} (Figure 6-22). This band was absent for normal abundance acids. For 2,3-dcp-d_1 acid, there were no band at 3500 to 3700 cm^{-1} regions. For Fe(OEP)(^{15}NO) with 2,3-dcp-d_1, the band at

2688 cm^{-1} shifted little to 2685 cm^{-1} and the band 2654 cm^{-1} shifted to 2650 cm^{-1} (Figure 6-23).

To confirm the NH_2OH band, Co(III)(OEP)$(NH_2OH)_2^+$ was synthesized chemically (Figure 6-24) This compound showed bands at 3683 and 3621 cm^{-1}. The difference in wavenumbers might be due to the cobalt and for the formation of bis complex.

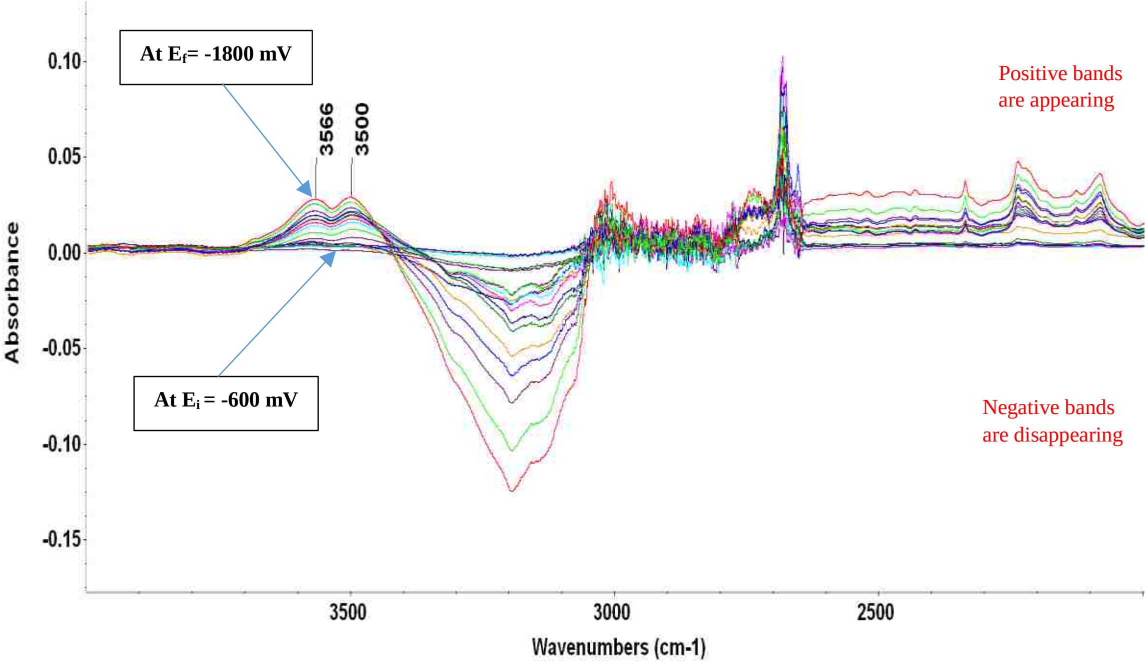

Figure 6-20. FTIR difference spectra for the reduction of 3.0 mM Fe(OEP)(NO) in presence of 10 mM 2,6-dcp in THF-d_8 with 0.1 M TBAP; E_i= -600 mV; E_f= -1800 mV vs Ag wire; scan rate = 1 mV/s; 64 scans, 2 cm^{-1} resolution.

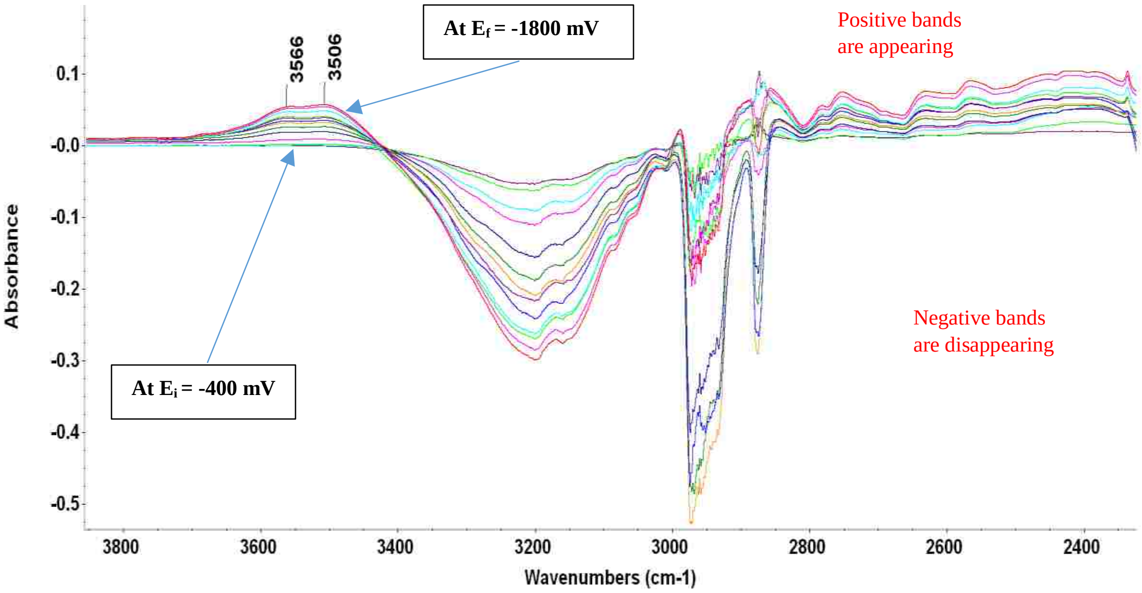

Figure 6-21. FTIR difference spectra for the reduction of 4.5 mM Fe(OEP)(NO) in presence of 10 mM 2,3-dcp in THF-d_8 with 0.1 M TBAP; E_i= -400 mV ; E_f= -1800 mV vs Ag wire; scan rate = 1 mV/s; 64 scans, 2 cm^{-1} resolution.

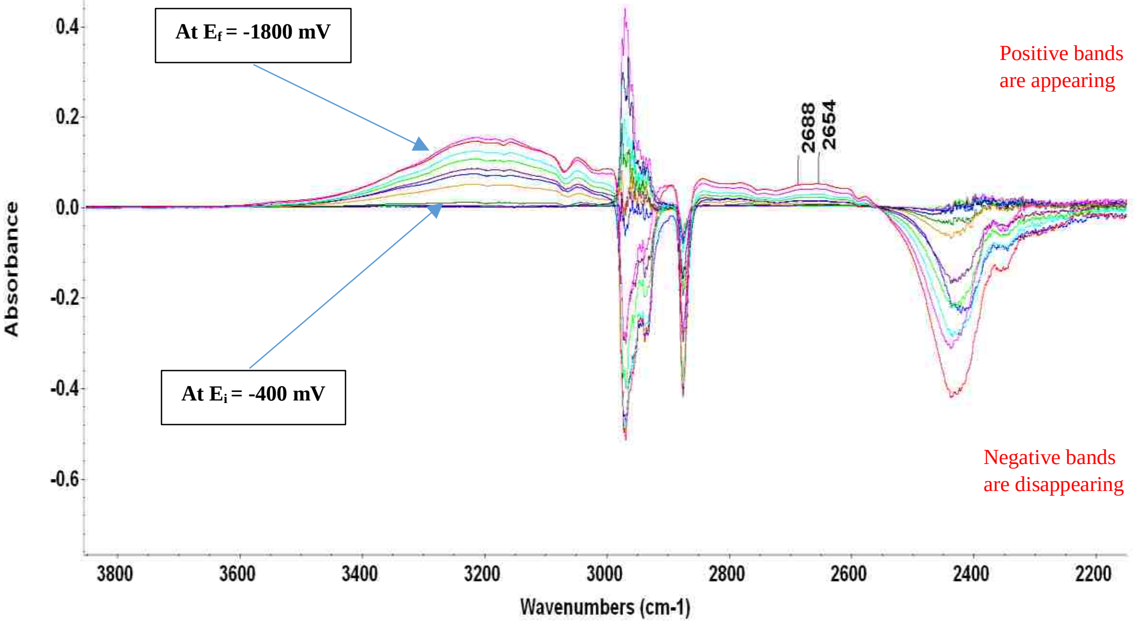

Figure 6-22. FTIR difference spectra for the reduction of 4.6 mM Fe(OEP)(NO) in presence of 10 mM 2,3-dcp-d_1 in THF-d_8 with 0.1 M TBAP; E_i= -400 mV ; E_f= -1800 mV vs Ag wire ; scan rate = 1 mV/s; 64 scans, 2 cm^{-1} resolution.

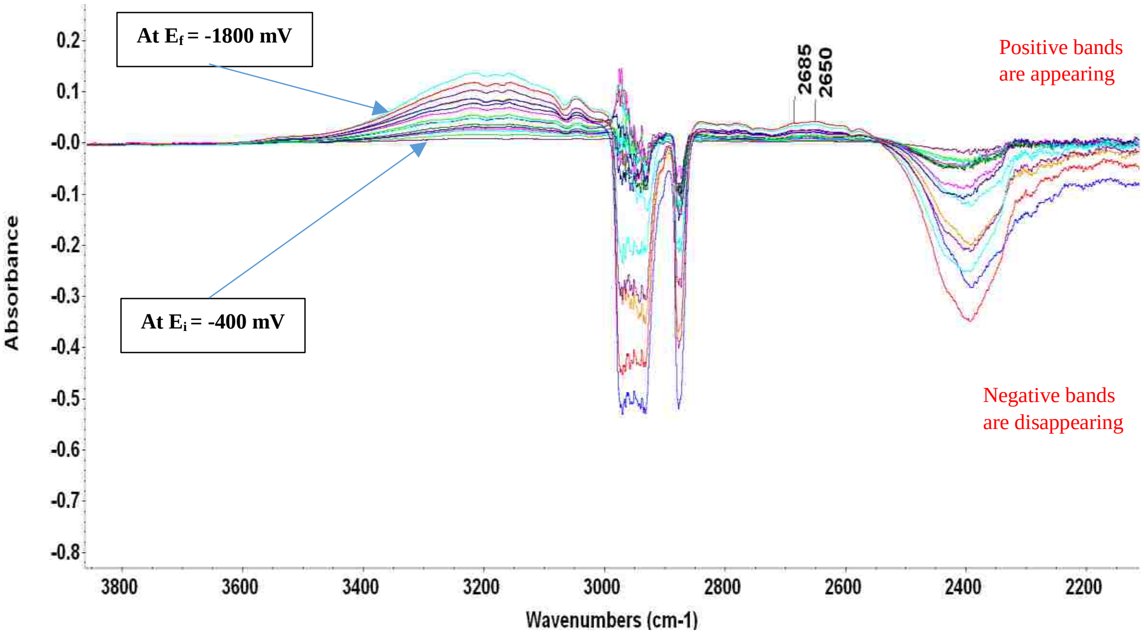

Figure 6-23. FTIR difference spectra for the reduction of 4.8 mM Fe(OEP)(^{15}NO) in presence of 10 mM 2,3-dcp-d_1 in THF-d_8 with 0.1 M TBAP; E_i= -400 mV ; E_f= -1800 mV vs Ag wire; scan rate = 1 mV/s; 64 scans, 2 cm^{-1} resolution.

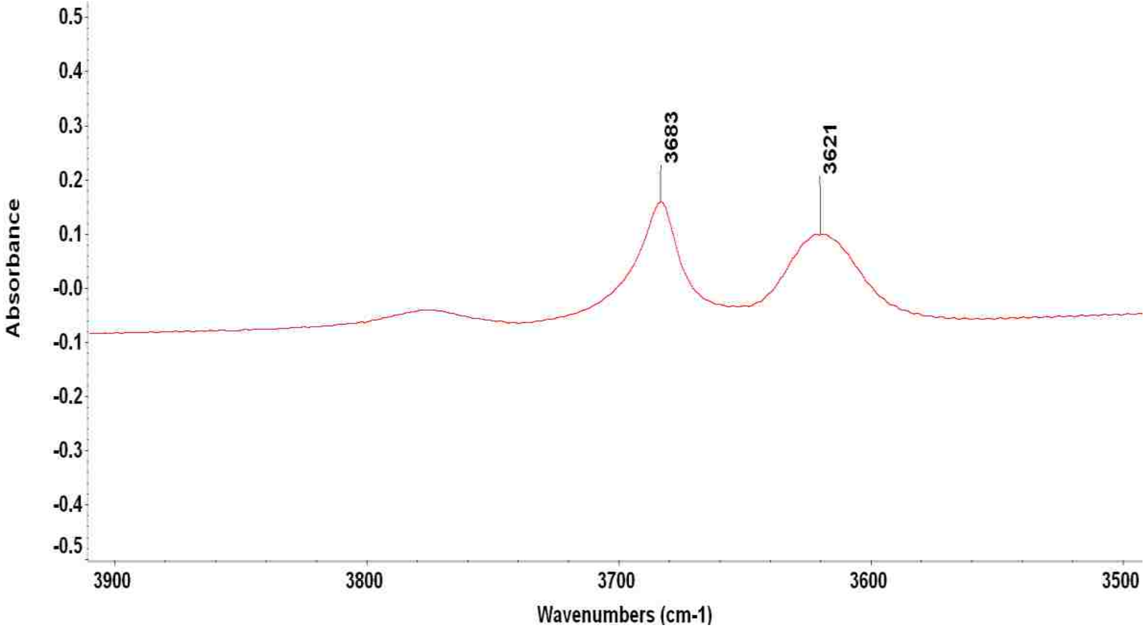

Figure 6-24. FTIR spectrum of Co(III)(OEP)(NH_2OH)$_2^+$ in $CHCl_3$ at room temperature.

6.8 *In Situ* FTIR Spectroelectrochemistry of Fe(OEPone)(NO)

The FTIR spectrum (in KBr) of Fe(OEPone)(NO) contained a strong band at 1715 cm^{-1} and 1679 cm^{-1} . The former one for carbonyl vibration and the later one for nitrosyl vibration. The bands were consistent to the literature.[75] The nitrosyl band shifted to 1640 cm^{-1} upon isotopic (^{15}N) substitution (Figure 6-25). There was a new band observed at 1658 cm^{-1} in THF. Upon isotopic substitution, the band shifted to 1628 cm^{-1} (Figure 6-26). This shift indicated that the band was related to the nitrosyl moiety. This band might be due to solvent ligation to the iron center of Fe(OEPone)(NO). To verify the solvent interaction, the FTIR spectrum was taken in dichloromethane. The spectra showed one band at 1680 cm^{-1} which was shifted to 1650 cm^{-1} upon isotopic substitution (Figure 6-26). The additional 1658 cm^{-1} and 1628 cm^{-1} for Fe(OEPone)(NO) and Fe(OEPone)(^{15}NO) observed for THF ligation. The downshift of nitrosyl band was observed upon six coordination by Betro et al. [109] In THF, two types of Fe(OEPone)(NO) may be present, one was ligated to THF and other was not. The reason was unknown why all Fe(OEPone)(NO) were not ligated. The ligation might be the reason for observing some Fe(OEPone)$^-$ (nitrosyl dissociates) upon electrolysis. Because of the six coordination, strong trans effect for nitrosyl moiety was lost which resulted the weakening (back donation from Fe to N decrease) of Fe-N(NO) and N-O bands and accelerated the Fe-N(NO) bond break.

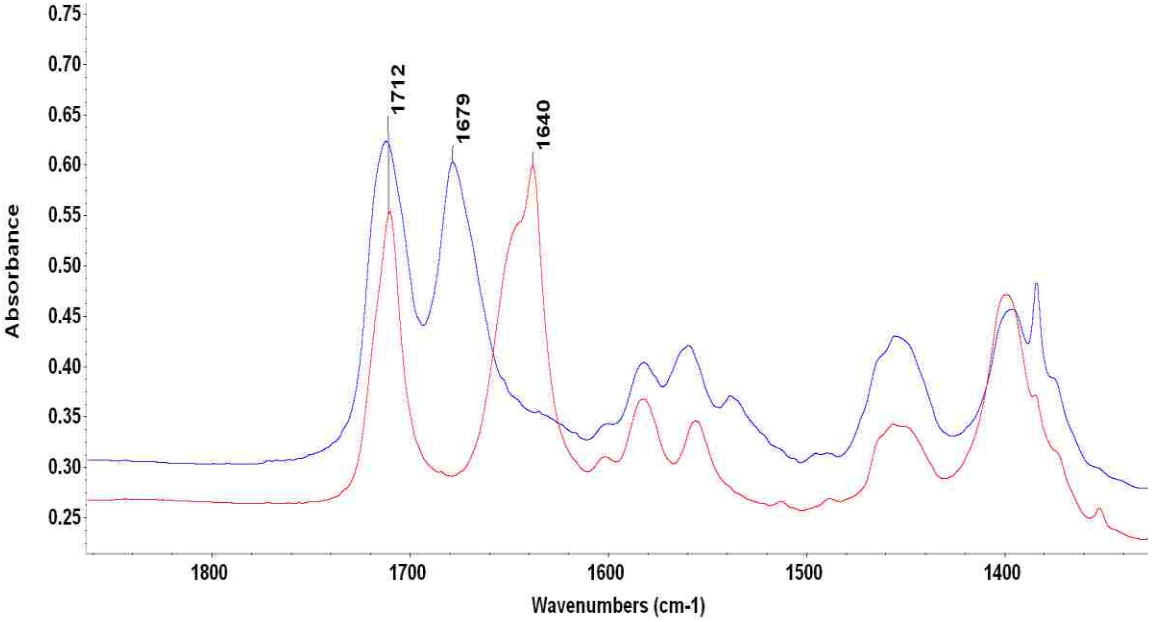

Figure 6-25. Fe(OEPone)(NO) (Blue) and Fe(OEPone)(^{15}NO) (Red) in KBr matrix.

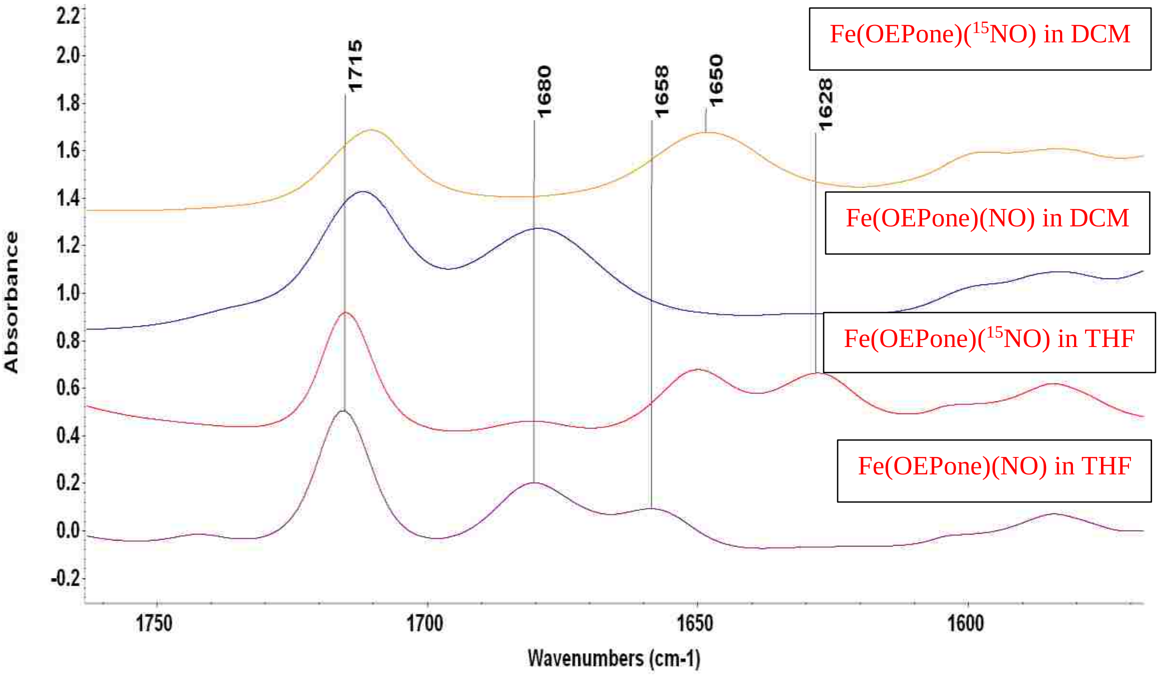

Figure 6-26. Fe(OEPone)(NO) and Fe(OEPone)(^{15}NO) in THF-d_8 and DCM.

Thin layer FTIR spectroelectrochemical data were collected during the reduction and the result was shown in Figure 6-27. A series of bands disappeared and appeared upon reduction at a more negative potential. The bands at 1715 cm^{-1} (for C=O vibration), 1682 cm^{-1} and 1658 cm^{-1} (N-O vibration) disappeared at the same time that the bands at 1702,1670, 1558, 1521, 1466, 1457, 1447, 1440,1380, 1362, 1335, 1298, 1266,1244 and 1219 cm^{-1} appeared . The bands for NO and CO reappeared upon re-oxidation. The band at 1440 cm^{-1} is for the reduced N-O stretching vibration. Several new bands may occur because of coupling of various ring modes.

The spectra for Fe(OEPone)(^{15}NO), the bands at 1682 and 1658 cm^{-1} for Fe(OEPone)(NO) shifted to 1650 and 1629 cm^{-1} (Figure 6-27). The shift for ^{15}NO band from NO band was almost same the shift from 1682 cm^{-1} to 1650 cm^{-1}. Upon the electrolysis, those three bands disappeared. The bands at 1702, 1574, 1548, 1436, 1421, 1389, 1363, 1335, 1317, 1261 and 1243 cm^{-1} appeared. There was no band at 1440 cm^{-1} and a band at 1421 cm^{-1} from ^{15}NO^{-} vibration. The other bands should be similar theoretically but there was some deviation observed for Fe(OEPone)(^{15}NO). This discrepancy might be due to coupling among various vibrational modes.

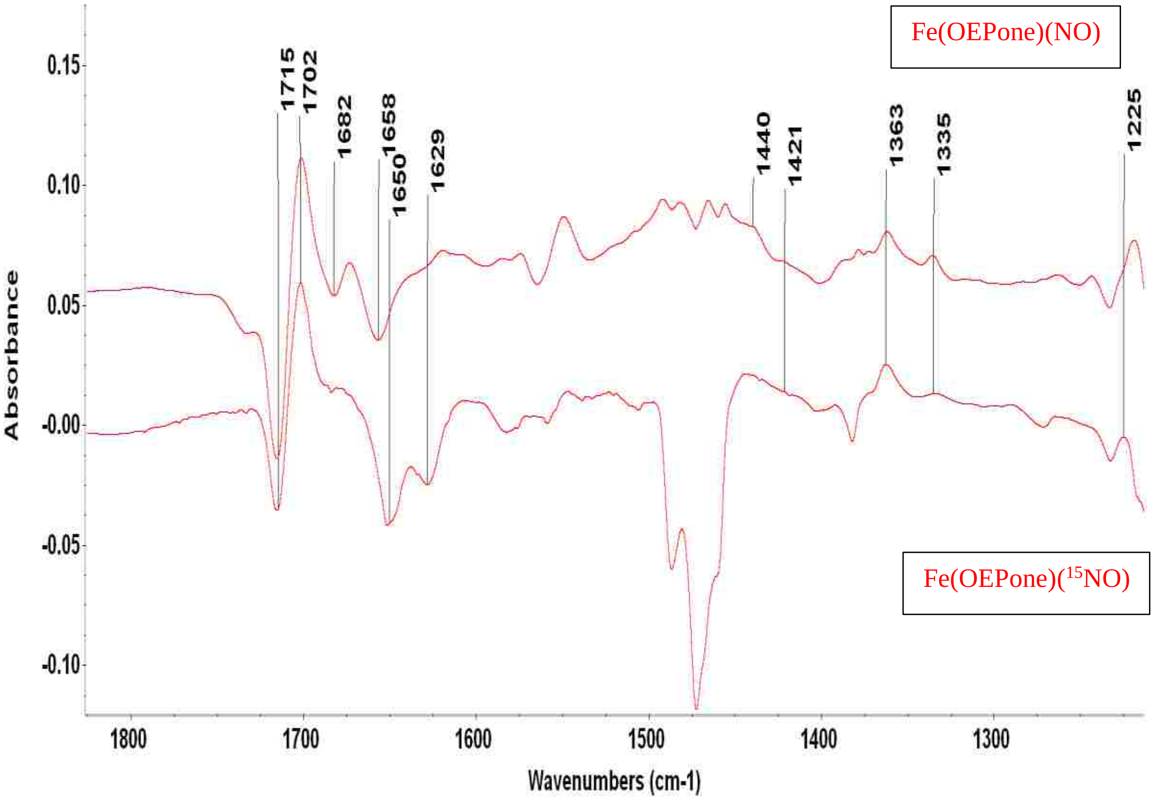

Figure 6-27. FTIR difference spectra for the reduction of Fe(OEPone)(NO) and Fe(OEPone)(^{15}NO) in THF-d_8 with 0.1 M TBAP; E_i= 0 mV; E_f= -1000 mV vs Ag wire; scan rate = 1 mV/s; 64 scans, 2 cm^{-1} resolution.

FTIR spectra of Fe(OEPone)(NO) were collected in presence of phenol while the potential was scanned from 0 mV to -1000 mV with a scan rate of 1 mV/s. The Figure 6-28 shows a series of difference spectra of Fe(OEPone)(NO) in THF-d_8 solvent in the presence of phenol. The wavenumbers are given in Table 6-3.

Table 6-3. Appearance and disappearance of IR bands for 4 mM of Phenol and 2,6-dcp with Fe(OEPone)(NO) upon electrolysis.

Compound	Disappeared bands	Appeared bands
Phenol and TBAP	1612, 1601, 1593,1580, 1512, 1493, 1462, 1448, 1440,1377, 1280, 1250	
Fe(OEPone)(NO)	1715, 1681, 1659	1702,1670, 1550, 1521, 1493,1466, 1456, 1447, 1440,1380, 1362, 1335, 1298, 1266,1244,1219
Fe(OEPone)(^{15}NO)	1715, 1650, 1629	1702, 1677, 1574,1548, 1436, 1421, 1389,1363,1335, 1317, 1290, 1261, 1243
Fe(OEPone)(NO) in 4 mM phenol	1715, 1682, 1658	1702, 1673, 1619, 1600, 1549, 1509, 1484, 1466, 1432, 1383, 1372, 1336, 1298, 1257, 1217
2,6-dcp and TBAP	1568, 1501, 1454, 1433, 1296, 1263, 1228	
Fe(OEPone)(NO) in 4 mM 2,6-dcp	1715, 1684, 1658	1702, 1673, 1619, 1576, 1548, 1500, 1487, 1434, 1383, 1372, 1364, 1348, 1336, 1262, 1216

In the spectral region 1200 cm^{-1} to 1800 cm^{-1} several bands were observed. The bands at 1619 cm^{-1}, 1600 cm^{-1}, 1509 cm^{-1} and 1257 cm^{-1} were observed from phenolate. With the phenolate bands, all the bands for Fe(OEPone)(NO)$^-$ were also observed indicating the acid concentration was not sufficient to react with reduced Fe(OEPone)(NO). Similar experiment was carried out with higher pK_a 2,6-dcp. The band at 1548 cm^{-1} was also seen in the presence of 2,6-dcp which is shown in Figure 6-29. The band at 1364 cm^{-1} and 1348 cm^{-1} were observed only for 2,6-dcp. The peak at 1500 cm^{-1} was appeared for 2,6-dcp, but the peak for the reduced species Fe(OEPone)(NO)$^-$ were still present in that concentration of 2,6-dcp.

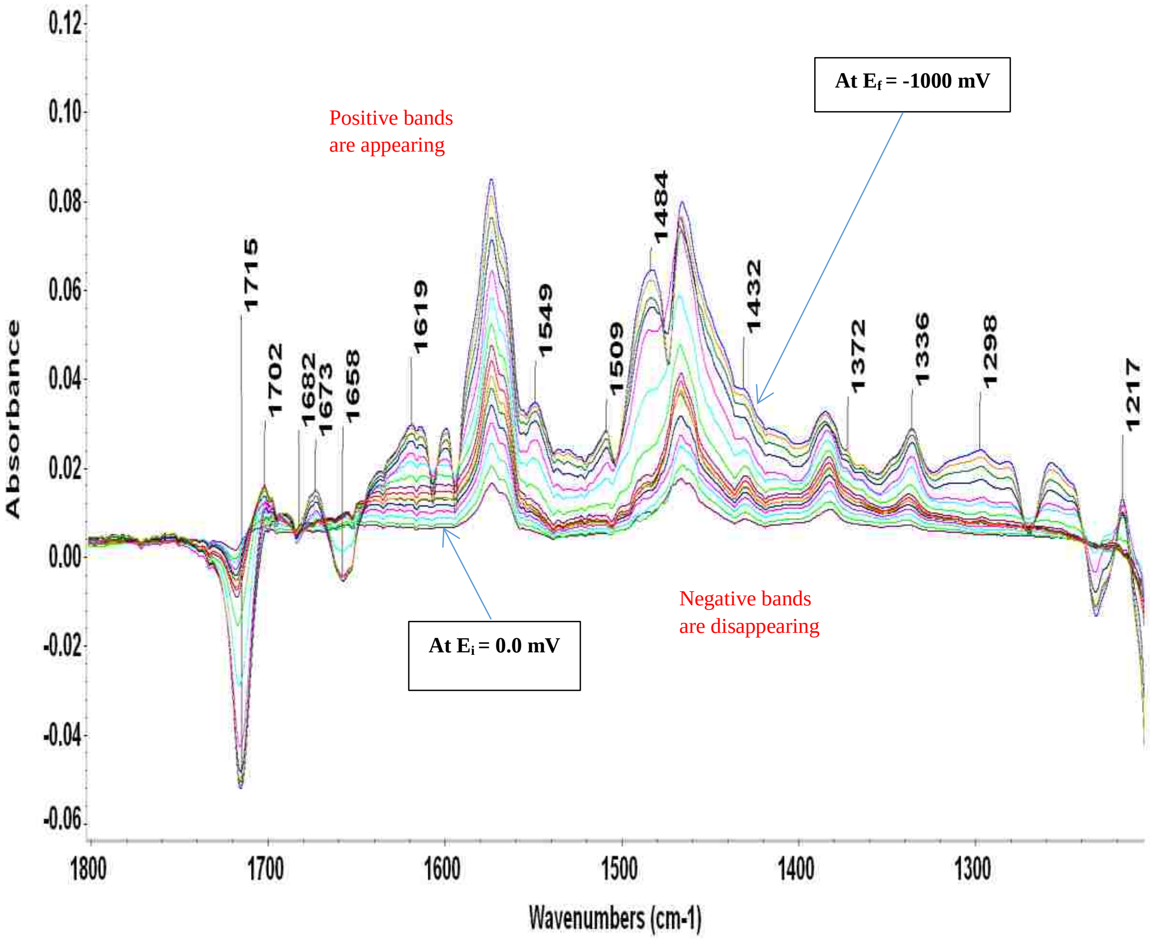

Figure 6-28. FTIR difference spectra for the reduction of 2 mM Fe(OEPone)(NO) with 4 mM phenol in THF-d_8 with 0.1 M TBAP; E_i= 0 mV ; E_f= -1000 mV vs Ag wire ; scan rate = 1 mV/s; 64 scans, 2 cm^{-1} resolution.

Unfortunately, the reversibility was not observed in the presence of acid. In addition, most of the bands for Fe(OEPone)(NO)$^-$ were observed even in the presence of substituted phenols indicating that the reduced species were not react with acids. This was consistent with the voltammetric results that this porphinone nitrosyls were not as reactive as Fe(OEP)(NO) or it might be reactive at very high concentration of substituted phenols.

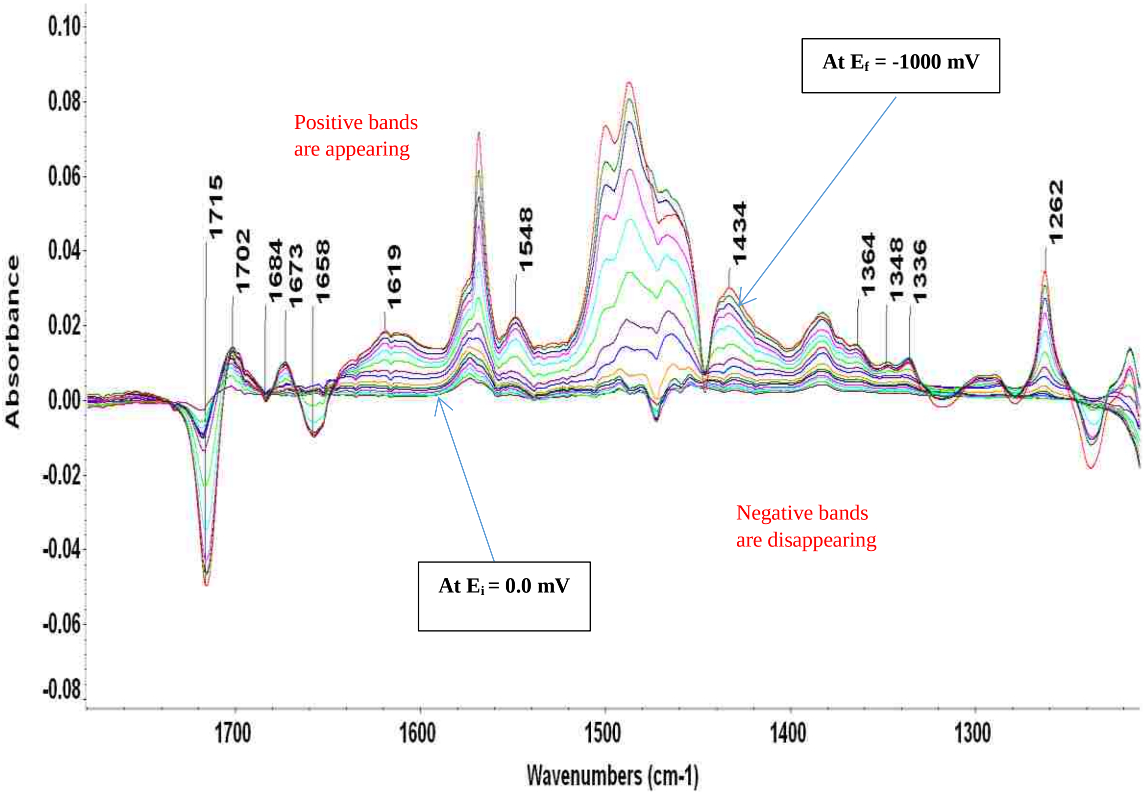

Figure 6-29. FTIR difference spectra for the reduction of 2.0 mM Fe(OEPone)(NO) with 4 mM 2,6-dcp in THF-d_8 with 0.1 M TBAP; E_i= 0 mV ; E_f= -1000 mV vs Ag wire ; scan rate = 1 mV/s; 64 scans, 2 cm^{-1} resolution.

To ensure the reaction between reduced Fe(OEPone)(NO) and substituted phenols, higher concentration of acid (40-100 mM) supplied to observe the protonated species. The spectra showed (Figure 6-30 & 6-31) that the bands from one electron reduced species were totally gone with prominent phenolate bands. As a result, it was difficult to find the Fe(OEPone)(HNO) band. But as the potential scanned to more negative potential the band for Fe(OEPone)(NH_2OH) appeared (Figure 6-32), which is consistent with UV-visible spectroeletrochemistry results and with the Fe(OEP)(NO) complex. As we already observed that with more negative potential and higher acid concentration, hydroxylamine complex formation was accelerated. Similar behavior was observed for

Fe(OEPone)(^{15}NO) in the presence of acids. Extensive study was avoided for two reasons. First, the porphinone was less reactive than Fe(OEP)(NO) which required higher concentration of substituted phenols, and the phenolate bands became prominent which made it difficult to observe protonated species bands. Second, this porphyrin contains a ketone group which disturb the ring current significantly. As a result, various vibrational modes couple each other causes a numerous number of vibrational bands in the region of interest. For this reason, the isotopic substitution did not give consistent vibrational bands for reduced species even though before electrolysis, the band for nitrosyls were consistent.

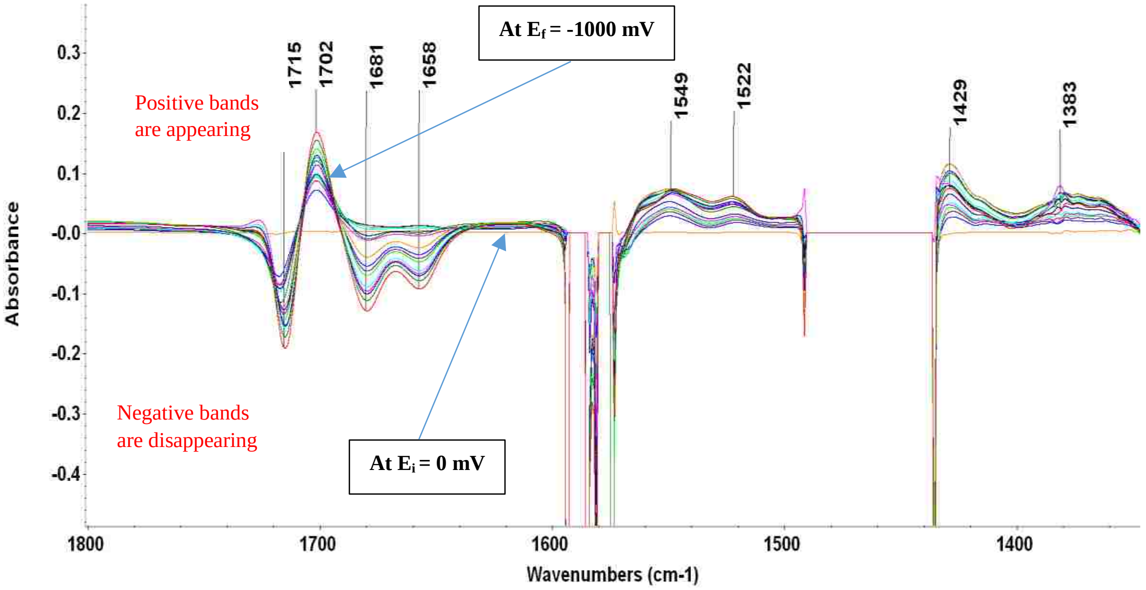

Figure 6-30. FTIR difference spectra for the reduction of 6.0 mM Fe(OEPone)(NO) with 120 mM 2,3-dcp in THF-d_8 with 0.1 M TBAP; E$_i$= 0 mV; E$_f$ = -1000 mV vs Ag wire ; scan rate = 1 mV/s; 64 scans, 2 cm^{-1} resolution.

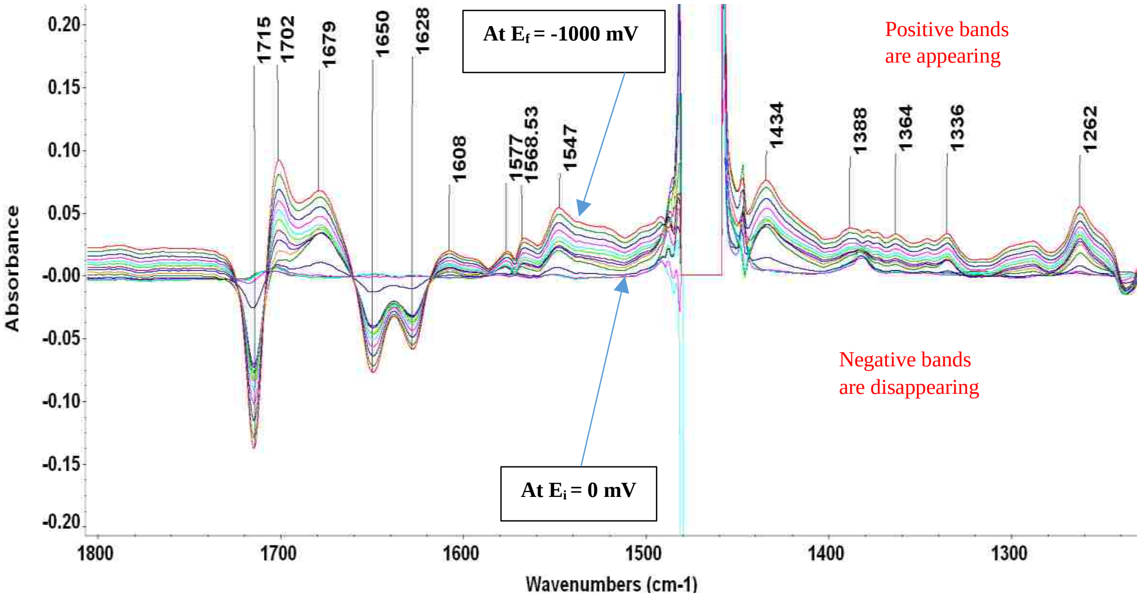

Figure 6-31. FTIR difference spectra for the reduction of 5.0 mM Fe(OEPone)(^{15}NO) with 40 mM 2,6-dcp in THF-d_8 with 0.1 M TBAP; E$_i$= 0 mV; E$_f$= -1000 mV vs Ag wire; scan rate = 1 mV/s; 64 scans, 2 cm^{-1} resolution.

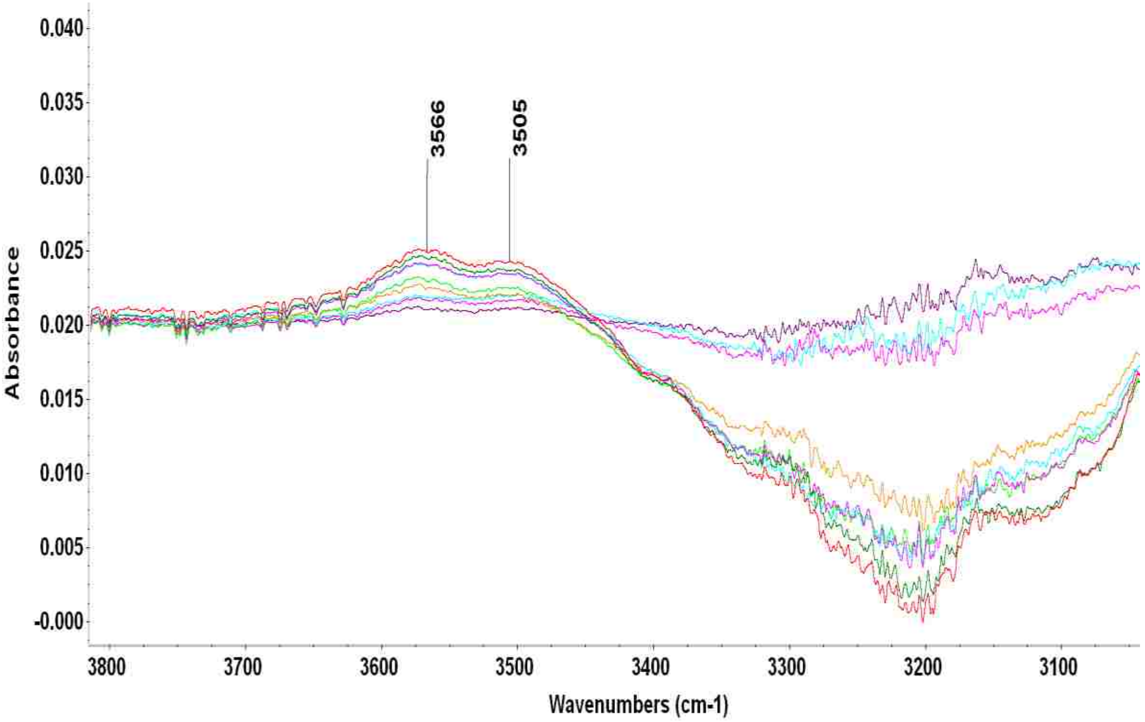

Figure 6-32. FTIR difference spectra for the reduction of 5.0 mM Fe(OEPone)(^{15}NO) with 40 mM 2,6-dcp in THF-*d_8* with 0.1 M TBAP; E_i= 0 mV; E_f= -1000 mV vs Ag wire; scan rate = 1 mV/s; 64 scans, 2 cm^{-1} resolution.

6.9 Study on Iron(II)(PPDME)(NO)

The voltammetry of Fe(PPDME)(NO) was carried out in THF over a potential range from 0.00 V to -2.0 V for different scan rates. The voltammograms (Figure 6-33) showed that the ΔEp was more than what was expected for reversible process due to high solution resistance of THF. The one electron transfer was completely reversible. The $E_{1/2}$ value (-1.335 V) of Fe(PPDME)(NO) was almost similar to Fe(OEP)(NO).

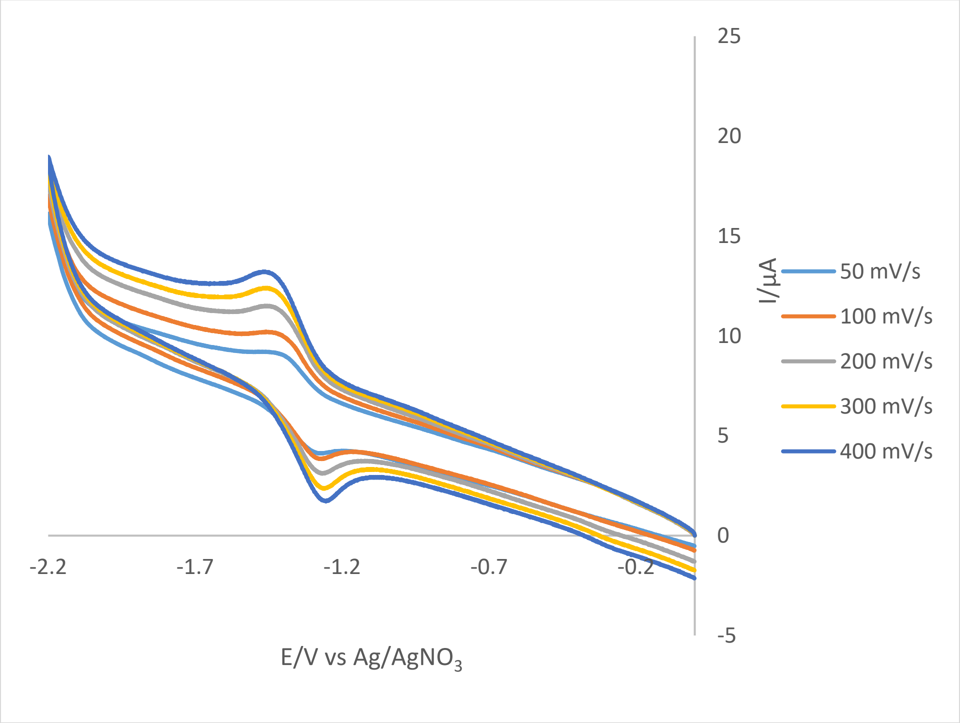

Figure 6-33. Cyclic voltammograms of Fe(PPDME)(NO) in THF with 0.1 M TBAP at different scan rate, Working electrode Pt.

The thin layer FTIR spectroelectrochemistry of Fe(PPDME)(NO) and Fe(PPDME)(^{15}NO) in THF-d_8 was carried out over a potential range -0.6 V to -1.0 V at a slow scan rate. The difference spectra (Figure 6-34) showed that the band at 1673 cm^{-1} for NO band disappeared upon reduction and new bands at 1440 and 1340 cm^{-1} appeared along with some other porphyrin bands. For Fe(PPDME)(^{15}NO) the band for NO at 1643 cm^{-1} disappeared and new bands at 1420 and 1340 cm^{-1} appeared along with some other weak porphyrin bands. The difference spectrum of the difference spectra of Fe(PPDME)(NO) and Fe(PPDME)(^{15}NO) showed derivative peaks at 1673 and 1443 cm^{-1} which clearly confirmed those peaks are related to isotope replacement and the peaks at 1440 and 1420 cm^{-1} due to one electron reduced species. The bands for one electron reduced species were similar to Fe(OEP)(NO).

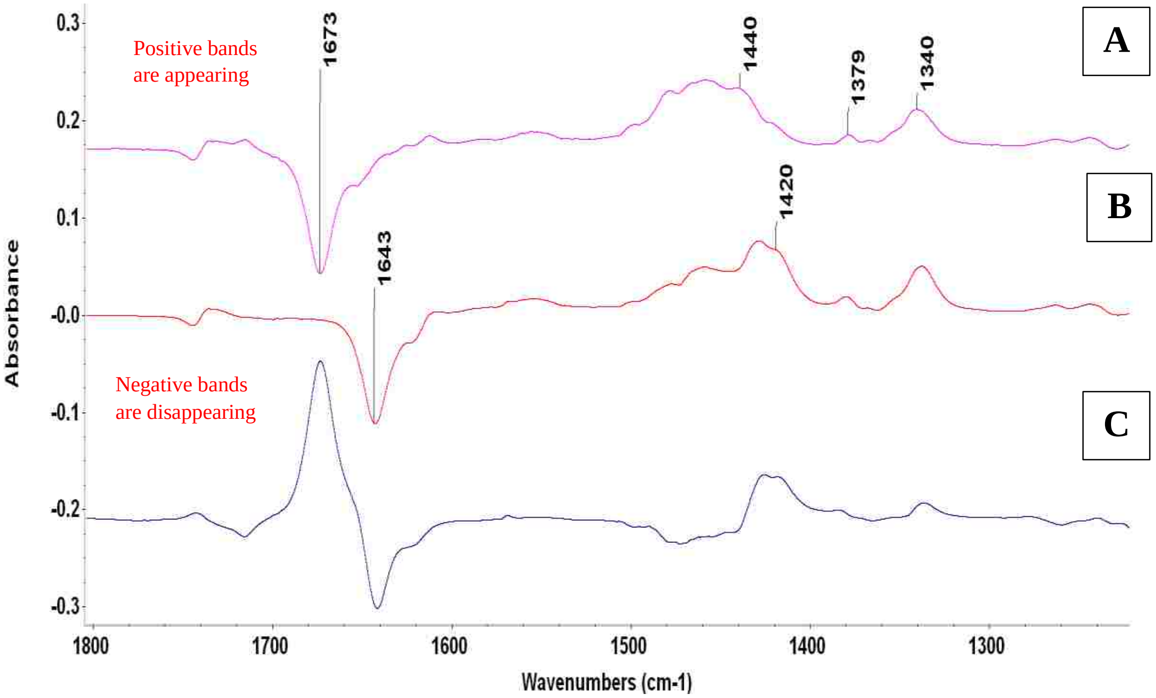

Figure 6-34. FTIR difference spectra for the reduction of Fe(PPDME)(NO) in THF-d_8 A) Fe(PPDME)(NO) B) Fe(PPDME)(^{15}NO) C) Difference spectrum of difference spectra of NO$^-$ - ^{15}NO$^-$, supporting electrolyte, 0.1 M TBAP; E_i= -400 mV; E_f= -1000 mV vs Ag wire; scan rate = 1 mV/s; 64 scans, 2 cm^{-1} resolution.

The FTIR spectroelectrochemistry of Fe(PPDME)(NO) and Fe(PPDME)(^{15}NO) were also carried out in the presence of 2,3-dcp. The difference spectra (Figure 6-34) showed the complete reaction of reduced species with acids. No isotope sensitive band was observed for HNO. It is possible that the HNO band might be at higher region (1450- 1550 cm^{-1}) which is obscured by phenol bands or the band is too weak to observe like Fe(OEP)(HNO) complexes showed (Chapter 6).

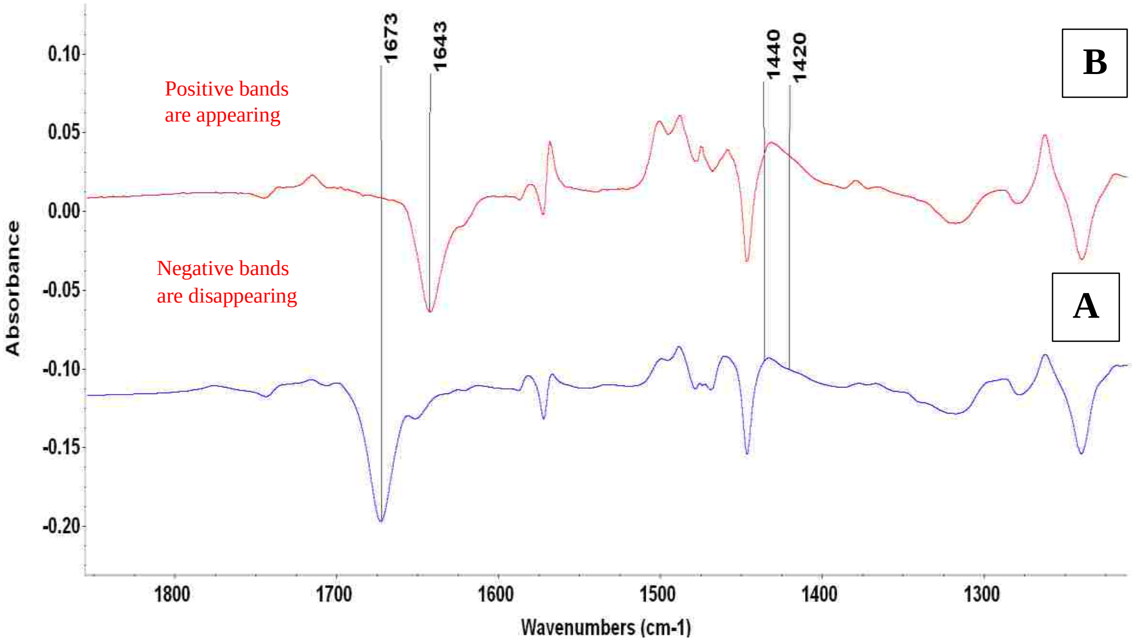

Figure 6-35. FTIR difference spectra for the reduction of Fe(PPDME)(NO) with 20 mM 2,3-dcp in THF-*d*$_8$, A) Fe(PPDME)(NO) B) Fe(PPDME)(^{15}NO); 0.1 M TBAP; E$_i$= -400 mV; E$_f$= -1000 mV vs Ag wire; scan rate = mV/s; 64 scans, 2 cm^{-1} resolution.

CHAPTER 7 STUDY ON IRON CORROLE NITROSYLS

The Soret maxima for the compounds, Fe(TpCF$_3$PC)(NO), Fe(TPC)(NO), Fe(TpMePC)(NO) and Fe(TpOMePC)(NO) red shifted (Figure 7-1A/B) with the addition of electron donating substituents on the para position on the meso-aryl groups. This behavior arises from aryl to corrole charge transfer in certain transition in Soret region.[113,140]

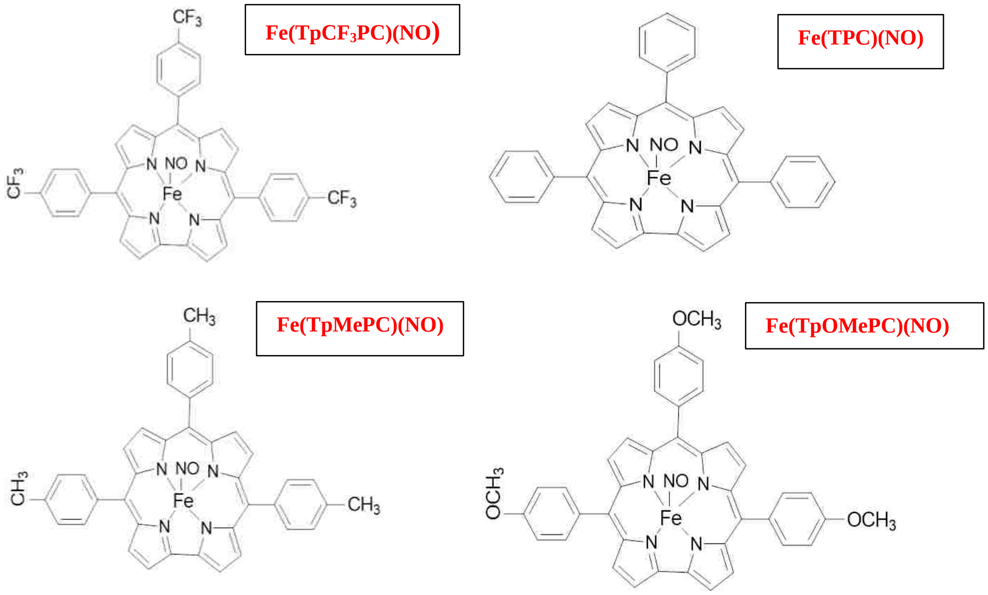

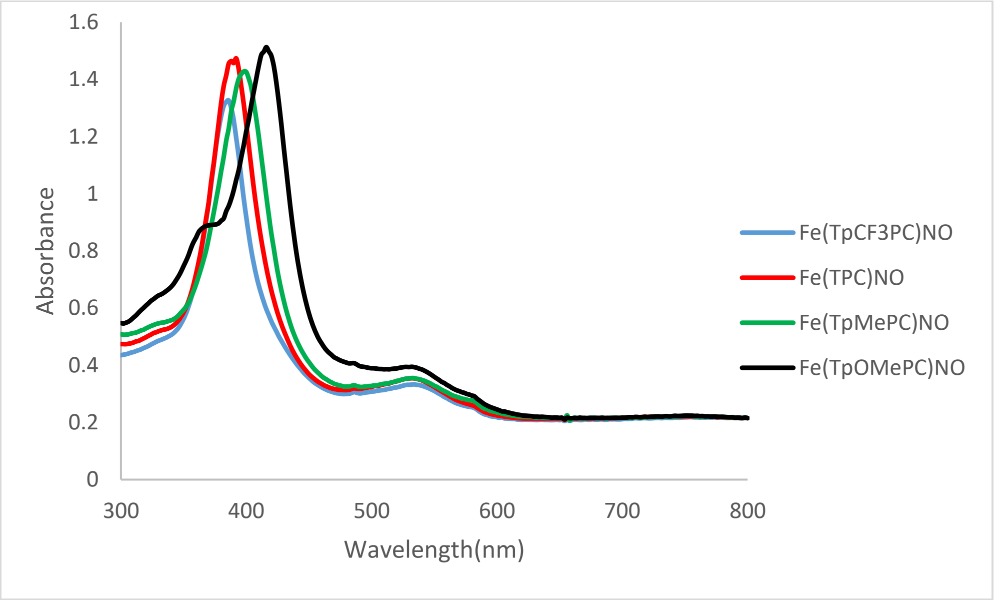

Figure 7-1. Top) Structure of Iron corrole nitrosyls, Bottom) UV-visible spectra of four different Iron corrole nitrosyls in THF.

7.1 Cyclic Voltammetry of Iron Corrole Nitrosyls

The cyclic voltammograms for the above compounds (Figure 7-2) showed that the redox products of the above compounds were chemically stable on the voltammetric time scale ($i_a/i_c \approx 1$) and the electron transfers were reversible, the large ΔEp might be due to high solution resistance. The redox potentials shifted to more negative potentials as the substituents become more electron donating (Table 7-1). These iron corrole nitrosyl reductions were easier (at more positive potential) than Fe(OEP)(NO) and Fe(OEPone)(NO) complexes (Chapter 3). The lower reduction potentials were ascribed to the non-innocent character of the corrole macrocycle (π- cation radical).

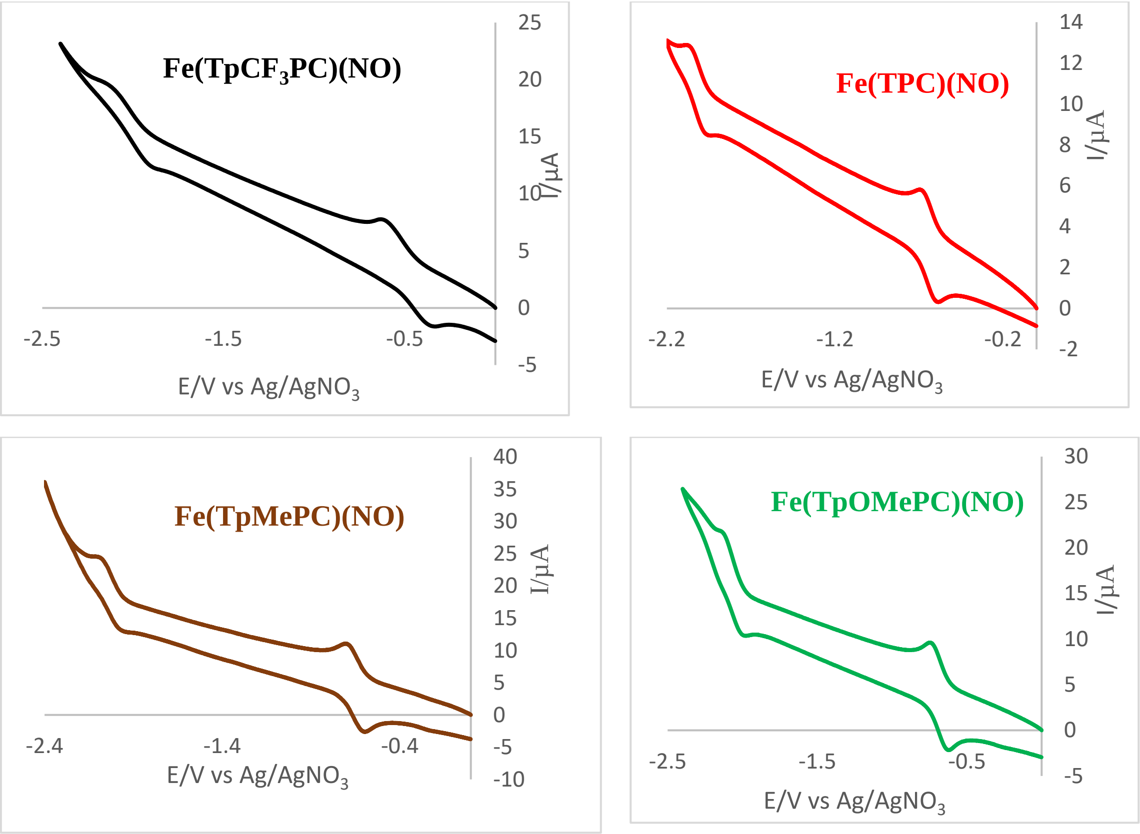

Figure 7-2. Cyclic voltammograms of Iron Nitrosyl Correles at 100 mV/s in THF, 0.1 M TBAP, working electrode Pt.

The second reductions were observed at very negative potential compared to first reduction. The second reduction was reversible and the reduced species were chemically stable ($i_a/i_c \approx 1$). The second reduction potentials are in Table 7-1. All four complexes showed almost same redox potential indicated the substituents did not affect the second redox potentials. The second reduction for all iron corrole nitrosyls were more negative than the second reduction of the iron porphyrin nitrosyls.[70] The high second redox potential indicated that the second electron resided in the antibonding orbitals of iron corrole nitrosyl complexes. For iron porphyrin nitrosyls, the first and second electrons from reduction resided in the antibonding orbitals of nitrosyl ligand. [70,76] As for iron corrole nitrosyls the first reduction was more positive than the second electron reduction.

Table 7-1. First and second reduction potentials for Iron Corrole Nitrosyls.

Complex	1st reduction (E°)	2nd reduction (E°)
Fe(TpCF$_3$PC)(NO)	-0.47 V	-2.01 V
Fe(TPC)(NO)	-0.62 V	-2.01 V
Fe(TpMePC)(NO)	-0.63 V	-2.01 V
Fe(TpOMePC)(NO)	-0.69 V	-2.08 V

7.2 UV-visible Spectroelectrochemistry of Iron Corrole Nitrosyls

The visible spectroelectrochemistry were carried out for all four compounds over a potential range from 0.0 V to -1.0 V (Figure 7-3 to 7-6). All four compounds were stable in the experimental time scale. A set of isobestic points for all the compounds showed that only two spectral species were present in spectroelectrochemical time scale. For all the compounds, the Soret bands were red shifted and a broad band at Q region appeared which indicated that these shifts could be metal based, using only visible spectra as evidence. For compound Fe(TpCF$_3$PC)(NO), the Soret band was strongly red shifted. For all the compounds, it was observed that all reduction happened on macrocycle or metal centers unlike metal porphyrin macrocycles. For metal porphyrin nitrosyls, the reduction was ligand based but for corroles the reduction was metal center or corrole macrocycle like non- heme nitrosyls which was consistent with the literature. [113,140]

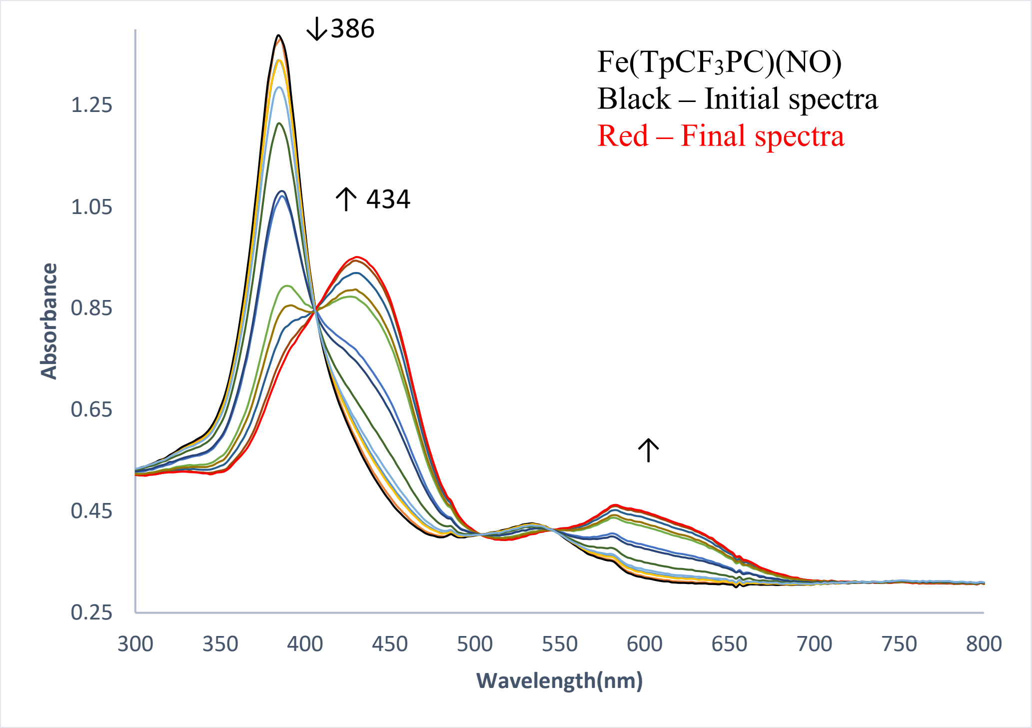

Figure 7-3. UV-visible spectroelectrochemistry of 0.05 mM Fe(TpCF$_3$PC)(NO) in THF, 0.1 M TBAP, E_i = 0.0 V, E_f =-1.0 V, scan rate 1 mV/s, Reference electrode Ag/AgNO$_3$, Working electrode Pt.

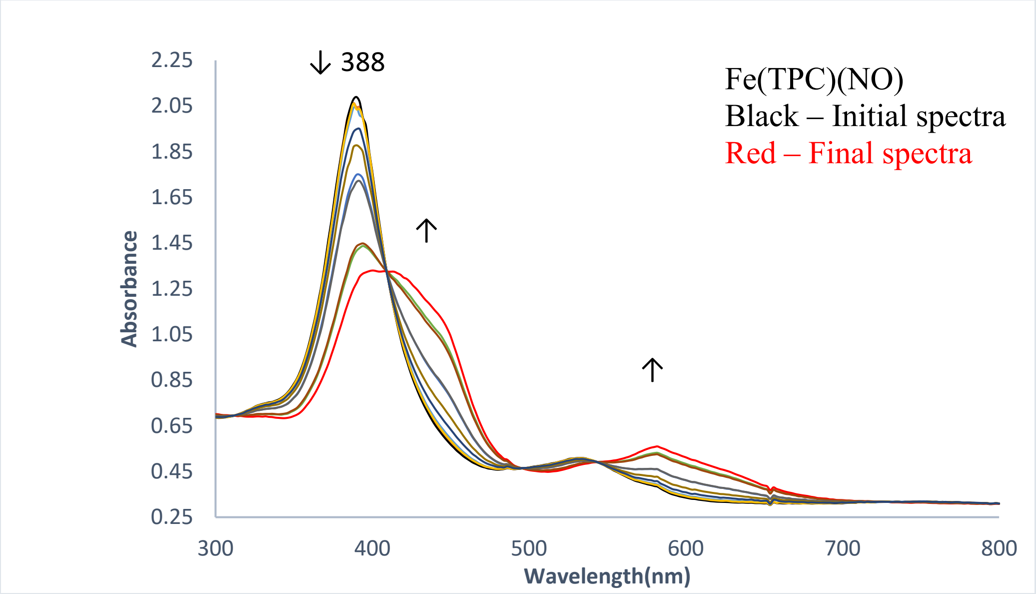

Figure 7-4. UV-visible spectroelectrochemistry of 0.08 mM Fe(TPC)(NO) in THF, 0.1 M TBAP, E_i = 0.0 V, E_f =-1.0 V, scan rate 1 mV/s, Reference electrode Ag/AgNO$_3$, Working electrode Pt.

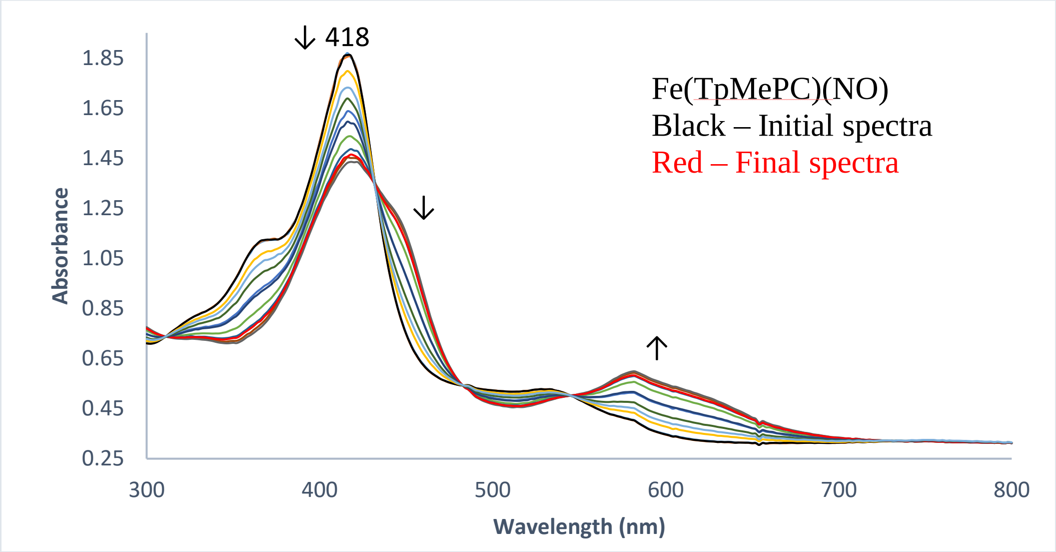

Figure 7-5. UV-visible spectroelectrochemistry of 0.06 mM Fe(TpMePC)(NO) in THF, 0.1 M TBAP, E_i = 0.0 V, E_f =-1.0 V, scan rate 1 mV/s, Reference electrode Ag/AgNO$_3$, Working electrode Pt.

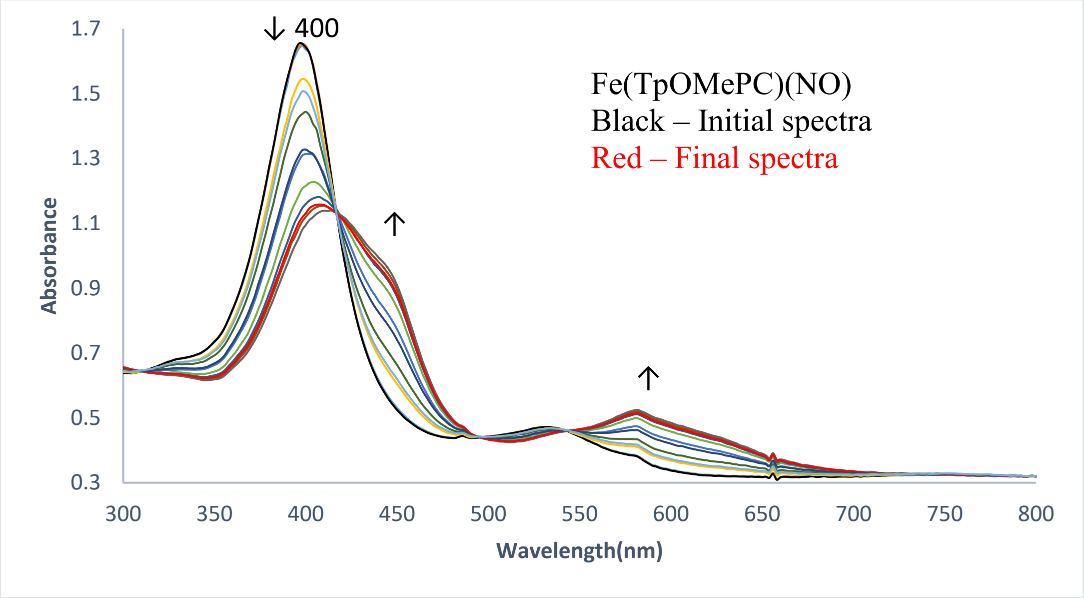

Figure 7-6. UV-visible spectroelectrochemistry of 0.055 mM Fe(TpOMePC)(NO) in THF, 0.1 M TBAP, E_i = 0.0 V, E_f =-1.0 V, scan rate 1 mV/s, Reference electrode Ag/AgNO$_3$, Working electrode Pt.

The UV-visible spectroelectrochemistry was carried out to identify the second redox species for all the iron corrole nitrosyls (Figure 7-7). The potentials were scanned from -0.8 V to -2.0 V vs Ag/AgNO$_3$. The changes were observed in Soret and Q band region. The redox species were reversible when the potential was returned to the initial potential. The initial spectrum was recovered for all species. For all the complexes, the changes in the Q band region were increasing and broadening of bands like first electron reduction. In the Soret band region, for complexes Fe(TpCF$_3$PC)(NO) and Fe(TPC)(NO) a new Soret bands at 432 nm and 422 nm appeared with decreasing of the original Soret bands at 388 nm and 386 nm. For all the complexes, the initial Soret bands were decreased but did not disappeared totally. The broadening of the Q band with attenuating the Soret bands indicated an anion radical like character. It is difficult to compare these complexes with porphyrin characteristics because of different electronic configuration. It is also difficult to say the formation of anion radial because ligand to metal π- bonding and back donation.

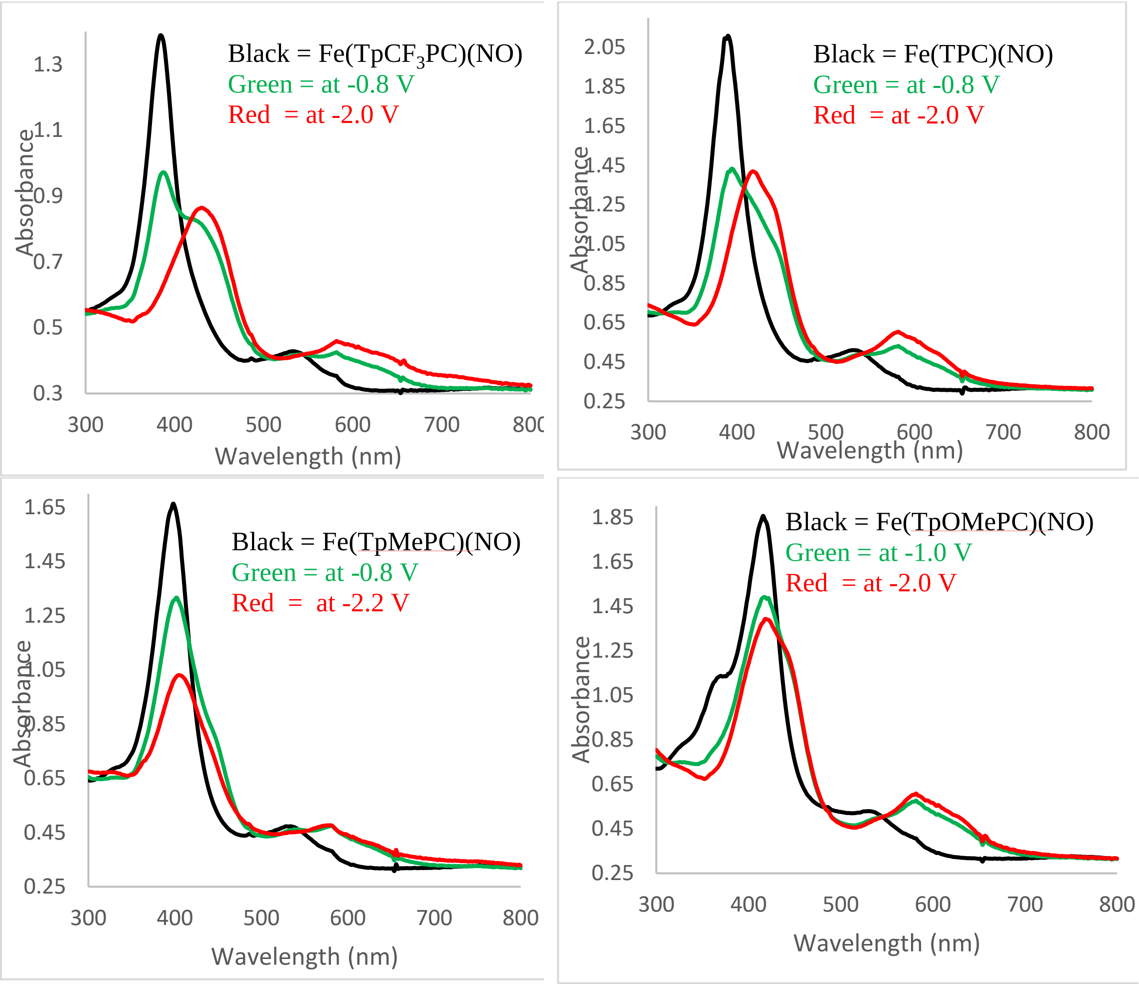

Figure 7-7. UV-visible spectroelectrochemistry of Iron corrole nitrosyls in THF, 0.1 M TBAP, scan rate 1 mV/s, Reference electrode Ag/AgNO$_3$, Working electrode Pt.

7.3 FTIR Spectroelectrochemistry of Iron Corrole Nitrosyls

FTIR Spectra for Fe(TpCF$_3$PC)(NO), Fe(TPC)(NO), Fe(TpMePC)(NO) and Fe(TpOMePC)(NO) showed bands at 1780, 1770, 1769 and 1767 cm^{-1} respectively in THF. The bands were consistent with the literature values i.e 1781, 1767, 1767 and 1761cm $^{-1}$.[113] FTIR spectroelectrochemistry for all compounds were carried out over a potential range from 0.0 V to -0.8 V (Figure 7-8 to 7-11). For all corroles, the nitrosyl bands at 1780, 1770, 1769 and 1767 cm^{-1} disappeared and new bands at 1626,1621,1618 and 1620 cm^{-1} appeared upon reduction. For all the corroles, the nitrosyl bands downshifted indicating that the nitrosyl bond became weaken upon reduction as a result of adding extra electron to anti-bonding orbital of nitrosyl bonding orbitals. This type of behavior was seen for porphyrin nitrosyls where reduction was ligand based.[75] The drop of iron corrole nitrosyls bands upon reduction were 154, 149, 151, 147 cm^{-1} respectively for Fe(TpCF$_3$PC)(NO), Fe(TPC)(NO), Fe(TpMePC)(NO) and Fe(TpOMePC)(NO) complexes which were less than porphyrin nitrosyl bands drop (drop 230 for Fe(OEP)(NO) and 185 for Fe(TPP)(NO). The downshift of nitrosyl bands was almost same which indicated that the substituents effect was insignificant on the nitrosyl vibration after one electron reduction. The DFT calculation by Speelman et al. [76] showed that the reduction for non-heme system was metal based and the drop of nitrosyl band for non-heme system was 130 cm^{-1}. The nitrosyl band drop for the iron corrole nitrosyls were in between the heme and non heme system. It is difficult to conclude the electronic occupancy and configuration based on vibrational band shift.

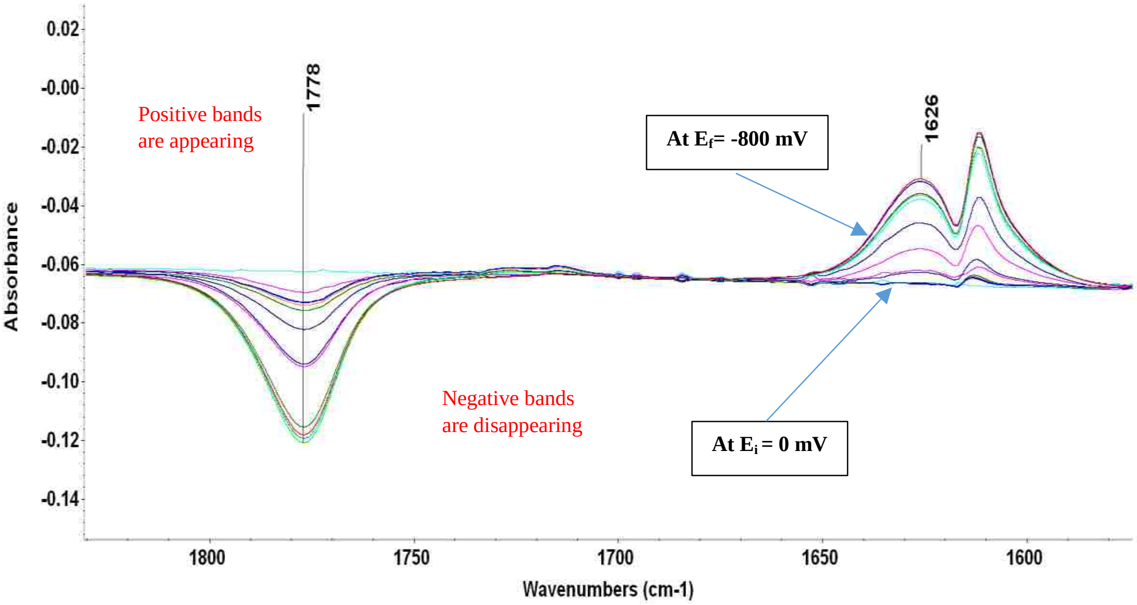

Figure 7-8. FTIR difference spectra of 0.7 mM of Fe(TpCF$_3$PC)(NO) in THF, 0.1 M TBAP, E_i = 0.0 V, E_f = -0.8 V, scan rate 1 mV/s, 64 scans, 2 cm^{-1} resolution, Reference electrode Ag wire, working electrode Pt.

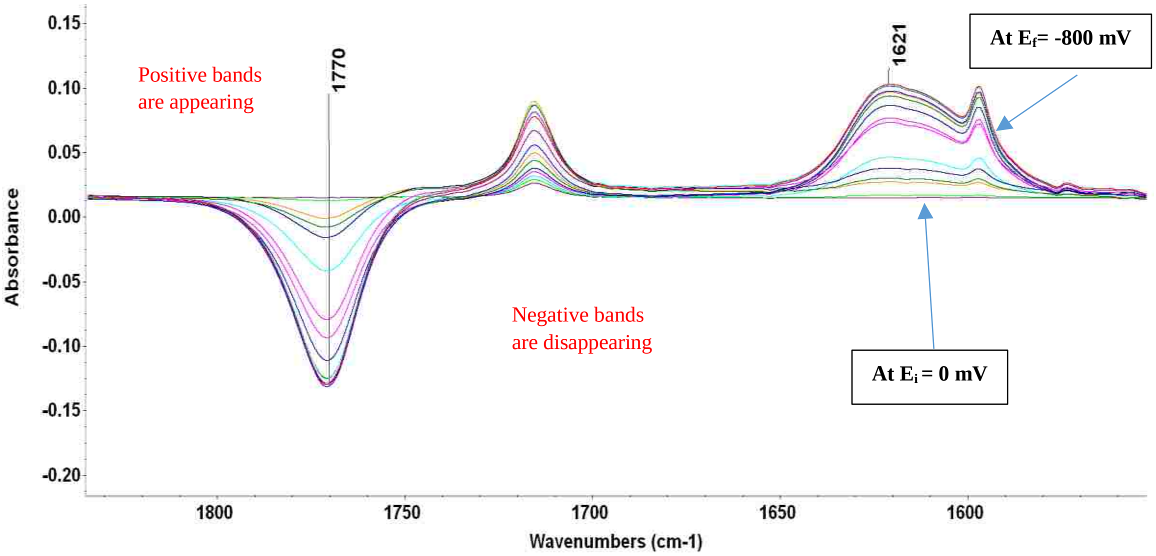

Figure 7-9. FTIR difference spectra of 1.1 mM of Fe(TPC)(NO) in THF, 0.1 M TBAP, E_i = 0.0 V, E_f = -0.8 V, scan rate 1 mV/s, 64 scans, 2 cm^{-1} resolution, Reference electrode Ag wire, working electrode Pt.

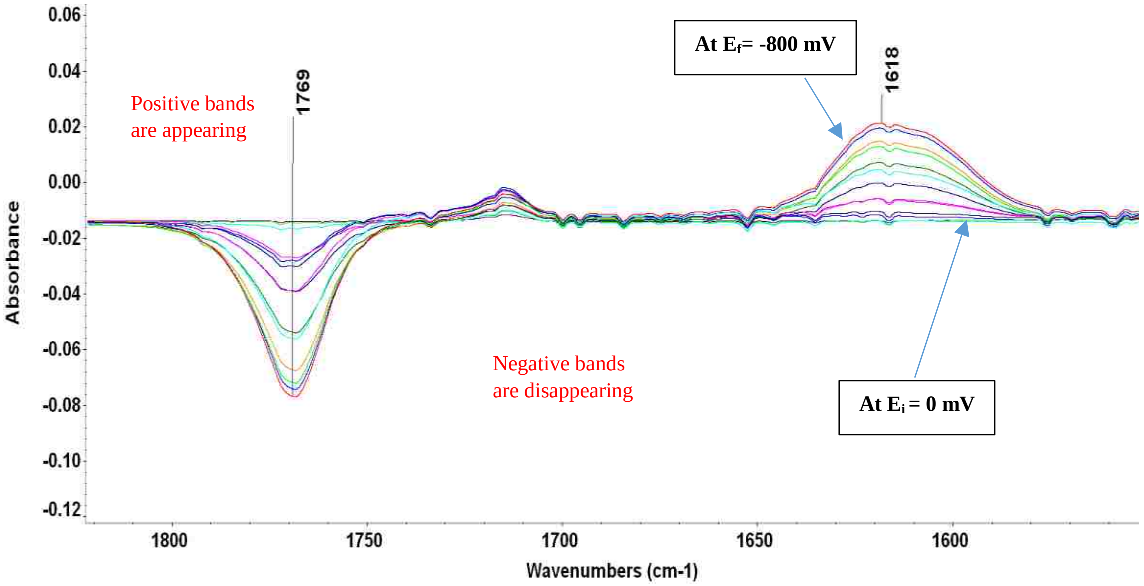

Figure 7-10. FTIR difference spectra of 0.6 mM of Fe(TpMePC)(NO) in THF, 0.1 M TBAP, E_i = 0.0 V, E_f = -0.8 V, scan rate 1 mV/s, 64 scans, 2 cm^{-1} resolution, Reference electrode Ag wire, working electrode Pt.

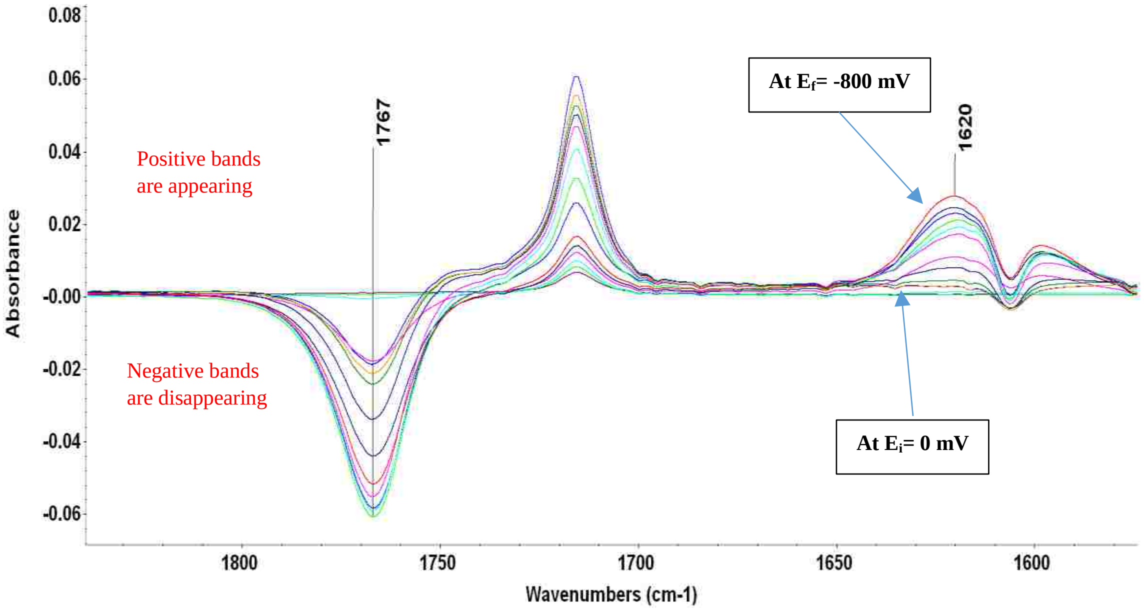

Figure 7-11. FTIR difference spectra of 0.5 mM of Fe(TpOMePC)(NO) in THF, 0.1 M TBAP, E_i = 0.0 V, E_f = -0.8 V, scan rate 1 mV/s, 64 scans, 2 cm^{-1} resolution, Reference electrode Ag wire, working electrode Pt.

7.4 SWV of Iron Corrole Nitrosyls in the Presence of Weak Acids

Square wave voltammetry (SWV) was carried out for all iron corrole nitrosyls in the presence of 2,6-dcp. Surprisingly the voltammetry showed an unusual behavior. In all cases, the wave was shifted to more negative unlike the positive shift of wave that was observed upon the addition of acids for Fe(OEP)(NO) and Fe(OEPone)(NO). If the reduced corrole nitrosyls was protonated, we should have seen positive shift in the wave upon the addition of acids.

In case of all the corroles, such behavior was observed, even though for the compound Fe(TpCF$_3$PC)(NO), the ratio of peak currents were consistent which were expected for chemically reversible system (Figure 7-12). There was a reaction wave shifted. We do not currently have an explanation for this. For Fe(TPC)(NO) and Fe(TpMePC)(NO) complexes, the waves were shifted to positive potentials initially, but at higher concentration of acids, they moved to negative with less re-oxidation current (Figure 7-13 & 7-14). The Fe(TpOMePC)(NO) complex showed a positive shift in the potentials with decreasing the peak current in the presence of 2,6-dcp. This behavior was not consistent with the following reaction (protonation) (Figure 7-15).

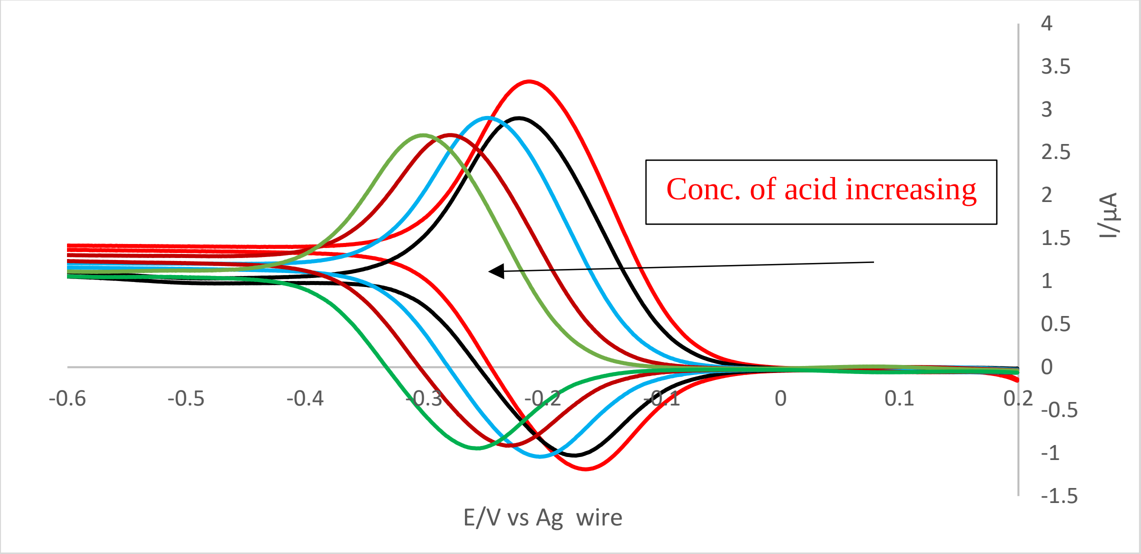

Figure 7-12. SWV of Fe(TpCF$_3$PC)(NO) in THF with different concentration of 2,6-dcp , 0.1 M TBAP, frequency 5 Hz, Increment 1 mV, amplitude 25 mV, working electrode BDD.

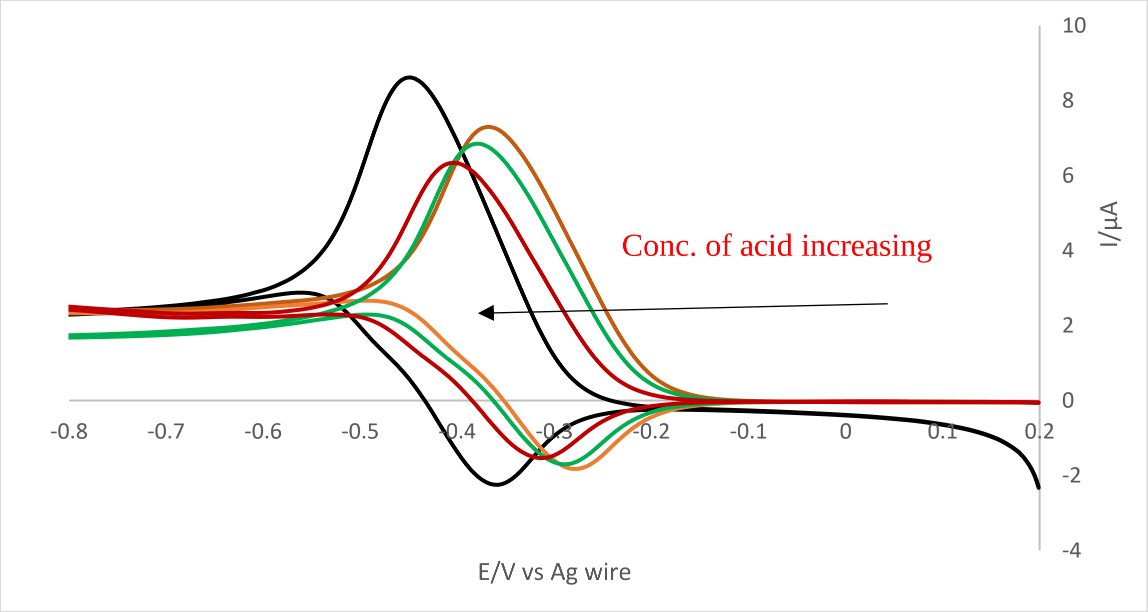

Figure 7-13. SWV of Fe(TPC)(NO) in THF with different concentration of 2,6-dcp, 0.1 M TBAP, frequency 5 Hz, increment 1 mV, amplitude 25 mV, working electrode BDD.

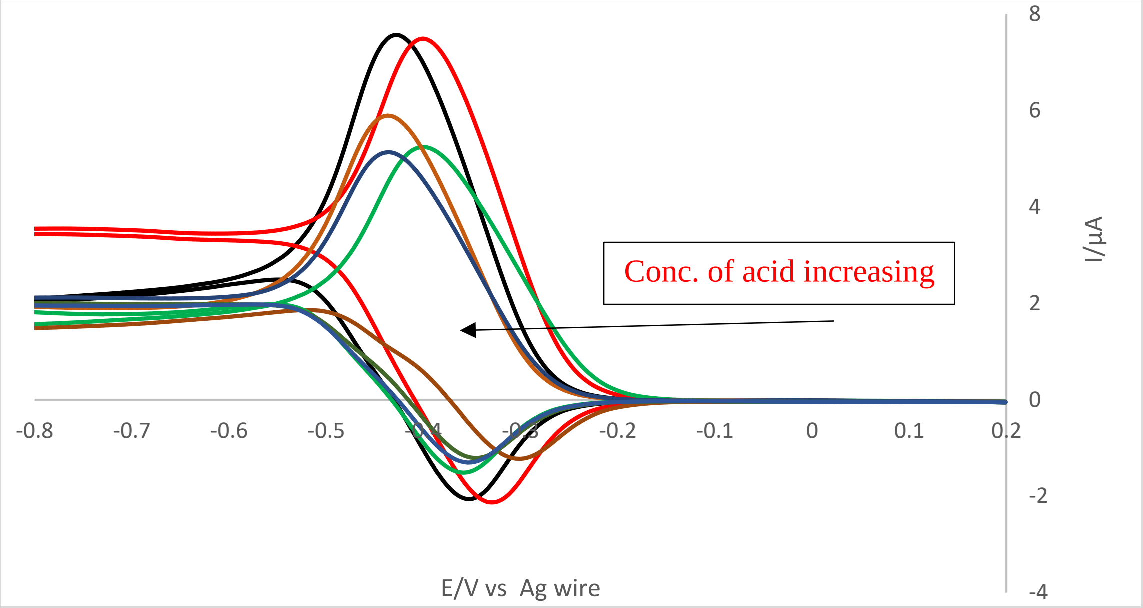

Figure 7-14. SWV of Fe(TpMePC)(NO) in THF with different concentration of 2,6-dcp, 0.1 M TBAP, frequency 5 Hz, increment 1 mV, amplitude 25 mV, working electrode BDD.

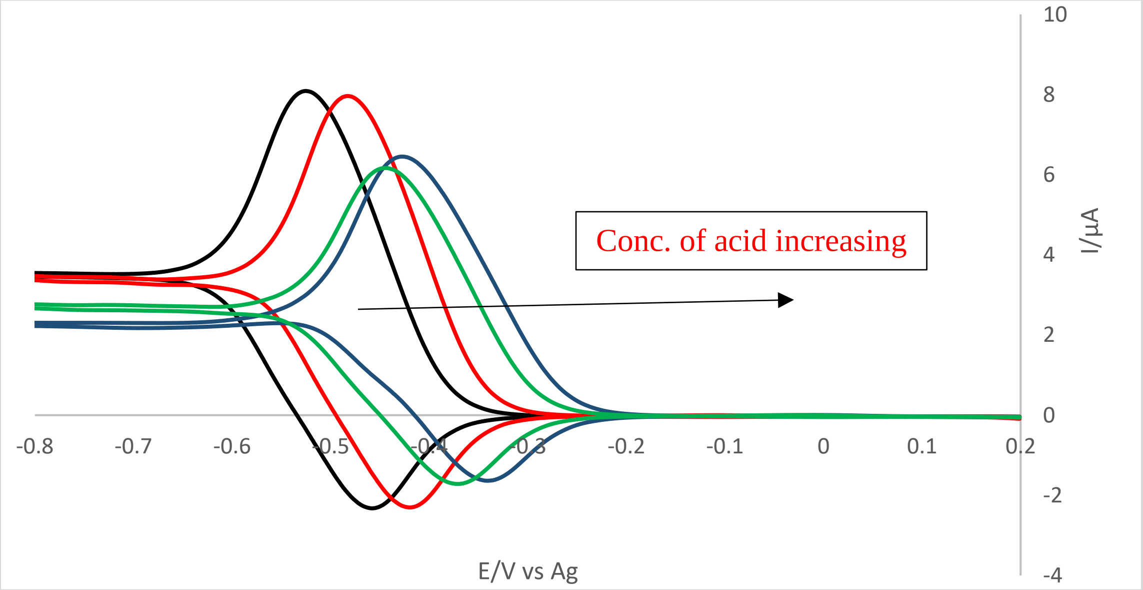

Figure 7-15. SWV of Fe(TpOMePC)(NO) in THF with different concentration of 2,6-dcp, 0.1 M TBAP, frequency 5 Hz, increment 1 mV, amplitude 25 mV, working electrode BDD.

In order to investigate this mechanism, visible spectroelectrochemistry of Fe(TpCF$_3$PC)(NO) with 2,6-dcp was carried out and the spectra (Figure 7-16) showed that the compounds were reversible in the experimental time scale and a set of isobestic points indicates only two spectral species were present. Broadening of the Soret band before reduction would indicate that the corroles might have reacted with phenols from solution before reduction. ^{1}H NMR of Fe(TpCF$_3$PC)(NO) with 2,6-dcp showed two additional resonances at 7.33 and 7.35 ppm where acid resonance at 8.8 ppm. (Figure 7-17). The change in the presence of 2,6-dcp clearly indicated a reaction or interaction between corroles and 2,6-dcp. It is possible that the corroles were protonated before electrolysis or the phenolate was bound to the iron center.

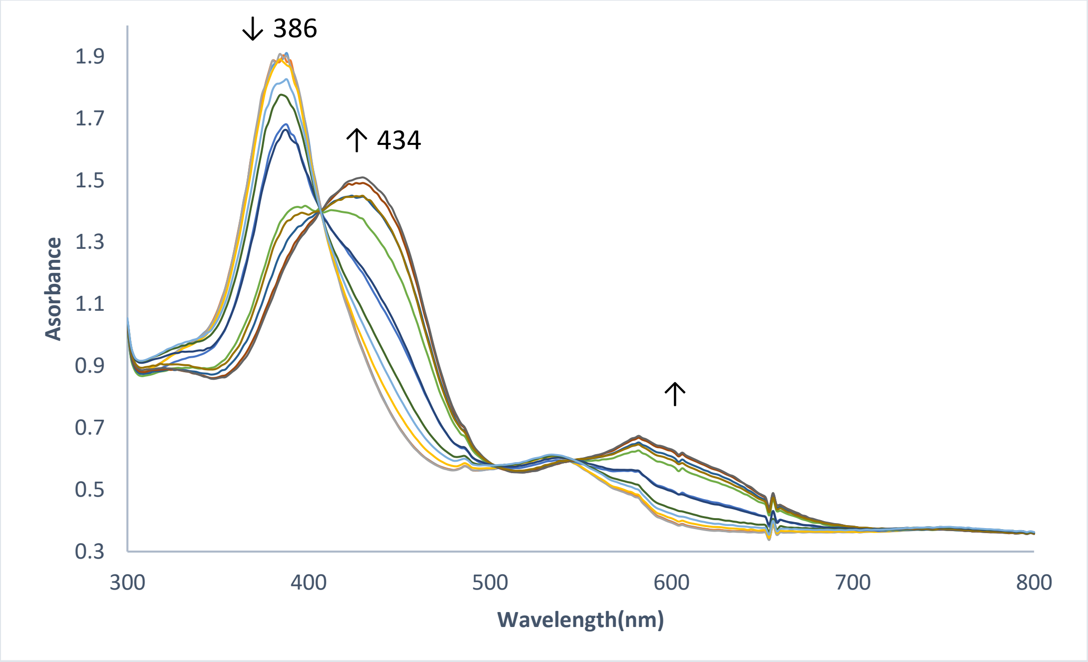

Figure 7-16. UV-visible spectroelectrochemistry of Fe(TpCF$_3$PC)(NO) in THF with 100 mM 2,6-dcp, 0.1 M TBAP, E_i = 0.0 V, E_f =-1.0 V scan rate 1 mV/s, Reference electrode AgNO$_3$/Ag, Working electrode Pt.

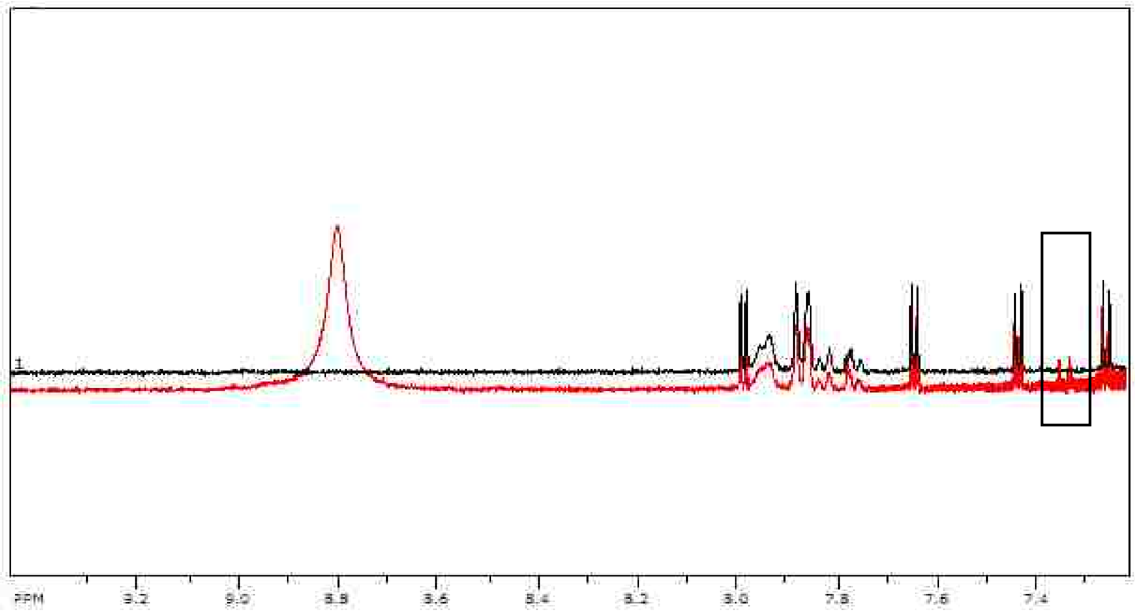

Figure 7-17. ^{1}HNMR of Fe(TpCF$_3$PC)(NO) (Black trace) in THF-d_8 only and with 2,6-dcp (Red trace).

CHAPTER 8 CONCLUSIONS

The acid/base chemistry of redox properties of $Fe(P)(NO)^-$ were studied in detail. The stability of the iron porphyrin nitroxyl anion, $Fe(P)(NO)^-$, was confirmed by voltammetry and by UV-visible and FTIR spectroelectrochemistry. The bands related to the nitroxyl anion were consistent with literature values. [70,75] The iron porphyrin nitroxyl anion was also generated chemically. Cyclic voltammetric results showed that the one electron reduction wave shifted to more positive potentials with the addition of phenols and substituted phenols. This indicated that the $Fe(P)(NO)^-$ readily reacted with phenols and substituted phenols to form Fe(P)(HNO) complexes. The disproportionation of Fe(P)(HNO) to Fe(P)(NO) and H_2 slowed down significantly with weak acids such as substituted phenols. The results showed that the formation of Fe(P)(HNO) complexes were chemically reversible if a slow scan rate was maintained. At higher scan rates, the reverse peak current deviated from the chemically reversible values. This behavior indicated that the reverse reaction was slow. If the potential was scanned to more negative potentials after first wave, a second wave was observed. Using the semi-derivative method, the ratio of second and first wave was found to be more than one electron, indicating a multi-electron reduction. The wave height was dependent on the pK_a and concentration of the acid. Based on the available literature,[72] the species formed by the second wave was $Fe(II)(P)(NH_2OH)$.

According to the voltammetric results, the following mechanism was proposed.

Wave I: $\mathrm{Fe(P)(NO)^-} + e^- \leftrightarrow \mathrm{Fe(P)(NO)}$ (8-1)

$\mathrm{Fe(P)(NO)^-} + \mathrm{PhOH} \leftrightarrow \mathrm{Fe(P)(HNO)} + \mathrm{PhO^-}$ (8-2)

Wave II: $\mathrm{Fe(P)(HNO)} + 2e^- + 2\mathrm{PhOH} \leftrightarrow \mathrm{Fe(P)(NH_2OH)} + 2\mathrm{PhO^-}$ (8-3)

RRDE voltammetry was used to find the reaction kinetics of the oxidation of Fe(P)HNO to Fe(P)(NO). The ring current was significantly smaller than the reversible value, indicating that the re-oxidation was slow. The kinetic parameter, the collection efficiency (N_k), decreased with an increase in the acid concentration, and an increase in the rotation rate. This indicated that the oxidation of the protonated species was slow. The formation of Fe(P)(HNO) complexes was dependent upon the strength of the acid and its concentration. For the weakest acid used (phenol), 100-200 mM was needed to form the Fe(P)HNO complex while 10-50 mM was needed for 2,6-dcp, 2,3-dcp and 3,5-dcp. Based on the aqueous pK_a's of the acids, these results indicated that the pK_a for Fe(P)(HNO) must be greater than 8 which was consistent with the Ru-HNO complex.[157] The FTIR spectroelectrochemistry of Fe(OEP)(NO) with 25 mM of phenol showed the presence of $\mathrm{Fe(OEP)(NO)^-}$, indicating that there was no reaction at this acid concentration. These results indicated that the pK_a of Fe(OEP)(HNO) must be between 8-10. Digital simulation was carried out to determine the kinetic parameters. The $\sqrt{k_f}/K$ values were weakly dependent upon pK_a because the k_f and K values are correlated. Overall, the K values decreases faster than the $\sqrt{k_f}$, causing the ratio to increase as the pK_a increased. This was also observed for 2,3-dcp-d_4 where $\sqrt{k_f}/K$ was higher than the normal abundance acids. The potential shifts and collection efficiency changes compared to normal abundance acids were qualitatively consistent with a slower reaction. The N_k values increased with the increase of the conjugate base. In the presence of the conjugate base, the rate of oxidation of Fe(OEP)(HNO) increased. The kinetics of the formation of Fe(P)(NH_2OH) were not studied in detail in this work (Reaction 8-3), this was already done previously.[75]

The Fe(OEPone)(NO) showed the similar behavior towards acids. The Fe(OEPone)(HNO) formation needed higher acid concentration than the Fe(OEP)NO. The $\sqrt{k_f/K}$ value for Fe(OEPone)(NO) was lower than the Fe(OEP)(NO). In this case, the $\sqrt{k_f}$ value decreased more than K for reaction 8-2.

The RRDE data were consistent with the formation of Fe(OEP)(HNO). It was the goal of this work to find the direct evidence for its existence. The first spectroscopic technique was UV-visible spectroelectrochemistry. The UV-visible spectroelectrochemistry results showed that the first product from the reduction of Fe(OEP)(NO) in the presence of weak acids was Fe(OEP)(HNO). The Soret band for Fe(OEP)(HNO) was slightly red shifted and broadened with a new band in the Q band region at 552 nm which was consistent with the literature.[86] The ^{1}H NMR spectrum of chemically generated Fe(OEP)(HNO) showed a unique resonance at 12.6 ppm which was downfield from the meso protons. Previous study showed that the proton resonance for Fe(OEP)(HNO)(5-MeIm) was at 14.0 ppm [93] and for Mb-(HNO) was at 14.8 ppm. [86] The small upfield shift of proton resonance for Fe(OEP)(HNO) might be due to lack of trans-coordination, as well as to hydrogen bonding between the complex and excess phenols. The $J_{N\text{-}H}$ coupling was not observed due to rapid proton exchange between complex and excess acid. The low temperature ^{1}H NMR showed that hydrogen bonding was important to stabilization of

Fe(OEP)(HNO) complex. At lower temperatures, the reaction was controlled by thermodynamic factors. The ^{2}H NMR showed a weak resonance for Fe(OEP)(^{2}HNO).

FTIR spectroelectrochemistry results showed a complete reaction of Fe(OEP)(NO)$^-$ with substituted phenols. Previous study showed a ν_{NO} band for Mb-HNO at 1385 cm^{-1} using resonance Raman spectroscopy.[87] A ν_{NO} band was also observed at 1383 cm^{-1} for Fe(OEP)(HNO)(5MeIm) in the infrared spectroscopy.[93] In our work, this band was not observed by either chemical or electrochemical methods. A significant difference between our work and theirs was the coordination number (6 vs 5) which may account for the difference. At higher frequency region (3000-3800 cm^{-1}), the band for NH was not observed. The Fe(OEP)(HNO) band might be too weak to be observed or might be in the 1450- 1550 cm^{-1} region which was obscured by phenol and porphyrin macrocycle bands.

It was thought that the Fe(P)(HNO) complexes were very unstable in the voltammetric time scale [72] so that protected porphyrin models (bis-picket fench porphyrin) were needed to stabilized the HNO complex.[74] Our study showed that the Fe(OEP)(HNO) could be generated electrochemically and chemically and that was stable for at least a few hours.

A Previous study[72] showed that the formation of Fe(OEP)(NH_2OH) from Fe(OEP)(NO)$^-$ involved an intermediate Fe(OEP)(NH_2O)$^+$ which was a kinetically important species in the reduction of Fe(OEP)(HNO) to Fe(OEP)(NH_2OH). The Soret band for Fe(OEP)(NH_2OH) at 402 nm was similar to other ferrous-OEP complexes such as Fe(OEP)(py)$_2$, 409 nm, [152] Fe(OEP)(CO)(py), 409 nm [152] and Fe(OEP)(O_2)(CH_3CN), 410 nm.[153] While all these were six- coordinate complexes, Fe(OEP)(NH_2OH) might be coordinated with THF as was observed for Fe(OEP)(O_2) in acetonitrile. No evidence was observed for the formation of bis-hydroxylamine complex, Fe(OEP)($NH_2OH)_2$[154] which might convert to Fe(OEP)(NO). The re-oxidation of Fe(OEP)(HNO) and Fe(OEP)(NH_2OH) to Fe(OEP)(NO) was slow which was consistent with the voltammetric results. The presence of the conjugate base such as phenolate accelerated the reverse Reaction of 8-2 & 8-3. The UV-visible spectra of chemically generated Fe(OEP)(HNO) and Fe(OEP)(NH_2OH) were consistent with the UV-visible spectroelectrochemical spectra. The voltammetric and the spectroscopic evidence showed that the Fe(OEP)(HNO) formed readily when Fe(OEP)(NO) was reduced but further reduction from Fe(OEP)(HNO) to Fe(OEP)(NH_2OH) required additional time and/or negative potential. The formation of Fe(OEP)(NH_2OH) was dependent on kinetics rather than thermodynamic factors. The fact that Fe(OEP)(HNO) and Fe(OEP)(NH_2OH) were oxidized back to Fe(OEP)(NO) which indicated that the Fe-N(ligand) bond was not broken during the process. If the disproportionation reaction occurred, then the Fe(OEP)(NO) should appear at during the spectroelectrochemical experiments.

The vibrational bands for Fe(OEP)(NH_2OH) were observed at higher wavenumber region. A broad band with two peaks at 3566 and 3500 cm^{-1} was observed for NH_2OH moiety which was upshifted than substituted phenol band. The bands for Fe(OEP)(ND_2OD) was observed at 2688 and 2654 cm^{-1} using 2,3-dcp-d_1. The Co(OEP)(NH_2OH) complex showed two bands at 3683 and 3621 cm^{-1}. The stability of Fe(OEP)(NH_2OH) might be due to weakly THF binding.

The re-oxidation of hydroxylamine mimics the hydroxylamine oxidoreductase mechanism [83] where the hydroxylamine oxidation needs two electrons to return to the Fe(P)(HNO) complex. In our case, the ligand was bound which converted to Fe(P)(NO) upon re-oxidation. This result also similar to the conversion of Fe(P)(NH_2OH)$_2$ to Fe(P)(NO) with excess hydroxylamine.

A set of iron corrole nitrosyls were studied. The voltammetry showed a reduction potential positive than the Fe(OEP)(NO), Fe(OEPone)(NO) and Fe(PPDME)(NO) complexes which further confirmed the non-innocent (cation radical) character of corrole macrocycles. In case of the second reduction, the iron corrole nitrosyl complexes showed very negative potentials than the iron porphyrin nitrosyls.

The UV-visible spectroelectrochemistry experiments showed a red shift in the Soret bands and a broad band at Q band region. All complexes were reversible in the experimental time scale. The second electron reduction generated a new Soret bands for Fe(TpCF$_3$PC)(NO) and Fe(TPC)(NO) complexes were observed where for Fe(TpMePC)(NO) and Fe(TpOMePC)(NO) complexes the band was decreased. All the complexes showed an increased Q-band for first and second electron reductions. This behavior was consistent with the formation of anion radical.

The FTIR spectroelectrochemistry spectra showed a decrease of nitrosyl band to lower wavenumber region indicated the bond order for nitrosyl moiety was decreased. The substituents effect on phenyl ring in corrole macrocycle was insignificant. The shift of nitrosyl band was lower than Fe(OEP)(NO) and Fe(TPP)(NO). The drop of nitrosyl bands was in between heme and non-heme systems.[76]

The square wave voltammetry of iron corrole nitrosyls showed an unusual behavior in the presence of acids. With the addition of acids, the first wave shifted to negative even though the reduced species was chemically reversible. The UV-visible spectrum showed a broad Soret band in the presence of acid and was reversible in UV-visible spectroelectrochemical time scale. The ^{1}H NMR spectrum showed additional resonances which were not observed in the absence of acid. This clearly indicated that the iron corrole nitrosyls reacted with acids before electrolysis.

APPENDIX

Derivation of the flux equation for the heterogeneous equivalent.

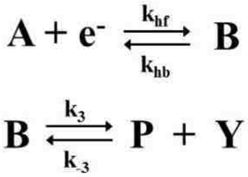

where $K_3 = k_3/k_{-3}$ and k_{hf} and k_{hb} are the forward and reverse heterogeneous electron transfer rates. Using the approach of Ruzic and Feldberg, the diffusion/kinetic equation for B is given by:

$$\frac{dB}{dt} = D_B \frac{d^2B}{dx^2} + k_3B - k_{-3}PY = 0 \tag{1}$$

Where B, P and Y are the concentrations for the respective species. It is assumed that the concentration of B is at steady state. The concentrations of Y and P at the reaction layer is given by:

$$Y \approx Y_o \approx Y_\mu \text{ and } P \approx P_o \approx P_\mu \tag{2}$$

Where Y_o and P_o are the concentrations at the electrode surface, and Y_μ and P_μ are the concentrations at the reaction layer thickness. The solution to Eq. 1 is:

$$B_\mu - B_x = a_1 \exp(-b_1x) + a_2 \exp(b_2x) \tag{3}$$

Because the solution must be bounded, $a_2 = 0$. At x = 0,

$$B_\mu - B_x = a_1 \quad \text{and} \quad -\frac{d^2B_0}{dx^2} = b_1^2a_1 \tag{4}$$

Substituting Eq. 4 into Eq. 1, we obtain,

$$-D_Bb_1^2\left(B_\mu - B_0\right) + k_3B_0 - k_{-3}P_\mu Y_\mu = 0 \tag{5}$$

The concentration of B_μ can be obtained in terms of P_μ and Y_μ using the equilibrium constant, K_3.

$$K_3 = \frac{P_\mu \, Y_\mu}{B_\mu} \tag{6}$$

and,

$$-D_B b_1^2 \left(\frac{P_\mu Y_\mu}{K_3} \right) + k_3 B_0 - k_{-3} P_\mu Y_\mu = 0 \tag{7}$$

Solving for b_1, we obtain,

$$b_1^2 = \frac{k_3}{D_B} \tag{8}$$

With the constants known in terms of other parameters, Eq. 3 becomes:

$$B_\mu - B_x = a_1 \exp(-b_1 x) = (B_\mu - B_0) \exp\left(-x\sqrt{k_3 / D_B}\right) \tag{9}$$

Solving Eq. 9 for B_x and substituting+ Eq. 6 for B_μ, we obtain,

$$B_x = \frac{P_\mu Y_\mu}{K_3} + \left(B_0 - \frac{P_\mu Y_\mu}{K_3} \right) \exp\left(-x\sqrt{k_3 / D_B}\right) \tag{10}$$

The flux of A and B at the electrode surface is given by the following equations:

$$(f_A)_0 = \frac{D_A (A_1 - A_0)}{\frac{1}{2}\Delta x} = 2D_A (A_1 - A_0) \tag{11}$$

$$(f_A)_0 = k_{hf} A_0 - k_{hb} B_0 \tag{12}$$

$$(f_B)_0 = 2D_B (B_1 - B_0) \tag{13}$$

$$(f_B)_0 = -(f_A)_0 \tag{14}$$

Combining Eq. 11-14, the flux of A at the electrode surface can be determined.

$$(f_A)_0 = \frac{\left(k_{hf}A_1 - k_{hb}B_1\right)}{1 + k_{hf}/2D_A + k_{hb}/2D_B} \tag{15}$$

The flux of B can be obtained from the derivative of Eq. 10.

$$(f_B)_0 = D_B\frac{dB_0}{dx} = D_B\left(k_3/D_B\right)^{1/2}\left(\frac{P_\mu Y_\mu}{K_3} - B_0\right) \tag{16}$$

$$(f_B)_0 = -k_{hf}A_0 + k_{hb}B_0 \tag{17}$$

$$(f_B)_0 = (f_Y)_\mu \tag{18}$$

$$(f_Y)_0 = 0; \quad (f\ )_0 = 0; \quad (f_B)_\mu = (f_Y)_\mu; \quad (f_P)_\mu = (f_Y)_\mu \tag{19}$$

The flux of Y is:

$$(f_Y)_0 = 2D_Y\left(Y_1 - Y_\mu\right); \quad (f_P)_0 = 2D_P\left(P_1 - P_\mu\right) \tag{20}$$

$$(f_Y)_\mu = (f_A)_0 \tag{21}$$

From Eq. 17, the concentration of B at x=0 is:

$$B_0 = \frac{(f_B)_0 + k_{hf}A_0}{k_{hb}} \tag{22}$$

Substituting Eq. 16 into Eq. 22,

$$(f_B)_0 = \left(D_B k_3\right)^{1/2}\left\{\frac{P_\mu Y_\mu}{K_3} - \left[\frac{(f_B)_0 + k_{hf}A_0}{k_{hb}}\right]]\right\} \tag{23}$$

Combining Eq. 11 and 14, the concentration of A₀ can be calculated:

$$A_0 = A_1 + \frac{(f_B)_0}{2D_A} \tag{24}$$

Substituting Eq. 24 into Eq. 23, A_0 will be eliminated.

$$(f_B)_0 = \left(D_B k_3\right)^{1/2}\left\{\frac{P_\mu Y_\mu}{K_3} - \left[\frac{(f_B)_0}{k_{hb}} + \frac{k_{hf}\left(A_1 + (f_B)_0/2D_A\right)}{k_{hb}}\right]]\right\} \tag{25}$$

Using Eq. 18, Eq. 25 can be expressed in terms of the flux of Y at the reaction layer.

$$\left(f_Y\right)_\mu = \left(D_B k_3\right)^{1/2}\left\{\frac{P_\mu Y_\mu}{K_3} - \left[\frac{\left(f_Y\right)_\mu}{k_{hb}} + \frac{k_{hf}\left(A_1 + \left(f_Y\right)_\mu / 2D_A\right)}{k_{hb}}\right]\right\} \tag{26}$$

The concentrations of P and Y at the reaction layer can be removed by using Eq. 20.

$$\left(f_Y\right)_\mu = \left(D_B k_3\right)^{1/2}\left\{\frac{1}{K_3}\left(Y_1 - \frac{\left(\left(f_Y\right)_\mu\right)}{2D_Y}\right)\left(P_1 - \frac{\left(\left(f_Y\right)_\mu\right)}{2D_P}\right) - \left[\frac{\left(f_Y\right)_\mu}{k_{hb}} + \frac{k_{hf}\left(A_1 + \left(f_Y\right)_\mu / 2D_A\right)}{k_{hb}}\right]\right\} \tag{27}$$

Combining all the terms in order to create a quadratic equation, the following result was obtained:

$$A_q\left(f_Y\right)_\mu^2 + B_q\left(f_Y\right)_\mu + C_q = 0 \tag{28}$$

where:

$$A_q = \frac{1}{4K_3 D_P D_Y} \tag{29}$$

$$B_q = -\left[\frac{1}{\sqrt{k_3 D_B}} + \frac{P_1}{2K_3 D_Y} + \frac{Y_1}{2K_3 D_P} + \frac{\theta}{2D_A} + \frac{1}{k_{hb}}\right] \tag{30}$$

$$C_q = \frac{Y_1 P_1}{K_3} - \theta A_1 \tag{31}$$

$$\theta = \frac{k_{hf}}{k_{hb}} \tag{32}$$

At the beginning of each cycle, the flux of Y was calculated (two solutions). The root that made physical sense (all concentrations must be positive) was used.

BIBLIOGRAPHY

1)Rosswall, T. "*Some perspectives of the major biogeochemical cycles",* ed. G. E. Likens, John Wiley & Sons Ithaca, New York, USA, **1981**, *2*, 199.

2) Moncada, S.; Palmer, R. M.; Higgs, E. A. *Pharmacol. Rev*. **1991**, *43,* 109-142.

3) Watkins C. S.; Stolz, J. F.; Basu, P. *Chem. Soc. Rev.* **2014**, *43*, 676-706.

4) Cole, J. A; Ferguson, S. J.*"The Nitrogen and Sulfur Cycles",* **1988**.

5) Campbell, W. H.; Kinghom, J. R. *Trends Bio-Chem. Sci.* **1990**, *15,* 315-319.

6) Wray, J. L.; Kinghom, J. R. *"Molecular and Genetics Aspects of Nitrate Assimilation",* **1989**, 88-190.

7) Murphy, M. J.; Siegel, L. M.; Tove, S. R.; Kamin, H. *Proc. Natl. Acad. Sci. U.S.A* **1974**, *71,* 612-616.

8) Murphy M. J.; Siegel, L.M. *J. Biol. Chem.* **1973**, *248,* 6911-6919.

9) Lancaster, J. R.; Vega, J. M.; Kamin, H.; Orme-Johnson, N. R.; Orme-Johnson,W. H.; Kruger, K. J.; Siegel, L. M. *J. Biol. Chem.*, **1979**, *254*, 1268-1272.

10) Lahners, K.; Kramer,V.; Back, E.;Privalle, L.; Rothstein, S. *Plant Physiol*. **1988**, *88*, 741-746.

11) Cole, J.A. *Molecular and Genetic Aspects of Nitrate Assimilation*, Wary, J.L.; Kinghor, J.R. Eds.; Oxford Science, **1989** ,229.

12) Hucklesby, D. P.; James, D. M.; Banwell, M. J.; Hewitt, E. J. *Phytochem.,* **1976**, *15*, 599-603.

13) Vega, J. M.; Kamin, H. *J. Biol. Chem.* **1977**, *252*, 896-909.

14) Cammack, R.; Hucklesby, D. P.; Hewitt, E. J. *Biochem. J.* **1978**,*171,* 519-526.

15) Hirasawa, M.; Tamura, G. *Agric. Biol.Chem.*, **1980**,*44,* 749-758.

16) Ida S.; Mikami, B. *Biochim. Biophys. Acta.* **1986,** *871,* 167-176.

17) Hirasawa, M.; Shaw, R. W.; Palmer, G.; Knaff, D. B. *J. Biol. Chem.* **1987,** *262,* 12428-12433.

18) Zumft, W. G. *Biochim. Biophys. Acta.* **1972,** *276,* 363-375.

19) Ho, C. H.; Ikawa, T.; Nildzawa, K. *Plant and Cell Physiol.* **1976,** *17,* 417-430.

20) Romero, L. C.; Galvan, F.; Vega, J. M. *Biochim. Biophysi. Acta.* **1987,** *914,* 55-63.

21) Vega, J. M., Garrett, R. H,, Siegel, L. M. *J. Biol. Chem.* **1975,** *250,* 7980-7989.

22) Prodouz, K. N.; Garrett, R. H. *J. Biol. Chem.* **1981,** *256,* 9711-9717.

23) Jackson, R. H.; Comish-Bowden, A., Cole, *J.* A. *Biochem. J.* **1981,** *193,* 861-867.

24) Swamy, U.; Wang, M.; Triphathy, J. N.; Kim S.K.; Hirasawa, M.; Knaff, D.B; Allen J.P. *Biochemistry,* **2005**, *44*, 16054-16063.

25) Ostrowski,J; Wu, J,Y.; Rueger, D.C.; Milller,B.E.; Seigle, L.M.; Kredish N.M. *J. Biol. Chem.***1989**, *264*, 15726-15737.

26) Tan, J; Cowan, J.A. *Biochemistry* **1991**, *30*, 8910-8917.

27) Kuznetsova, S.; Knaff, D.B.; Hirasawa, M.; Lagoutte, B.; Setif, P. *Biochemistry* **2004**, *43*, 510-517.

28) Kuznetsova, S.; Knaff, D.B.; Hirasawa, M; Lagoutte, B.; Setif, P.; Mattioli, T.A. *Biochemistry*, **2004**, *43*, 10765-10774.

29) Einsle,O.; Messerschmidt, A.; Huber, R.; Kroneck, M.H.; Neese F. *J. Am. Chem. Soc.* **2002**, *124*, 11737-11745.

30) Barkigia, K. M.;Chang, C. K.; Fajer, J.; Renner, M.W. *J. Am. Chem. Soc.,* **1992**, *114*,1701-1707.

31) Henry, Y.; Bessieres, P. *Biochimi* **1984**, *66*, 259-289.

32) Carr, G.J.; Page, M.D.; Ferguson, S.J. *Eur. J. Biochem.* **1989**, *179*, 683-692.

33) Zafiriou, O.C.; Hanley, Q.S.; Synder, G. *J. Biol. Chem.* **1989**, *264*, 5694-5699.

34) Goretski, J.; Hollocher, T.C. *J. Biol. Chem.* **1990**, *265*, 889-895.

35) Goretski, J.; Zafiriou, O.C.; Hollocher, T.C. *J. Biol. Chem.* **1990**, *265*, 11535-11538.

36) Toledo, Jr, J.C., Augusto, O. *Chem. Res. Toxicol.* **2012**, *25*, 975-989.

37) Wolin, M. S.; Wood, K. S.; Ignarro, L. J. *J. Biol. Chem.* **1982**, *257*, 3312−3320.

38) Barley, M. H.; Rhodes, M. R.; Meyer, T. *Inorg. Chem.* **1987**, *26*,1746-1750.

39) Ignarro, L. J., Byrns, R. E., Buga, G. M., and Wood, K. S. *Circ. Res.* **1987**, *61*, 866−879.

40) Ignarro, L. J., Buga, G. M., Wood, K. S., Byrns, R. E., Chaudhuri, G. *Proc. Natl. Acad. Sci.U.S.A.* **1987,** *84*, 9265−9269.

41) Speelman, A. L. ; Lehnert, N. *Acc. Chem. Res*. **2014**, *47*, 1106−1116.

42) Shafirovich, V.; Lymar, S. V. *Proc. Natl. Acad. Sci. USA* **2002,** *99*, 7340-7345.

43) Shafirovich, V., Lymar, S. V. *J. Am. Chem.Soc.* **2003**, *125*, 6547-6552.

44) Lymar, S.V.; Shafirovich, V.; Poskrebyshev, G.A. *Inorg.Chem*. **2005**, *44*, 5212-5221.

45) Gratzel, M.; Taniguchi, S.; Henglein, A. *Ber. Bunsen-Ges. Phys. Chem.* **1970**, *74*, 1003-1010.

46) Arnold, W. P.; Mittal, C. K.; Katsuki, S.; Murad, F. *Proc. Natl. Acad. Sci.U.S.A.* **1977**, *74*, 3203−3207.

47) Wolin, M. S.; Wood, K. S.; Ignarro, L. J. *J. Biol. Chem.* **1982**, *257*, 3312−3320.

48) Barley, M. H.; Rhodes, M. R.; Meyer, T. *Inorg. Chem.* **1987**, *26*,1746-1750.

49) Barley, M. H.; Takeuchi, K. J.; Meyer, T. J. *J. Am. Chem. Soc.* **1986**, *108*, 5876-5885.

50) Barley, M. H.; Takeuchi K.; Murray Jr, W. R.; Meyer, T. J. *J. Chem. Soc.,Chem. Commun.***1985**, 507-508.

51) Choi, l-K.; Ryan, M. D. *Inorg. Chim. Acta.* **1988**, *153*, 25-30.

52) Olson, L. W.; Schaeper, D.; Lancon, D.; Kadish, K. M. *J. Am. Chem. Soc.***1982**, *104*, 2042-2044.

53) Lancon, D.; Kadish, K. M. *J. Am. Chem. Soc.* **1983**, *105*, 5610-5617.

54) Mu, X. H.; Kadish, K. M. *Inorg. Chem.* **1988**, *27*, 4720-4725.

55) Fujita, E ; Faler, J. *J. Am. Chem. Soc*. **1983**, *105*, 6743-6745.

56) Scheidt, W. R.; Frisse, M. E. *J. Am. Chem. Soc.* **1975**, *97*, 17-21.

57) Scheidt, W. R.; Piciulo, P. L. *J. Am. Chem. Soc.* **1976**, *98*, 1913-1919.

58) Scheidt, W. R.; Bringar, A. C.; Ferro, E. B.; Kirner, J.F. *J. Am. Chem.Soc.***1977**, *99*,7315-7322.

59) Scheidt, W. R.; Lee, Y. J.; Hatano, K. *J. Am. Chem. Soc.* **1984**, *106*, 3191-3198.

60) Wayland, B. B.; Olson, L. W. *J. Am. Chem. Soc.* **1974**, *96*, 6037-6041.

61) Finnegan, M. G.; Lappin, A. G.; Scheidt, W. R. *Inorg. Chem.* **1990**, *29*.181-185.

62) Scholler, D. M.; Wang, M-Y. R,; Hoffman, B. M. *J. Biol. Chem.* **1979**, *254*, 4072-4078.

63) Chottard, G.; Battioni, P.; Battioni, J.P.; Lange, M.; Mansuy, D. *Inorg.Chem.***1981**, *20*, 1718-1722.

64) Stong, J. D.; Burke, J. M.; Weight, P. D.; Spiro, T. C. *J. Am. Chem. Soc.* **1980**, *102*, 5815-19.

65) Wayland, B. B.; Olson, L W. *J. Chem. Soc., Chem. Commun.* **1973**, 897-898.

66) Yoshimura, T. *Inorg. Chim. Acta*. **1986**, *125*, L27-L29.

67) Scheidt, W.R.; Duval, H.F.; Neal, T.J.; Ellison**,** M.K**.** *J. Am. Chem. Soc.* **2000,** *122*, 4651- 4659.

68) Janick, P. A. *Ph. D. Dissertation, Duke University,* **1982.**

69) Liu, Y. *Ph.D. Dissertation, Marquette University,* **1991.**

70) Liu Y.; DeSilva C.; Ryan M.D. *Inorg. Chim. Acta* **1997**, *258*, 247-255.

71) Praneeth, V. K. K.; Näther, C.; Peters, G.; Lehnert, N. *Inorg. Chem.* **2006**, *45*, 2795-2811.

72) Lui,Y.; Ryan M.D. *J. Electroanal. Chem.* **1994**, *368*, 209-219.

73) Choi, I.-K.; Liu, Y.; Feng, D.; Paeng, K.-J.; Ryan, M. D. *Inorg. Chem.* **1991,** *30*,1832−1839.

74) Goodrich, L.E.; Roy, S.; Alp, E.E.; Zhao, J.J.; Hu, M.Y.; Lehnert, N. *Inorg. Chem.* **2013**, *52*, 7766−7780.

75) Wei, Z.; Ryan, M. D. *Inorg. Chem.* **2010**, *49*, 6948-6954.

76) Speelman, A.L. ; Lehnert, N. *Acc. Chem. Res*. **2014**, *47*, 1106−1116.

77) Kumar, M.R.; Pervitsky, D.; Poulos, T.; Kundu, S.; Hargrove, M.S.; Rivera, E.J.; Diaz, A.;Colon, J.L.; Farmer, P.J. *Biochemistry,* **2009**, *48*, 5018-5025.

78) Miranda, K. M., *Coord. Chem. Rev.* **2005,** *249*, 433-455.
79) Einsle, O.; Messerschmidt, A.; Huber, R.; Kroneck, P. M. H.; Neese, F. *J. Am. Chem. Soc.***2002,** *124*, 11737-11745.

80) Bykov, D.; Neese, F. *Inorg. Chem.* **2015,** *54*, 9303-9316.

81) Daiber, A.; Shoun, H.; Ullrich, V. *J. Inorg. Biochem.* **2005,** *99*, 185-193.

82) Averill, B. A. *Chem. Rev* **1996,** *96*, 2951-2964.

83) Cabail, M. Z.; Kostera, J.; Pacheco, A. A. *Inorg. Chem.* **2005,** *44*, 225-231.

84) Sulc, F.; Immoos, C. E.; Pervitsky, D.; Farmer, P.J. *J. Am. Chem. Soc.* **2004**, *126*, 1096-1101.

85) Bartberger, M.D.; Liu, W.; Ford,E.; Miranda, K.M.; Switzer,C.; Fukuto,J.M.; Farmer,P.J.; Wink, D. A.; Houk, K.N. *Proc. Natl. Acad. Sci. U.S.A.* **2002**, *99*, 10958-10963.

86) Lin, R.; Farmer, P. J. *J. Am. Chem. Soc.* **2000,** *122*, 2393-2394.

87) Immoos, C. E.; Sulc, F.; Farmer, P. J.; Czarnecki, K.; Bocian, D. F.; Levina, A.; Aitken, J. B.; Armstrong, R. S.; Lay, P. A. *J. Am. Chem. Soc*. **2005**, *127,* 814−815.

88) Rich, A. M.; Armstrong, R. S.; Ellis, P. J.; Lay, P. A. *J. Am. Chem. Soc.* **1998**, *120,* 10827-10836.

89) Jacox, M.E.; Milligan,D.E. *J. Mol. Spectrosc.* **1973**, *48*, 536-559.

90) Czarnecki, K.; Kincaid, J. R. *J. Raman Spectrosc* **2012,** *43,* 1343-1345.

91) Lee, T.; Hwang, S.; Lim, M. *J. Phys. Chem. B* **2015**, *119*,1814-1822.

92) Conradie, J.; Ghosh, A. *J. Phys. Chem. B* **2016,** *120*, 4972-4979.

93) Abucayon, E. G.; Khade, R. L.; Powell, D. R.; Zhang, Y.; Richter-Addo, G. B. *J. Am.Chem.Soc.* **2016,** *138*, 104-107.

94) Hu, B.; Li, J. *Angew. Chem., Int. Ed.* **2015**, *54*, 10579−10582.

95) G. R. A. Wyllie, W. R. Scheidt, *Chem. Rev.* **2002**, *102,* 1067-1090.

96) N. Lehnert, W. R. Scheidt, M. Wolf in Nitrosyl Complexes in Inorganic Chemistry, *Biochemistry and Medicine II*, Vol. 154 (Ed.: D. M. P. Mingos), Springer, Berlin, **2014**, p.155.

97) Kundakarla, N.; Lindeman, S.; Rahman, M. H.; Ryan, M. D. *Inorg. Chem.* **2016,** *55*, 2070-2075.
98) Kadish, K.M.; Ou, Z.; Tan, X.; Boschi, T.; Monti, D.; Fares, V.; Tagliatesta, P. *J. Chem. Soc. Dalton Trans.* **1999,** 1595.

99) Ellison, M.K.; Scheidt, W.R. *Inorg. Chem.* **1998**, *37*, 382-383.

100) Godbout, N.; Sanders, L. K. ; Salzmann, R.; Havlin, R.H.; Wojdelski, M.; Oldfield, E. *J. Am.Chem. Soc.* **1999**, *121*, 3829-3844.

101) Grande, L.M.; Noll, B.C.; Oliver, A.G.; Scheidt, W.R. *Inorg. Chem.* **2010**, *49*, 6552-6557.

102) Davlieva, M. G.; Lü, J. M.; Lindeman, S. V.; Kochi, J. K. *J. Am.Chem. Soc.* **2004**, *126*, 4557−4565.

103) Yoshimura, T. *Bull. Chem. Soc. Japan*, **1978**, *51(4)*, 1237-1238.

104) Yoshimura, T. *Arch. Biochem. Biophys.* **1983**, *220*, 167-178.

105) Yoshimura, T. Ozaki, T.; *Arch. Biochem. Biophys.* **1984**, *229*, 126-135.

106) Scheidt, W. R.; Ellison, M. K. *Acc. Chem. Res.* **1999**, *32*, 350-359.

107) Graeme R.A.W.; Silvernail, N.J.; Oliver, A.G.; Schulz, C.E.; Scheidt, W.R. *Inorg. Chem*. **2014**, *53*, 3763-3768.

108) Berto, T. C.; Praneeth, V.K.K.; Goodrich, L.E.; Lehnert, N. *J. Am. Chem. Soc.* **2009**, *131*,17116-17126.

109) Hashimoto, T.; Dyer, R.L.; Crossley, M.J.; Baldwin, J. E.; Basolo, F. *J. Am. Chem. Soc.***1982**, *104*, 2101-2109.

110) Zakharieva, O.; Schunemann, V.; Gerdan, M.; Lioccia S.; Cai, S.; Walker, F. A.; Trautwein, A. X. *J. Am, Chem. Soc.* **2002**,*124*, 6636-6648.

111) Licoccia, S.; Paolesse, R. *Struct. Bonding* **1995**, *84*, 71-133.

112) Gross, Z. *J. Biol. Inorg. Chem.* **2001**, *6*, 733-738.

113) Horheim, H. K.; Capar, J.; Einrem, R.F.; Gagnon, K, J.; Beavers, C.M.; Lima, H.V.; Ghosh, A. *Dalton Trans*. **2016**, *45*, 681-689.

114) Alemayehu, A. B.; Conradie, J.; Ghosh, A.; *Eur. J. Inorg. Chem.* **2011**, *12*, 1857–1864.

115) Wasbotten, I. H.; Wondimagegn, T.; Ghosh, A. *J. Am. Chem. Soc.*, **2002**, *124*, 8104–8116.

116) Ou, Z. ; Shao, J. ; Zhao, H.; Ohkubo, K.; Wasbotten, I.H.; Fukuzumi, S.; Ghosh,A.; Kadish, K.M. *J. Porphyrins Phthalocyanines*, **2004**, *8*, 1236–1247;
117) Thomas, K.E.; Conradie, J.; Hansen, L.K.; Ghosh, A. *Eur. J. Inorg. Chem.*, **2011**,1865–1870.

118) Steene, E.; Wondimagegn, T.; Ghosh, A. *J. Phys. Chem. B*, **2001**, *105*, 11406–11413.

119) Steene, E.; Wondimagegn, T.; Ghosh, A. *J. Phys. Chem. B*, **2002**, *106*, 52312–5312.

120) Steene, E.; Wondimagegn, T.; Ghosh, A. *J. Am. Chem. Soc.*, **2003**,*125*, 16300–16309.

121) Ghosh, A.; Steene, E. *J. Inorg. Biochem.*, **2002**, *91*, 423–436.

122) Thomas, K. E. ; Alemayehu, A. B. ; Conradie, J.; Beavers, C.; Ghosh, A. *Inorg. Chem*., **2011**, *50*, 12844–12851.

123) Johansen, I.; Norheim, H.K.; S. Larsen, Alemayehu, A. B.; Conradie, J.; Ghosh, A. *J. Porphyrins Phthalocyanines*, **2011**, *15*, 1335–1344.

124) Alemayehu, A.B.; Gagnon, K.J.; Terner.J.; Ghosh,A. *Angew. Chem., Int. Ed.*, **2014**, *53*,14411–14414.

125) Alemayehu, A. B.; Vazquez-Lima, H.; Beavers, C.M.; Gagnon, K.J.; Bendix, J.; Ghosh, A. *Chem.Commun*., **2014**, *50*, 11093–11096.

126) Cai, S.; Walker, F. A.; Licoccia, S. *Inorg. Chem*. **2000**, *39*, 3466-3478.

127) Cai, S.; Licoccia, S.; Paolesse, R.; Nardis, S.; Bulach, V.; Zimmer, B.; Shokhireva, T. Kh.; Walker, F. A. *Inorg. Chimica. Acta*, **2002**, *339*, 171-178.

128) Vogel, E.; Will, S.; Schulze Tilling, A.; Neumann, L.; Lex, J.; Bill, E.; Trautwein, A. X.; Wieghardt, K. *Angew. Chem., Int. Ed. Engl.* **1994**, *33*,731-735.

129) Simkhovic,L.; Galili, N.; Saltsman, I.; Goldberg, I.; Gross,Z. *Inorg. Chem*.**2000**, *39*, 2704-2705.

130) Simkhovich, L.; Mahammed, A.; Goldberg, I.; Gross, Z. *Chem. Eur. J.* **2001**, *7*, 1041-1055.

131) Steene, E.; Wondimagegn, T.; Ghosh, A. *J. Phys. Chem. B* **2001**, *105*, 11406-11413.

132) Ghosh, A.; Steene, E. *J. Biol. Inorg. Chem.* **2001**, *6*, 739-752.

133) Walker, F. A. Proton NMR and EPR Spectroscopy of Paramagnetic Metalloporphyrins. In *The Porphyrin Handbook*; Kadish, K. M., Smith, K. M., Guilard, R., Eds.; Academic Press: San Diego, CA., **2000**, Vol. 5, Chapter 36, pp 81-183.

134) Walker, F. A.; Nasri, H.; Turowska-Tyrk, I.; Mohanrao, K.; Watson, C. T.; Shokhirev, N. V.; Debrunner, P. G.; Scheidt, W. R. *J. Am.Chem. Soc.* **1996**, *118*, 12109-12118.

135) Groves, J. T.; Shalyaev, K.; Lee, J. In *The Porphyrin Handbook*; Kadish, K. M., Smith, K. M., Guilard, R. Eds.; Academic: San Diego, **2000**, *Vol. 4*, Ch. 27, 17.

136) Scheidt, W. R. *J. Biol. Inorg. Chem.* **2001**, *6*, 727-732.

137) Buisson, G.; Deronzier, A.; Duee, E.; Gans, P.; Marchon, J.-C.; Regnard, J.-R. *J. Am. Chem. Soc.* **1982**, *104*, 6793-6796.

138) Phillippi, M. A.; Goff, H. M. *J. Am. Chem. Soc.* **1979**, *101*, 7641-7643.

139) Phillippi, M. A.; Shimomura, E. T.; Goff, H. M. *Inorg. Chem.* **1981**, *20*, 1322-1325.

140) Vazquez-Lima, H.; Horheim, H, Einrem, R.F.; Ghosh, A. *Dalton Trans*. **2015**, *44*, 10146-10151.

141) Nardis, S.; Paolesse, R.; Licoccia, S.; Fronczek, F.R.; Vicente, M. H.; Shokhireva.T.K.; Cai, S.; Walker, F.A. *Inorg. Chem*. **2005**, *44*, 7030-7046.

142) Bard, A. J.; Faulkner, L. R. "*Electrochemical Methods*', John Wiley & Sons, Inc., U.K.,**2004**; Chapter 9, pp 331-367.

143) Prater, K. B.; Bard, A. J. *J. Electrochem. Soc.* **1970,** *117*, 207-213.

144) Prater, K. B.; Bard, A. J. *J. Electrochem. Soc.* **1970,** *117*, 335-340.

145) Prater, K. B. Digital simulation of the rotating ring-disk electrode. In *Electrochemistry:Calculations, Simulation, and Instrumentation*, Mattson, J. S.; Mark, H. B., Jr.; MacDonald, H. C., Jr., Eds. Marcel Dekker: New York, **1972**; pp 219-240.

146) Richardson, P.F.; Chang, C.K.; Hanson, L.K.; Spaulding, L.D.; Fajer, J. *J.Phys. Chem.* **1979**, *83*, 3420-3424.

147) Bonnette, R.; Gale, A.D.; Stephenson, G.F. *J. Chem. Soc.* **1967,** 1168-1172.

148) Ruzic, I. *J. Electroanal. Chem.* **1983**, *144*, 433-436.

149) Ruzic, I. Feldberg, S. *J. Electroanal. Chem.* **1974**, *50*, 153-162.

150) Prater, K.B. *Chem. Instrum*. **1972**, *3*, 259-269.

151) Keesey, R. L.; Ryan, M. D. *Anal. Chem.* **1999,** *71*, 1744-1752.

152) Dolphin, D.; Sams, J. R.; Tsin, T. B.; Wong, K. L. *J. Am. Chem. Soc.* **1976,** *98*, 6970-75.

153) Welborn, C.; Dolphin, D.; James, B. R. *J. Am. Chem. Soc.* **1981,** *103*, 2869-2871.

154) Feng, D.; Ryan, M. D. *Inorg. Chem.* **1987,** *26*, 2480-2483.

155) Golubev, K.S.; Denisov, G. S.; KoI'tsov, A, I. *Proc.Acad. Sci. USSR*. **1976,** 144-147.

156) Ng, S. *Spectrochimica. Acta.* **1980**, *36A*, 927-928.

157) Codesido, N. O.; Weyhermuller, T.; Olabe, J. A.; Slep, L.D. *Inorg.Chem.* **2014**, *53*, 981-997.